METAMATERIALS AND METASURFACES FOR WAVEFRONT SHAPING AND DISPERSION MANAGEMENT

VINICIUS MARRARA PEPINO

Advisor: Prof. Titular Ben-Hur Viana Borges

EESC · USP

Vinicius Marrara Pepino

Metamaterials and metasurfaces for wavefront shaping and dispersion management

Doctoral thesis presented to the School of Engineering of São Carlos in fullfilment of the requirements for the academic degree of Doctor in Sciences - Graduate Program in Electrical Engineering

Area of concentration: Telecommunications

Advisor: Prof. Dr. Ben-Hur Viana Borges

Trata-se da versão corrigida da tese. A versão original se encontra disponivel na EESC/USP que aloja o Programa de Pos-Graduacão de Engenharia Eletrica.

São Carlos

2023

FOLHA DE JULGAMENTO

Candidato: Engenheiro **VINICIUS MARRARA PEPINO**.

Título da tese: "Metamateriais e metassuperfícies para modulação de frente de onda e gerenciamento de dispersão".

Data da defesa: 27/09/2023.

Comissão Julgadora	**Resultado**
Prof. Titular Ben Hur Viana Borges **(Orientador)** (Escola de Engenharia de São Carlos/EESC-USP)	APROVADO
Prof. Dr. Hugo Enrique Hernández Figueroa (Universidade Estadual de Campinas/UNICAMP)	APROVADO
Prof. Dr. Newton Cesario Frateschi (Universidade Estadual de Campinas/UNICAMP)	APROVADO
Prof. Dr. Marcos Roberto da Rocha Gesualdi (Universidade Federal do ABC/UFABC)	APROVADO
Prof. Associado Daniel Varela Magalhães (Instituto de Física de São Carlos/IFSC-USP)	APROVADO

Coordenador do Programa de Pós-Graduação em Engenharia Elétrica:
Prof Associado **Marcelo Andrade da Costa Vieira**

Presidente da Comissão de Pós-Graduação:
Prof. Titular **Carlos De Marqui Junior**

This work is dedicated to every curious mind in this world who wish to use this knowledge for the improvement of peoples lives.

ACKNOWLEDGEMENTS

The first thing that comes to mind when I look back to all those years of this arduous yet rewarding march that we call a Ph.D. program is that this is not a path that is possible to follow alone. Research depends on knowledge, which comes from the accumulation of previous research, and also depends on discussions, support (both emotional and financial), which comes from other people around you. This is particularly true when I remember that a whole pandemic happened during the course of my Ph.D., a pandemic from which I believe that no one who survived was left unscathed. In my case, the pandemic was responsible to keep me in lock-down from the week after I arrived in Columbus, OH for my exchange program until the end of the referred program, which blocked the possibilities of experimental studies, cultural and social interactions, and any type of in person interactions in a country I had barely arrived. After these considerations, I would like to thank people that were important during this journey.

The first person to be thanked is obviously my supervisor, Professor Ben-Hur V. Borges. I have worked with Professor Ben-Hur since my senior project in undergrad course in Electrical Engineering, and he has always been someone I could trust and someone who always brought important discussions, ideas and insights to the table. Professor Ben-Hur represents a very significant part of my academic development.

Next, I would like to thank Professor Fernando L. Teixeira, my supervisor in my period at OSU. Professor Fernando welcomed me as best as possible considering the situations at the time, and provided important guiding and insights for the research conducted in my period there.

Another person that deserves special thanks is Professor Achiles F. da Mota. I met Achiles while he was still concluding his Ph.D. as a student of Professor Ben-Hur. Achiles has always helped me in the initial stages of my research, and to this this he has collaborated in all of my published works, always participating in fruitful discussions and bringing valuable insights.

I would also like to thank Professors Emiliano R. Martins and Luiz G. Neto from USP, for their contributions in my work and for their valuable classes.

In a more personal side, I want to thank my family; my mother, Isabel, my father, Sergio, and my sister, Isabela, for all the emotional and economic support, before, during, and after the course of my Ph.D. program.

Thanks to my childhood friends that I still meet frequently and who were clearly important during various moments of stress and of joy: In no particular order, thanks to Igor, Henrique, Omar, Mario, Rafael, Daniel, Guilherme.

"Victory will belong only to those who have faith in the people, those who are immersed in the life-giving spring of popular creativity."

V. I. Ulianov

ABSTRACT

PEPINO, V. M. **Metamaterials and metasurfaces for wavefront shaping and dispersion management**. 2023. 193p.

Thesis (Doctor) - Escola de Engenharia de São Carlos, Universidade de São Paulo, São Carlos, 2023.

Metamaterials and metasurfaces, cutting-edge technologies, have recently garnered significant attention. They provide unprecedented control over electromagnetic wave behavior, enabling the manipulation of light, sound, and other waveforms in unprecedented ways. Engineered at a sub-wavelength scale, these materials possess unique properties not found in natural substances. The concept of metamaterials arose from the notion of crafting artificial structures with distinctive electromagnetic characteristics through precise internal structure manipulation, yielding materials with extraordinary traits like negative and near-zero refractive indices, perfect absorption or reflection, enhanced polarization, chirality effects, and dispersion management.

Within this thesis, four primary contributions are outlined. Initially, a three-dimensional, all-dielectric, planar metalens, fabricated through 3D printing, enhances microwave focusing into a receiving antenna. This structure elevates antenna gain by 7.5 dB at 32.5 GHz within a 2.4 GHz bandwidth. The metalens achieves a focus with a full-width at half-maximum of approximately 0.85λ and a 3 dB depth-of-focus of around 5 cm. In azimuthal and elevation planes, the antenna's half-power beamwidth is reduced from 36° to 3° and from 4.5° to 3°, respectively, with the assistance of the metalens. Notably, the metalens performs effectively under oblique incidence, spanning 50° in the azimuthal plane and 40° in the elevation plane.

Next, a tunable terahertz Bessel beam with variable depth of focus (ranging from 22 cm to 40 cm) and adjustable beam width (from 3.7 mm to 6 mm) is designed for imaging and communication applications. Silicon microholed metasurfaces are organized in an Alvarez-type configuration. The meta axicon operates at 850 GHz and exhibits self-healing capabilities against obstructions considerably larger than the operating wavelength.

Subsequently, a fully passive terahertz pulse amplification device harnesses the temporal Talbot effect within a highly dispersive silicon-based metamaterial Bragg fiber. Three distinct strategies, identified as coherent pulse addition, forward Talbot illuminator, and backward Talbot illuminator, are introduced and explored to maximize passive Talbot effect gain. These approaches accommodate a wide range of output pulse shapes and yield

gain factors of 5.8 dB (coherent pulse addition), 9.9 dB (forward Talbot illuminator), and 8.8 dB (backward Talbot illuminator). Numerical simulations indicate the potential of these methods for developing high-gain passive amplification terahertz devices.

The temporal Talbot effect practical observation in the microwave realm has been hindered by the requirement for controlled propagation through a highly dispersive waveguide. Overcoming this challenge, we implemented an ultra-wideband, linearly chirped Bragg grating within a standard microwave X-Band waveguide. Utilizing backwards Talbot array illuminators with particle swarm optimization, we achieved passive amplification with gains of 3.45 dB (for Gaussian pulses) and 4.03 dB (for raised cosine pulses). Moreover, numerical assessments indicate that the gain can theoretically exceed 8 dB with higher quality dielectrics. This breakthrough opens doors to various microwave applications of the Talbot effect, including temporal cloaking, sub-noise microwave signal detection, microwave pulse shaping, and microwave noise reduction.

Keywords: Metasurfaces, metamaterials, metalens, non-diffractive beams, wavefront shaping, dispersion management, passive amplification, Fano resonances, Talbot effect.

LEYMAN SUMMARY

PEPINO, V. M. **Metamaterials and metasurfaces for wavefront shaping and dispersion management**. 2023. 193p.

Thesis (Doctor) - Escola de Engenharia de São Carlos, Universidade de São Paulo, São Carlos, 2023.

Metamaterials and metasurfaces, cutting-edge technologies, and are increasingly gaining significant attention in the last years. They provide unprecedented control over electromagnetic wave behavior, enabling responses that go beyond the characteristics of the host materials. Engineered at a very tiny scale, these materials possess unique properties usually not found in nature.

Within this thesis, four primary contributions are outlined using these materials. Initially, we designed for the first time a 3D printed metasurface for applications in 5G cellular technology. This metasurface is designed to act as a lens, focusing a microwave signal into a receiving antenna. This structure increases the antenna receiving efficiency in over 5 times in a large bandwidth. The metalens achieves a very tight focus, almost at the physical limit, while also making the antenna more directive, improving its performance in the desired direction. Notably, the metalens performs effectively under oblique incidence, up to 50° x 40°.

Next, a metasurface for THz frequencies is designed. THz frequencies have an enormous potential for 6G communications and imaging, with its non ionizing radiation making it better suited than x-rays for medical applications. It is however limited by low power sources. Our Silicon metasurface generates high efficiency beams, called Bessel beams, with variable propagation distance and adjustable resolution, optimal for imaging and communication applications.

Subsequently, a fully passive terahertz pulse amplification device uses a dispersive effect, called the temporal Talbot effect within a precisely engineering metamaterial fiber. Three distinct strategies, identified as coherent pulse addition, forward Talbot illuminator, and backward Talbot illuminator, are introduced and explored to maximize passive Talbot effect gain. These approaches accommodate a wide range of output pulse shapes and yield gain factors of over 7 times, without the need for active components, that are lacking in THz frequencies.

Finally, we implemented, for the first time, practical observation of the temporal talbot

effect in the microwave realm using a 3D printed metamaterial, called a linearly chirped Bragg grating. Utilizing our previous techniques with optimization algorithms, we achieved passive amplification with gains 2 and a half times for precisely designed pulses. Moreover, we observed that we can theoretically increase the gain in an extra 2.5 times factor with higher quality 3D printing materials. This breakthrough opens doors to various microwave applications of the Talbot effect, including temporal cloaking, sub-noise microwave signal detection, microwave pulse shaping, and microwave noise reduction.

RESUMO

PEPINO, V. M. **Metamateriais e metassuperfícies para modulação de frente de onda e gerenciamento de dispersão**. 2023. 193p.

Tese (Doutorado) - Escola de Engenharia de São Carlos, Universidade de São Paulo, São Carlos, 2023.

Metamateriais e metassuperfícies, tecnologias de ponta, têm recentemente atraído atenção significativa da comunidade científica. Eles oferecem um controle sem precedentes sobre o comportamento de ondas eletromagnéticas, possibilitando a manipulação de luz, som e outras formas de ondas de maneiras inéditas. Fabricados em uma escala sub-comprimento de onda, esses materiais possuem propriedades únicas não encontradas em substâncias naturais. O conceito de metamateriais surgiu da ideia de criar estruturas artificiais com características eletromagnéticas distintas por meio de uma manipulação precisa de sua estrutura interna, resultando em materiais com traços extraordinários, como índices de refração negativos e próximos de zero, absorção ou reflexão perfeitas, efeitos de polarização e quiralidade aprimorados e gerenciamento de dispersão.

Nesta tese, são apresentadas quatro contribuições principais. Inicialmente, uma metalente plana tridimensional totalmente dielétrica, fabricada por meio de impressão 3D, aprimora o foco de micro-ondas em uma antena receptora. Essa estrutura eleva o ganho da antena em 7,5 dB a 32,5 GHz com uma largura de banda de 2,4 GHz. A metalente atinge um foco com uma largura completa à meia-altura de cerca de $0,85\lambda$ e uma profundidade de foco de 3 dB de aproximadamente 5 cm. Nos planos azimutal e de elevação, a largura do feixe à meia-potência da antena é reduzida de 36° para 3° e de 4,5° para 3°, respectivamente, com a ajuda da metalente. Vale ressaltar que a metalente funciona eficazmente sob incidência oblíqua, abrangendo 50° no plano azimutal e 40° no plano de elevação.

Em seguida, é projetado um feixe de Bessel sintonizável de terahertz, com profundidade de foco variando de 22 cm a 40 cm e largura do feixe ajustável de 3,7 mm a 6 mm, para aplicações de imagem e comunicação. Metassuperfícies de microfuros de silício são organizadas em uma configuração do tipo Alvarez. O meta-axicon opera a 850 GHz e demonstra capacidade de auto-regeneração contra obstruções muito maiores do que o comprimento de onda operacional.

Posteriormente, é proposto um dispositivo totalmente passivo de amplificação de pulsos de terahertz com base na exploração do efeito Talbot temporal em uma fibra de Bragg de metamaterial de silício altamente dispersiva. Três estratégias distintas, denominadas adição

coerente de pulsos, iluminador Talbot direto e iluminador Talbot reverso, são introduzidas e exploradas para maximizar o ganho passivo do efeito Talbot. Essas abordagens acomodam uma ampla gama de formatos de pulsos de saída e resultam em fatores de ganho de 5,8 dB (adição coerente de pulsos), 9,9 dB (iluminador Talbot direto) e 8,8 dB (iluminador Talbot reverso). Simulações numéricas indicam o potencial desses métodos para o desenvolvimento de dispositivos de amplificação de terahertz de alto ganho.

A observação prática do efeito Talbot temporal no domínio das micro-ondas tem sido prejudicada pela necessidade de propagação controlada por meio de um guia de ondas altamente dispersivo. Superando esse desafio, implementamos uma rede de Bragg linearmente chirpada de banda ultralarga em um guia de ondas de micro-ondas padrão na faixa X. Utilizando iluminadores de matriz Talbot reversa auxiliados pela otimização por enxame de partículas, alcançamos amplificação passiva com ganhos de 3,45 dB (para pulsos gaussiano) e 4,03 dB (para pulsos cosseno elevado). Além disso, avaliações numéricas indicam que o ganho pode teoricamente superar 8 dB com dielétricos de maior qualidade. Essa conquista abre portas para várias aplicações das micro-ondas do efeito Talbot, incluindo camuflagem temporal, detecção de sinal de micro-ondas abaixo do ruído, modelagem de pulsos de micro-ondas e redução de ruído de micro-ondas.

Palavras-chave: Metassuperfícies, metamateriais, metalentes, feixes não difrativos, modulação de frente de onda, gerenciamento de dispersão, amplificação passiva, ressonâncias Fano, efeito Talbot.

RESUMO PARA LEIGOS

PEPINO, V. M.   **Metamateriais e metassuperficies para modulacão de frente de onda e gerenciamento de dispersão**. 2023. 193p.

Tese (Doutorado) - Escola de Engenharia de São Carlos, Universidade de São Paulo, São Carlos, 2023.

Metamateriais e metassuperfícies, tecnologias avançadas, têm ganhado cada vez mais atenção nos últimos anos. Eles proporcionam um controle sem precedentes sobre o comportamento das ondas eletromagnéticas, permitindo respostas que ultrapassam as características dos materiais hospedeiros. Projetados em uma escala muito pequena, esses materiais possuem propriedades únicas normalmente não encontradas na natureza.

Nesta tese, são apresentadas quatro principais contribuições utilizando esses materiais. Inicialmente, projetamos, pela primeira vez, uma metassuperfície impressa em 3D para aplicações na tecnologia celular 5G. Essa metassuperfície é projetada para atuar como uma lente, concentrando um sinal de micro-ondas em uma antena receptora. Essa estrutura aumenta significativamente a eficiência da antena receptora em uma larga faixa de frequência. A metalente alcança um foco muito preciso, quase no limite físico, ao mesmo tempo em que torna a antena mais direcional, melhorando seu desempenho na direção desejada. Notavelmente, a metalente funciona muito bem sob incidência oblíqua, de até 50° x 40°.

Em seguida, projetamos uma metassuperfície para frequências de THz. As frequências de THz têm um enorme potencial para comunicações 6G e imagens, com sua radiação não ionizante tornando-a mais adequada do que raios-X em aplicações médicas. No entanto, é limitada por fontes de baixa potência. Nossa metassuperfície de silício gera feixes de alta eficiência, chamados feixes de Bessel, com distância de propagação variável e resolução ajustável, ideais para aplicações em imagens e comunicações.

Posteriormente, um dispositivo totalmente passivo de amplificação de pulsos de terahertz utilizando um efeito dispersivo, chamado efeito Talbot temporal, dentro de uma fibra metamaterial, chamada fibra de Bragg, precisamente projetada para tal aplicação, é descrito. Três estratégias distintas, denominadas adição coerente de pulsos, iluminador de Talbot direto e iluminador de Talbot inverso, são introduzidas e exploradas para maximizar o ganho passivo do efeito Talbot. Essas abordagens acomodam uma ampla gama de formatos de pulsos de saída e proporcionam ganhos de mais de 7 vezes, sem a necessidade de componentes ativos, que são escassos em frequências de THz.

Finalmente, implementamos pela primeira vez a observação prática do efeito Talbot temporal no domínio de micro-ondas usando um metamaterial impresso em 3D, chamado rede de Bragg linearmente chirpada. Utilizando nossas técnicas anteriores com algoritmos de otimização, alcançamos amplificação passiva com ganhos duas vezes e meia maiores para pulsos precisamente projetados. Além disso, observamos que teoricamente podemos aumentar o ganho em um fator adicional de 2,5 vezes com materiais de impressão 3D de maior qualidade. Essa descoberta abre portas para diversas aplicações de micro-ondas do efeito Talbot, incluindo camuflagem temporal, detecção de sinais de micro-ondas abaixo do ruído, moldagem de pulsos de micro-ondas e redução de ruído de micro-ondas.

LIST OF FIGURES

LIST OF TABLES

LIST OF ABBREVIATIONS AND ACRONYMS

2D	Two-dimensional
3D	Three-dimensional
4G	Fourth-generation cellular technology
5G	Fifth-generation cellular technology
6G	Sixth-generation cellular technology
ABS	Acrylonitrile butadiene styrene
ASF	Angular spectrum formalism
AWG	Arbitrary wave generator
B	Blue
BCE	Before the common era
BTAI	Backward Talbot array illuminator
CAD	Computer aided design
CCD	Charge-coupled device
CE	Common era
CGH	Computer generated hologram
CPA	Coherent pulse addition
CW	Continuous wave
DOE	Diffractive optical element
DOF	Depth of focus
EIT	Electromagnetic induced transparency
EMC	Evanescent mode cavity
FDM	Fused deposition modeling
FDTD	Finite-difference time domain
FEM	Finite element method

FoM	Figure of merit
FR	Fano resonance
FSS	Frequency-selective surface
FTAI	Forward Talbot array illuminator
FT	Fourier transform
FTR	Fano-type resonance
FWHM	Full-width at half-maximum
G	Green
GS	Gerchberg-Saxton
HFSS	High Frequency Electromagnetic Field Simulation
HPBW	Half-power beam-width
ITO	Indium tin oxide
LCD	Liquid crystal display
LSP	Localized surface plasmon
MEMS	Microelectromechanical system
MIMO	Multiple-input-multiple-output
mm-wave	Milimeter-wave
MR	Microstrip resonator
NA	Numerical aperture
PB	Pancharatnam-Berry
PSO	Particle swarm optimization
QCL	Quantum cascade laser
RC	Raised cosine
R	Red
RCA	Wafer cleaning method develop in the Radio Corporation of America
RCWA	Rigorous Coupled Wave Analysis

Si	Silicon
SIW	Substrate integrated waveguide
SLA	Stereolithography
SLM	Spatial light modulation
SNR	Signal-to-noise ratio
SRR	Split-ring resonator
TAI	Talbot array illuminator
TBB	Terahertz Bessel beam
TE	Transverse electric
THz	Terahertz
TiO_2	Titanium dioxide
TMD	Transition metal dichalcogenide
TMT	Transfer matrix technique
TMT-S	Transfer matrix technique - normal incidence
TMT-W	Transfer matrix technique - waveguide calculation
TTE	Temporal Talbot effect
VNA	Vector network analyzer
WGM	Whispering gallery mode
WR	Waveguide resonator
WRR	Waveguide ring resonator
WRR-FTR	Waveguide ring resonator-Fano-type resonance

LIST OF SYMBOLS

a Metasurface unit cell radius

a_{fit}, A_{fit}, b_{fit}, B_{fit}, $df1$, $df2$, $K1$, $K2$, $K3$, S_{fit}, λ_{sk}, σ_{fit} Curve fitting parameters

a_l Fourier series l-th harmonic amplitude of a signal U_o

b Integer number used for indexing variables

$\mathbf{B}$ Magnetic flux density vector

BW Signal bandwidth

c Light speed in vacuum

C Chirp factor

$C\varsigma$ Port ς of a circulator

d Displacement between the two layers of an Alvarez type metasurface

$\boldsymbol{D}$ Electric flux density vector

d_{FR} Fraunhofer far-field distance

DOF Depth of focus

e_ν Parity function. Returns 1 if ν is even and 0 otherwise

E Electric field

$\boldsymbol{E}$ Electric field vector

E_o Unperturbed electric field amplitude

$\boldsymbol{E_o}$ Unperturbed electric field vector

E_{ob} Bright mode electric field amplitude

$\boldsymbol{E_{ob}}$ Bright mode electric field vector

E_{od} Dark mode electric field amplitude

$\boldsymbol{E_{od}}$ Dark mode electric field vector

$\boldsymbol{E}_{\mathrm{ant}}$ Electric field vector at antenna position

E^{ob} Electric field after an obstruction

f	Operating frequency
f_c	Carrier frequency
f_i	Frequency relative to the i-th period of a LCBG or to the i-th oscillator
f_{ini}	Frequency relative to the first period of a LCBG
f_{fin}	Frequency relative to the final period of a LCBG
f_o	Unperturbed resonant frequency
$F_{1,2}$	External forces driving coupled oscillators 1 and 2
FoM	Figure of merit
$FWHM$	Full-width at half-maximum
g	Coupling factor between two coupled oscillators
G	Gain
G_o	Gain of a receiving antenna
h	Height
H	Bragg waveguide heigth
$\boldsymbol{H}$	Magnetic field vector
$\boldsymbol{H_{ant}}$	Magnetic field vector at antenna position
H_o	Unperturbed magnetic field amplitude
$\boldsymbol{H_o}$	Unperturbed magnetic field vector
H_{ob}	Bright mode magnetic field amplitude
$\boldsymbol{H_{ob}}$	Bright mode magnetic field vector
H_{od}	Dark mode magnetic field amplitude
$\boldsymbol{H_{od}}$	Dark mode magnetic field vector
H_{RC}	Transfer function of a raised cosine filter
i	Integer number used for indexing variables
j	Imaginary unit
J_ς	Bessel funciton of the first type and ς-th order

k	Wave-number
k_o	Free space wave-number
$\boldsymbol{k}$	Wave vector
k_r	Radial component of the wave vector
$k_{x,y,z}$	Wave vector component (spatial frequency) in the x, y or z direction
$k_{\parallel}$	Parallel component of the wave vector
K	Correction factor for effective antenna volume
K_T	Constant that defines the fraction of a period occupied by a given pulse of period T
K_{FWHM}	Relationship between T_{FWHM} and T
l	Harmonic index of a Fourier series
l_{ant}	Monopole antenna length
L	Propagation length for passive amplification with TTE
L_o	Total length of a LCBG
m	Order of a super Gaussian pulse
M	Number of phase levels in a metasurface
M_{in}	Number of layers of the inner Bragg reflector
M_{out}	Number of layers of the outer Bragg reflector
n	Refractive index
n_{eff}	Effective index
n_{eff}^{LCBG}	Effective index of a waveguide
n_{eff}^{LCBG}	Effective index of a LCBG
n_1	First refractive index in a Bragg grating
n_2	Second refractive index in a Bragg grating
n_i	Refractive index of the medium where an incident wave is located
n_t	Refractive index of the medium where a transmitted wave is located

n_{high}	Higher refractive index of the inner Bragg reflector
n_{high^m}	Higher refractive index of the outer Bragg reflector
n_{low}	Lower refractive index of the inner Bragg reflector
n_{low^m}	Lower refractive index of the outer Bragg reflector
n_{wafers}	Necessary number of Si wafers to build a Bragg waveguide
N	Number of periods in a Bragg grating
NA	Numerical aperture
p, q, ψ	Integer numbers used in Talbot effect calculations
$o\,(x,y)$	Arbitrary two dimensional function
$O\,(k_x, k_y)$	Fourier transform of an arbitrary two dimensional function
Ov	Over modulation parameter
P_M	Received power in the presence of a metalens
P_{Peakin}	Input peak power of a signal
P_{Peakout}	Output peak power of a signal
P_R	Received power
Q	Quality factor
Q_l	Loaded quality factor
r	Radial coordinate variable
R	Reflection coefficient
R'	Form factor of a signal
$R_{\varrho\varsigma}$	Reflection coefficient with incident polarization ς and reflected polarization ϱ, ϱ and ς can be x or y
R_{ax}	Axicon radius
R_{WRR}	Mean curvature radius of a WRR
r_{ob}	Obstruction's radius
$\boldsymbol{S}$	Poynting vector

$S_{\varrho\varsigma}$	Scattering parameter from port ς to port ϱ
$S_{\varrho\varsigma}^{\text{WG}}$	Scattering parameter from port ς to port ϱ of a waveguide
SNR	Signal-to-noise ratio
t	Time
t_{ax}	Layer separation in an Alvarez type metasurface
t_{core}	Bragg fiber's core width
t_{high}	High index layer thickness of the inner Bragg reflector
t_{high^m}	High index layer thickness of the outer Bragg reflector
t_{low}	Low index layer thickness of the inner Bragg reflector
t_{low^m}	Low index layer thickness of the outer Bragg reflector
t_{wafer}	Si wafer thickness
T	Temporal period of a signal
T'	Temporal period of a signal at the q-th fractional length of a Talbot carpet
T_{FWHM}	Temporal full width at half-maximum
Tr	Transmission coefficient
T_b^{RCWA}	Transmission coefficient of the b-th phase level calculated in RCWA
T_{PB}	Transmission coefficient modulus of a geometric phase unit cell with no rotation
$T^{\theta_{PB}}$	Transmission coefficient of a geometric phase unit rotated by an angle equal to θ_{PB}
$T_{\varrho\varsigma}$	Transmission coefficient with incident polarization ς and transmitted polarization ϱ, ϱ and ς can be x or y
T_o^{RC}	Zero-crossing time in a raised cosine pulse
$S_{\varrho\varsigma}^{\text{circ}}$	Transmission coefficient from port ς to port ϱ of a circulator
$\tan(\delta)$	Dielectric loss tangent
u	Integer number used for indexing variables

U	Arbitrary temporal or spatial signal in a Talbot carpet
U_o	Initial value of an arbitrary temporal or spatial signal in a Talbot carpet
v	Integer number used for indexing variables
V	Propagating signal in a passive amplification system
V_{ideal}	Ideal output signal in a passive amplification system
V_{output}	Output temporal signal
V_{traget}	Target output signal
V_{avg}	Average value of a signal V
V_{ant}	Antenna volume
V_g	Group velocity
V_o	Input signal in a passive amplification system
V_r	Ripple of a signal V
Vol	WRR volume
w	Waveguide width
W_e	Stored electric field energy
W_m	Stored magnetic field energy
x, y	Spatial variables in a planes transverse to the propagation direction
X	Spatial period of a signal
$x_{1,2}$	Positions of coupled oscillators 1 and 2
x_{ob}	Obstruction's transverse position
y_{SGauss}	Super Gaussian function
z	Propagation direction
z_f	Focal length
z_{ob}	Obstruction's longitudinal position
z_{sh}	Self-healing distance of a Bessel beam
z_T	Talbot length

z_T^u	u-th repetition of the Talbot length
z_{TT}	Temporal Talbot length
Z_o	Free space impedance
Z_{TE}	Waveguide TE mode impedance
α	Bulk axicon angle
$\alpha_{1,2}$	Dampening factors for oscillators 1 and 2
α_{RC}	Roll-off factor of a raised cosine filter
α_{WRR}	Phase correction factor in WRR field distribution
β	Propagation constant
β'	Corrected propagation constant
β_2	Second-order dispersion coefficient
β_b	b-order dispersion coefficient
β_h	Unperturbed propagation constant in a H-plane bent waveguide
γ_b	Phase modulation of the $(b$-1$)$-th pulse in a Talbot carpet, b=0,...(q-1)
$\delta\left(t\right)$	Impulse function
Δ	Mode separation in a WRR
Δf	Resonant frequency shift
$\Delta f_{b,d}$	Resonant frequency shift for bright and dark modes
ΔV	Amplitude variation of a signal V
ΔVol	Perturbation volume inside a WRR
$\Delta V'$	Effective perturbation volume inside a WRR
ΔW_e	Stored electric field energy variation
ΔW_m	Stored magnetic field energy variation
$\Delta\beta$	Propagation constant shift due to antenna perturbation
ϵ	Electric permittivity
ϵ_o	Electric permittivity of the vaccum

ε_r	Relative permittivity
$\bar{\bar{\epsilon}}$	Complex electric permittivity tensor
$\bar{\bar{\zeta}}, \bar{\bar{\xi}}$	Complex magneto-electric coefficients tensors
θ	Angular spacing between antennas in a WRR
θ'	Angular spacing between antennas in a WRR with shifted origin
$\theta_{i,r,t}$	Incidence, reflection or transmission angle of a plane wave
θ_{PB}	Rotation angle of a geometric phase unit cell
$\Theta(r)$	Heaviside step function
κ	Integration variable in polar coordinates
λ	Operating wavelength
λ_o	Free-space wavelength
λ_g	Guided wavelength
λ_h	Guided wavelength in a H-plane bent waveguide
λ_g^i	Guided wavelength relative to the i-th period of a LCBG
λ_o^i	Free-space wavelength relative to the i-th period of a LCBG
Λ	Bragg grating period
Λ_i	i-th period of a LCBG
μ	Magnetic permeability
μ_o	Magnetic permeability of the vaccum
$\bar{\bar{\mu}}$	Complex magnetic permeability tensor
ρ	Metasurface period
σ	Electric conductivity
σ_{copper}	Electric conductivity of copper
τ	Group delay
τ_i	Group delay relative to the i-th period of a LCBG
υ	Constant tuning parameter in phase functions

$\Upsilon\left(\theta_{PB}\right)$	Rotation matrix for a rotation angle θ_{PB}
ϕ	Azimuth coordinate variable
Φ	Phase function
φ	Composite phase function of an Alvarez type metasurface
φ_o	Constant phase term in the phase function of an Alvarez type metasurface
ϕ_2	Second derivative of the phase function in respect to ω
Φ_s	Saturated phase function
ω	Angular frequency
ω_o	Central angular frequency
$\mathcal{B}$	Fourier-Bessel transform operator
$\mathcal{F}$	Fourier transform operator

CONTENTS

1 INTRODUCTION

1.1 Overview of metamaterials and metasurfaces

For centuries, even millenia, the manipulation of electromagnetic waves has fascinated mankind. The first artificially created mirrors can be traced back to around 6000 BCE in what is now modern-day Turkey. These mirrors were crafted using polished obsidian stones (1). As early as the second century BCE, Greek mathematician Diocles delved into studying concave surface mirrors that could concentrate light (2). Furthermore, transmissive elements like lenses have been utilized since at least 750-710 BCE in Assyria (3) with the use of polished quartz stones (known as Nimrud lens) and possibly even earlier than that. Ground quartz eye structures discovered in Egyptian statues dating from 2500-2400 BCE also suggest their early existence (4). However, it was not until the archaic Greek period (800-480 BCE) that lenses with a satisfactory optical quality capable of magnification were found on Crete (5). In more recent times, there were significant advancements in the understanding of light refraction and reflective properties. In 1666 CE, Isaac Newton researched dispersive prisms to investigate the phenomenon of light refraction (6). Additionally, Michael Faraday's study in 1857 CE focused on examining the transmissive and reflective characteristics of ultrathin gold sheets (7) which can be considered as one of the early works in plasmonics. Plasmonics is a field of research that studies the photon-electron interaction in metals, mostly at optical wavelengths (8). Currently, plasmonic devices include sensors (9), slow wave devices (10), wave guiding (11) and so on. These studies share a common characteristic - they rely entirely on exploiting atomic or molecular properties present within various materials such as metals, stones, or crystals to achieve desired effects.

The next significant advancement in electromagnetic technology lies in the utilization of complex structures such as multilayer films and periodic arrangements composed of diverse materials or alterations within a bulk material. This allows for precise manipulation of the spectral response exhibited by a device, surpassing the limitations imposed by its constituent material alone. Nature itself has already manifested such intricate structures (12,13) through various organisms to address the scarcity of blue pigments that possess high bandgaps required for avoiding absorption at shorter wavelengths. For instance, butterflies (14), birds (15), fish (13) and insects (16) have evolved specific structural adaptations enabling them to reflect vibrant colors. These structures bear a striking resemblance to thin film filters and photonic crystals, both of which were introduced in the late 19th and early 20th centuries. Thin film filters, resembling these structures closely, were first created and observed by Rayleigh in the 1880s (17), which can be regarded as one dimensional (1D) photonic crystals, even though it was not until the late 1900s that formal descriptions

of photonic crystals emerged (18). Simultaneously, a number of different techniques for microwave transmission, guiding, and even lensing have been developed before the 20th century (19).

Even though photonic crystals have a spectral response that depends on its lattice size and geometry, they can´t be described in terms of homogenized effective constitutive relations since their periodicity is larger than the operating wavelength. The study of sub-wavelength engineered structures is widely recognized as a paradigm shift in electromagnetic engineering, marking the beginning of the branch of metamaterials (20). As the prefix (meta) suggests, these artificial electromagnetic materials based on sub-wavelength structures can exhibit unconventional light propagation effects that are not observed in their constituent materials or found naturally. In other words, metamaterials present characteristics that go beyond their host material's, and even beyond those found in nature. Such characteristics which arise from the microscopic resonances of periodic or quasi-periodic arrangements of man-made scatterers, which, due to the sub-wavelength dimensions of both the scatterers size and periodicity, behave as an homogeneous medium for the sensing electromagnetic field (20, 21). Metamaterials have revolutionized the field of photonics by enabling precise control over light-scattering processes. In metamaterials, its constitutive relations arise from its macroscopic structure rather than atomic or molecular interactions. They can be described as:

$$\begin{pmatrix} \boldsymbol{D} \\ \boldsymbol{B} \end{pmatrix} = \begin{pmatrix} \bar{\bar{\epsilon}} & \bar{\bar{\xi}} \\ \bar{\bar{\zeta}} & \bar{\bar{\mu}} \end{pmatrix} \begin{pmatrix} \boldsymbol{E} \\ \boldsymbol{H} \end{pmatrix},$$ (1.1)

where $\boldsymbol{E}$ and $\boldsymbol{H}$ are the electric and magnetic vector fields, $\boldsymbol{D}$ and $\boldsymbol{B}$ are the electric and magnetic vector flux densities, and $\bar{\bar{\epsilon}}, \bar{\bar{\mu}}, \bar{\bar{\xi}}, \bar{\bar{\zeta}}$ are the complex tensors for the electric permittivity, magnetic permeability and magneto-electric coefficients, respectively. Note that they can be dispersive (dependent on the operating frequency f) (22), non-local or spatially dispersive (dependent on the parallel component of the wave-vector $k_{\parallel}$) (23, 24), or temporally modulated (dependent on the time t) (25). Moreover, they can also present non-reciprocal behavior (26). Note that the magneto-electric coupling described by $\bar{\bar{\xi}}, \bar{\bar{\zeta}}$ result in different material responses for different handedness of circular polarization. This effect is called chirality (27).

The concept of artificial materials, which are now referred to as metamaterials, has been explored since the late 19th and early 20th centuries. Bose [1897] and Lindman [1920] were the first to report on these materials, demonstrating an artificial chiral response in microwave devices using helical structures. Subsequently, Kock (28) proposed the use of artificial dielectrics composed of metallic spheres mixed with a host dielectric matrix, which achieved a lensing effect. Additionally, Brown (29) and Rotman (30) created artificial media using metallic rods, resulting in permittivity values smaller than unity and negative values,

respectively. In 1955, Thompson introduced ferrite wires to implement artificial magnetism with negative permeability values (31), although practical application was hindered by high losses until the rise of split-ring resonators (SRRs) (32). Perhaps the most ground-breaking study on artificial media was reported by Veselago in 1968 (33). By studying the dynamics of simultaneously negative ϵ and μ, he demonstrated multiple unexpected phenomena (anomalous refraction, reverse Doppler shift etc.). Note that such media present negative refractive index, and therefore, the wave-vector **k** and the Poynting vector **S** are in opposite directions. In his seminal work, Veselago postulated the possibility of a flat lens, frequently referred to as "perfect lens" (34). Unfortunately, owing to technological limitations of the time, such media were only experimentally observed three decades later.

It was only in the 1990s that Pendry experimentally demonstrated tunable artificial dielectrics in the GHz range with periodic wires (35) and low loss tunable artificial magnetic materials, the SRRs (32). In 2000, Smith combined the two previous Pendry approaches to design a negative ϵ and μ material (36, 37) and coined the term metamaterial (38), which was experimentally confirmed by Shelby one year later (39). The unpreceded degree of freedom allowed by metamaterials allowed for an impressive myriad of applications, such as lensing (34), cloaking (40–42), artificial reflectors (43–45) and absorbers (46), reflection-less waveguide bending (47), dispersion management (48), enhancement of dipoles emission (49, 50), hyper-lensing (24, 51), biosensors (52), directive emission of antennas (53), among many others.

The impact that metamaterials had in the scientific community is confirmed by a bibliometric review. Figure 1 shows (thin blue lines, squares) the number of publications by year with the term "metamaterial" or "metamaterials" in the title, abstract, or keywords, according to the Scopus database (retrieved on July 24th, 2023). Note that the terms "thermal" and "acoustic" were excluded from the review, to account only for electromagnetic metamaterials, since this paradigm is now overtaking acoustic (54) and thermal (55) engineering as well. The number of yearly publications is ever-growing, aside from the 2019-2020 transition, which is explained by the COVID-19 pandemic. However, there are some drawbacks in metamaterial engineering. On the one hand, the use of metallic, bulky structures in the optical regime results in high losses and fabrication challenges. On the other hand, ohmic losses are less significant in microwave frequencies, but the size of bulky structures can result in prohibitive sizes. This has motivated researchers to design sub-wavelength thick devices, which are currently known as metasurfaces, the two-dimensional (2D) counterpart of metamaterials, enabling planar electromagnetic engineering (56, 57). The bibliometric review for "metasurface" or "metasurfaces", also excluding the terms "thermal" and "acoustic", is shown in Fig. 1 (thick red lines, circles). Note that, from 2019 on, metasurfaces have the upper lead on research volume, showing an exponential increase, with only a slight decrease in its growth in the 2020 period, confirming that the paradigm started by metamaterials has reached a new stage with metasurfaces.

Metasurfaces, which are composed of periodic or quasi-periodic arrays of sub-wavelength structures, have emerged as a versatile and efficient platform for lensing (58), imaging (59), holography (60), frequency-selective surfaces (FSSs) (61,62), high-Q filtering (63), electromagnetic-induced transparency (EIT) (64), sensing (65), lasing (66), antennas (67), antenna beam-forming (68), non-diffractive beam generation (69), energy harvesting (70), electromagnetic absorbing (71), information encryption (72) among many others. With their smaller physical footprint, simpler fabrication process, and lower losses compared to bulk three dimensional (3D) metamaterials, metasurfaces have become a promising frontier in photonics in communications, sensing, imaging and even signal processing and computing (73) applications; metasurfaces revolutionized every region of the electromagnetic spectrum, from radio frequency (74) to ultraviolet (75) and even x-rays (76). Metasurfaces are understood in terms of discontinuous boundary conditions (77) instead of constitutive parameters and can be their reflection (R) or transmission (T_r) characteristics can be described in the form of Jones matrices:

$$R = \begin{pmatrix} R_{xx} & R_{xy} \\ R_{yx} & R_{yy} \end{pmatrix}, \tag{1.2}$$

$$Tr = \begin{pmatrix} T_{xx} & T_{xy} \\ T_{yx} & T_{yy} \end{pmatrix}, \tag{1.3}$$

where the first sub-index denotes the polarization of the scattered wave and the second sub-index denotes the polarization of the incident wave. Note that metasurfaces usually
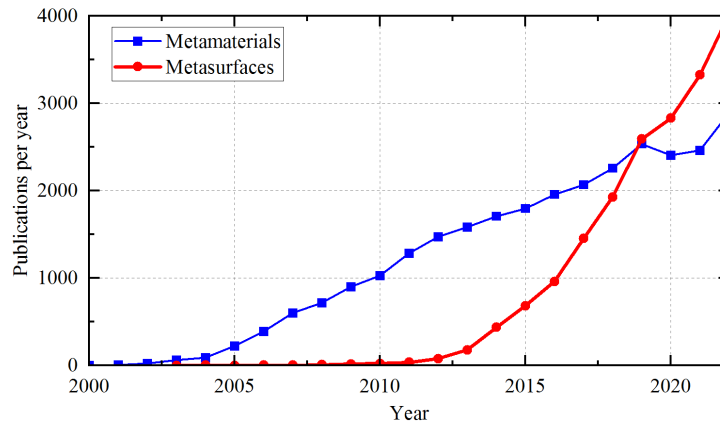
Figure 1 – Bibliometric review for publications on metamaterials (thin blue lines, squares) and metasurfaces (thick red lines, circles). The terms "acoustic" and "thermal" were removed to include only electromagnetic metamaterials and metasurfaces. Note that metasurfaces were only popularized in the early 2010s, but lead the amount of yearly publications since 2019 with an exponential growth while metamaterials present an almost linear growth since 2004. The odd transition from 2019 to 2020 is explained by the COVID-19 pandemic. retrieved from the Scopus database on July 24th, 2023.

present spatial modulation, and dependence on frequency and incident angle, possibly possessing time modulation as well. Thus, each term in (1.2) and (1.3) is actually a function of $x, y, f, t, k_\parallel$, where (x, y) is the spatial position in a plane transverse to the propagation direction z. Moreover, metasurfaces can also have non-reciprocal responses, known as Janus metasurfaces (78), and the Jones matrix itself can present non-reciprocity when chiral unit cells are used (79). In other words, metasurfaces locally modulate the amplitude, phase and polarization of the scattered wave, and this modulation can be multiplexed for different frequency (80), polarization (81), incident angle (82), propagation distance (83), host medium (84), orbital angular momentum (85) and diffraction order (86) channels. This modulation can be spatial (87), temporal (88), or spatial-temporal (89).

1.1.1 Spatial modulation with metasurfaces

Now that the concept of metasurfaces is well defined, we briefly describe the principles of spatial modulation with metasurfaces. First metasurfaces presented homogeneous spatial distribution, with applications limited to absorption (71), FSSs (61, 62) and impedance matching (90), to name a few. Those can be regarded as the first generation of metasurfaces, which started with the century old FSS (62), while the term "metasurface" was first used in 2003 (91). The second generation of metasurfaces present spatial modulation. A precursor of this generation is the 1966 Lohmann detour phase grating (92), which possessed too much energy in higher diffraction orders due to its greater than wavelength periods. But it was only with Capasso's 2011 paper (77) that a complete and accurate description and implementation of a spatially modulated metasurface was reported. This metasurface used a plasmonic nano-antenna array and the authors provided a generalized version of the Snell's law to analyze it, which goes as follows (77): Assume a linearly distributed phase discontinuity $\Phi(x, y) = \upsilon x$, where υ is a constant and consider an incident plane wave with free space wave-number k_o in a medium with refractive index n_i and incidence angle θ_i. The transmitting medium has refractive index n_t and angle of transmission θ_t. We analyze two infinitesimally close light paths crossing the phase discontinuity. Since they are infinitesimally close, their difference must be zero.

$$[k_o n_i \sin(\theta_i)\,\mathrm{d}x + (\Phi + \mathrm{d}\Phi)] - [k_o n_t \sin(\theta_t)\,\mathrm{d}x + \Phi] = 0, \qquad (1.4)$$

$$n_i \sin(\theta_i) + \frac{1}{k_o}\frac{\mathrm{d}\Phi}{\mathrm{d}x} = n_t \sin(\theta_t). \qquad (1.5)$$

By applying the previous definition of $\Phi(x, y)$,

$$\frac{\upsilon}{k_o} = n_t \sin(\theta_t) - n_i \sin(\theta_i). \qquad (1.6)$$

Therefore, by tuning υ, the incident beam can be deflected to an arbitrary direction, which is known as anomalous refraction. The same procedure can be accomplished for a reflective boundary resulting in

$$\frac{\upsilon}{k_o n_i} = \sin\left(\theta_r\right) - \sin\left(\theta_i\right), \tag{1.7}$$

where θ_r is the angle of the reflection. Now assume that $n_i = n_t = 1$ and normal incidence ($\theta_i = 0$). Equations (1.6) and (1.7) reduce to:

$$\theta_{r,t} = \arcsin\left(\frac{\upsilon}{k_o}\right). \tag{1.8}$$

Thus, $\upsilon = k_x$ for this particular case of beam deflection. This simple example describes the basic design procedure of a metasurface. Similar procedures can be used to retrieve the source fields of more complex metasurfaces, such as metalenses (58) and holograms (93), with the aid of diffractive optics (94) and iterative algorithms such as the Gerchberg-Saxton (GS) (93). Note that a key assumption in the design of spatially modulated metasurfaces is that metasurfaces are locally periodic so the local response of a unit cell is close to the response of its periodic array. This is only true when the field is strongly localized in each unitary scatterer (weak electromagnetic coupling between neighboring atoms). This requirement limits the minimum value of the metasurface period, since the closer the scatterers are, the higher is the coupling between them. With this in mind, we next analyze the different types of metasurfaces based on their unit cells.

1.1.2   Types of metasurfaces

There are multiple strategies to implement sub-wavelength scatterers, which are the building blocks of metasurfaces. Such units are responsible to locally modulate the amplitude, phase, or polarization of the incident wave, and therefore must satisfy a few requirements (95): strong light-matter interaction, tunability and possibility of fabrication. We divide unit cells into five categories: Plasmonic nano-antennas, Huygens' metasurfaces, non-resonant propagation phase metasurfaces, geometric phase or Pancharatnam-Berry (PB) metasurfaces, and quasi-continuous metasurfaces. Note that there are many other design strategies that are not detailed here, such as detour phase (96), topological optimization (97) and complex macro cells that present complex amplitude (83) modulation and wavelength multiplexed (98) modulation. Figure 2 shows the different types of metasurface unit cells described here.

1.1.2.1   Plasmonic metasurfaces

Localized surface plasmons (LSP) are an obvious candidate for locally modulating an incident wavefront in the sub-wavelength regime due to its strong light-matter interaction.
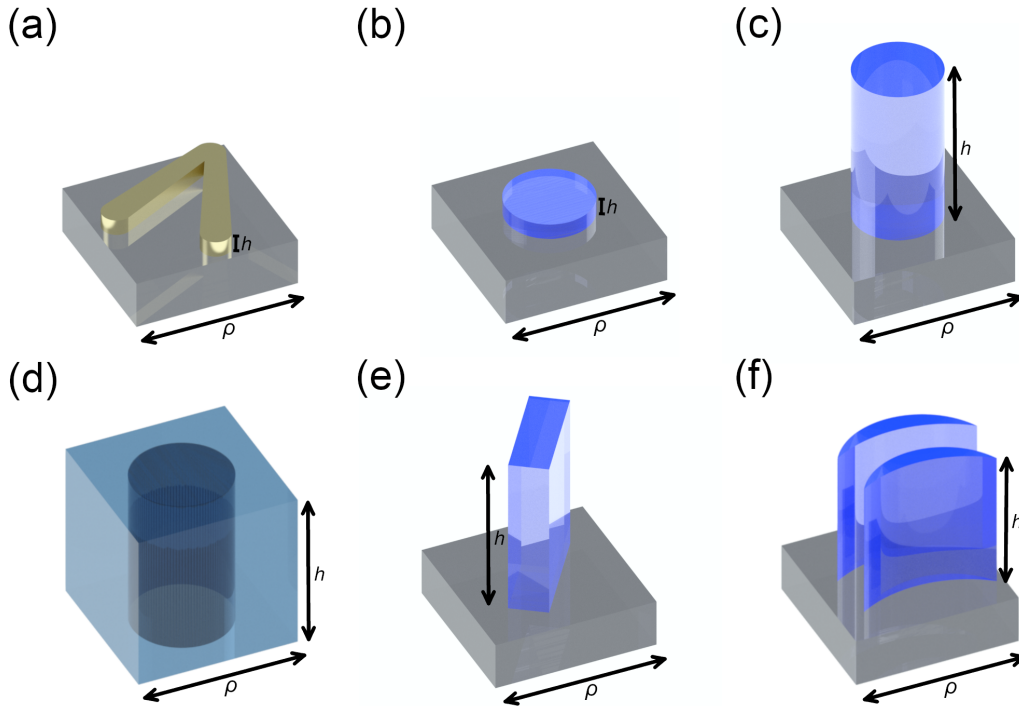
Figure 2 – Types of metasurface unit cells. (a) Plasmonic nanoantenna; (b) Huygens'
metasurface; (c) Propagation phase metasurface - pillar type; (d) Propagation
phase metasurface - hole type; (e) Geometric phase metasurface; (f) Quasi-
continuous metasurface. All metasurfaces have height h and period ρ. Note
that the period is smaller than the operating wavelength in all cases but (f).

By tuning the LSP resonance, phase can be modulated from 0 to π, however interference
between multiple modes allow for a complete 2π phase modulation control (77). Some
examples are V-shaped (77), H-shaped (99), and C-shaped (100) antennas. However, the
coupling of photons and electrons in the LSP induce high ohmic losses, severely limiting
the efficiency in this type of metasurface to only 10% in transmission mode (101).

1.1.2.2   Huygens' metasurfaces

Huygens' metasurfaces rely on impedance matching with the surrounding media
to avoid back-scattering of the incident wave. Moreover, huygens' metasurfaces possess
both electric and magnetic dipolar resonances, allowing for a complete phase modulation
from 0 to 2π, each unit serving as a secondary spherical wave source, following the
Huygens principle (94). The examples were accomplished with copper strips in microwave
metasurfaces (102). Later, all dielectric unit cells were used to avoid ohmic losses, especially
in the optical regime (103). Such metasurfaces are composed of low aspect ratio Mie
resonators, and are polarization insensitive (104).

1.1.2.3   Propagation phase metasurfaces

Although they presented a major breakthrough, metasurfaces based on resonant scatterers present strongly dispersive responses (105). Moreover, by moving away from the resonance to modulate the transmitted phase, the transmitted amplitude is simultaneously modulated, which motivated researchers to look for non-resonant metasurfaces. The mechanism behind these metasurfaces is propagation phase, or locally modulating the optical path via wave-guiding unit cells, such as dielectric posts. Each post acts as an individual waveguide of height h, and effective index n_{eff}. The accumulated phase is:

$$\Phi = k_o n_{eff} h, \tag{1.9}$$

where h is usually fixed and n_{eff} is tuned by changing the cross section of each post. The main drawback of the non-resonant phase approach is the higher aspect ratio, which might bring challenges for its fabrication when extreme heights are required. The necessary height to obtain complete phase control is:

$$h \geq (n-1)\, k_o, \tag{1.10}$$

where n is the refractive index of the material used to build the metasurface. This suggests the use of high n materials such as silicon (Si) or titanium dioxide (TiO_2) (106). However, we show in Chapter 2 complete phase control isn't strictly necessary in every application, by designing and experimentally characterizing the first microwave metasurface using 3D printing, low permittivity material, and 0 to π phase control to focus an incoming plane wave in a patch antenna, increasing its gain. Note that, while mostly dielectric, non-resonant phase can be implemented using plasmonic wave-guides as well (107), which isn't frequently used due to higher losses.

1.1.2.4   Pancharatnam-Berry metasurfaces

Another common phase modulation mechanism is the geometric or PB phase (108). It consists on optimizing the unit cell for the maximum circular polarization conversion (which happens when the anisotropic post acts as a half-wave plate). This cell is then rotated by an angle θ_{PB}. The transmission Jones matrix for such cells is:

$$T^{\theta_{PB}} = \Upsilon(\theta_{PB})\, T \Upsilon^{-1}(\theta_{PB}) =$$
$$\begin{pmatrix} \cos\theta_{PB} & -\sin\theta_{PB} \\ \sin\theta_{PB} & \cos\theta_{PB} \end{pmatrix} \begin{pmatrix} T_{xx} & T_{xy} \\ T_{yx} & T_{yy} \end{pmatrix} \begin{pmatrix} \cos\theta_{PB} & \sin\theta_{PB} \\ -\sin\theta_{PB} & \cos\theta_{PB} \end{pmatrix}, \tag{1.11}$$

where Υ is the rotation matrix. In a perfect half-wave plate, $T_{xx} = -T_{yy}$, $|T_{xx}| = T_{PB}$ and $T_{xy} = T_{yx} = 0$. By applying these assumptions into (1.11) and multiplying it by a

circularly polarized wave $\begin{bmatrix} 1 & j \end{bmatrix}^{\mathrm{T}}$, we have (note that we neglected any constant phase element of T_{xx}):

$$T^{\theta_{PB}} = \begin{pmatrix} T_{PB}\left[\cos^2(\theta_{PB}) - 1\right] & 2T_{PB}\cos\theta_{PB}\sin\theta_{PB} \\ 2T_{PB}\cos\theta_{PB}\sin\theta_{PB} & -T_{PB}\left[\cos^2(\theta_{PB}) - 1\right] \end{pmatrix} \begin{pmatrix} 1 \\ j \end{pmatrix} = T_{PB}\mathrm{e}^{-j2\theta_{PB}} \begin{pmatrix} 1 \\ -j \end{pmatrix}. \tag{1.12}$$

By looking at (1.12), it is easy to see that $\Phi = 2\theta_{PB}$, and thus the transmitted phase is solely determined by the rotation angle of the unit cell, while the transmission efficiency and polarization conversion rate can be optimized *a priori* by tailoring the geometry of the unit cell. Furthermore, the transmitted wave has opposite handedness to the incident one. The PB phase is also non dispersive, allowing for broadband operation, limited only by the reduction in the polarization conversion efficiency. Note that if the incident wave has opposite polarization $\begin{bmatrix} 1 & -j \end{bmatrix}^{\mathrm{T}}$, $\Phi = -2\theta_{PB}$. An extra degree of freedom is permitted by using chiral metasurfaces (79), which decouple the metasurface response for left and right-handed polarization. The main drawback of this type of design is the need of circular polarized light.

1.1.2.5 Quasi-continuous metasurfaces

Quasi continuous metasurfaces, sometimes called catenary metasurfaces, recently surged as a way to address the limitations of discrete cell metasurfaces (109). When a metasurface is required to generate high spatial frequencies (k_x, k_y), the spatial sampling must be finer. In other words, the maximum spatial frequency is limited by the metasurface period ρ.

$$k_{x,y} \leq \frac{\pi}{\rho}. \tag{1.13}$$

Nevertheless, extremely low periods increase the difficulty of fabrication. Furthermore, bringing the posts closer increases the electromagnetic coupling between them. In designs where the spatial phase changes rapidly (high spatial frequencies), the local periodicity requirement is no longer satisfied. Quasi continuous metasurfaces use catenary shaped dielectric posts to continuously modulate the phase. This is a new design approach that has obtained impressive results in beam deflecting and high numerical aperture (NA), wide angle lenses (109, 110), simultaneously increasing its efficiency and reducing the thickness. Other implementations include vortex (111) and Bessel (112) beam generation. Its main drawback is the higher computational cost, as techniques of simulating the unit cell with periodic boundaries are no longer possible.

1.1.3   Tunable metasurfaces

If spatially modulated metasurfaces can be considered the second generation of metasurfaces, those that allow real-time tuning (or space-time modulation) can be considered the third generation (113). Here we briefly describe some tuning mechanisms and applications. Tunable metasurfaces have a myriad of new applications, including dynamic holography (88), focus-tunable lenses (114), tunable resonances (115), beam steering (91, 116) etc. The temporal modulation can assume three basic types: modulating the whole metasurface (117, 118), modulating sectors of the metasurface (119), and pixel-by-pixel modulation (88, 120), which is by far the most complex design. Such tuning techniques are achieved in the microwave range with diodes (120) and varactors (91) inserted into each unit cell and even optical modulation of photo-diodes (121, 122). Moreover, terahertz (THz) and optical active metasurfaces include liquid crystals (114, 116, 117, 123–127), graphene (115, 117, 128–134), thermal (135–137) and optical (121) tuning etc. These tuning techniques might requires intricate designs to electronically control each pixel, making it difficult to fabricate and implement, when transparent conducting oxides aren't viable options (for example in THz where most oxides aren't transparent).

When pixel-by-pixel tuning isn't required and global modulation is a viable option, such as in tunable lenses and resonators, mechanical tuning is an easy and smart way to circumvent this problem. The two main mechanisms are stretchable metasurfaces (118), where the period is changed by an external force, and the concept of Alvarez lenses (138, 139), in which two complementary metasurfaces are longitudinally aligned and a displacement is applied along the x or y directions to change a desired parameter of the device (140, 141). The design procedure of an Alvarez metasurface is described in details in Chapter 3, where we design an Alvarez axicon for THz imaging and communication applications with tunable depth-of-focus (DOF) and beam width.

1.2   Dispersion management

An important subject where metamaterials and metasurfaces have important contributions is dispersion management. Dispersion is phenomenon in which the refractive index of a material or the effective index of a waveguide changes as the operating frequency changes. In communications, this can lead to pulse broadening in long propagation distances (142), which leads to the requirement of dispersion compensation fibers (143–147). In diffractive optics, the change in the refractive index of a lens results in different focal lengths as the wavelength changes. Meanwhile, dispersion can be engineering for different applications such as ultrashort high-energy laser pulses, which granted the authors the 2018 Nobel prize in physics (148).

There are several ways in which metamaterials and metasurfaces act in dispersion management (88). A metamaterial based on omega cells is capable of compressed chirped

microwave pulses and compensate for the broadening in long propagation lengths (48). Slow light phenomena required elevated dispersion coefficients, which are found in both metamaterials and metasurfaces (149,150). Periodic sub-wavelength grating structures in microstrip microwave lines can mimic the dispersion characteristics of surface plasmon polariton waveguides, known as spoof surface plasmon polaritons (151), without the elevated ohmic losses, providing and extreme control of wave propagation in microwave transmission lines. Moreover, dispersion management in metasurfaces are observed in achromatic lenses (152). The dispersion effect stems from engineering a complex unit cell (98), from stacking nanoposts of different materials (153), or from combining dispersive propagation and non-dispersive geometric phases to achieve broadband devices (154).

An interesting application is the implementation of the temporal Talbot effect (TTE) (155). Its mechanisms are discussed in details later in this thesis, for now it suffices to mention the TTE happens when a periodic signal propagates through dispersive media. By applying carefully calculated temporal phase modulations, the TTE performs passive amplification of the input signal, either by stacking multiple pulses (156) or by converting continuous wave (CW) signals into pulses (157). The term passive amplification denotes that the peak power of the output signal is higher than the input peak power. Extremely high dispersion coefficients are required to observe the TTE in non-prohibitive propagation lengths, which are typically observed only in dispersion compensation fibers. In Chapter 4 we design a metamaterial based Bragg fiber and numerically demonstrate the first passive amplifier for THz frequencies, which lack high power sources. Later, we demonstrate the first experimental observation of the TTE in microwave frequencies in Chapter 5 by using an ultra-wide band linearly chirped Bragg grating (LCBG), and generate nanosecond pulses with optimized passive gain or signal-to-noise ratio (SNR).

1.3   Organization of this thesis

This thesis is divided in two parts. Part I contains Chapters 2 and 3, relative to spatial modulation of electromagnetic wavefronts with metasurfaces and Part II introduces new techniques for dispersion management using metamaterials, in Chapters 4 and 5.

Chapter 2 introduces the first all-dielectric metasurface in the microwave range. We use Acrylonitrile butadiene styrene (ABS) plastic to design a metasurface with 180º phase control, which is characterized in the Ka band, using a patch antenna. The gain of the patch antenna increased in 7.5 dB at 32.5 GHz, with a bandwidth of 2.4 GHz. Radiation patterns with and without the lenses are compared to evaluate the performance of the metalens.

Chapter 3 presents the design and simulation of a tunable terahertz Bessel beam (TBB) by using the Alvarez concept for tunable metasurface design. The TBB DOF and full width at half-maximum (FWHM) are evaluated for different tuning positions of the

metasurface, and the self-healing performance of the non-diffractive beam is calculated for different obstruction sizes and positions.

In Chapter 4, we present the first study of passive amplification in THz via TTE. The current limitations of THz generation are presented, and the TTE is identified as a possible solution. The Talbot effect is rigorously described, and so are the passive amplification mechanisms. We propose a completely new passive amplification mechanism based on backward propagation, design a Bragg waveguide using a Si metamaterial for extremely low propagation losses and completely characterize it numerically in terms of necessary propagation length, gain and SNR.

Chapter 5 provides the first experimental observation of the TTE in microwave frequencies. The difficulties for such observation are described, and fundamental limitations of the TTE are examined. A trade off between maximum dispersion and dispersive bandwidth is defined, and the LCBG is identified as the ideal structure for broadband dispersion in long wavelengths. The fabrication procedure and experimental results are then described in details.

Finally Chapter 6 presents the concluding remarks of this thesis.

Extra works not closely related to the scope of this thesis are presented in Appendix A. A dynamic stereoscopic hologram created with a multimedia projector is shown in A.1 and a waveguide ring resonator with tunable Fano resonances is shown in A.2. Extra discussions of the main works are presented in Appendices B, C and D. Finally, the metasurface design and fabrication procedure, as well as the models and parameters of the 3D printers and machining equipment used, are found in Appendix E.

Copyright permissions for presentation of published works are found in Appendix F.

1.4 Published and submitted works

Here is a list of published and submitted works, in international periodicals and conferences that the author participated participated either as first author (works present in this thesis) or as a coauthor:

1. PEPINO, V. M.; MOTA, A. F.; MARTINS, A.; BORGES, B.-H. V. 3-D-Printed Dielectric Metasurfaces for Antenna Gain Improvement in the Ka-Band. **IEEE Antennas and Wireless Propagation Letters**, vol. 17, no. 11, pp. 2133-2136, Nov. 2018

2. PEPINO, V. M.; MOTA, A. F.; MARTINS, A.; MARTINS, E. R.; BORGES, B.-H.V.; TEIXEIRA, F. L. Fano-Assisted Tunable X-Band Microwave Ring Resonator.

IEEE Transactions on Microwave Theory and Techniques, vol. 69, no. 4, pp. 2155-2164, April 2021

3. PEPINO, V. M.; MOTA, A. F.; BORGES, B.-H. V.; TEIXEIRA, F. L. Terahertz passive amplification via temporal Talbot effect in metamaterial-based Bragg fibers. **Journal of the Optical Society of America B,** 39, 1763-1774, 2022

4. PEPINO, V. M.; MOTA, A. F.; BORGES, B.-H.V.; Experimental demonstration of passive microwave pulse amplification via temporal Talbot effect. **Scientific Reports,** 13, 15330, 2023

5. MARTINS A.; LI, J.; MOTA, A. F.; PEPINO, V. M.; WANG, Y.; NETO, L. G.; TEIXEIRA, F. L.; MARTINS, E. R.; BORGES, B.-H. V. Broadband c-Si metasurfaces with polarization control at visible wavelengths: applications to 3D stereoscopic holography. **Opt. Express** 26, 30740-30752, 2018

6. MOTA, A. F.; MARTINS A.; PEPINO, V. M.; OTTEVAERE, H.; MEULEBROECK, W.; TEIXEIRA, F. L.; BORGES, B.-H. V. Semianalytical modeling of arbitrarily distributed quantum emitters embedded in nanopatterned hyperbolic metamaterials. **Journal of the Optical Society of America B,** 36, 1273-1287, 2019

7. SOUZA, M. I. O.; MOTA, A. F.; PEPINO, V. M.; CARMO, J. P.; BORGES, B.-H. V. Multi-Purpose Microwave Biosensor Based on Signal Encoding Technique and Microfluidics for Improved Sensitivity. **IEEE Sensors Journal**, vol. 21, no. 4, pp. 4571-4581, 15 Feb.15, 2021

8. GOUNELLA, R.; MARTINS, A.; PEPINO, V. M.; BORGES, B.-H.V.; CARMO, J.P. A Low-Cost Instrument for Multidimensional Characterization of Advanced Wireless Communication Technologies. **Applied Sciences,** 13, 6581, 2023

9. ARRUDA, G. S.; PEPINO, V. M.; BORGES, B.-H.V.; MARTINS, E. R.; Fourier control of air modes in high-Q metasurfaces. **Advanced Optical Materials,** 2301563, 2023

10. PEPINO, V. M.; FRANCISCO, B. A.; MOTA, A. M.; BORGES, B.-H.V. Metamaterials in the microwave regime. **Anais. São Carlos, SP**: EESC/USP, 2017

11. PEPINO, V. M.; MARTINS, A.; MOTA, A. F.; DOMINGUES, C.; BENINI, F. A. V.; NETO, L. G.; MARTINS, E. R.; BORGES, B.-H.V. Static and dynamic stereoscopic computer-generated holography (CGH) with spatial light modulators (SLM). **Imaging and Applied Optics Congress, OSA Technical Digest** (Optica Publishing Group, 2020), paper HF1D.6, 2020

12. MOTA, A. F.; MARTINS, A.; PEPINO, V. M.; MARTINS, E. R.; WEINER, J.; TEIXEIRA, F. L.; BORGES, B.-H. V. 2D semi-analytical model for optimizing the radiation emission of quantum emitters embedded in a bounded nano-patterned hyperbolic metamaterial. **2018 12th International Congress on Artificial Materials for Novel Wave Phenomena (Metamaterials)**, Espoo, Finland, pp. 128-130, 2018

13. TOGO, H.; PEPINO, V. M.; BORGES, B.-H.V.; MOTA, A. F. Design of a highly efficient and dynamically controlled transmissive metasurface with linear polarization rotation for microwave applications. **2021 Fifteenth International Congress on Artificial Materials for Novel Wave Phenomena (Metamaterials)**, NYC, NY, USA, 2021, pp. 296-298, 2021

14. KONDO, J. D. M.; GOMES, N. D.; PEPINO, V. M.; BORGES, B.-H. V.; MAGAL-HÃES, D. V.; MARCASSA, L. G. Improving electric field sensitivity by combining electromagnetically induced transparency, polarization spectroscopy, and microwave 3D printed lenses using hot vapor of Rydberg atoms as fundamental atomic sensors. **Bulletin of the American Physical Society**, 2023

Part I

Wavefront shaping with metasurfaces

2 3D-PRINTED DIELECTRIC METASURFACES FOR ANTENNA GAIN IMPROVEMENT IN THE KA-BAND

The work in the chapter has been published as: PEPINO, V. M.; MOTA, A. F.; MARTINS, A.; BORGES, B.-H. V. 3-D-Printed Dielectric Metasurfaces for Antenna Gain Improvement in the Ka-Band. **IEEE Antennas and Wireless Propagation Letters**, vol. 17, no. 11, pp. 2133-2136, Nov. 2018. Permission for reuse is found in Appendix F

2.1 Introduction

The emergence of fifth-generation (5G) cellular technology, expected to occur around 2020, has set unprecedented new challenges to the scientific community regarding energy and spectral efficiency, as well as data rate capacity. So much so, it is fair to say this technology represents a paradigm shift for mobile communication (158). The required aggregate data rate, or the amount of data supported by this network, is about 1000 times higher than that of the fourth generation (4G) (159). Consequently, many techniques have been proposed to attend these requirements, such as increased cell density (160), massive multiple-input–multiple-output (MIMO) systems (161), and, notably, the use of the millimeter (mm)-wave spectrum (162).

Mm-waves are an appropriate choice since they allow higher bandwidths if compared to microwaves while keeping the same fractional bandwidth. Unfortunately, this benefit comes at the cost of a high path loss (163,164). This drawback has motivated the search for highly efficient antennas, especially in the Ka-band, in the past years (165). Alternatives currently adopted to increase the antenna efficiency include multibeam antennas (166) and microwave lenses (167). The latter has also been used to improve the signal-to-noise ratio of an MIMO system by focusing the desired signal while rejecting interference signals (168).

Microwave lenses are usually bulky devices, whose dielectric material is tailored to achieve a desired phase profile (169–171). Fortunately, the advent of additive manufacturing technologies, or three-dimensional (3D) printing, has increased the degree of freedom in the design of electromagnetic structures significantly. This fabrication technology has proved to be particularly attractive for microwave applications because its printing resolution is much smaller than the operating wavelength. Therefore, this printing technology is perfectly adequate for the fabrication of all-dielectric metasurfaces, which consist of an array dielectric posts whose diameter and/or height are designed to control the phase and amplitude of an electromagnetic wave that propagates through them. These all-dielectric metasurfaces are particularly attractive due to the absence of ohmic losses that normally occur in their metallic counterparts. Surprisingly, the literature concerning microwave or

mm-wave 3D-printed metasurfaces is scarce (172). Recently, antennas and lenses with beam-steering capabilities have received much attention (167, 173) since this capacity eases the operation of the 5G small cells.

In this chapter, we propose an all-dielectric, 3D-printed, metasurface lens capable of increasing the antenna gain of about 7.5 dB at 32.5 GHz with a bandwidth of 2.4 GHz. Moreover, differently from current lens approaches that have shown limited steering capability (167, 173), the proposed lens allows azimuth and elevation angle variations as high as 50° and 40°, respectively. The lens' focus FWHM is $\sim 0.85\lambda$ with a 3 dB DOF of approximately 5 cm.

This chapter is organized as follows: Section 5.2 presents the metalens design given in terms of phase and diffraction efficiency maps. Section 5.3 shows numerical and experimental results, while Section 5.5 presents some concluding remarks.

2.2   Metalens design

The metalens is designed with ABS plastic cylindrical posts as building blocks to create the required phase map. The design of these elements is usually carried out by assuming an infinite array of identical posts arranged in a sub-wavelength periodic lattice. Only the zero-order propagates in this design. The phase shift and diffraction efficiency imparted by the array are both functions of the structure geometrical parameters such as post aspect ratio, fill factor, and/or unit cell size. We calculate these values using the rigorous coupled-wave analysis (RCWA) method (174), which assumes an infinite and periodic array of equal posts in a square lattice with unit cell size ρ. The posts' height is fixed at $h = 16$ mm, which is a good compromise between thickness and phase control range of the structure. The design frequency is 30 GHz. The relative permittivity and loss tangent of the ABS plastic adopted here are shown in Fig. 3 (parameters extracted according to (175)) with the solid lines representing the polynomial fit of the extracted parameters. Although the fitted loss tangent value is fairly constant around 0.006, we have used its maximum value ($\tan(\delta) = 0.01$) in our simulations for rigorousness.

Fig. 4(a) and (b) shows the phase and transmittance maps as function of both ρ and a/ρ. The phase shift is restricted here to the range $[0–\pi]$ rad due to the ABS's small permittivity due to printing limitation. However, a full $[0–2\pi]$ control is possible by doubling the posts height and, consequently, the structure aspect ratio. As shown in Fig. 4, the transmitted phase and transmittance are not significantly dependent on the lattice constant a, and the transmittance is always higher than 64%. Therefore, we choose $\rho = 6$ mm, which is a good compromise between structure size and fabrication resolution. A total of six phase levels are used, with the corresponding posts diameters ($2a$) listed in Table 1. The impedance of the metalens is calculated in the same manner as its phase map because the homogenization procedure we have adopted (176) demands the structure to be periodic.

However, this approximation is valid in the present design because the proposed metalens is a low-contrast grating. More importantly, when we average the transmission of the unit cells of all individual cylinders of the metalens, we end up with a total transmittance of 84%. This value also agrees with the finite-difference time-domain simulation of the complete structure, which resulted in 83% transmission, therefore proving that the unit cell approximation is indeed perfectly adequate for this design. In this sense, an effective impedance can be obtained for each cylinder diameter as listed in Table 1. As expected, the impedance decreases for increasing diameters because more pixel area is filled with ABS plastic. The reflectance of the smallest (largest) cylinder diameter is only 1% (16%), indicating that the metasurface impedance is well matched with that of air.

The metalens is created by assembling a spatial phase profile that obeys the following equation:

$$\Phi\left(x, y\right) = -\frac{2\pi}{\lambda}\left(\sqrt{x^2 + y^2 + z_f^2} - z_f\right), \tag{2.1}$$

where x and y are the in-plane coordinates, z_f is the lens focal length, and λ is the free-space wavelength. The proposed metalens has a focal length $z_f = 10$ cm and a discretized phase profile, with 26×26 posts. Since our post design is constrained to a phase range $[0, \pi]$, or equivalently $[-\pi/2, \pi/2]$, we saturate the wrapped spatial phase profile of the lens as follows:

$$\Phi_s\left(x, y\right) = \begin{cases} \text{wrap}\left[\Phi\left(x, y\right)\right], & \text{for } -\frac{\pi}{2} < \text{wrap}\left[\Phi\left(x, y\right)\right] < \frac{\pi}{2} \\ \frac{\pi}{2}, & \text{for wrap}\left[\Phi\left(x, y\right)\right] > \frac{\pi}{2} \\ -\frac{\pi}{2}, & \text{for wrap}\left[\Phi\left(x, y\right)\right] < -\frac{\pi}{2} \end{cases} \tag{2.2}$$
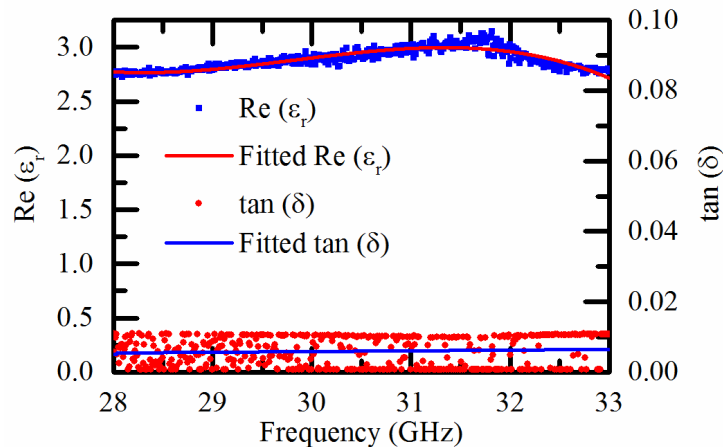
Figure 3 – Extracted relative permittivity and loss tangent of the ABS plastic. The solid lines represent a polynomial fit of the extracted permittivity (squares) and loss tangent (circles) data.
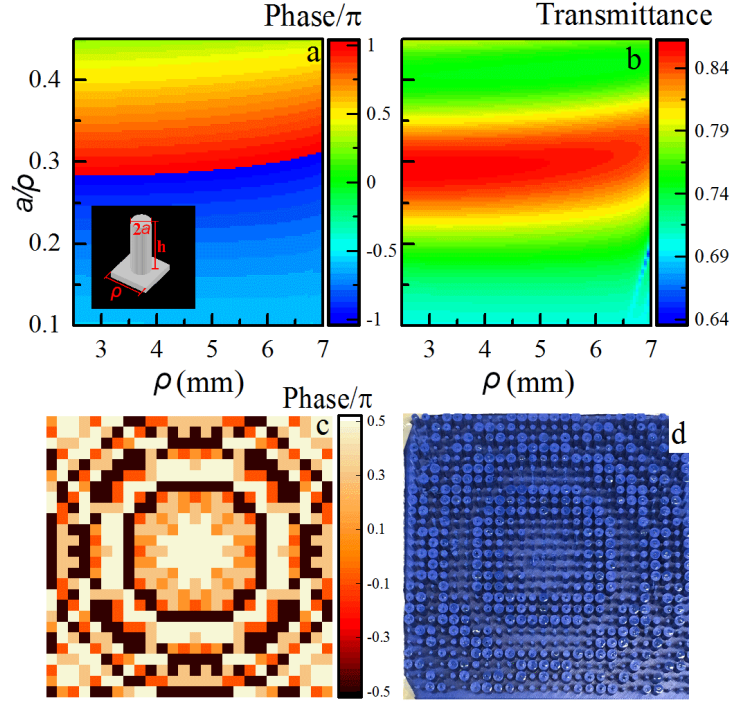
Figure 4 – (a) Phase in units of π and (b) transmittance maps for $h = 16$ mm at 30 GHz. (c) Phase map of the metalens. (d) Fabricated metalens. The inset in (a) shows the metalens unit cell. The posts have period ρ, radius a, and height h.

where wrap is an operator that wraps the phase profile to the $[-\pi, \pi]$ interval. Although this approximation reduces the lens efficiency, numerical calculations show that the phase profile $\Phi_s(x, y)$ still works as a lens with a FWHM of $\sim 0.85\lambda$ at the focal point. Fig. 4(c) shows the metalens phase profile, while Fig. 4(d) shows the fabricated structure.

2.3   Results

The setup used for the metalens characterization is shown in Fig. 5. It consists of a vector network analyzer (VNA, Rohde&Schwarz ZVA 40), a standard WR-34 horn (transmitting) antenna, a patch (receiving) antenna array, and a pedestal to support the metalens. The feed antenna is a standard gain WR-34 horn antenna (Pasternack PE9851)

Table 1 – Corresponding diameters and impedances for each phase shift value

Diameter (mm)	Relative impedance	Phase (rad.)	Normalized phase (rad.)
5.25	0.73	$0.4\,\pi$	$-0.5\,\pi$
4.77	0.80	$0.6\,\pi$	$-0.3\,\pi$
4.23	0.83	$0.8\,\pi$	$-0.1\,\pi$
3.60	0.87	π	$0.1\,\pi$
2.73	0.93	$-0.8\,\pi$	$0.3\,\pi$
1.38	0.98	$-0.6\,\pi$	$0.5\,\pi$

with a nominal 20 dBi gain and 17° (17.4°) vertical (horizontal) half-power beamwidth (HPBW). The distance between metalens and transmitting antenna ($\sim$1 m) is limited by the cable length of the VNA. Note that this distance is larger than the Fraunhofer far-field distance (d_{FR}) (177) for the horn antenna at the lower frequency ($d_{FR} = 0.378$ m). The receiving antenna is a patch antenna array (chosen due to its improved spatial resolution), positioned at the metalens focal point. The patch antenna measured return loss, with (dashed line) and without (solid line) the metalens, is shown in Fig. 6. The antenna itself is in the inset of the figure. Note that the metalens has negligible influence on the return loss of the patch antenna. To guarantee that only the metalens response is measured, aluminum foil is placed around the metalens, as shown in Fig. 4(a). Finally, the antennas are connected to the VNA to measure the transmission (S_{21}) in the 28–33 GHz band.
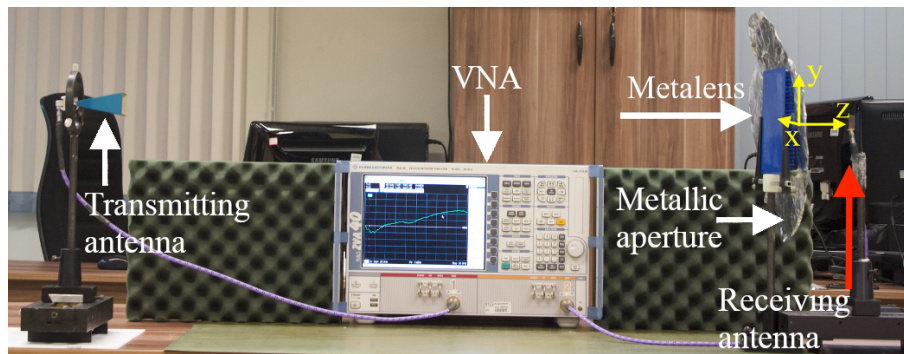
Figure 5 – Experimental setup: A patch antenna on the right (indicated by the red arrow) is positioned at the metalens focal point, while a horn antenna on the left is used to excite the structure. Coordinate system is shown in yellow.
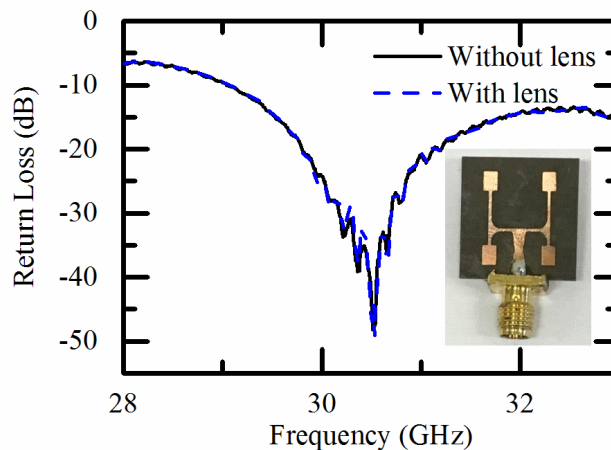
Figure 6 – Measured patch antenna return loss with (blue dashed lines) and without (black solid lines) the metalens. Inset shows the patch antenna used in the measurements.

First, we measure the transmitted power without the metalens (P_R) and use it as a

reference value. Then, we measure the transmitted power with the metalens present (P_M)
at several positions along the x-(with $y = 0$ and $z = z_f$) and z-axes (with $x = y = 0$). The
gain map in dB ($G = 10 \log(P_M/P_R) + G_o$), with G_o as the patch antenna gain, is then
calculated as function of the receiving antenna's position and frequency, as shown in Fig.
7(a) and (b). The dots in these figures indicate the map boundaries, which refer to the
FWHM for Fig. 7(a), and the 3 dB DOF for Fig. 7(b). The dots start at 29 GHz because
there is no focus below this frequency, as shown in Fig. 7(c). Although frequency variations
do not shift the focus point along the x-axis, the focal point changes from approximately
10–13 cm, as shown in Fig. 7(a) and (b). The maximum gain obtained with this approach
is 7.5 dB at 32.5 GHz (about 5% difference from the desired operating frequency due to
fabrication imperfections). The FWHM at focus, shown in Fig. 7(c), is approximately 7
mm for frequencies lower than 30 GHz and increases to 8mm($\sim$0.85λ) at 32.5 GHz. Note
that even though the FWHM is above the diffraction limit, it can still be reduced in future
designs with the increase of the metalens resolution. The 3 dB DOF is approximately 5
cm for all frequencies, with a slight decrease for lower wavelength. A bonus with this lens
is its high operational bandwidth (2.4 GHz), which enables applications in high-speed
communications.
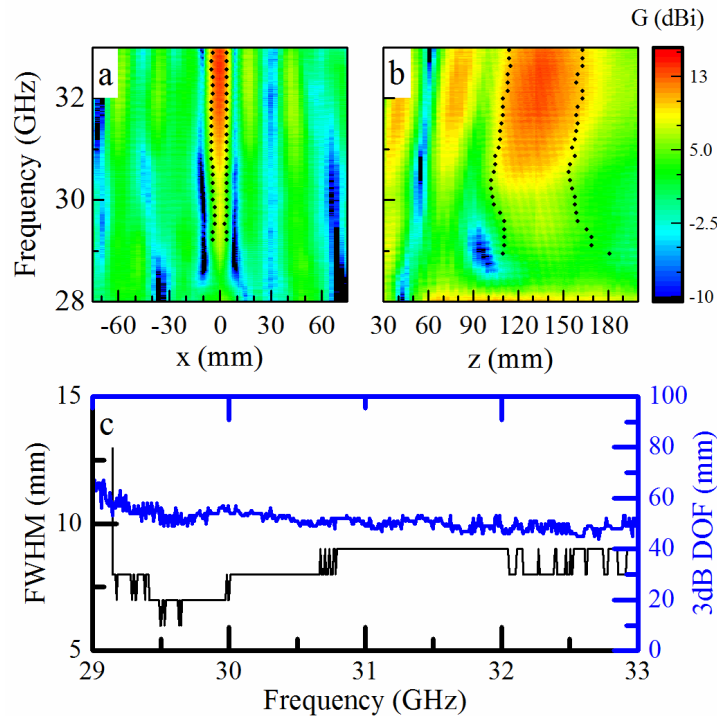
Figure 7 – Measured power (normalized) (a) at $z = 132$ mm as function of x, and (b) at
$x = 0$ cm as function of z in the 28–33 GHz band. (c) FWHM and 3 dB DOF
in the 28–33 GHz band. Dotted lines in (a) and (b) show the 3 dB boundaries.

The radiation patterns for the azimuthal (a) and elevation (b) planes with (solid
line) and without (dashed line) the metalens are shown in Fig. 8. Note that the maximum
gain reaches 13.6 dBi with and 6.1 dBi without the metalens, i.e., an additional 7.5 dB

gain to the antenna. The metalens also increases the antenna directivity, especially on the azimuthal plane [see Fig. 8(a)], with the HPBW being reduced from 36° to 3° and from 4.5° to 3° for the azimuthal and elevation planes, respectively. Moreover, because of the gain and directivity enhancements provided by the metalens, the antenna sidelobe level is reduced, and the front-back relation increases from 15 to 21 dB, as shown in Fig. 8(a) and (b).
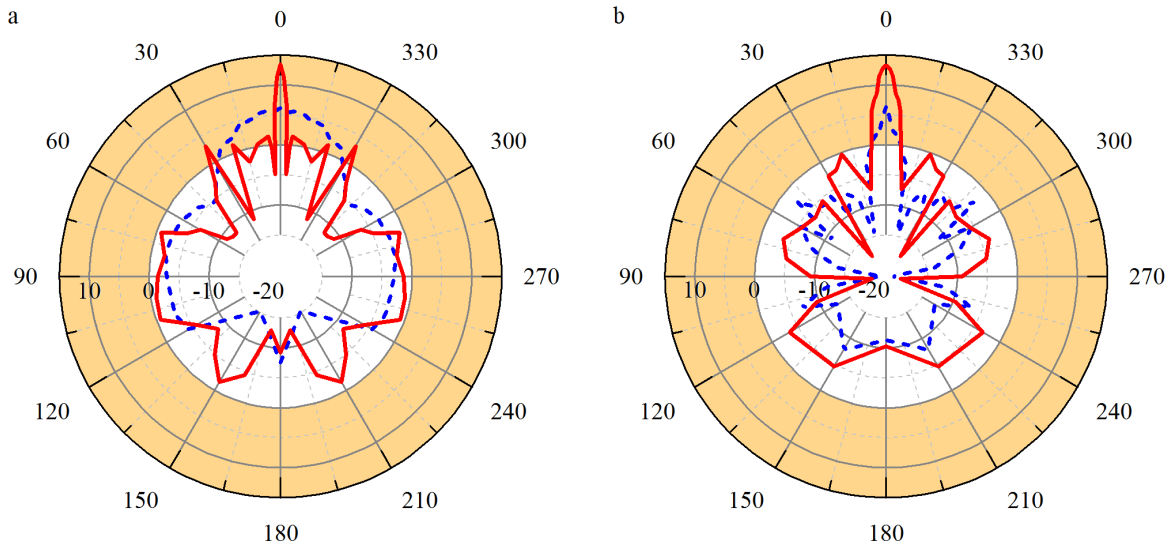
Figure 8 – Normalized gain (dB) radiation pattern for (a) azimuthal and (b) elevation planes, with (red solid lines) and without the metalens (blue dashed lines). The left side of both diagrams is mirrored onto the right side due to the lens symmetry. Yellow regions highlight the gain area.

An important aspect relative to this lens is that each pixel is designed assuming a plane wavefront. However, in real applications, the antenna can be illuminated from different angles. Therefore, it becomes crucial to investigate its performance under oblique incidence. To carry out this task, we rotate the lens along the *y*- (azimuthal angle) and *x*-axes (elevation angle). During this measurement, the antenna is maintained at the lens focal point with the frequency fixed at 32.5 GHz (for best performance). Fig. 9 shows the measured (symbols) and the third order polynomial fit (lines) gain G as function of the azimuth (asterisks, solid line) and elevation (circles, dashed line) angles. Note that the lens is not perfectly symmetric [see Fig. 4(d)], thus it does not behave equally whether the wavefront impinges with different azimuthal or elevation angles. The gain drops 3 dB at the azimuthal (elevation) angle of 25° (20°). Therefore, the proposed lens has azimuthal and elevation steering spans of 50° and 40°, respectively, which are substantially higher than those at (167) (8° and 34°) and (173) (27° for both cases).
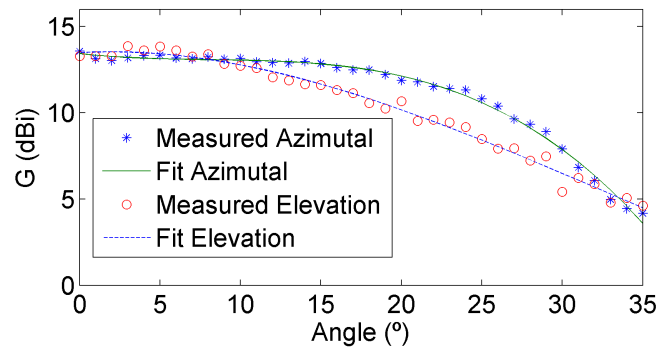
Figure 9 – Measured gain at focus for different azimuth (asterisks, solid line) and elevation (circles, dashed line) angles.

2.4   Conclusion

In this chapter, we demonstrated the first all-dielectric, 3D printed, microwave metalens with diffraction efficiency in excess of 70% (numerically) and measured gain of 7.5 dB at 32.5 GHz. Its HPBW (0.85λ) is only slightly above the diffraction limit. In addition, we have shown that this metalens increases the directivity of the receiving antenna by reducing its HPBW to approximately 3° relative to both azimuthal and elevation planes. Furthermore, the metalens is still able to focus the beam into the receiving antenna even when rotated, with a 50° and 40° span at azimuthal and elevation planes, respectively. We have also demonstrated that it is possible to design functional metasurfaces with a phase control of π $[-\pi/2, \pi/2]$, allowing low-permittivity materials to be used while still maintaining small thicknesses. The proposed low-loss and low-cost all-dielectric metalens, with a measured gain as high as 7.5 dB at 32.5 GHz, outperforms conventional all-dielectric lenses, such as that in (169) whose gain is 6.6 dB.

3 EXTENDING THE ALVAREZ LENS SCHEME TO ACHIEVE TUNABLE TERAHERTZ BESSEL BEAM GENERATION WITH SILICON MICROHOLED METASURFACES.

The work present in the chapter is part of a collaboration with The Ohio State University and Professor Fernando L. Teixeira.

3.1 Introduction

The terahertz (THz) frequency range has received a lot of attention due to its unpreceded potential for communications (178–181), sensing (182) and imaging (183–187) applications. However, many challenges remain. Free space attenuation is elevated when compared to microwave and millimeter wave frequencies (183). Moreover, the lack of high power sources (188) is a motivation to design devices with increased efficiency and reduced losses.

One way to increase the propagation efficiency is to use non diffractive beams (189–191) which reduce free space losses. In particular, Bessel beams have been shown to lower the bit error rate in free space communications (192). Moreover, its self-regenerative properties (193–195) and increased depth of focus (DOF) (196–198) due to non-diffracting properties make the Bessel beam a strong candidate for communication (192, 199, 200) and imaging applications (190, 198, 201–203), such as in vivo terahertz imaging (186, 204), tomography (190, 196, 198, 205) and microscopy (190, 206).

Bessel beams have been implemented in the THz range by conventional and 3D-printed bulk axicons (196, 202, 207, 208), discrete bulk axicons (201, 209), direct emission via light pumping of Indium tin oxide coated axicons (210), 3D printed pyramid lenses (211), and metasurfaces (112, 212–215). The latter permits a more precise control of the radial and azimuthal phase distributions for higher order beams and achieving long DOF without increasing the axicon's radius, while using very thin structures. However, an increased DOF is associated with an increased beam full width at half maximum (FWHM) due to both being inversely proportional to the axicons numerical aperture (NA) (69), leading to a tradeoff between DOF and image resolution.

One way to circumvent this issue is to use a tunable metasurface. Active THz meta devices can be implemented with graphene (115, 117, 128–134), liquid crystal (114, 116, 117, 123–127), thermally or optically tunable semiconductors (216, 217), and phase change materials (135–137). However, dynamically reprogrammable metasurfaces require complex design to electronically control each pixel or region independently. Another way is to use mechanically tunable devices. The Alvarez (218) and Lohman (219) lenses are originally bulk dual devices that present variable focus when a displacement between

the two devices is applied in the transverse plane. The Alvarez lens has a focal length proportional to an horizontal displacement while the Lohman lens allows both horizontal and vertical adjustment of dual cylindric phase profiles. It has also been implemented using rotational displacements (220–222). This Alvarez concept has been implemented using bi-layer metasurfaces in the optical (138), infrared (139) and THz regime (140), and generalized for arbitrary phase distributions (140, 141). By simply applying a mechanical displacement between the two layers, tunable diffractive devices can be implemented using easily fabricated metasurfaces.

Here, we propose and experimentally characterize a tunable THz axicon using two silicon microholed layers. The microholed structure allows a simpler fabrication process via laser micro-machining of the whole dielectric substrate, as opposed to deep etching processes (223) that may require multiple steps. We achieve a DOF tunable from 20 to 40 cm and a FWHM tunable from 6 to 3.2 mm. When obstructed with by objects of one to two orders of magnitude larger than the wavelength diameter opaque obstacle, the Terahertz Bessel beam (TBB) self regenerates after a propagation length of a few centimeters.

This chapter is organized as follows: first we introduce the Alvarez lens concept and how to calculate the necessary spatial phase profiles for a tunable axicon. Then, we provide the metasurface design and fabrication procedure. Next, we present and discuss the results. Finally we add out concluding remarks. Scalar diffraction theory of the Bessel beam and its self-regenerative properties, choice of phase levels and inter layer axial separation distance phase error analysis, are found in Appendix B.

3.2 Design and fabrication

3.2.1 Tunable spatial phase profile

The Alvarez lens is composed of two horizontally displaced complementary devices (224). By neglecting the diffraction in the air gap between both layers we have:

$$\varphi(x, y) = \Phi(x + d, y) - \Phi(x - d, y), \tag{3.1}$$

where x and y are the horizontal and vertical directions in the DOE plane, d is the displacement applied between the layers, $\varphi(x, y)$ is the desired phase distribution and $\Phi(x, y)$ $[-\Phi(x, y)]$ is the necessary phase distribution in the first [second] layer. In metasurface zero-order axicons (69),

$$\varphi(x, y) = \varphi_o - k_o NA\sqrt{x^2 + y^2}, \tag{3.2}$$

where φ_o is a constant spatial phase term that can be ignored, k_o is the free space wavenumber and axicon's NA is the numerical aperture. In bulk axicons, it is related to

(a) (b) (c)

$\varphi(x,y) = \varphi_o$
$-k_o(n-1)\tan(\alpha)\sqrt{x^2+y^2}$

$\varphi(x,y) = -k_o NA\sqrt{x^2+y^2}$

$\varphi(x,y) = \phi(x-d,y) - \phi(x+d,y)$
$\phi(x,y) = -\dfrac{k_o}{2}[x\sqrt{x^2+y^2} + \ln(x+\sqrt{x^2+y^2})]$
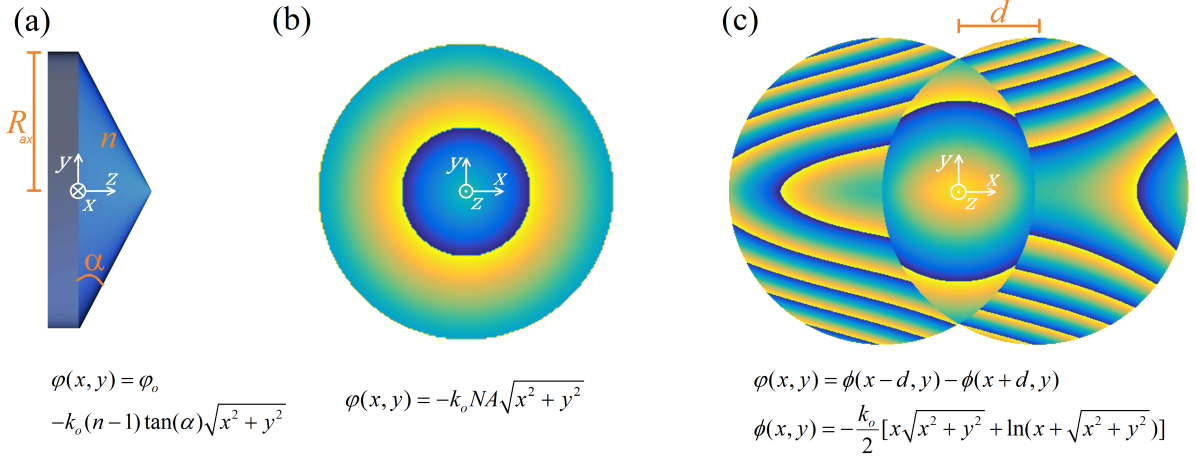
Figure 10 – (a)Bulk axicon representation. Its transmitted phase is a function of the angle α and of the refractive index n. (b) Meta axicon. The same phase distribution is obtained with planar optics. (c) Bi-layer meta axicon. By using the Alvarez lens principle, we design a tunable axicon with $NA = \upsilon d$, $\upsilon = 2$.

the DOE refractive index and its angle (see Fig. 10(a)). The DOF and $FWHM$ of an axicon with radius R_{ax} is given by $(69, 207)$:

$$DOF \simeq \frac{R_{ax}}{NA}, \tag{3.3}$$

$$FWHM = \frac{0.358\lambda}{NA}, \tag{3.4}$$

where λ is the operating wavelength. As observed in (140), (3.1) resembles a derivative.

$$\frac{\partial \Phi(x,y)}{\partial x} = \lim_{d\to 0} \frac{\Phi(x+d,y) - \Phi(x-d,y)}{2d}. \tag{3.5}$$

Thus, for $d \ll (x,y)$,

$$\Phi(x,y) = \frac{1}{2d}\int \varphi(x,y)\ \mathrm{d}x, \tag{3.6}$$

$$\Phi(x+d,y) - \Phi(x-d,y) \simeq 2d\varphi(x,y). \tag{3.7}$$

By using (3.2) in (3.6), we get

$$\Phi(x,y) = -\frac{k_o NA}{2}\frac{1}{2d}\left[x\sqrt{x^2+y^2} + y^2\ln\left(x+\sqrt{x^2+y^2}\right)\right]. \tag{3.8}$$

To achieve tunable DOF, we need $NA = \upsilon d$, where υ is a proportionality constant with dimension of $[\mathrm{m}^{-1}]$; in this work we use $\upsilon = 2$, which is small enough to achieve long

DOF and large enough so that the phase necessary distribution is achievable with 16-level phase discretization.

$$\Phi\left(x,y\right) = -\frac{k_o v}{4}\left[x\sqrt{x^2+y^2} + y^2\ln\left(x+\sqrt{x^2+y^2}\right)\right],\tag{3.9}$$

$$\varphi\left(x,y\right) = \Phi\left(x+d,y\right) - \Phi\left(x-d,y\right) \simeq -2k_o v d\sqrt{x^2+y^2},\tag{3.10}$$

$$DOF \simeq \frac{R_{ax}}{vd},\tag{3.11}$$

$$FWHM = \frac{0.358\lambda}{vd}.\tag{3.12}$$

Equation (3.9) and its complementary phase give the necessary phase distributions for each layer of our tunable TBB generator. Note that (3.3)-(3.4) and consequently (3.11)-(3.12) assume that the spatial frequencies generated by the diffraction in the incident beam's aperture is negligible when compared to the spatial frequencies induced by the axicon, which is the geometric optics limit approximation $k_o \to \infty$. This is analyzed in depth in Appendix B.1, where we show they are not valid approximations for our case and compare the ray optics approximation with the results obtained using the angular spectrum formalism (ASF). Figure 10 (a)-(c) shows a bulk axicon, a metasurface axicon and our proposed bi-layer tunable meta axicon, respectively.

3.2.2   Unit cell

We choose high resistivity silicon (Si) as our dielectric, due to high refractive index and low loss tangent (225). The complex relative permittivity at wavelength $\lambda = 350$ μm is equal to $11.68 \cdot (1 - 2.095 \cdot 10^{-5}i)$. This wavelength is chosen due to the lower atmospheric absorption (226). We choose micro holes as our unit cell. It allows easy fabrication and is shown in the inset of Fig. 11(a), with w being the hole's diameter and ρ being the period of the holes array. Figure 11(a)-(b) show the phase and transmittance maps for a period ρ varying between 80 and 200 μm and hole diameter w swept from 10% to 90% of the period.

The necessary silicon thickness to achieve complete phase control is 600 μm, while we only had 300 μm wafers available. Thus, we stack two wafers for each layer. The maps were obtained using RCWA (174). Red lines show fabrication and design constraints. The hatched area is the region that satisfies all constraints, which consist of: the minimum hole diameter is 65 μm; the minimum distance between two max-sized holes, that is, the amount of material left is 20 μm; to avoid unwanted resonances, the maximum period is set to 130 μm. We choose to use 16 phase levels and define a figure of merit (FoM) as

the average transmittance divided by the average phase error (in degrees) to optimize the period.

$$FoM = \frac{1}{M} \sum_{b=1}^{M} \frac{\left|T_b^{\mathrm{RCWA}}\right|^2}{\frac{180}{\pi} \left|\left(\frac{2\pi b}{M} - \pi\right) - \arg\left(T_b^{\mathrm{RCWA}}\right)\right|}, \tag{3.13}$$

where $b = 0, 1, \ldots M$, M is the number of phase levels and T_b^{RCWA} is the complex transmission of the b-th phase element obtained via RCWA. Red circles in Figs. 11(a)-(b) mark the optimal diameters for the optimal period of 118 μm and Fig. 11(c) shows FoM as a function of the period ρ, for values smaller than 130 μm (no resonance region). Finally, we average the transmittance of the metasurface and sort the unit cells in order to maximize it (see Table 7 in the Appendix B.3). Note that this does not change the operation of the metasurface since sorting the cells only impose a constant phase shift over the whole surface. More details on the unit cell design and choice of phase levels are found in Appendix B.3. Figure 3 shows the fabricated metasurfaces. The layers are two inches wide, with a margin of 5mm left for alignments. Inset shows the microscope view.

3.2.3 Fabrication

The metasurfaces are fabricated in high resistivity silicon wafers. Due to our limited availability of high resistivity silicon, we used two 300 μm wafers for each layer of the meta axicon, which are later alignment. We used laser micro-machining (LPKF ProtoLaser U3), in both sides of each wafer, to avoid conical holes, due to limited depth of focus of the machining laser. Unfortunately the metasurfaces broke during experimental
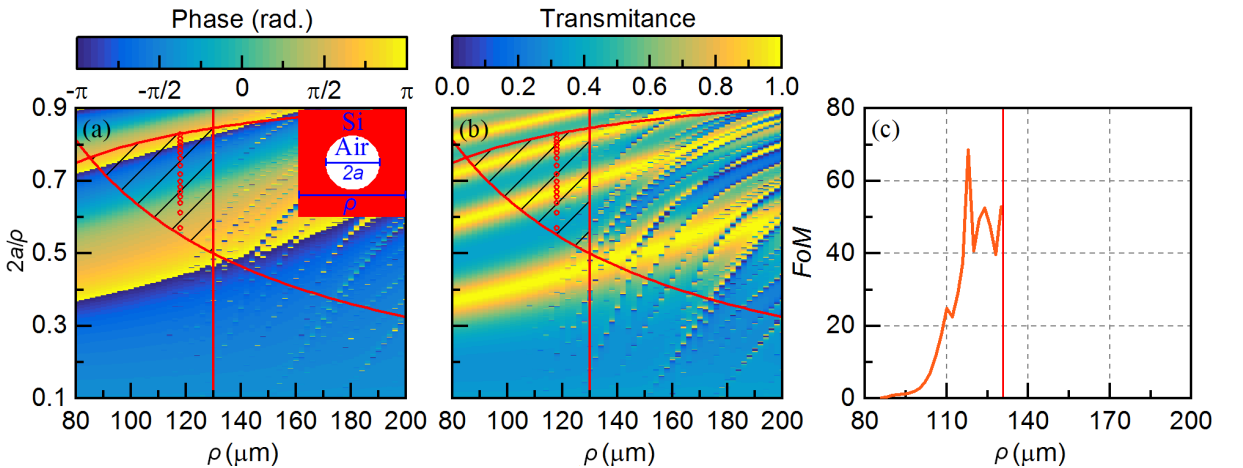
Figure 11 – RCWA (a) phase and (b) transmittance maps. Inset in (a) shows the unit cell geometry and relevant dimensions. Red lines are representation of design constraints (maximum period, minimum diameter and minimum distance between two holes). The hatched area limits the region where all the constraints are satisfied. (c) FoM used to optimize the metasurface period. Note that FoM is only calculated for periods smaller than 130 μm.
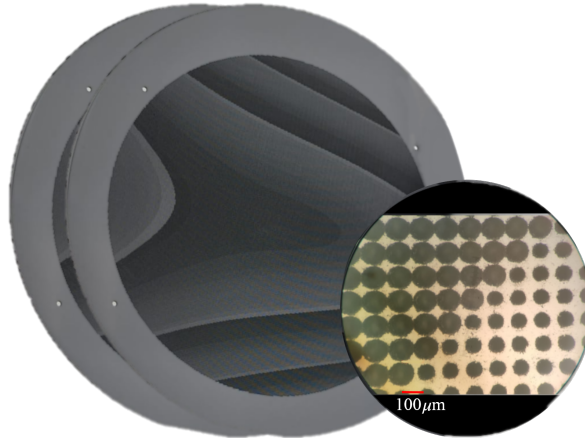
Figure 12 – Fabricated silicon metasurfaces. Each silicon wafer has a diameter of 2 inches and an active region defined by a circle with a diameter of 4 cm. Microscope view is show as an inset, with scale bar shown in red.

characterization, and thus only simulation results are presented in this Chapter. Nonetheless, the metasurfaces are being fabricated again to be experimentally characterized in the future.

3.3 Results

3.3.1 Beam characterization

We begin by analyzing the TBB spatial profile. In simulations, we use the angular spectrum formalism (94), for rigorous wave optics treatment while also faster than finite difference time domain (FDTD) or finite elements simulations. The phase profile $\Phi\left(x+d,y\right)$ is applied on an incident beam with radius $R_{ax} = 1$ cm and propagates for a distance $t_{ax} = 700$ μm. We choose this distance to minimize the phase error due to phase discretization (more details in Appendix B.3).

Note that the non-diffracting distance, or the DOF, here defined as the length in which the beam intensity is higher than half of its maximum value, is longer for lower values of d. The same is true for the $FWHM$, as expected from (3.11) and (3.12). Figure 13 (a) plots the simulated values of DOF and $FWHM$ as d varies. Figure 13 (b) shows the transmission efficiency as a function of d. Note that both DOF and $FWHM$ are saturated for $d > 13$ mm). This happens because the approximation in (3.7) loses its validity when d is comparable to (x, y). However, the TBB is still reconstructed in these cases.

To better observe the TBB, we present a 3D simulation of the beam propagation in Fig. 14 for $d = 4$ mm. A non diffracting pattern is clearly observed for 14 cm $< z <$ 43 cm.
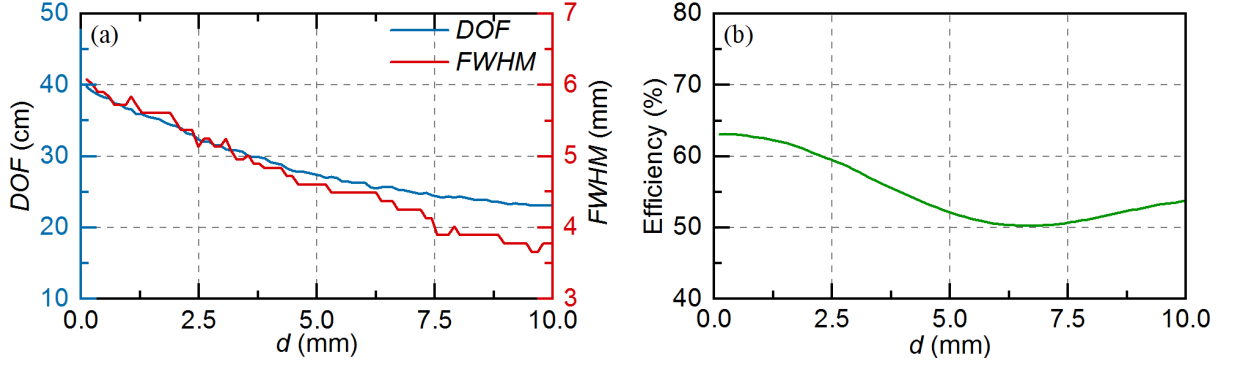
Figure 13 – (a) DOF (blue lines) and $FWHM$ (red lines) as the meta axicon is tuned. (b) Transmission efficiency. Results refer to simulations only.
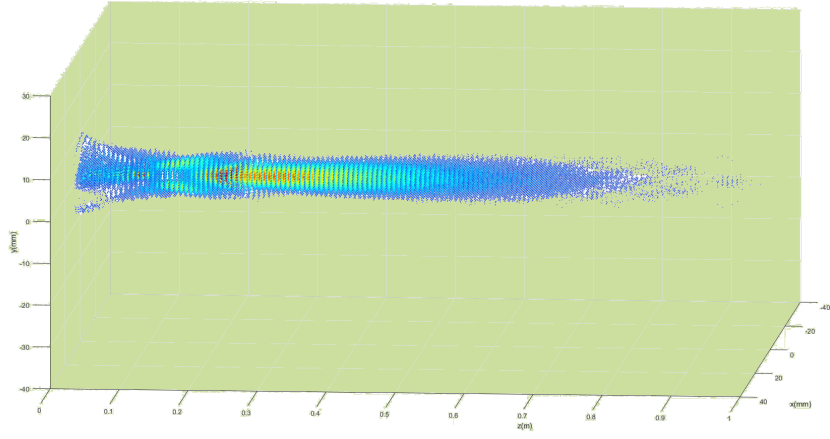
Figure 14 – 3D simulation of the TBB propagation. The beam is shown only in positions where the intensity of the electric field is higher than 1% of the peak value. Note that the non diffracting region is between 14 cm $< z <$ 43 cm, with a DOF approximately equal to 29 cm.

3.3.2 Self-healing properties

Here we simulate the self-healing properties of the TBB. We obstruct the TBB with a circular opaque object of radius r_{ob} placed at $(x_{ob}, 0, z_{ob})$. By using the ASF, we calculate the distance z_{sh} in which the correlation coefficient between the electric field before $[E(r, z_{ob})]$ and after $\left[E^{ob}(r, z)\right]$ the obstruction is higher than 0.90. Figure 15shows z_{sh} as a function of (a) r_{ob} for $d = 4$ mm, $z_{ob} = 20$ cm and $x_{ob} = 0$; (b) x_{ob} for $d = 4$ mm, $z_{ob} = 20$ cm and $r_{ob} = 2.5$ mm; (c) d for $z_{ob} = 20$ cm, $r_{ob} = 2.5$ mm and $x_{ob} = 0$. Note that z_{sh} has an average value of 20 cm, which allows for non-diffractive beam propagation after its regeneration, based on DOF values from Fig. 13(a). The obstructions transverse position has the least influence on the regeneration distance, while its size has the most influence. Note that there is a discontinuity at $r_{ob} = 2$ mm, which is due to the overshoot behavior of the correlation curve as z changes. When the correlation overshoot does not reach values above 90%, there is a sudden increase on z_{sh}.
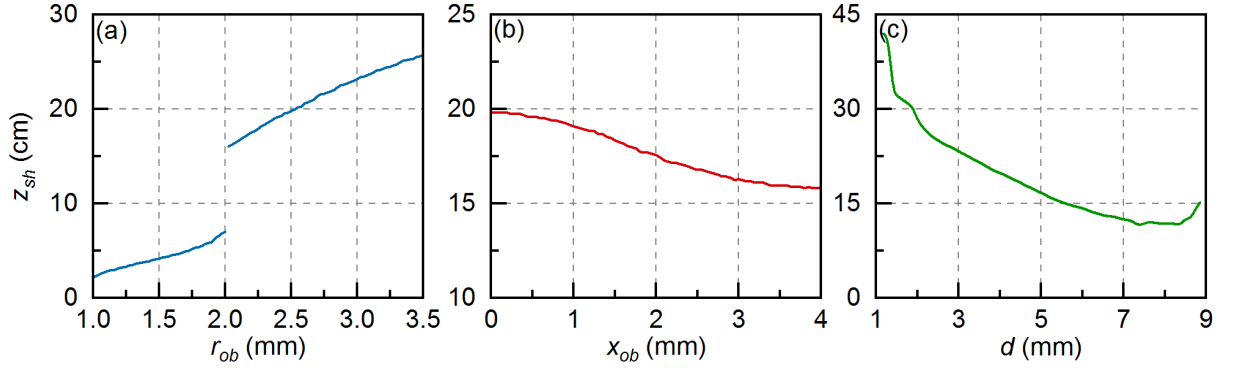
Figure 15 – z_{sh} as a function of (a) r_{ob} for $d = 4$ mm, $z_{ob} = 20$ cm and $x_{ob} = 0$; (b) x_{ob} for $d = 4$ mm, $z_{ob} = 20$ cm and $r_{ob} = 2.5$ mm; (c) d for $z_{ob} = 20$ cm, $r_{ob} = 2.5$ mm and $x_{ob} = 0$. Note that there is a discontinuity at $r_{ob} = 2$ mm, which is due to the overshoot behavior of the correlation curve as z changes.
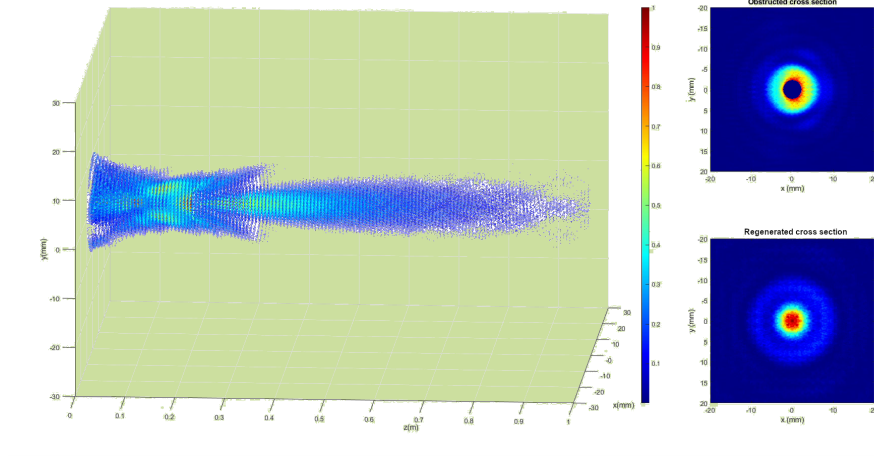
Figure 16 – Left panel: 3D simulation of the TBB regeneration for $d = 4$ mm, $z_{ob} = 20$ cm, $x_{ob} = 0.0$ mm and $r_{ob} = 2.5$ mm. It is clear to observe the obstruction and subsequent regeneration of the Bessel beam. The beam is shown only in positions where the intensity of the electric field is higher than 1% of the peak value. Top right panel: Obstructed cross section at $z = 20$ cm. Bottom right panel: reconstructed cross section at $z = 40$ cm.

To observe the TBB regeneration, we present a 3D simulation of the beam regeneration in Fig. 16 for $d = 4$ mm, $z_{ob} = 20$ cm, $x_{ob} = 0.0$ mm and $r_{ob} = 2.5$ mm. The top right panel shows the obstructed cross section, which is clearly observed in the 3D plot at $z = 20$ cm. After an extra 20 cm propagation, the beam is completely regenerated and its cross section is that of a Bessel beam, as seen in the bottom right panel.

3.4 Conclusion

In this chapter we proposed and numerically verified an innovating method of generating tunable Bessel beams for applications in THz communications and imaging. We

extended the Alvarez lens concept to the phase distribution of an axicon to achieve tunable DOF from 22 cm to 40 cm and FWHM from 6 mm to 3.7 mm. High resistivity Si is used as the substrate and micro air holes are chosen as the unit cell for complete phase control. The meta axicon is designed to operate at 850 GHz, and self-healing capacity is observed for obstructions from tens to hundreds of times larger than the operating wavelength. Moreover, we defined the conditions of validity of the commonly used geometric optics approximation and showed that it isn't valid for lower frequencies such as the THz range and low NA values, requiring numerical simulations for accurate characterization of DOF and regenerating distances.

Part II

Dispersion management with metamaterials

4 TERAHERTZ PASSIVE AMPLIFICATION VIA THE TEMPORAL TALBOT EFFECT IN METAMATERIAL-BASED BRAGG FIBERS

The work present in the chapter has been published as: PEPINO, V. M.; MOTA, A. F.; BORGES, B.-H. V.; TEIXEIRA, F. L. Terahertz passive amplification via temporal Talbot effect in metamaterial-based Bragg fibers. **J. Opt. Soc. Am. B** 39, 1763-1774 (2022). Permission for reuse in the author's thesis is found in Appendix F.

4.1 Introduction

In the last few years, there has been a dramatic surge of interest in new THz devices in applications as diverse as non-destructive imaging and sensing (227–231), light–matter interaction, wireless communications (178–181), and spectroscopy (232–236). However, the limited emitted power (188) of THz sources is still a major roadblock in many applications. Currently, there are four main approaches to tackle this limitation, all of them based on active amplification: (1) oscillators associated with antennas (limited by the current electronic technology, which is only now achieving THz operation (237)), (2) radiation emission from materials (based on quantum emitters (238)), (3) graphene-based structures as amplifiers (239), and (4) beam combination from quantum cascade lasers (QCLs) (240). The latter requires low temperature to work properly (241, 242), which may limit practical applications in low-cost devices.

Unfortunately, there is a lack of passive amplification strategies tailored for THz frequencies. Nevertheless, such approaches are not uncommon in other frequency ranges. For instance, passive amplification has been proposed in optical frequencies by (243, 244), which used a sequence of pulses coherently added in high-Q resonant cavities to increase the output peak power (however, a precise synchronization of the pulse envelope and phase is required to guarantee coherent addition). Another way to achieve coherent pulse addition (CPA), without the need for precise cavity synchronization, is through the temporal Talbot effect (TTE). In particular, this effect was used to produce noiseless intensity amplification of repetitive optical pulses (156) and arbitrary non-periodical signals (245). With that in mind, it is reasonable to expect that the TTE can be a viable route for passive THz amplification.

The Talbot effect, first discovered in the spatial domain, is a self-imaging effect that occurs after a periodic input signal propagates over a distance dubbed Talbot length (or z_T). The input pattern is repeated at integer multiples of z_T, while at its rational fractions, it is reproduced with different repetition rates and, therefore, with different periodicity. Its temporal counterpart (TTE) presents the same behavior for temporally periodic signals propagating through a first-order dispersive medium (155). Propagation

at rational fractions of z_T causes the periodicity to increase, resulting in a train of pulses with lower amplitude and higher repetition rate. Fortunately, as we describe later, we can also turn a train of low-amplitude high-repetition rate pulses into high-amplitude and low-repetition ones and, therefore, achieve passive amplification (156). However, for the TTE-assisted passive amplification to occur, a high second-order dispersion coefficient (β_2) is required, especially in the THz range, because it accelerates the self-imaging effect and reduces the propagation length (and consequently the losses), favoring passive amplification. Therefore, the choice of materials plays a critical role in this process.

There are different materials currently available for THz applications, such as polymers (246–248), glasses (249, 250), two-dimensional materials (251) {i.e., graphene (252, 253) and transition metal dichalcogenide (TMD) (254)}, and semiconductors (i.e., silicon (225) and gallium arsenide (255)). The choice of materials strongly depends on the constraints and functionalities of the desired application. Terahertz TTE-assisted passive amplification requires high contrast refractive index modulation, low propagation losses, and, as just noted, a dispersion coefficient (i.e., β_2) as high as possible. As will be shown later, these characteristics are simultaneously achieved more efficiently with silicon-based metamaterials.

A most challenging task is to design a waveguide structure that fulfills all these requirements simultaneously. A good candidate for such a structure is the Bragg fiber since the mode confinement occurs in an air core surrounded by multilayered dielectric mirrors. Bragg fibers (143, 144, 256), with one or more defect layers, act as highly dispersive media over a well-defined wavelength range. More importantly, β_2 can be made arbitrarily large depending only on the materials choice and geometric parameters.

In this chapter, we propose a novel highly dispersive silicon based metamaterial Bragg waveguide fiber capable of passively amplifying THz signals via TTE (155–157, 257). To this end, we use the conversion of a phase-modulated continuous wave (CW) into a sequence of pulses [also known as the Talbot array illuminator (TAI) (157)], but in a backward manner (thus, we dub it here BTAI). Such a procedure determines both the device length and the input signal shape that maximizes passive gain. The phase modulation profile of the input signal plays a critical role in this method. Thus, to define it properly, we choose the desired pulse shape at the fiber output (target output) and backward-propagate it from 0 to $-z_T/2$. We then calculate the signal ripple ($V_r = \Delta V / V_{avg}$, where ΔV is the amplitude variation and V_{avg} is the average amplitude of the signal) at each propagation step. The stop criterion is the propagation length for which the signal ripple $V_R \leq 10\%$. With this procedure, we define the optimum fiber length that maximizes the gain and reduces undesired spurious spectral components. This method allows pulse generation without the need for amplitude modulation, resulting in more efficient energy use of THz sources. Then, we compare our method with two existing ones, namely, CPA

(156) and forward CW-to-pulse conversion (157), or FTAI. All three methods use the TTE to manipulate the periodicity of a pulse train by splitting or combining these pulses (232) as they propagate through the fiber, resulting in a narrow intensity amplified pulse at a given fractional Talbot length. The Bragg fiber used here consists of a large, squared air core with alternating silicon metamaterial claddings. Each metamaterial clad consists of an array of squared airholes (etched directly on silicon wafers) whose fill factor defines its homogenized index of refraction. We stack as many wafers as needed to achieve the desired fiber length. The homogenized index of each cladding layer, calculated according to the parameter extraction method in (176), is then used in the analytical and numerical simulations carried out, respectively, with the transfer matrix techniques (TMT) (258) (for the Bragg mirrors) and (259) (for the waveguide analysis), and finite element method (FEM) results obtained using the Comsol Multiphysics 5.6 software (260). We explore different pulse shapes and chirped pulses with CPA and different gain factors with BTAI and FTAI. The simulations show a 5.8 dB gain (for a 9.8 cm long fiber) with CPA, a 9.9 dB gain with FTAI (1.37 cm long), and a 8.8 dB gain with BTAI (1.25 cm long).

The outline of this chapter is as follows. Section 5.2 provides the theoretical background on the Talbot effect and how to achieve passive amplification. Section 5.3 discusses the design procedure of the dispersive structure and the validity of the TMT simulations as an optimization tool. Section 5.4 presents the numerical results of the TTE for passive amplification. Section 5.5 presents some concluding remarks. Finally, the dielectric properties of different THz materials and the metamaterial homogenization procedure are provided in Appendix C (along with the adopted data processing technique for the full-wave simulation, additional time domain results, and a brief discussion about potential fabrication processes and alternative structures).

4.2 Theoretical background

To facilitate the exposition, we begin this section by first briefly describing the spatial Talbot effect. We then contrast it to its temporal counterpart.

As is well-known, the Talbot effect manifests itself in any domain where its Fourier counterpart has a quadratic phase profile (261). Therefore, the demonstration of a spatial Talbot effect is also valid for its temporal analog in a first-order dispersive medium.

The spatial Talbot effect appears when a periodic wave diffracts as it propagates through a homogeneous medium. The diffraction pattern at a plane z, $U(x, y, z)$, of an arbitrary signal at $z = 0$, $U_0(x, y) = U(x, y, 0)$, can be described by the Fresnel diffraction equation (94),

$$U(x, y, z) = A(x, y, z)\, \mathcal{F}\left\{ U_o(x, y)\, \mathrm{e}^{\left[\frac{j\pi}{\lambda z}\left(x^2 + y^2 \right) \right]} \right\}, \tag{4.1}$$

where x and y represent the directions of a plane transverse to the propagation, z is the propagation direction, $\mathcal{F}$ denotes the Fourier transform along the x and y coordinates, k is the wavenumber, λ is the wavelength, and

$$A\left(x, y, z\right) = \frac{\mathrm{e}^{-jkz}}{j\lambda z} \mathrm{e}^{\frac{j\pi}{\lambda z}\left(x^2+y^2\right)}. \tag{4.2}$$

Since the Talbot effect is only observed when the excitation wave $U_0\left(x, y\right)$ is a periodic signal, we can write it as a Fourier series:

$$U_0\left(x, y\right) = \sum_{l=-\infty}^{\infty} a_l \mathrm{e}^{\frac{j2\pi l x}{X}}, \tag{4.3}$$

$$a_l = \frac{1}{X} \int_{-X/2}^{X/2} U\left(x, y\right) \mathrm{e}^{-\frac{j2\pi l x}{X}} \, \mathrm{d}x, \tag{4.4}$$

where X is the period along the x axis, l is the harmonic index, and a_l is the l-th harmonic amplitude. By substituting (4.3) into (4.1),we obtain after straightforward manipulations:

$$U\left(x, y, z\right) = A\left(x, y, z\right) \sum_{l=-\infty}^{\infty} a_l \mathcal{F}\left\{\mathrm{e}^{\frac{j2\pi l x}{X}}\right\} * \mathcal{F}\left\{\mathrm{e}^{\left[\frac{j\pi}{\lambda z}\left(x^2+y^2\right)\right]}\right\}, \tag{4.5}$$

where the asterisk denotes the convolution operation. Thus, we have that

$$\mathcal{F}\left\{\mathrm{e}^{\frac{j2\pi l x}{X}}\right\} = \delta\left(k_x - \frac{2\pi l}{X}\right) \delta\left(k_y\right), \tag{4.6}$$

and

$$\mathcal{F}\left\{\mathrm{e}^{\left[\frac{j\pi}{\lambda z}\left(x^2+y^2\right)\right]}\right\} = j\lambda z \mathrm{e}^{-j\pi\lambda z\left(k_x^2+k_y^2\right)}, \tag{4.7}$$

where $k_x = x/\left(\lambda z\right)$ and $k_y = y/\left(\lambda z\right)$ are the 2π-normalized spatial frequencies along the x and y axis, respectively. After carrying out the convolution in (4.5),we obtain

$$\mathcal{F}\left\{\mathrm{e}^{\frac{j2\pi l x}{X}}\right\} * \mathcal{F}\left\{\mathrm{e}^{\left[\frac{j\pi}{\lambda z}\left(x^2+y^2\right)\right]}\right\} = j\lambda z \mathrm{e}^{-j\pi\lambda z\left[\left(k_x - \frac{2\pi l}{X}\right)^2 - k_y^2\right]}, \tag{4.8}$$

Finally, after substituting (4.8) into (4.5), we obtain the diffraction pattern of a periodic function at the plane z $\left(U\left(x, y, z\right)\right)$, i.e.,

$$U\left(x, y, z\right) = \mathrm{e}^{-jkz} \sum_{l=-\infty}^{\infty} a_l \mathrm{e}^{\frac{j2\pi l x}{X}} \mathrm{e}^{-\frac{j\pi\lambda z l^2}{X^2}}, \tag{4.9}$$

Note from (4.9) that there is a length where $\exp\left(-j\pi\lambda z l^2/X^2\right) = 1$, resulting in $U\left(x, y, z\right) = e^{-jkz_T^r}U_o\left(x, y\right)$, i.e., the output signal becomes a copy of the input signal. We define this length as:

$$z_T^u = u\frac{2X^2}{\lambda}, \tag{4.10}$$

where u is an integer number. Equation (4.9) indicates a periodic behavior, with the diffraction pattern repeating itself at every z_T^u, described in (4.10). Here we are interested in the first occurrence of the self-replication effect $z_T^1 \triangleq z_T$, also known as the Talbot length. Another interesting effect occurs at rational multiples of z_T, say at $z = z_T\left(p/2q\right) = \left(p/2q\right) \times \left(2X^2/\lambda\right)$, where p and q are coprime integers. At these distances, the l-th harmonic phase of $U\left[x, y, z_T\left(p/2q\right)\right]$ becomes $j\pi l^2 p/q$. According to Fourier series properties, when adding quadratic harmonic phases ($\sim l^2$) to $U_0\left(x, y\right)$, we obtain the same signal $U_0\left(x, y\right)$, but with period X/q and shifted along the x axis by $pX/2q$. Consequently, at these distances, the signal repetition rate is multiplied by q. Furthermore, conservation of energy requires that the pulse intensity scales inversely to the increase of the repetition rate.

Analogously to the spatial Talbot effect, the TTE (155) appears when a periodic signal propagates through a first-order dispersive medium ($\beta_b\left(\omega_o\right) \triangleq \left[d^b\beta\left(\omega\right)/d\omega^b\right]_{\omega=\omega_o} \neq 0$ when $b = 2$, where $\beta\left(\omega\right)$ is the propagation constant and ω is the angular frequency). Assuming a periodic pulse train with period T at $z = 0$ defined by its Fourier series ($U_o\left(t\right) = U\left(t, z = 0\right)$), the propagated pulse $U\left(t, z\right)$ becomes

$$U\left(t, z\right) = \sum_{l=-\infty}^{\infty} a_l e^{\frac{j2\pi l t}{T}} e^{-j\beta(\omega)z}, \tag{4.11}$$

where

$$a_l = \frac{1}{T}\int_{-T/2}^{T/2} U_o\left(t\right) e^{-\frac{j2\pi l t}{T}}\ dt, \tag{4.12}$$

Writing $\beta\left(\omega\right)$ as a Taylor series of ω

$$\beta\left(\omega\right) = \beta_o + \beta_1\left(\omega\right) + \frac{\beta_2}{2}\left(\omega\right)^2 + \dots, \tag{4.13}$$

and substituting this expression back into (4.11), we obtain

$$U\left(t, z\right) = \sum_{l=-\infty}^{\infty} a_l e^{\frac{j2\pi l t}{T}} e^{-j\left(\beta_o + \beta_1(\omega l) + \frac{\beta_2}{2}(\omega l)^2 + \dots\right)z}, \tag{4.14}$$

where $\omega_l = 2\pi l/T$ is the angular frequency of the l-th harmonic. The first factor $\exp\left(j\beta_o z\right)$ has constant magnitude and does not change the envelope of $U\left(t, z\right)$; thus, it can be discarded. Next, we assume an ideal first-order dispersive medium (where $\beta_b = 0$ for $b > 2$)

only to study the main aspects of pulse addition using the TTE. Consequently, we obtain the following simplified equation:

$$U(t,z) = \sum_{l=-\infty}^{\infty} a_l e^{\frac{j2\pi l(t-\beta_1 z)}{T}} e^{-j\left(\frac{2\pi^2 l^2 \beta_2}{T^2}\right)z}.$$ (4.15)

Comparing the quadratic phase terms in (4.1) and (4.15), we note that the temporal and spatial Talbot effects are related according to the following equivalence: $x \leftrightarrow t - \beta_1 z$ and $\lambda z \leftrightarrow -2\pi\beta_2 z$. Thus, the TTE appears whenever a pulse train with period T propagates through a dispersive medium, exhibiting the following temporal Talbot length:

$$z_{TT} = \frac{T^2}{\pi |\beta_2|}.$$ (4.16)

It is worth mentioning that the pattern observed for rational multiples of z_T also applies to z_{TT}. Analogously to the spatial domain, the pulse train periodicity is multiplied by q and shifted in time by $pT/2q$. Note also that the pulse intensity scales inversely to q so as to conserve the total energy. The higher-order dispersion terms distort the pulse format (262, 263) and, therefore, should be accounted for in the simulations. For this reason, we utilize (4.11) in all pulse propagation analysis. But for the sake of clarity and to help us visualize the pulse multiplication at $z = z_{TT}(p/2q)$, we recast the simplified (4.15) as follows:

$$U(t,z) = [U(t-\beta_1 z)] * \sum_{l=-\infty}^{\infty} a_l e^{-j\pi\frac{z}{z_{TT}}l^2} e^{-\frac{j2\pi lt}{T}}.$$ (4.17)

When $z = z_{TT}(p/2q)$ (only in this scenario) (264), we obtain

$$\sum_{l=-\infty}^{\infty} a_l e^{-j\pi\frac{z}{z_{TT}}l^2} e^{-\frac{j2\pi lt}{T}} = \delta\left(t - e_{pq}\frac{T}{2}\right) * \left[\frac{1}{\sqrt{q}}\sum_{b=0}^{q-1} e^{j\gamma_b}\delta\left(t - b\frac{T}{q}\right)\right],$$ (4.18)

where $e_\nu = 1$ or 0 whenever ν is even or odd, respectively, an

$$e^{j\gamma_b} = \frac{1}{\sqrt{q}}e^{j\pi\frac{\psi}{q}b^2}\sum_{v=0}^{q-1} e^{-j\pi\frac{s}{q}(v-b)^2},$$ (4.19)

where ψ is an integer defined in terms of p and q (see Table 1 of (264)). Substituting (4.18) into (4.17), we obtain

$$U\left(t, z = \frac{p}{2q}z_{TT}\right) = \left[U_o\left(t - \beta_1\frac{p}{q}z_{TT} - e_{pq}\frac{T}{2}\right)\right] * \left[\frac{1}{\sqrt{q}}\sum_{b=0}^{q-1} e^{j\gamma_b}\delta\left(t - b\frac{T}{q}\right)\right].$$ (4.20)

In (4.20), the second term of the convolution denotes a pulse train with period T/q and constant phase $\gamma_b = \gamma_o + e_q\pi + (\psi/q)\,\pi b^2$ over the period T/q, where n is an integer. In summary, at $z = z_{TT}\,(p/2q)$, $U\,(t,z)$ consists of q repetitions of U_o scaled by $1/\sqrt{q}$ (for power conservation), with the m-th repetition having a constant phase of γ_b.

4.2.1 TTE for passive amplification

We explore the TTE here to achieve passive amplification via three methods: (1) CPA (156), (2) forward propagation CW-topulse conversion, or FTAI (157), and (3) backward propagation CW-to-pulse conversion, or BTAI. All three methods are discussed separately in the next subsections.

4.2.1.1   Coherent pulse addition

Equation (4.20) shows that, at rational fractions of z_{TT}, the signal $U\,(t, z = (p/2q)\,z_{TT})$ has the same behavior as $U_o\,(t)$, but with a repetition rate q times higher and intensity q times lower, while at integer multiples of z_{TT}, $U\,(t, z = z_{TT}^u) = U_o\,(t)$. Note that a phase $\mathrm{e}^{j\gamma_b}$, constant within each $T' = T/q$ interval, is added to the signal. To achieve passive amplification, we need to transform a low intensity and high-repetition-rate signal into another one with high intensity and low-repetition rate. To realize this objective, the output signal after a propagation distance of L, $V\,(t, L)$, must be equal to $U\,(t, z_{TT})$. Thus, the required input signal $V\,(t, 0)$ depends on q and is equal to $U\,(t, z_{TT}\,(p/2q))$. Moreover, by choosing $p = 2q - 1$ {from (4.19), $\psi = p$ (264)}, the propagated distance is smallest and equal to $z_{TT}/2q$, resulting in reduced losses. Each pulse of the input signal $V\,(t, 0)$ has a time slot T' preconditioned by a phase modulator with phase γ_b defined according to (4.20). The procedure illustrated in Fig. 17(a) consists in calculating the phase term γ_b for the desired q value with $p = 2q - 1$. The phase value for the b-th pulse ($b = 0 \ldots q - 1$) and required propagation length are as follows:

$$\gamma_b = \gamma_o + e_q\pi + \pi\tfrac{q-1}{q}b^2, \quad \text{for } (b-1)\,T' < t < bT' \tag{4.21}$$

$$L = \frac{z_{TT}}{2q} = \frac{T^2}{2\pi q\,|\beta_2|}, \tag{4.22}$$

4.2.1.2   Forward Talbot array illuminators

The second method uses a phase-modulated CW signal as input. It can be understood as a sequence of square pulses with 100% duty cycle. This signal is then modulated by a phase grating and propagated over a fractional Talbot length $(p/2q)\,z_{TT}$. The process of designing the phase grating and calculating the propagation length is discussed in detail in (157, 264, 266–268). The period of the phase grating is also T, with each bin having
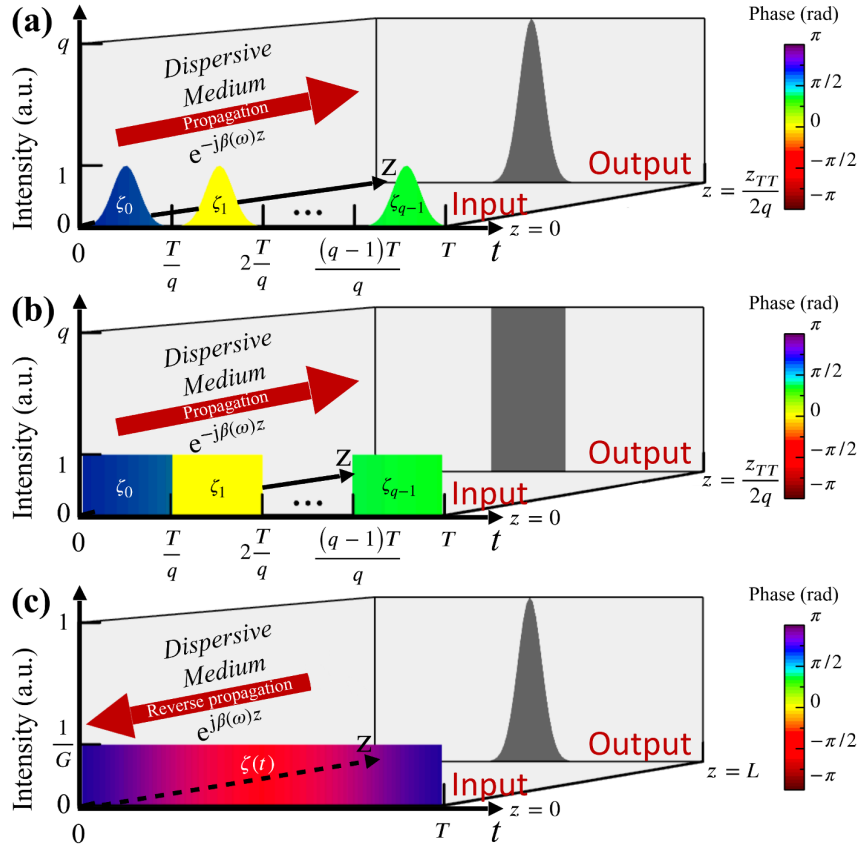
Figure 17 – (a) Illustration of the TTE coherent pulse addition method. A phase-modulated pulse train (each pulse phase has a different color) propagates for a fractional Talbot distance $Z_{TT}/2q$. The output is a single pulse for every T, and its intensity is amplified q times. (b) Illustration of the FTAI method (forward propagation and CW-to- pulse conversion). In this case, a phase-modulated CW signal propagates for a fractional Talbot distance $z_{TT}/2q$. The output is a single rectangular pulse for every T, and its intensity is amplified q times when compared to the CW input signal. (c) Illustration of the BTAI method (backward propagation and CW-to-pulse conversion). A target pulse shape is defined at the output and propagated backwards to obtain a quasi-CW signal whose phase profile is used to modulate a CW signal. This signal is then propagated for a distance L to form the desired output pulse. The gain G depends on the peak-to-averaged power ratio of the target pulse. Adapted with permission from (265)© Optica Publishing Group.

a time slot T'. The signal at the output is a periodic train of identical chirp-free square pulses, each with duration T' repeating at an interval T. This process results in a peak power gain (when compared to the CW signal intensity) of the order of q (if q is too high, part of the signal may be outside the "on" pulse region, which may reduce the gain). This is not a fundamental upper limit to q, but it is rather caused by non-idealities in the spectral phase, which become more significant as q increases and, consequently, the signal bandwidth increases. Furthermore, since the phase modulation speeds are limited, larger errors are induced in the phase grating as q increases (more phase transitions happen in

the same time slot).

Note that this method, depicted in Fig. 17(b), is similar to the CPA and differs only in the input signal, which is a phase-modulated CW signal. The constant phase of the b-th ($b = 0 \ldots q - 1$) CW-bin at the time t calculated inside the signal slot (period T) is defined by (4.21), while the required propagation length is calculated with (4.22). Note that L is proportional to the square of T in both the CPA and FTAI cases but inversely proportional to q, suggesting that the necessary propagation length decreases for increasing gain factor and increases for a given period T.

4.2.1.3 Backpropagated CW-to-pulse conversion

The FTAI approach relaxes the bandwidth requirement for the dispersive medium because it only uses phase modulation. However, as q increases, it becomes difficult to control the output pulse shape (157) due to the fast-switching discrete phase profile and (especially in the THz case) the higher-order dispersion coefficients. Here, we propose a new CW-to-pulse design method to circumvent this problem, denoted as backward propagation TAI (BTAI). It consists in first defining the desired output waveform, such as a Gaussian pulse train, and then backward propagating this signal [see Fig. 17(c)] until we find the length at which the waveform more closely resembles a CW. The resulting signal will have the required phase profile to be used as signal preconditioning in this method. Then, we propagate this signal forward and evaluate its performance parameters (gain, propagation length, and noise). We optimize this process further by changing the modulation depth of the target signal to compensate for any undesirable overmodulation effects in the output (see more details in Appendix C.3). This process is illustrated in Fig. 18. As will become clear in Section 5.4, this method obtains the best overall performance in terms of gain and propagation distance.

The maximum theoretical gain G depends on the desired pulse shape. In a lossless system, the energy, and subsequently the average value of the signal, is preserved. Let R' be the form factor (peak-to-average power ratio) of the modulated target signal. Since the form factor of a CW signal is 2 (note that we are calculating R' based on a modulated signal, not on the envelope), then

$$G = \frac{P_{\text{Peakout}}}{P_{\text{Peakin}}} = \begin{cases} q & \text{, for CPA and BTAI} \\ \frac{R'}{2} & \text{, for BTAI} \end{cases}. \tag{4.23}$$

Note that, while both q and R' are used to describe the gain in (4.23), q comes from the fractional Talbot distance and the number of discretization levels in the phase grating, and R' comes from the target pulse format. They are, therefore, fundamentally different parameters.

As mentioned before, a realistic dispersive medium, especially in the THz range, has higher-order dispersion coefficients that perturb the expected propagation pattern, including distortion of the pulse shape at fractional Talbot lengths and imperfect pulse addition, leaving spurious signals outside the pulse region. This reduces the realized gain.Moreover, the phase modulation profile is crucial for both CPA and FTAI realizations. However, the limited time response of phase modulators leads to imperfections in the phase transition that increase spurious signals and limit the gain, as noted in (156,157). These imperfections are modeled here as noise and quantified with the signal-to-noise ratio (SNR) figure-of-merit. The SNR allows us to evaluate the energy transfer efficiency from the input signal into the output pulse, such that

$$SNR = \frac{[V(t,L)]_{\text{RMS}}}{[V(t,L) - V_{\text{ideal}}(t,L)]_{\text{RMS}}}, \qquad (4.24)$$

where $V_{\text{ideal}}(t,L)$ is the output pulse train in an ideal system (perfect phase profile and $\beta_b = 0$ for $b > 2$) with the difference between the real and ideal outputs $V(t,L) - V_{\text{ideal}}(t,L)$ defined as the system noise. The BTAI method also stands out from the two previous methods because it does not have an explicit q parameter, although the input is a periodic signal.

Note that the first steps in BTAI (from target output until phase demodulation; see Fig. 18) can only be carried out numerically, not only because the target signal is not readily available but also because a dispersive medium with complementary dispersive profile is
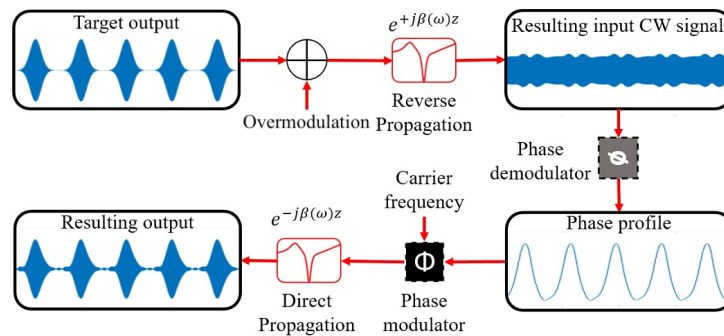
Figure 18 – Schematic representation of the backward propagation method (BTAI) for the TTE. The backward propagation is only a mathematical tool to calculate the optimum phase profile to be imposed onto a CW signal at the fiber input. First, a target output pulse train is defined and added to a controllable intensity CW signal. The resulting signal is backward propagated through the Bragg fiber until we obtain a signal with the least amplitude modulation, i.e., a quasi-CW wave (ideally it would be a CW signal). We then phase demodulate this signal to obtain its phase profile. This calculated phase profile can now be imposed onto a phase grating to phase modulate a CW signal at $z = 0$. This process guarantees peak gain at the fiber output. Adapted with permission from (265)© Optica Publishing Group.

required. However, in the absence of a proper numerical model of the dispersive medium, a vector network analyzer with THz frequency extenders can be used to experimentally extract $\beta(\omega)$.

The next section deals with the design of the Bragg fiber and includes the effects of non-idealities, such as higher-order dispersion coefficients.

4.3 Designing the dispersive medium

Bragg fibers, originally proposed by Yeh *et al.* (143) in 1978 for optical frequencies, usually consist of a core with a lower refractive index than that of the cladding medium. These fibers exhibit many attractive properties such as omnidirectional reflection, reduced confinement loss, large transmission window, and high dispersion coefficients (144, 256). In fact, dispersion coefficients in excess of 500,000 ps/nmkm have been reported for these fibers (144). Moreover, we can tailor the magnitude of this coefficient by introducing one or more defect layers (usually thicker layers) in the multilayer cladding. Such arrangement causes the core mode to interact more strongly with the defects at certain wavelengths, quickly changing the mode profile and consequently its effective index. More importantly, these fibers can also use a hollow (air) core to reduce propagation losses, which is particularly attractive for THz applications.

With that in mind, we propose a THz Bragg fiber made of silicon semiconductor with a multilayer metamaterial cladding (primary Bragg reflector), as shown in red in Fig. 19. The refractive index of each individual clad layer is controlled by simply adjusting the area fill factor of the square airholes (more details on this are provided in Appendix C.1). Defect layers (shown in green) are also added to the primary reflector to control the mode dispersion. Then, we calculate its homogenized index value with a standard parameter extraction method (176). To reduce leakage loss, we include a second metamaterial cladding layer (secondary Bragg reflector), shown in blue in Fig. 19.

We begin the Bragg fiber design with a TMT intended to maximize the transverse reflection coefficient of the multilayer stack (including the secondary Bragg reflector) at the desired wavelength region assuming normal incidence (258). We dub this technique TMT-S. Then, we use a second TMT (dubbed TMT-W) to calculate the waveguide modes of the entire planar multilayer stack (259). Both TMT-S and TMT-W are analytical and scalar methods. The large aspect ratio of the Bragg fiber core in Fig. 19 favors the use of these planar techniques, making them an excellent tool for optimizing the fiber physical and geometrical parameters. After concluding the optimization step, we fine-tune the structure parameters with FEM simulations based on the Comsol Multiphysics package. To guarantee grazing incidence, the thickness of the cladding layers has to obey the following

relation (144):

$$\frac{t_\text{high}}{t_\text{low}} = \sqrt{\frac{n_\text{low} - 1}{n_\text{high} - 1}}, \qquad (4.25)$$

where t_high and t_low are the thicknesses of the layers with high (n_high) and low (n_low) refractive indices, respectively. Assuming transverse electric (TE) polarization, the TMT-S first determines the number of layers that maximize the reflection coefficient at normal incidence. At this stage, the analysis resembles the reflection coefficient calculation of a planar double Bragg reflector grating. The thicknesses of the defect layers do not significantly impact the magnitude of the reflection coefficient, but strongly affect the mode confinement. Moreover, the defect layers should only appear in the primary reflector. To highlight the influence of the additional reflectors on the mode confinement, we show in Fig. 20 the electric field profile of the fundamental mode at 362.1 μm without [Fig. 20(a)] and with [Fig. 20(b)] this reflector included. The secondary reflector has M_{out} layers, with refractive index and thickness of the high and low index layers of $\left(n_\text{high}^m, t_\text{high}^m\right)$ and $(n_\text{low}^m, t_\text{low}^m)$, respectively. Note that we choose $n_\text{high}^m = n_\text{high}$. The index profile of the complete fiber is depicted in Fig. 20(c). After this process is complete, we are left with a structure whose parameters (index profile, number of layers in both primary (M_{in}) and secondary (M_{out}) reflectors, and core thickness) are listed in Table 2 for the wavelength range of $360 - 370$ μm. The overall reflection coefficient for these parameters is $\sim 99.5\%$.

Next, we proceed to the planar waveguide mode analysis with the TMT-W. Al-
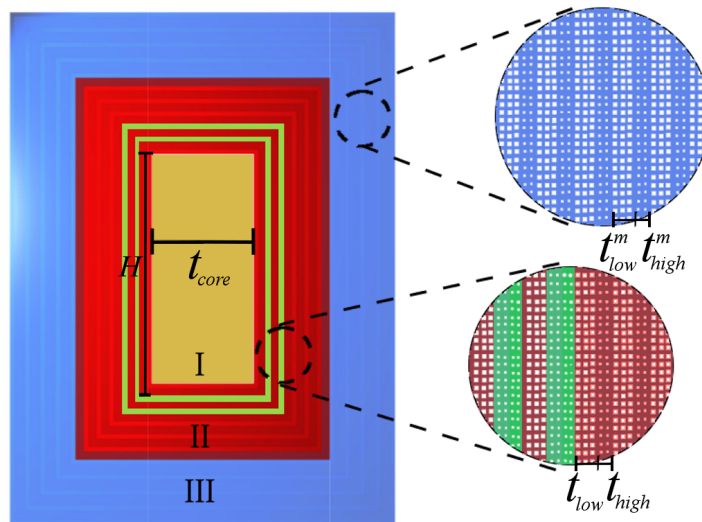
Figure 19 – Different sections of the proposed Bragg fiber. Region I (in yellow) represents the air core. Region II (in red) is the primary cladding. Region III (in blue) is the secondary cladding used to prevent leakage losses. Defects in the primary cladding are shown in green. Regions II and III are zoomed-in on the right side to show the air hole pattern inside the cladding. Adapted with permission from (265)© Optica Publishing Group.
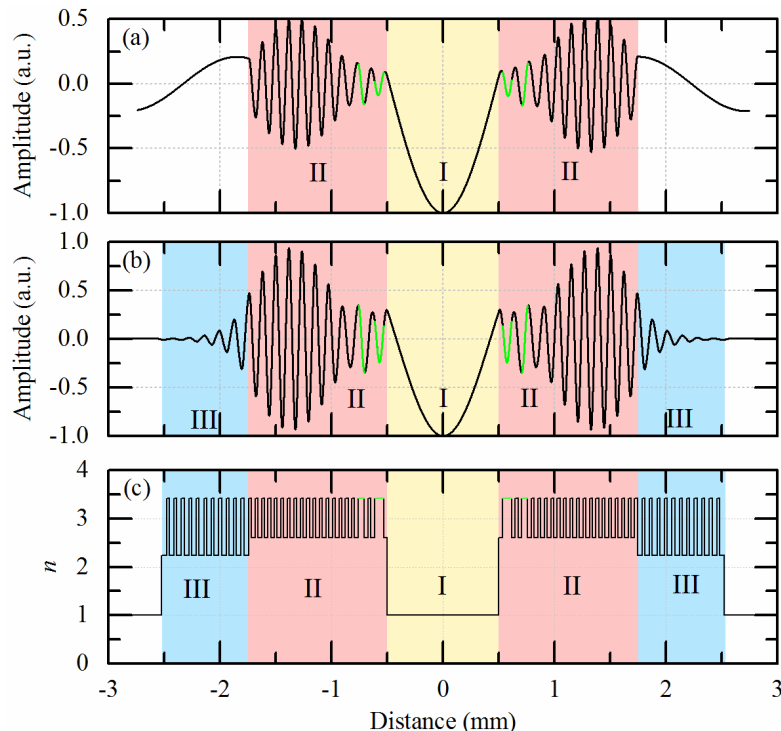
Figure 20 – Different sections of the proposed Bragg fiber. Region I (in yellow) represents the air core. Region II (in red) is the primary cladding. Region III (in blue) is the secondary cladding used to prevent leakage losses. Defects in the primary cladding are shown in green. Regions II and III are zoomed-in on the right side to show the air hole pattern inside the cladding. Adapted with permission from (265)© Optica Publishing Group.

Table 2 – Bragg fiber design parameters

t_{core} (mm)	t_{high} (μm)	t_{low} (μm)	t_{high}^m (μm)	t_{low}^m (μm)	n_{high}	n_{low}	n_{low}^m	M_{in}	M_{out}
1.02	24.6	33.3	25.4	41.6	3.42	2.61	2.24	40	23

though we have defined the waveguide core thickness t_{core} in the previous step, it is worth emphasizing that the larger the waveguide core is, the higher the dispersion coefficients (and the lower the propagation losses due to the reduced mode interaction with the cladding material). Therefore, we choose a core size H large enough so that the planar mode analysis with the TMT-W holds. At this stage, we can fine-tune the defect layers thicknesses to obtain the largest possible dispersion coefficient for the fundamental mode. The defect layers are located in the primary cladding at the second and sixth layers from the core (see Fig. 19), with optimized thicknesses of $3.3 \times t_{\text{high}}$ and $2.2 \times t_{\text{high}}$, respectively.

Finally, we validate the TMT simulations with FEM results assuming an infinitely long waveguide with rectangular cross section. With t_{core} already defined, we now choose H to match as closely as possible the TMT-W results. Figures 21(a)–(c) show the effective index ($n_{eff} = \beta/k_o$, where β is the mode longitudinal propagation constant and k_o is

the vacuum wavenumber), dispersion coefficient ($2\pi\beta_2$), and attenuation constant for the fundamental mode calculated with both the TMT-W (black solid lines) and FEM (solid lines with symbols) results for $H = 3000\ \mu$m, $5000\ \mu$m, and $7000\ \mu$m. Note that the TMT-W results are redshifted by only $1.87\ \mu$m from FEM results, with both showing essentially the same dispersion magnitude. As expected, the losses increase as the core height decreases due to increased field interaction with the upper and lower claddings, but remain at acceptable levels. The dispersion curves obtained with the FEM results are discussed in Appendix C.2.
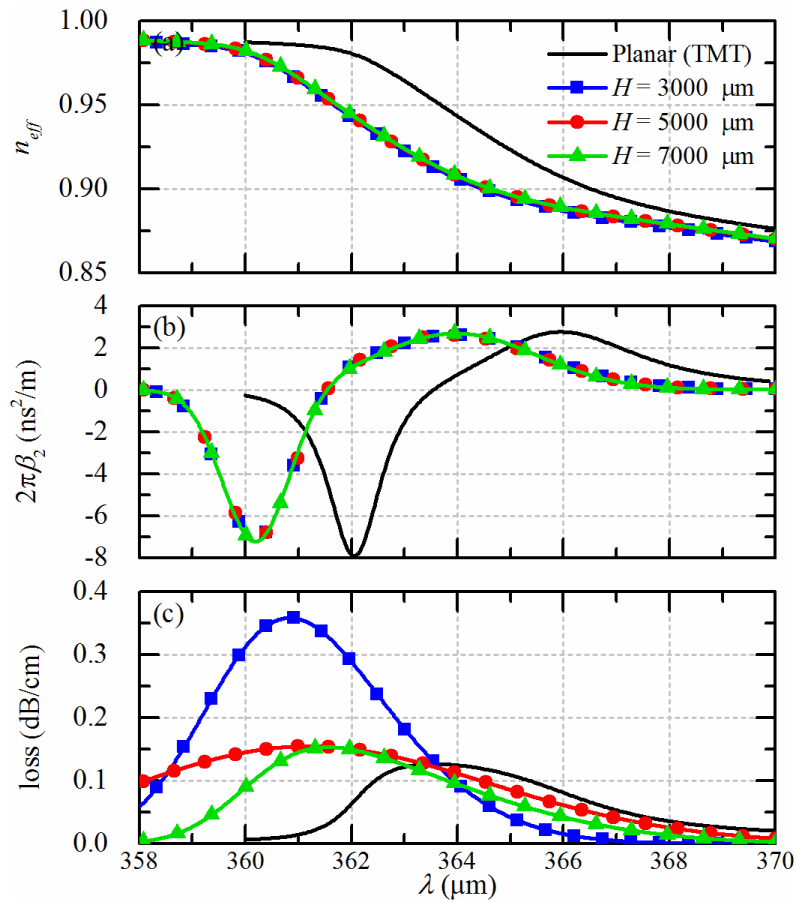
Figure 21 – Analytical and simulation results of the proposed fiber. (a) Effective index, (b) dispersion coefficient, and (c) propagation losses. Black lines refer to scalar 2D simulations via TMT-W, while blue, red, and green lines refer to FEM simulations for $H = 3000\ \mu$m, $5000\ \mu$m, and $7000\ \mu$m, respectively. As the height increases, the structure behaves closely to a planar waveguide, and FEM results approach those from TMT-W (a redshift of only $1.87\ \mu$m is observed). The maximum value of the dispersion coefficient is -7.9 ns^2/m for the TMT-W and -7.2 ns^2/m for the FEM simulations. Symbols are used as a guide to the eye. The actual data processing is detailed in Appendix C.2. Adapted with permission from (265)© Optica Publishing Group.

4.4 Results

The results in Fig. 21(b) show that a high dispersion coefficient occurs only at a narrow wavelength range, which limits the input signal bandwidth. This limitation defines a lower bound for the pulse period T. Observe that (4.22) indicates that the propagation length scales with T^2. However, the values predicted from these equations may be impacted by higher-order dispersion terms. Consequently, we need to test different values of T to find the conditions for optimal performance for all three methods.

Next, we apply these definitions to the three methods considered here.

4.4.1 Coherent pulse addition

As should be expected, the limited bandwidth of the dispersive medium causes different pulse shapes to produce different values of G, L, and SNR. We assess the performance of the proposed structure by using four different pulse trains as excitation with the following super-Gaussian profile $y_{SGauss}(t)$:

$$y_{SGauss}(t) = \frac{e^{-\left[\frac{1+jC}{2}\left(\frac{t}{T_o}\right)^{2m}\right]} + Ov}{1 + Ov}, \tag{4.26}$$

$$T_o = \frac{T_{FWHM}}{2\ln\left(2^{\frac{1}{2m}}\right)}, \tag{4.27}$$
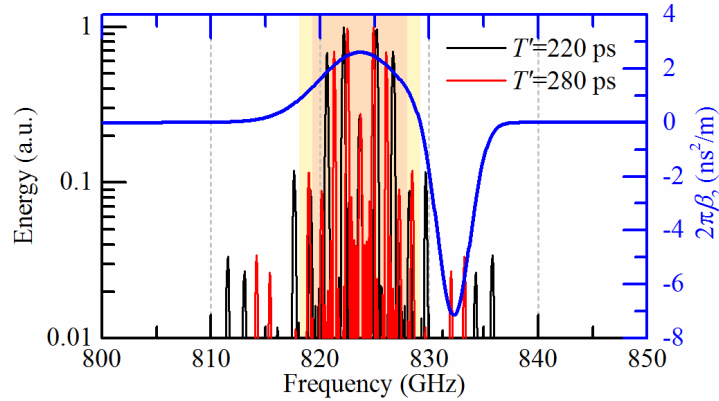
Figure 22 – Frequency spectra of a fourth-order ($m = 4$) super-Gaussian pulse train with $T_{FWHM} = 0.5T'$ for $T' = 220$ ps (black lines) and 280 ps (red lines). Blue lines refer to the dispersion coefficient for a fiber height $H = 7000$ μm. Lower values of T' cause the frequency spectrum to spread, with fewer components affected by the high dispersion region, resulting in decreased performance. Light yellow and red areas limit the region that contains 90% of the signal energy for the 220 ps and 280 ps pulse trains, respectively. Adapted with permission from (265)© Optica Publishing Group.

where m is the super-Gaussian order, C is the chirp factor, Ov is an overmodulation parameter, and T_{FWHM} is the half-width pulse power time. The large bandwidth of the pulse train places the central frequency at the positive dispersion peak, which has low dispersion values (2.7 ns^2/m at 363.9 μm) but wide bandwidth. Figure 22 shows the spectra of a fourth-order super-Gaussian pulse train ($T_{FWHM} = 0.5T'$) superimposed to the dispersion coefficient (blue lines) for $T' = 220$ ps (black solid line) and $T' = 280$ ps . red solid line). The light yellow and light red rectangles delimit the 90% energy region in the 220 ps and 280 ps pulses, respectively. From Fig. 22, we see how the pulse bandwidth influences the TTE performance. A narrow spectrum means energy confinement over a region with low dispersion coefficient variation, leading to results close to the ideal TTE; see (4.15). In contrast, a broader spectrum, such as that for $T' = 220$ ps, results in a less effective pulse addition and, thus, smaller gain. A spectrum narrower than that in Fig. 22 would produce G and L values closer to those predicted by (4.22).

Figure 23 shows the time-varying amplitude distribution for $H = 7000$ μm, $q = 3$, $m = 4$, and $T' = 240$ ps. The red line indicates a fractional Talbot length ($z_{TT}/6$) of 7.92 cm, where the maximum gain (3.91 dB) occurs. By propagating another $z_{TT}/2$, the signal should repeat itself (see Section 5.2), except for propagation losses and group delay effects. Observe that, for our realistic medium (with higher dispersive orders and limited bandwidth), pulse repetitions occur at slightly longer distances. Also, they occur at distances close to $z_{TT}/6$ and $z_{TT}/6 + z_{TT}/4$, compatible with the fractional distance for the $q = 2$ pattern. As mentioned in (262), there are different Talbot distances for each dispersive order, which causes input pulses to be added in multiple regions, therefore hiding the pattern associated to $q = 2$. Furthermore, pulse repetitions are observed at slightly longer distances than expected $z = (p/2q)\,z_{TT}$. This is because part of the pulse energy concentrates in the lower dispersive regions of the spectrum (see Fig. 22). This behavior illustrates the difference between the ideal TTE from (4.15) and the realized TTE.

To have a clearer view of the performance of our fiber when using the TTE, we sweep T' from 220 ps to 280 ps for $m = 1$, 2, 3, and 4 and compare the results with those from the TMT-W (planar) and full-wave simulations for three different values of H (see Fig. 24), with a fixed $q = 3$. Note that, due to the frequency shift between planar and full-wave simulations (see Fig. 21), we use slightly different carrier frequencies for the two cases (819.0 GHz for the TMT-W and 823.7 GHz for FEM). In Fig. 24, we define the pulses full width at half-maximum (T_{FWHM}) as $0.5T'$ for $m = 1$ (black lines), 2 (blue lines), 3 (red lines), and 4 (green lines). The first row [Figs. 24(a)–(d)] shows the required propagation length L to achieve passive amplification via CPA. The second row [Figs. 24(e)–(h)] shows the peak gain G, while the third row [Figs. 24(i)–(l)] shows the SNR. Column 1 refers to the results from the TMT-W (planar), and columns 2 to 4 refer to FEM simulations with $H = 3000$ μm, 5000 μm, and 7000 μm, respectively. Again the wide
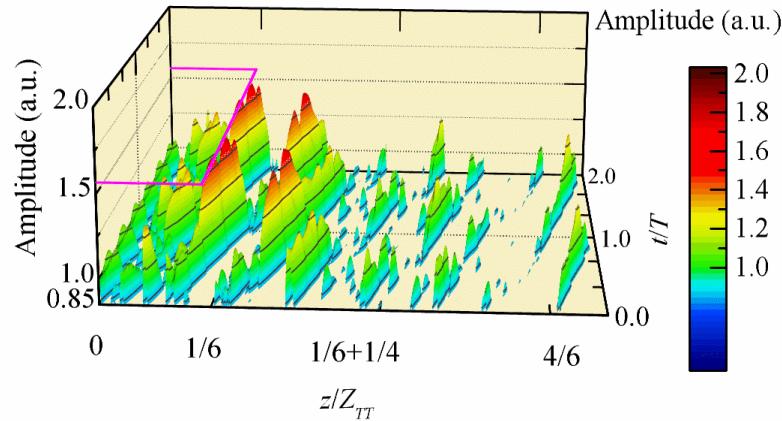
Figure 23 – Amplitude surface plot of the propagation through the Bragg fiber with $H = 7000\ \mu$m for $q = 3$, $m = 4$, and $T' = 240$ ps. The axes are normalized by the first fractional Talbot length and by the pulse period T. Maximum amplitude gain of 3.91 dB occurs at the realized fractional Talbot length of 7.92 cm, shown by a magenta guideline. Different pulse periodicities and repetitions caused by higher-order dispersion coefficients appear at points corresponding to other rational multiples of the Talbot length. Results are truncated to values above 0.85 to highlight the gain regions. Adapted with permission from (265)© Optica Publishing Group.

bandwidth of the pulse train places the central frequency at the positive dispersion peak, which has low dispersion values (2.6 ns^2/m at 823.5 GHz) but a larger bandwidth.

The required propagation length is similar for all values of m (i.e., on the order of centimeters). The highest gain ($G = 5.2$ dB) occurs for $m = 4$, while pure Gaussian pulses ($m = 1$) have the best overall SNR (>12 dB) with a 5 dB gain. Note that G and L have a similar pattern for different values of H, which helps relax their fabrication tolerance. Due to its narrower spectrum, $m = 1$ sequences require shorter propagation lengths and obtain higher gain than those with $m = 2$ and 3. However, $m = 4$ sequences present an even higher G. Note that, as T' increases, both G and SNR increase, indicating that a narrower spectrum that fits inside the highly dispersive region is the correct choice. L should have a quadratic behavior with T', but, instead, it is close to linear due to the changing spectrum. According to (4.22), the dispersion value (or propagation length) depends on the square of the output pulse period. However, that equation does take into account bandwidth limitations in the dispersive region. As the pulse period increases, the bandwidth decreases in such a way that the pulse spectrum becomes increasingly localized in the highly dispersive region, therefore increasing the effective dispersion coefficient.

Note the similarity between the results of each column of Fig. 24. This behavior is another indication that the TMT-W is indeed a good tool for designing this Bragg fiber. To have the most realistic results, however, we only use the FEM curves from $H = 7000\ \mu$m from this point on.
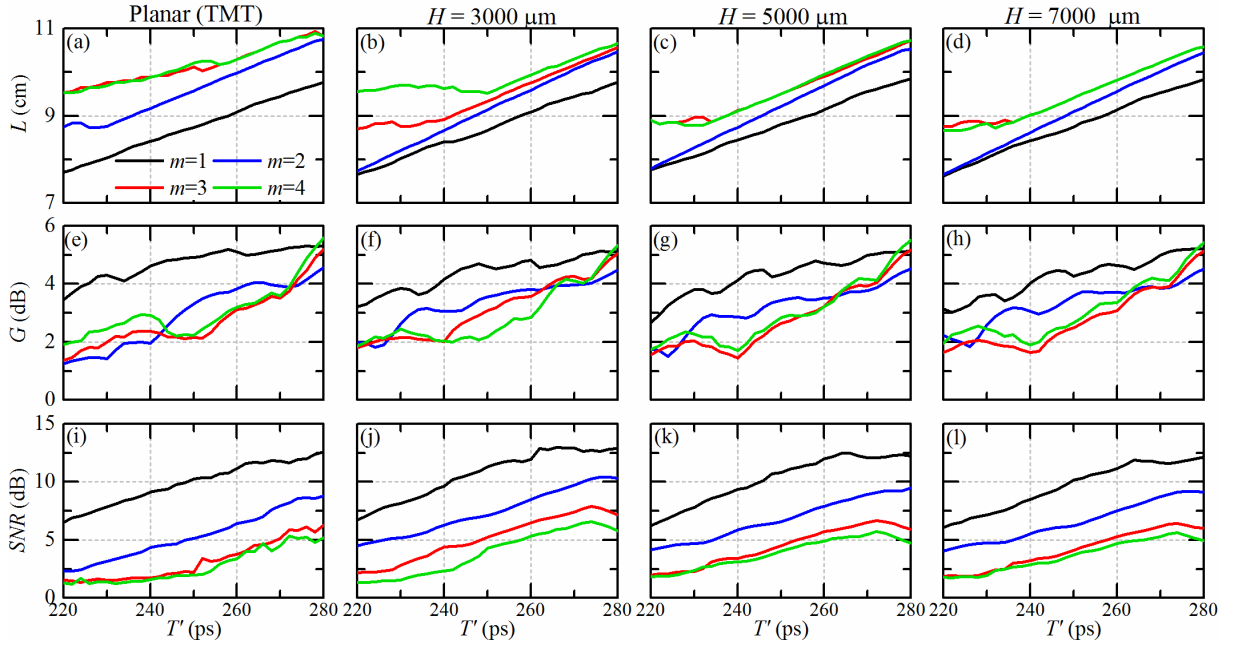
Figure 24 – Comparison for the coherent pulse addition method for different structures and pulse shapes. Black lines refer to Gaussian pulses with a full width at half-maximum time T_{FWHM} equal to $0.5T'$. Blue, red, and green lines refer to second-, third-, and fourth-order super-Gaussian pulses with $T_{FWHM} = 0.5T'$. The first row (a)–(d) presents the required propagation length L to achieve passive amplification via CPA. The second row (e)–(h) shows the peak gain G, and the third row (i)–(l) the SNR. Column 1 refers to TMT-W, and columns 2–4 refer to finite element results for heights $H = 3000\ \mu$m, $5000\ \mu$m, and $7000\ \mu$m, respectively. Adapted with permission from (265)© Optica Publishing Group.

The most appealing result is indeed the maximum achievable gain. However, it is noteworthy that the maximum expected gain given by (4.23) for a lossless dispersive medium operating as a Talbot amplifier with $q = 3$ is $G = 10\log_{10} 3 = 4.77$ dB, while $G = 5.2$ dB for $q = 3$, $m = 4$, and $T' = 280$ ps (time waveforms for this result are shown in Appendix C.3). Given the propagation length and the losses involved, this value should not be realizable. Nevertheless, our results suggest that the pulse is also compressed during the propagation due to higher-order dispersion coefficients, allowing for a peak value higher than expected for the addition of uncompressed pulses.

Next, we investigate the fiber performance for chirped pulses, assuming the chirp parameter C ranging from -1 to $+1$. Chirping allows pulse compression when propagating through dispersive media, leading to higher gain. Figure 25 shows the simulated results with the line colors associated with the C values as follows: -1 (red), -0.5 (purple), 0 (black), 0.5 (green), and 1 (blue). The first [Figs. 25(a)–(d)], second [Figs. 25(e)–(h)], and third [Figs. 25(i)–(l)] rows indicate the fiber length L, gain G, and SNR, respectively. Columns 1 to 4 refer to $m = 1, 2, 3$, and 4, respectively. Note that chirped pulses show a

higher gain compared to unchirped ones due to pulse compression. The gain is as high as 5.8 dB at $T' = 280$ ps for $C = -1$ and $m = 1$. Only negative C values favorably impact G due to the chirp influence on both the phase of each frequency component and their location in the dispersion curve. The SNR degrades as m increases, indicating that the output pulse shape gets distorted due to the broader frequency spectrum.
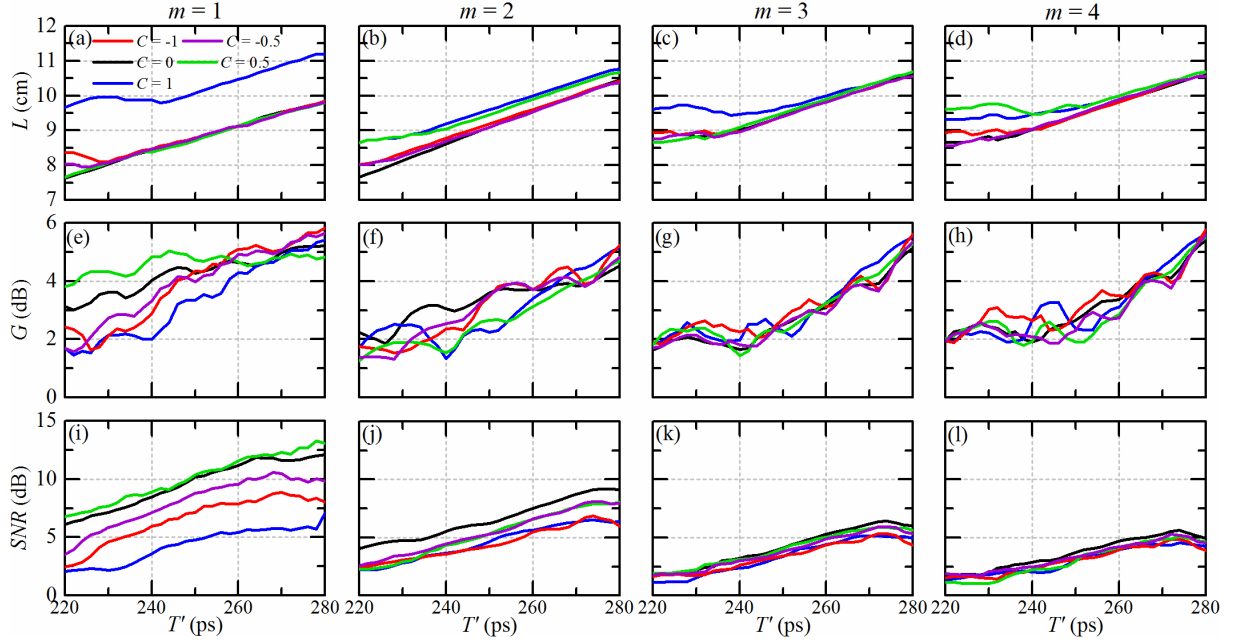
Figure 25 – Performance comparison for the coherent pulse addition method using chirped super-Gaussian pulses. Red, purple, black, green, and red lines refer to $C = -1, -0.5, 0, 0.5$ and 1, respectively. The first row (a)–(d) presents the required propagation length L to achieve passive amplification via CPA. The second row (e)–(h) shows the peak gain G and, the third row (i)–(l) the SNR. Columns 1–4 refer to $m = 1, 2, 3$, and 4, respectively. All pulses have $T_{FWHM} = 0.5T'$. Adapted with permission from (265)© Optica Publishing Group.

Since we calculate the SNR based on the input pulse shape, both chirped and high-order unchirped pulses (which experience more pulse compression) show reduced SNR. However, this does not necessarily mean that there is more energy outside the pulse slot. We observe that G is higher when T' is higher, as expected when more frequency components are inside the high dispersion region (see Fig. 22). However, as T' increases, so does L, but the average power decreases because the energy gets more dispersed over time.

4.4.2 Forward Talbot array illuminator

As discussed in Section 5.2, the FTAI method explored here uses phase grating (157) to define the ideal phase modulation at the input CW signal for highest gain at the shortest possible distance. The procedure is straightforward, and we analyze and compare the device performance for $q = 2, 3, 5$, and 7.

Note that the FTAI method uses only phase modulation, which requires a narrower bandwidth when compared to the CPA (which uses both amplitude and phase modulation). Thus, the period T used in each method differs, but the occupied bandwidth is similar for both. Furthermore, the bandwidth relaxation allows us to use the higher negative dispersion peak at 360.2 μm [see Fig. (21)(b)], resulting in shorter propagation lengths. In the CPA, the broader peak at 363.9 μm is used instead. Simulations (not shown here) of the CPA passive amplification at 360.2 μm resulted in a peak gain of 3.6 dB with $SNR = 3$ dB, or peak SNR of 6 dB for a gain of only 2.5 dB. Figures 26(a)–(c) show the propagation length L, gain G, and SNR, respectively, as function of the final pulse periodicity T, allowing us to compare different values of q, where the black, red, green, and blue curves refer to $q = 2, 3, 5$, and 7, respectively. The maximum gain of 9.9 dB occurs for $L = 1.37$ cm at $T = 600$ ps and $q = 5$. For $q = 7$, the maximum achievable gain is just below the theoretical maximum of $10 \log_{10} 7 = 8.45$ dB, while for the other values of q, the obtained gain is higher than its theoretical maximum in (4.23), indicating that the pulses are heavily distorted and compressed, as suggested by the low SNR. L is almost unchanged with T in this case, suggesting that the frequency spectrum plays a significant role. When compared to the CPA method, the SNR is lower for all cases.

According to (4.22), the propagation lengths are inversely proportional to q. At the same time, higher amplification factors lead to larger bandwidths that increase the propagation length due to the energy contained in the lower dispersion regions. Furthermore, the pulses also appear at multiples of the calculated value (the shortest L is calculated when $V(t, 0) = U(t, z_{TT}(p/2q))$, $p = (2q - 1)$. However, p can assume other integer values, resulting in different propagation lengths. Since higher-order dispersive coefficients introduce higher-order Talbot lengths (262), this might result in better pulse reconstruction (higher gain) than the shortest length.

Comparing the results of this section with those from the CPA, we notice that the FTAI allows 1 order of magnitude reduction in the fiber length L, with G exceeding the theoretical maximum. The CPA method, in turn, also exceeds the theoretical limit whenever we use chirped pulses, with better noise performance than the FTAI since the latter does not allow output pulse shape control. But the FTAI needs only a phase modulator to be implemented (we use the TTE to generate the pulses), which significantly simplifies the setup and allows a more efficient energy use of the THz source.

Appendix C.3 shows time waveforms for both CPA and FTAI, using ideal and realistic (bandwidth limited) phase modulation profiles.

4.4.3 Backpropagated CW-to-pulse conversion

Finally, we address the BTAI method to optimize the phase grating. The idea is to improve further the original FTAI noise performance, besides reducing the fiber length L
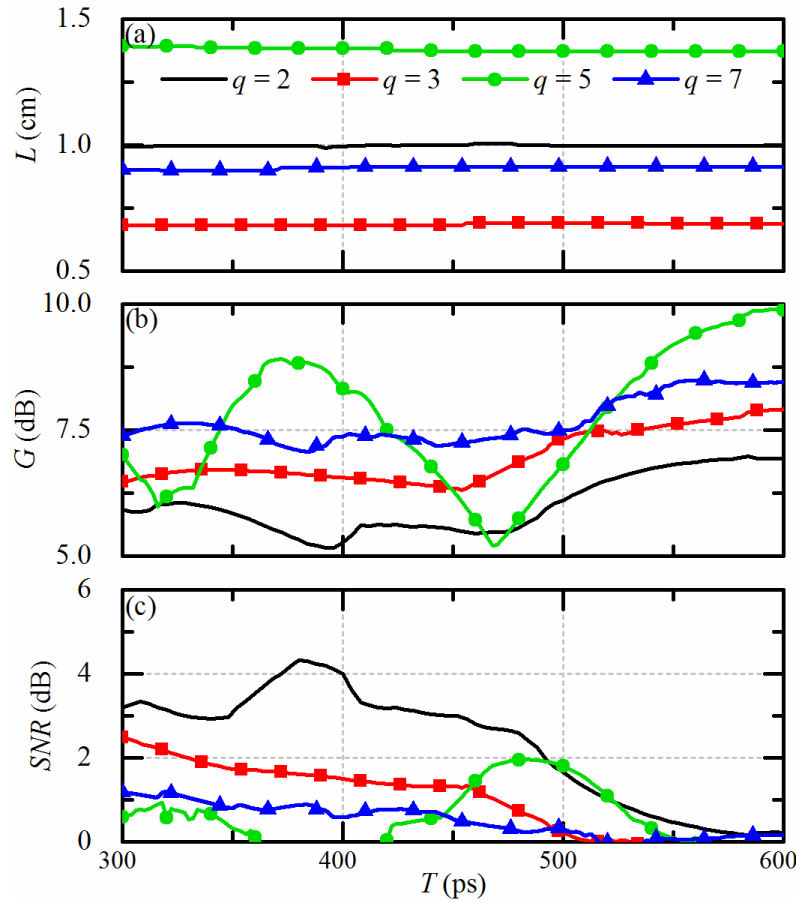
Figure 26 – Simulated results for the (a) fiber length L, (b) gain G, and (c) SNR for the FTAI method. Black, red, green, and blue curves refer to $q = 2, 3, 5$, and 7, respectively. The SNR decreases as T increases and shows acceptable values for $T < 500$ ps. Symbols are only a guide to the eye. Adapted with permission from (265)© Optica Publishing Group.

compared to the CPA method. To tune the performance of the designed phase grating, we use the pulse described in (4.26) with $m = 1$ and vary Ov in the desired output waveform to eliminate spurious signals and increase the SNR.

Figures 27(a)–(c) show the performance obtained for overmodulation values ranging from -0.3 to 0.3. We set the desired output waveform as a Gaussian pulse with $T = 400$ ps and $T_{FWHM} = 60, 70, 80, 90$, and 100 ps (shown as purple, green, red, blue, and black lines, respectively). The highest SNR of 16 dB occurs for $T_{FWHM} = 100$ ps and $Ov = 0.15$, with $G = 6.5$ dB and $L = 1.32$ cm, while the highest G of 8.8 dB occurs for $T_{FWHM} = 60$ ps and $Ov = -0.14$ and $SNR = 7.5$ dB. The SNR obtained with the BTAI method exceeds all previous results, with L of the same order of magnitude as the conventional FTAI but with a higher gain. The maximum achievable gain for this case, according to (4.23), is $R'/2 = 7.96$ dB for $T_{FWHM} = 60$ ps. When comparing the methods, the CPA method provides both high gain (higher than the theoretical value) and SNR at the cost of longer propagation lengths. The BTAI method, on the other hand, can be tuned for
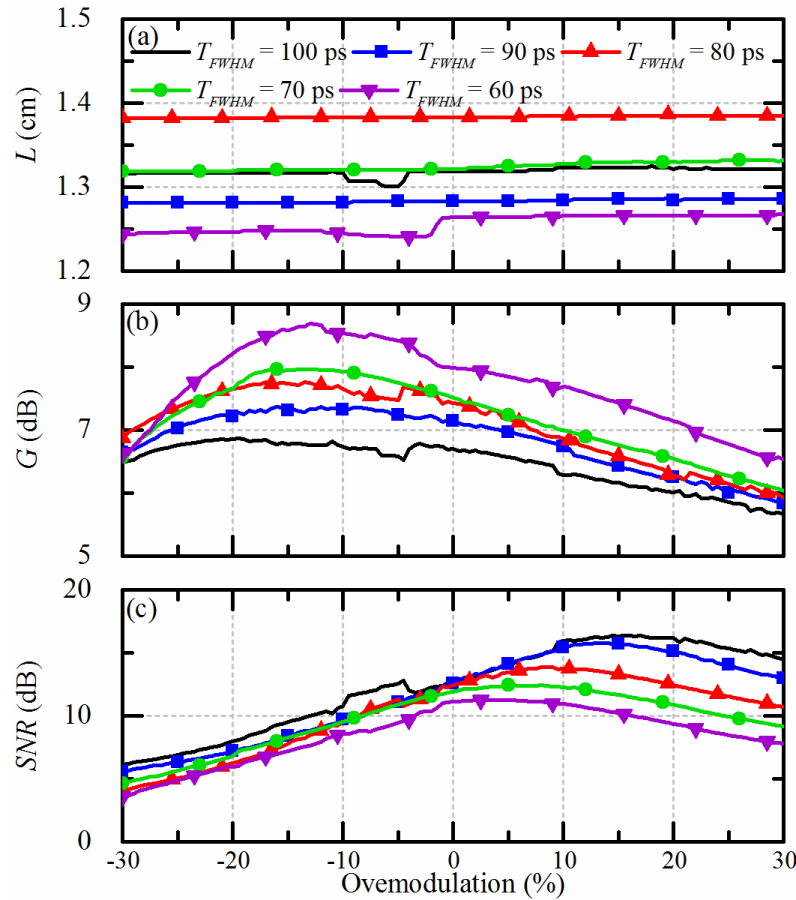
Figure 27 – Simulated results for the (a) fiber length L, (b) gain G, and (c) SNR for the BTAI method for $T = 400$ ps with a phase grating designed using the backward propagation method. Purple, green, red, blue, and black lines refer to $T_{FWHM} = 60$, 70, 80, 90, and 100 ps, respectively. Symbols are only a guide to the eye. Adapted with permission from (265)© Optica Publishing Group.

better G or SNR (time waveforms can be seen in Appendix C.3), with a short propagation length, suggesting it is the most versatile method of all three. Moreover, lower propagation lengths mean ease of fabrication since it would require less silicon wafer stacking to obtain the desired fiber length. A brief discussion on Si wafer stacking is included in Appendix C.4. It is worth mentioning that the CPA method is of particular interest for sources that do not operate in the CW regime, such as QCLs (241), while both TAI-based methods perform more efficiently with CW sources.

The pulse width acts inversely on both the bandwidth and on the realizable gain (via R'). A decrease of L is expected as the bandwidth narrows (T_{FWHM} increases), while an increase in L is expected as the gain factor R' decreases, analogously to the effect of the parameter q in CPA and FTAI. The two factors (bandwidth and gain factor) have opposing influences on L, which explains why it increases from $T_{FWHM} = 60$ to 80 ps but decreases when T_{FWHM} is 90 ps.

Figures 24–27 help the designer to optimize the fiber parameters (L) and operation

mode (CPA, FTAI, BTAI) for the desired pulse rate T. Once L has been fixed, varying T will negatively impact the gain and SNR of the system.

Figures 24(e)–(g) and 25(e)–(g) show the gain as function of the input period T'. These curves take into account the propagation losses provided in Fig. 21(c). Larger periods result in higher gains because the (narrower) spectrum becomes more confined in the highly dispersive spectral region where the propagation losses are small. The same is true for the FTAI in Fig. 26, which shows the gain as function of the final period T. Although we show BTAI results for $T = 400$ ps only, the same arguments apply to it aswell.

4.5   Conclusion

In this chapter, we proposed the first fully passive THz pulse amplification device based on a highly dispersive silicon-based metamaterial Bragg fiber and on the TTE. To achieve this goal, we introduced and explored three different methods to maximize the passive gain, namely the CPA, FTAI, and BTAI. All three methods used the TTE to manipulate the periodicity of a pulse train by splitting or combining these pulses as they propagate through the fiber, resulting in a narrow intensity amplified pulse at a given fractional Talbot length. The BTAI method has more degrees of freedom for the output pulse shape, overcomes the limitations of implementing discrete phase gratings in limited time-response phase modulators, produces the optimum fiber length that maximizes the gain, and reduces undesired spurious spectral components. Moreover, this method allows pulse generation without the need for amplitude modulation, resulting in more efficient energy use of THz sources. The Bragg fiber proposed here consisted of a large, squared air core with alternating silicon metamaterial claddings. Each metamaterial clad consisted of an array of squared airholes (etched directly on the silicon wafers) whose homogenized indices are controlled by the airhole fill factor. We calculated the homogenized index of each metamaterial cladding layer via a parameter extraction method, and we then plugged these values into analytical and numerical methods and compared the results at every step of the optimization process. The fiber length was considered as an assembly (stacking) of as many silicon wafers as required to obtain the desired fiber length. We explored different pulse shapes and chirped pulses with the CPA and different gain factors with the BTAI and FTAI methods. Finally, numerical results indicated a 5.8 dB gain for a 9.8 cm long fiber with the CPA method, a 9.9 dB gain with the FTAI (1.37 cm long) method, and a 8.8 dB gain with the BTAI (1.25 cm long) method. We believe that the proposed passive amplification devices based on the TTE may pave the way to a myriad of new applications involving high power THz sources.

5 PASSIVE AMPLIFICATION OF MICROWAVE PULSES VIA TEMPORAL TALBOT EFFECT: EXPERIMENTAL DEMONSTRATION AND POTENTIAL APPLICATIONS

The work in the chapter has been published as: PEPINO, V. M.; MOTA, A. F.; BORGES, B.-H.V.; Experimental demonstration of passive microwave pulse amplification via temporal Talbot effect. **Scientific Reports,** 13, 15330, 2023. Permission for reuse is found in Appendix F

5.1 Introduction

The Talbot effect, first observed in 1836, is a well-known phenomenon in wave optics where a periodic structure is self-replicated at regular intervals when a coherent beam of light passes through it. In the Talbot effect, the replicated structure appears at a distance equal to the original grating's length, known as the Talbot distance (269, 270). The TTE, in turn, is a similar phenomenon in the time domain, first proposed in 1981 (271) and experimentally verified in 1993 (272). It occurs when a pulsed light source, such as a pulsed laser, is sent through a first order dispersive medium. The replicated pulses, known as the Talbot fractional images, are observed at regular intervals, which are shorter than the period of the input signal (273–278), and can even convert continuous wave (CW) signals into pulses by propagating the input signal through a first-order dispersive medium (157). The temporal Talbot effect has found numerous applications in signal processing, including pulse rate multiplication (277, 279–281), pulse generation (157, 282), passive amplification (156, 265), signal denoising (245), sub-noise detection (283), pulse compression (257), and temporal cloaking (284, 285).

Despite its potential, every TTE implementation to date has been achieved with optical fibers because it requires long propagation lengths, high dispersion, and low loss. For instance, previous TTE implementations have utilized either single-mode standard fibers (156, 272), requiring up to kilometers of fibers, or linearly chirped fiber Bragg gratings (286, 287), which requires only a few centimeters (155). Dispersion compensating fibers, such as Bragg (143, 144) or photonic crystal fibers (145–147), have also been used for this purpose (265, 277). The high dispersion coefficient of these fibers originates from a rapidly varying electric field profile as the operating wavelength is changed, leading to a fast change in the effective index. However, these fibers have limited dispersive bandwidth and their cross-sectional area is large compared to the wavelength, which is problematic for microwave frequencies. In contrast, fiber Bragg gratings can be realized in single mode waveguides, significantly reducing the cross-sectional area, close to the diffraction limit, which is crucial for microwave applications. Furthermore, the dispersive bandwidth of fiber Bragg gratings depends only on the initial and final period of the grating, making

them a more versatile option for implementing TTE in the microwave and mm-wave range. More recently, we have theoretically demonstrated passive amplification in the terahertz range using a low-loss all-silicon rectangular waveguide with metamaterial clad in a Bragg fiber-type configuration (265), suggesting that the TTE may find broader use in the future.

Despite the numerous applications of TTE, its implementation in longer wavelengths requires large structures. As a result, only its spatial counterpart has been realized in the microwave range, with a limited number of applications, such as antenna power combining (288, 289). Meanwhile, the previously mentioned myriad of applications of TTE remains unexplored. Additionally, lower repetition rates require either extremely high dispersive media or prohibitively long propagation lengths, with the latter simultaneously complicating the device's fabrication besides increasing propagation losses. Notably, the propagation length necessary for TTE is proportional to the square of the signal period, which is limited by both the carrier frequency and the operational bandwidth of the dispersive waveguide. Usually, there are two approaches to overcome these limitations. Firstly, by increasing the dispersion coefficient of the propagating medium and, secondly, by increasing its dispersive spectral bandwidth. Our work demonstrates that, in cases where there is a trade-off between maximum dispersion and dispersive bandwidth, the latter is preferred. This approach allows for shorter pulse periods and propagation lengths, making the TTE implementation more feasible in the microwave and mm-wave ranges.

In this chapter, we present the first experimental demonstration of the TTE in the microwave regime using an ultra-wideband linearly chirped Bragg grating (LCBG) fabricated with stereolithography (SLA) technology. The LCBG is designed to operate over the entire X-band (8.2–12.4 GHz) and is incorporated into a standard WR-90 metallic waveguide. To extract the output signal, we use a broadband microwave circulator due to the reflective nature of the LCBG. By varying the input pulse repetition rate, we observe the complete Talbot carpet in a hybrid numerical-experimental strategy and experimentally observe the Talbot fractional images relative to 1/2 and 1/3 of the Talbot length. Moreover, we utilize the backward Talbot array illuminator (BTAI) technique to generate gaussian and raised cosine pulses with a passive gain of 3.44 dB and 4.03 dB, respectively. The BTAI is a recently developed application of the TTE for continuous wave (CW)-to-pulse conversion. It is based on the Talbot array illuminator (157) and provides passive amplification, accounting for all non-idealities of the dispersive medium (265).

This chapter is organized as follows. First, we present the theoretical background of the propagation length requirements for the TTE and discuss the trade-offs between the dispersion coefficient and dispersive bandwidth in a LCBG in Section 5.2. Then, in Section 5.3 we detail the design strategy of our LCBG, the fabrication procedure, and experimental frequency response measurements. We then show in Section 5.4 our simulation and experimental methods, and present the simulated and experimental results of the

temporal Talbot carpet and BTAI pulse generation. Finally, we summarize our findings and provide some concluding remarks in Section 5.5. In Appendix D, we present the frequency-dependent complex permittivity of the SLA resin and explore the potential for passive amplification with lower loss dielectrics, which can potentially yield gains over 8 dB.

5.2 Theoretical background

5.2.1 Temporal Talbot effect limitations and implementation requirements

The TTE occurs when a periodic signal $(U_o(t))$ propagates through a first-order dispersive medium with propagation constant given by $\beta(\omega) = [\beta_o + \beta_1\omega + (\beta_2\omega^2)/2]$, where ω is the angular frequency and $\beta_b(\omega_o) = \left[\mathrm{d}^{(b)}\beta(\omega)/\mathrm{d}\omega^b\right]_{\omega=\omega_o}$. The temporal and spatial evolution of the signal $(U(t,z))$ is calculated on page 83, repeated here for convenience:

$$U(t,z) = \sum_{l=-\infty}^{\infty} a_l \mathrm{e}^{\frac{j2\pi l(t-\beta_1 z)}{T}} \mathrm{e}^{-j\left(\frac{2\pi^2 l^2 \beta_2}{T^2}\right)z}. \tag{5.1}$$

As explained in Chapter 4, the first exponential term in (5.1) is responsible for the group delay, while the second term distorts the pulses shape by applying a linear chirp. For the specific cases where $z = z_{TT}/2q$, called fractional Talbot lengths, (5.1) can be rewritten as (4.20),

$$U\left(t, z = \frac{z_{TT}}{q}\right) = \left[U_o\left(t - \beta_1\frac{z_{TT}}{q} - e_{pq}\frac{T}{2}\right)\right] * \left[\frac{1}{\sqrt{q}}\sum_{b=0}^{q-1} \mathrm{e}^{j\gamma_b}\delta\left(t - b\frac{T}{q}\right)\right], \tag{5.2}$$

where z_{TT} is calculated as $T^2/(2\pi|\beta_2|)$, the second term of the convolution is a pulse train with period T/q ans constant phase γ_b, while the first term corresponds to the input signal U_o shifted in time. In summary, after the pulse propagates a distance $z = z_{TT}/q$, $U(t,z)$ will consist of q repetitions of U_o scaled by $1/\sqrt{q}$.

This formalism can also be employed to obtain the Talbot carpet, a fractal pattern of sub-images with an ever increasing repetition rate that results from the Talbot effect. The Talbot carpet consists of observing $U(t,z)$ as it propagates through a distance z_{TT}/q and observing the q repetitions of U_o. Although it is the most common approach to generate the Talbot carpet, in applications with fixed propagation length $(L = z_{TT}/q)$, the carpet can also be generated by varying T instead of z. In this sense, only specific values of T fulfill the requirements for the TTE fractional images, and, by applying the definition of L in z_{TT} the q repetition rate occurs when

$$T = \sqrt{2\pi q|\beta_2|L}. \tag{5.3}$$

However, to generate the Talbot carpet, the medium must have a first-order dispersion profile over the bandwidth BW occupied by the signal U_o. Assuming U_o occupies a fraction of the period $K_T T$ (where $0 < K_T < 1$), the signal occupies a bandwidth $BW = 1/K_T T$. Moreover, defining $\phi_2 = |\beta_2 L|$ as the second derivative of the accumulated phase over the propagation length, (4.16) can be rewritten as,

$$2\pi\phi_2 = \frac{q}{K_T^2 BW^2}. \tag{5.4}$$

A key parameter in dispersive structures is its total available dispersive bandwidth. In the microwave regime, achieving high β_2 over a large bandwidth is a challenging task. Consequently, the Talbot carpet has never been realized in this frequency range. However, increasing BW (or reducing T) quadratically decreases the necessity of large β_2, as seen in (5.4). By recasting z_{TT} as a dependance of the signal bandwidth, we can compare it with the dispersion coefficient-dispersive bandwidth relationship of dispersive structures such as a LCBG, which is thoroughly analyzed in the next Subsection. This comparison allows us to determine the optimal parameters of the LCBG. In other words, it helps us decide if we should use a wideband structure to take advantage of lower values of T and therefore reduce the necessary ϕ_2, or if we should sacrifice the dispersive bandwidth to increase ϕ_2 of the LCBG.

5.2.2 The linearly chirped Bragg grating characteristics

The LCBG is a Bragg grating structure in which the grating period Λ varies linearly along its length (286). Each period is composed of two quarter wavelength sections with different refractive indexes, n_1 and n_2, resulting in a broad reflective spectrum with a varying group delay $\tau(\omega)$. Quarter wavelength plates are reflective structures, and by linearly increasing Λ, the initial plates reflect longer wavelengths while the final ones reflect shorter wavelengths. As a result, longer wavelengths experience a shorter round-trip time, and the opposite occurs for shorter wavelengths. To further understand the impact of this device on the Talbot effect, let us consider a LCBG with N periods, where the i-th period $[\Lambda_i = \lambda_o^i/(4n_1) + \lambda_o^i/(4n_2)]$ is responsible for reflecting the frequency f_i (with wavelength $\lambda_o^i = c/f_i$). The delay experienced by f_i (τ_i) is given by:

$$\tau_i = \frac{2}{V_g} \sum_{u=1}^{i} \Lambda_u, \tag{5.5}$$

where the summation represents the path traveled by the wave (multiplied by two since it is a round trip) and V_g is the group velocity, assumed here as not dispersive since the filling factor of all periods is the same, and the materials are essentially non-dispersive in the frequency range of interest. To adequately perform TTE, the device should have first

order dispersive behavior and $2\pi\phi_2 = \partial\tau/\partial f$ must be constant, thus $\Delta\tau_i/\Delta f_i = $ cte. To ensure this behavior,

$$2\pi\phi_2 = \frac{\Delta\tau_i}{\Delta f_i} = \frac{2}{c/V_g}\left(\frac{n_1 + n_2}{n_1 n_2}\right)\left(\frac{1}{(f_{i+1} - f_i)\, f_{i+1}}\right), \tag{5.6}$$

where $V_g/c = n_{eff}^{\text{LCBG}}$is the effective index of the LCBG.

Equation (5.6) provides a roadmap on how to design a LCBG. Once the device's initial frequency ($f_o = f_{\text{ini}}$) and desired ϕ_2 are known, the dispersive behavior is achieved by calculating the N steps of f_{i+1} using (5.6). Moreover, it is interesting to note that even if the procedure starts by defining the device's final frequency ($f_N = f_{\text{fin}}$) and calculating f_{i-1}, the obtained Λ_i would remain the same. In practical terms, it means that the device would present the same $|\phi_2|$ with opposite signs when excited from either side. It is crucial to note that Λ_i is proportional to λ_0^i , and therefore, using small frequency steps (for a continuous reflective profile) would result in a lengthy structure. However, for the purpose of qualitatively understanding the relationship between the dispersion coefficient and the dispersive bandwidth of a LCBG, this idealization is justified. After defining Λ_i, ϕ_2 can be calculated as:

$$2\pi\phi_2 = \frac{2L_o}{\sum \Delta f_i} n_{eff}^{\text{LCBG}}, \tag{5.7}$$

where L_o is the total length of the device. A complete rigorous analysis of the LCBG can be found in (286). For a fixed grating length and refractive index (which are determined by the materials used), the dispersion coefficient is inversely proportional to the dispersive bandwidth, $\phi_2 \propto 1/\sum \Delta f_i$. Nevertheless, according to (5.4), the required $\phi_2 \propto 1/BW^2$ and $\sum \Delta f_i \geq BW$. Thus, maximizing $\sum \Delta f_i$ while reducing ϕ_2 is desired for implementing the TTE.

So far, the LCBG formalism has been developed for a wave propagating in free space. However, to facilitate the measurement procedure, we place the LCBG inside a metallic WR-90 waveguide. In this sense, the i-th guided wavelength λ_g^i inside a rectangular metallic waveguide operating in the TE$_{10}$ mode is given by:

$$\lambda_g^i = \frac{\lambda_o^i}{\sqrt{1 - \left(\frac{\lambda_o^i}{2w}\right)^2}}, \tag{5.8}$$

where λ_o is the free space wavelength, and w is the waveguide cross-section width. Note that the relation between λ_g^i and f_i is not inversely proportional, and V_g becomes dispersive when the LCBG is placed inside a waveguide. In this case, to maintain the relation

$\Delta \tau_i / \Delta f_i = \mathrm{cte}$, we have

$$2\pi \phi_2 = 2 n_{eff}^{\mathrm{guide}} (f) \left(\frac{n_1 + n_2}{n_1 n_2} \right) \left(\frac{1}{(f_{i+1} - f_i) f_{i+1}} \right), \tag{5.9}$$

$$n_{eff}^{\mathrm{guide}} (f) = \sqrt{1 - \left(\frac{\lambda_o^i}{2w} \right)^2} n_{eff}^{\mathrm{LCBG}}. \tag{5.10}$$

Using the same procedure to design the LCBG in free space, we first define the initial frequency ($f_o = f_{\mathrm{ini}}$) and the desired ϕ_2. Then, we calculate f_{i+1} and Λ_{i+1}, until the N-th period. Finally, ϕ_2 can be obtained as,

$$2\pi \phi_2 = \frac{2 L_o}{c \Delta f} \left(\frac{n_1 + n_2}{n_1 n_2} \right) \sqrt{1 - \left(\frac{\lambda_o^N}{2w} \right)^2}. \tag{5.11}$$

It is worth noting that the dispersive behavior of n_{eff}^{guide} results in the structure exhibiting different ϕ_2 values when excited from different sides. In addition, the i-th period also changes when the structure is designed from the initial or final frequency. Therefore, we conclude that the LCBG exhibits different dispersive characteristics when excited from either the shorter or longer period ends, as experimentally confirmed in the next section.

5.3 Design, fabrication and characterization

To assess the TTE in the microwave regime, we design the LCBG to operate in the X-band (8.2 – 12.4 GHz) due to its high central frequency, allowing fast modulation rates (shorter T). Another advantage of using the X-band is the possibility of placing the structure inside a standard metallic waveguide WR-90 (rectangular cross-section, dimensions 22.86×10.16 mm), facilitating the measurements. The LCBG is built using SLA printing technology, where the resin permittivity ε_r and loss tangent $\tan \delta$ at 10 GHz are equal to 2.7 and 0.027, respectively. The dispersive behavior and the approach to characterize the resin (175) are presented in Appendix D.

As well known, the building blocks of the Bragg reflector demand two different materials, chosen here as the printed resin spaced by air layers. To guarantee operation inside the desired dispersive bandwidth, we choose the initial and final period corresponding to free space wavelengths of $\lambda_o^0 = 25$ mm, and $\lambda_o^N = 40$ mm, corresponding to the lower and upper limits of the X-Band. From (5.11), the calculated value of the dispersion coefficient assuming $L_o = 0.3$ m (chosen to fit inside two 6" [152.4 mm] waveguide sections) is $2\pi \phi_2 = 0.47$ ns^2 when excited from the longer period end (or 0.28 ns^2 if we chose the shorter period end instead), suggesting that exciting the LCBG from the longer end is preferable. Hereon, we define ports 1 and 2 as the excitation at the shorter and longer period ends, respectively.
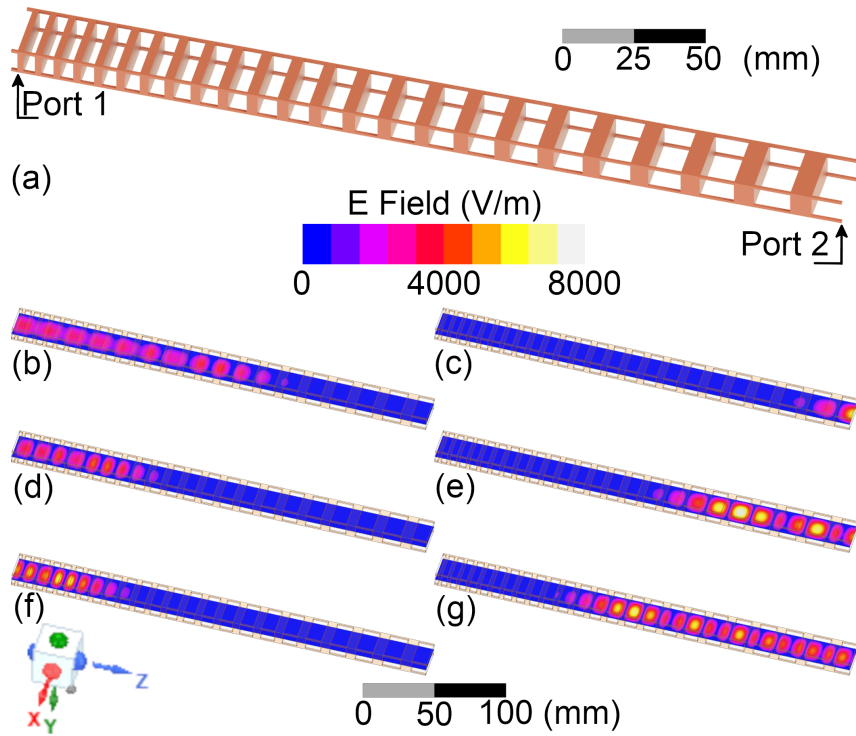
Figure 28 – (a) Three-dimensional model of the designed LCBG. Electric field at 8 GHz with the excitation at ports (b) 1(left side) and (c) 2(right side). Electric field at 10.5 GHz with the excitation at ports (d) 1 and (e) 2. Electric field at 13 GHz with the excitation at port (f) 1 and (g) 2. Note how the excitation from port 2 (right side figures) result in a shorter penetration distance, which results in lower losses, and a greater difference in the penetration distance from 8 GHz and 13 GHz, which results in a higher dispersion coefficient.

A model of the designed LCBG is presented in Fig. 28(a). Figures 28(b)-(g) show the simulated electric field inside the waveguide, simulated with Ansys HFSS software, for $f = 8$ GHz in (b) and (c), 10.5 GHz in (d) and (e), and 13 GHz in (f) and (g), when excited from port 1 [(b), (d) and (f)] or port 2 [(c), (e), and (g)]. As expected, the electric field propagates a shorter distance for lower frequencies when excited from port 1 than when excited from port 2. Moreover, longer propagation entails higher attenuation since the resin presents a considerable loss, which can be seen by the weaker electric field when the LCBG is excited from port 1. Another important aspect is that a higher $2\pi\phi_2$ implies a faster delay variation, meaning that the wave excited from port 2 (higher dispersion) experiences a faster round trip (less lossy) when the frequency is changed. This behavior means the structure presents less loss and more linear reflection when excited from port 2.

All these observations are confirmed by the reflection coefficients of the filled waveguide, S_{11}^{WG} and S_{22}^{WG}, measured by a Rohde & Schwartz ZVA-40 Vector Network Analyzer (VNA), shown in Fig. 29. Figures 29(a) and (b) show the amplitude and phase, respectively, of $S_{11,22}^{\mathrm{WG}}$ in thin blue lines and thick red lines, respectively. Figure 29(b) shows the fabricated LCBG as an inset. Moreover, we use a second-order polynomial
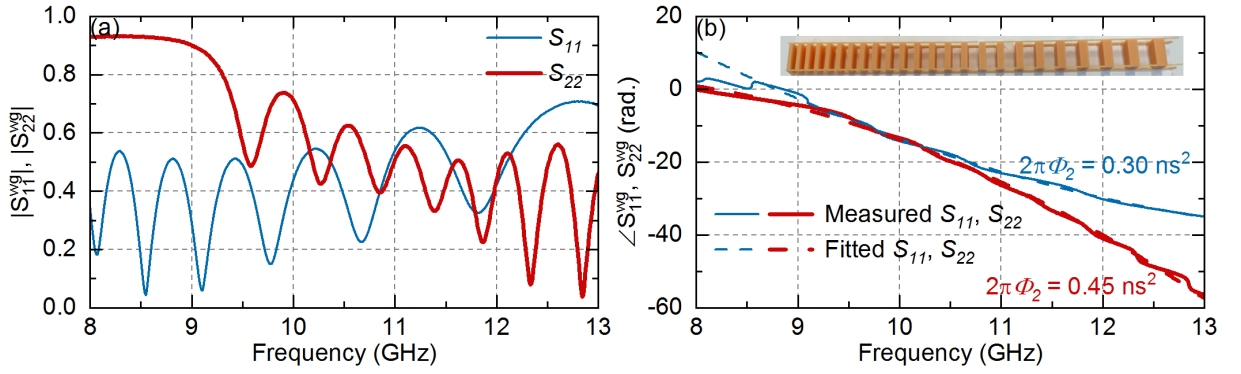
Figure 29 – (a)Measured values of the reflection coefficients of the fabricated LCBG inside a WR-90 waveguide when excited from port 1 (thin blue lines) and 2 (thick red lines). (b) Unwrapped argument of the reflection coefficients (solid line) and its respective quadratic fits (dashed lines). Note that exciting the LCBG from port 2 is preferred, both due to higher reflected average amplitude and higher dispersion coefficient, as well as a broader dispersive bandwidth (look at the phase response below 8.5 GHz). Fabricated LCBG is shown in inset of (b).

fit to determine the average value of $|2\pi\phi_2|$ because the LCBG non-idealities (both due to the low number of periods and high dielectric loss tangent) create oscillations in the ideal quadratic phase response. The polynomial fit is shown as a dashed line in Fig. 29(b) and provides an average value of $|2\pi\phi_2|$ of 0.30(0.45) ns^2 when excited from port 1(2), supporting the validity of the proposed approach in creating a first-order dispersive medium. It is important to highlight that although the oscillations in the ideal phase response create non-idealities in the TTE, the effect is still achievable, as observed in previous works with non-ideal dispersive media (262).

5.4 Results and discussion

5.4.1 Talbot carpet

The experimental setup for implementing the TTE is illustrated in Figure 30(a), where the LCBG is inserted inside two straight sections of WR-90 waveguide, terminated with a matched waveguide load. To measure the reflected signal, we use a broadband circulator (Pasternack PE83CR002, 8-18 GHz) with its port C1 connected to port 2 of the waveguide. Port C2 of the circulator is connected to a oscilloscope (Keysight DSOV134A, 80 GS/s, 13.6 GHz bandwidth), while port C3 is connected to an arbitrary wave generator (AWG, Keysight M8195A, 64 GS/s) with a 25 GHz bandwidth. To account for the non-flat frequency response of the circulator over the entire bandwidth, we characterize the transmission from port C3 to port C2 of the circulator with port 1 loaded with the dispersive waveguide. The resulting transmission coefficient T_{23}^{circ} is shown in Fig. 30(b) and compared with S_{22}^{WG}, where the former exhibits a slightly lower amplitude than the

latter due to the loss inserted by the circulator. Importantly, the phase response and the dispersion coefficient are not significantly affected.

To visualize the Talbot carpet in a fixed propagation length, we must vary the input period T. From (5.3), $T = \sqrt{2\pi q |\beta_2| L}$, and thus we can correlate the propagation length with the input period, resulting in periods of 0.95 ns, 1.16 ns, and 1.34 ns for $q = 2$, 3, and 4, respectively. Due to phase oscillations and other non-idealities in the dispersive profile inducing higher order dispersion coefficients (262), we expect the necessary period to be higher than the calculated value for an ideal structure. Thus, we sweep T from 1.0 ns to 2.0 ns to visualize the temporal Talbot carpet in a hybrid simulation-experimental strategy, where the pulse propagations are numerically calculated by multiplying the Fourier series spectrum of the input signal by the measured frequency response T_{23}^{circ} shown in Fig. 30(b). We use Gaussian input pulses defined as:

$$U_o\left(t\right) = \mathrm{e}^{-\left(\frac{t^2}{2T_o^2}\right)}, \tag{5.12}$$

$$T_o = \frac{TK_{FWHM}}{2\ln\sqrt{2}}, \tag{5.13}$$

where K_{FWHM} is the relationship between the input period and the pulses' full width at half maximum (FWHM), chosen as 10% of the temporal slot T to avoid pulse overlapping when the repetition rate is multiplied by the TTE. The carrier frequency f_c is chosen to be 10.5 GHz, and we limit the bandwidth to $8-13$ GHz, which is below the cutoff of
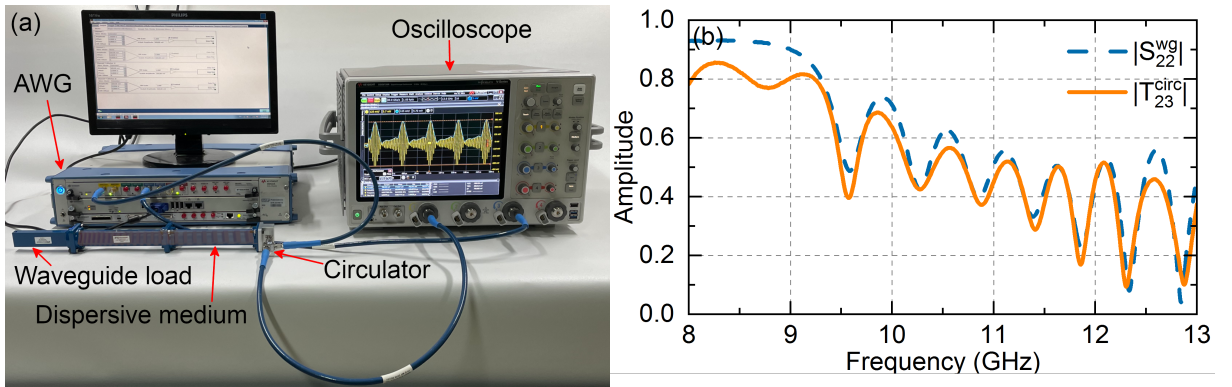
Figure 30 – (a)Experimental setup for measuring the TTE. The two waveguide sections are loaded with our LCBG (dispersive medium shown in transparency to visualize its full length inside the waveguide), with a broadband waveguide load in port 1 and a microwave circulator in port 2. Ports 2 and 3 of the circulator are connected to a oscilloscope and an AWG respectively. (b) Effect of the circulator on the frequency response. T_{23}^{circ} , shown in solid orange lines, adds extra losses to the system when compared to S_{22}^{WG}, in dashed blue lines. To perform a correct design optimization, we use T_{23}^{circ} in all of our simulations. The phase response does not change and thus is omitted.
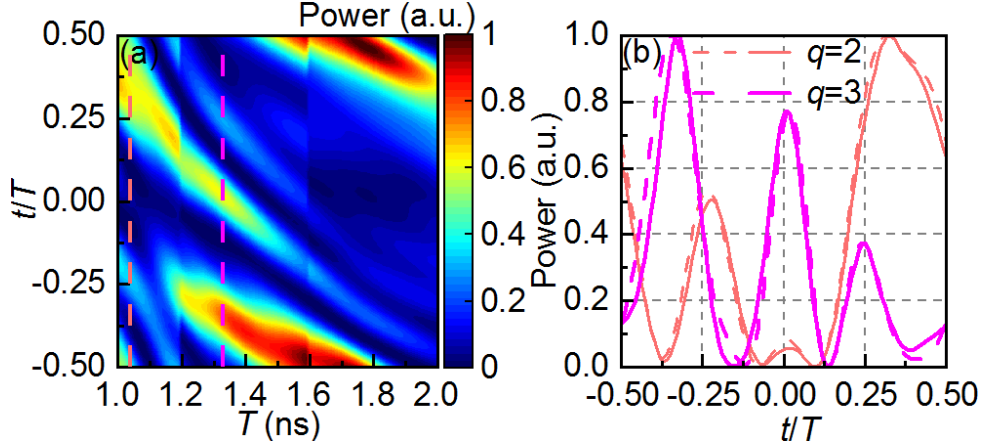
Figure 31 – (a) Talbot carpet obtained via a hybrid numerical/experimental strategy for simulating pulse propagation using the measured frequency response of the LCBG T_{23}^{circ}. The time axis is normalized by the period T and the period axis indirectly represents the propagation length. Talbot fractional images relative to $q = 2, 3$ occur at $T = 1.04$ ns, 1.33 ns, highlighted by red and magenta dashed lines, respectively. Note how the pulse peaks get closer as T increases, suggesting the occurrence of other fractional images ($q > 3$) that do not appear properly due to non-idealities in the dispersive profile and limited bandwidth. Discontinuities at $T = 1.2$, 1.6 ns are related to frequency components of the input pulse being outside the dispersive band and thus are filtered out. (b) Slices of the highlighted regions in (a) (dashed lines) and fully experimental (solid lines) Talbot fractional images for $q = 2$ (red lines) and 3 (magenta lines). Note that, although the pulses shapes and amplitudes are distorted, their periods are divided by 2 and 3, respectively, as expected in Talbot fractional images.

the second mode of the WR-90 waveguide. The normalized output intensity is mapped in terms of the period T, which indirectly represents the propagation length and the normalized time t/T.

Results are shown in Fig. 31(a). The time axis is normalized by the period T with the period axis indirectly representing the propagation length. We observe that the results differ from the ideal theoretical Talbot carpet due to the non-idealities in the frequency response, including valleys in the reflection amplitude caused by dielectric losses, oscillations in the phase behavior, and limited bandwidth. The first two cause the system to deviate from the TTE ideal formulation, while the limited bandwidth filters the spectra of the ideal Gaussian pulses and creates secondary peaks, turning the gaussian pulses into sinc-like shapes and broadening its temporal width; this causes partial overlapping of the output pulses. Nonetheless, we observe that the pulse repetition rate changes, typical of the TTE approach. At $T = 1.04$ ns, the resulting pulse period is approximately half of the input period, which corresponds to the fractional Talbot image relative to $q = 2$; at $T = 1.33$ ns, the output signal exhibits a period approximately equal to a third of T, or the factional Talbot image relative to $q = 3$, both highlighted in light red and

pink dashed lines, respectively. The discontinuities in the simulated carpet at $T = 1.2$ ns and $T = 1.6$ ns are caused by limited bandwidth filtering extra harmonics of the input signal, resulting in changes in the pulses' shape and amplitude. The difference between the expected pulse periods for q equal to 2 and 3, and the obtained values, are caused mainly by the oscillations in the phase response, which add higher order dispersive coefficients to the system (262). Additionally, it should be noted that as T increases, the output peaks have a shorter period, which is typical of higher q values. However, due to the dispersive non-idealities and the heavy pulse overlapping, the signal is heavily distorted, and no extra pulses are observed for $q > 3$. The Talbot fractional images for $q = 2, 3$ are plotted in Fig. 31(b), where dashed lines refer to slices of Fig. 31(a) and solid lines refer to fully experimental results. Thin red lines are used for $q = 2$ and thick magenta lines for $q = 3$. Note that experimental results agree very well with simulations.

5.4.2 Pulse generation via backwards Talbot array illuminators

A novel method of converting CW to pulses using the TTE, the BTAI, is proposed in Chapter 4. One advantage of this method is the use of a numerical backpropagation, considering the actual dispersive characteristics of the propagating medium and accounting for all the non-idealities, to optimize the input phase modulation profile that generates the desired pulse shape at the output. Note that from energy conservation, the pulse peak should indeed be higher than the CW amplitude, resulting in a passive gain.

The method works as follows: First, we specify the target output pulse shape. Subsequently, we backpropagate the signal through the dispersive LCBG using the inverse of $[T_{23}^{\mathrm{circ}}]$. Since the LCBG has a fixed length, there is no need to sweep the propagation length, as done in Section 4.2.1.3, where z is swept to obtain the lowest signal ripple. We then perform phase demodulation on the backpropagated signal to obtain the phase modulation profile, which is used to modulate a CW signal. Finally, the phase-modulated CW signal is transmitted through the LCBG to generate the desired output pulse train. To optimize the target pulse parameters, such as the period, carrier frequency, and temporal width, we employ the particle swarm optimization (PSO) algorithm to maximize the desired objective, such as the gain G (defined as the peak output power divided by the average input power) or signal-to-noise ratio (SNR), defined in (4.24) and adapted here as:

$$SNR = \frac{[V_{\mathrm{output}}(t)]_{\mathrm{RMS}}}{[V_{\mathrm{output}}(t) - V_{\mathrm{target}}(t)]_{\mathrm{RMS}}}, \tag{5.14}$$

where $V_{\mathrm{output}}(t)$ is the output signal and $V_{\mathrm{target}}(t)$ is the target pulse shape. The SNR is used to quantify the distortion in the desired pulse shape that comes from non-idealities in the dispersive profile and amplitude response of the LCBG.

In this study, we investigate the generation of Gaussian and raised cosine (RC) pulses. As previously explained, the narrower the pulse's temporal width, the higher the achievable G due to energy conservation. However, generating narrower pulses come at the cost of broadening the spectral bandwidth, which is limited to the X-Band frequency range (8.2–12.4 GHz). Filtering out parts of the spectrum can distort the signal, making it difficult to preserve the shape of a narrow Gaussian pulse. To address this issue, we also generate RC pulses and compare the results with those of Gaussian pulses. These pulses are known for their efficient use of the available bandwidth and reduced inter-symbol interference in communications (290), and are generated with the use of a RC filter $H_{\mathrm{RC}}(f)$, defined as:

$$
H_{\mathrm{RC}}(f) = \begin{cases} 1 & , |f| \leq \frac{1-\alpha_{\mathrm{RC}}}{2T_o^{\mathrm{RC}}}, \\ \frac{1}{2}\left\{1 + \cos\left[\frac{\pi T_o^{\mathrm{RC}}}{\alpha_{\mathrm{RC}}}\left(|f| - \frac{1-\alpha_{\mathrm{RC}}}{2T_o^{\mathrm{RC}}}\right)\right]\right\} & , \frac{1-\alpha_{\mathrm{RC}}}{2T_o^{\mathrm{RC}}} < |f| < \frac{1+\alpha_{\mathrm{RC}}}{2T_o^{\mathrm{RC}}}, \\ 0 & , |f| > \frac{1+\alpha_{\mathrm{RC}}}{2T_o^{\mathrm{RC}}}, \end{cases} \quad (5.15)
$$

where T_o^{RC} is the temporal distance between the main pulse peak and the first zero crossing, also known as symbol period, and α_{RC} is the roll-off factor. Note that when α_{RC} is equal to 0, $H_{\mathrm{RC}}(f)$ reduces to an ideal brick-wall filter, and the resulting pulse is a sinc function.

The lower and upper bound constraints for PSO are chosen as $f_c \in (10.0, 10.6)$ GHz, $T \in (1.0, 2.0)$ ns, and $K_{FWHM} \in (0.10, 0.25)$ for Gaussian, and $f_c \in (10.0, 10.6)$ GHz, $T \in (1.0, 2.0)$ ns, $T_o^{\mathrm{RC}} \in (0.2, 0.8)$ ns, and $\alpha_{\mathrm{RC}} \in (0.00, 0.75)$ for RC pulses. We use PSO to maximize both G or SNR (while keeping $G > 0$ dB) in Gaussian pulses, and to maximize G in RC pulses. A final optimization is done by maximizing G while keeping side peak intensity lower than 1/6 of the main peak intensity. This optimization is found to improve the SNR at a small cost in gain. The optimized input parameters are listed in Table 3 for G optimized Gaussian (case 1), SNR optimized Gaussian (case 2), gain optimized RC (case 3), and gain/side peak optimized RC pulses (case 4). Table 4 summarizes the obtained G and SNR for each case, both simulated and measured values. Note that the SNR optimization provides lower G when compared to the gain optimization, because we do not set a target gain when optimizing SNR, which may limit its practical application. However, intermediate values of G and SNR can be obtained by using a weighted objective function in the PSO stage to fit the desired application, such as an intermediate pulse gain with reduced distortion.

Figure 32 shows the target (dotted blue lines), simulated (dashed blue lines), and measured (solid blue lines), as well as the input phase profile (solid red lines). Cases 1-4 are shown in (a)-(d). Note that in all cases the input signal is a phase modulated CW with constant amplitude equal to 1, marked by gray dashed lines in all plots. The target signals are shown with amplitude equal to 1 a.u., while the simulated and measured outputs are

Table 3 – Gaussian and RC BTAI input parameters

Parameter	Case 1	Case 2	Case 3	Case 4
f_c (GHz)	10.00	10.47	10.20	10.10
T (ns)	1.91	1.25	2.00	2.00
K_{FWHM}	0.15	0.17	-	-
T_o^{RC} (ns)	-	-	0.32	0.29
α_{RC}	-	-	0.37	0.15

Table 4 – Gaussian and RC BTAI output parameters

Parameter		Case 1	Case 2	Case 3	Case 4
G (dB)	Simulated	3.02	0.02	4.20	3.17
	Measured	3.45	1.68	4.03	3.60
SNR (dB)	Simulated	9.29	14.66	11.25	11.52
	Measured	8.89	12.34	7.10	12.12

normalized to the input signals to highlight the passive amplification provided by BTAI. Note that target waveforms represent only the target pulse shape. We do not define a target gain, as the PSO routine is responsible for maximizing it. We observe that RC pulses achieve higher gains than Gaussian ones, while also achieving high SNR, confirming the advantage of their flatter frequency spectrum. Case 4 slightly lowers G, but it helps reducing the experimental SNR, as seen in Fig. 32 (d), and listed in Table 4.

Finally, to better visualize the bandwidth usage efficiency, we show the Fourier spectra of the four pulse trains together with $|T_{23}^{\mathrm{circ}}|$ (shown in blue line) in Fig. 33. The light-yellow region limits the X-Band. Filled symbols show the harmonics where 95% of the pulse's total energy is contained. Red circles, green squares, purple diamonds, and orange triangles are used for the spectra of G-optimized Gaussian, SNR-optimized Gaussian, G-optimized RC, and SNR-optimized RC, respectively. Note that the SNR optimized Gaussian spectrum has its frequency components localized at lower amplitude values, which explains its lower Gain. Note also that the RC spectra are more well-distributed across the X-Band. This broader spectral width results in narrower temporal width and higher G. Furthermore, by making f_c a tuning parameter in the PSO algorithm, we avoid T_{23}^{circ} valleys, increasing the realized gain. An experimental gain of 4.2 dB is observed for the RC pulse train, while a gain of 3.45 dB is observed for the Gaussian pulse, showing the potential of the TTE for microwave passive amplification and signal generation, especially with the aid of the BTAI technique. Although the high dielectric loss tangent (higher than 0.025) limits the realized gain, the use of better dielectrics can improve the system's performance even further, allowing gains above 8 dB for RC pulses and 6.5 dB for Gaussian pulses, as discussed in Appendix D.
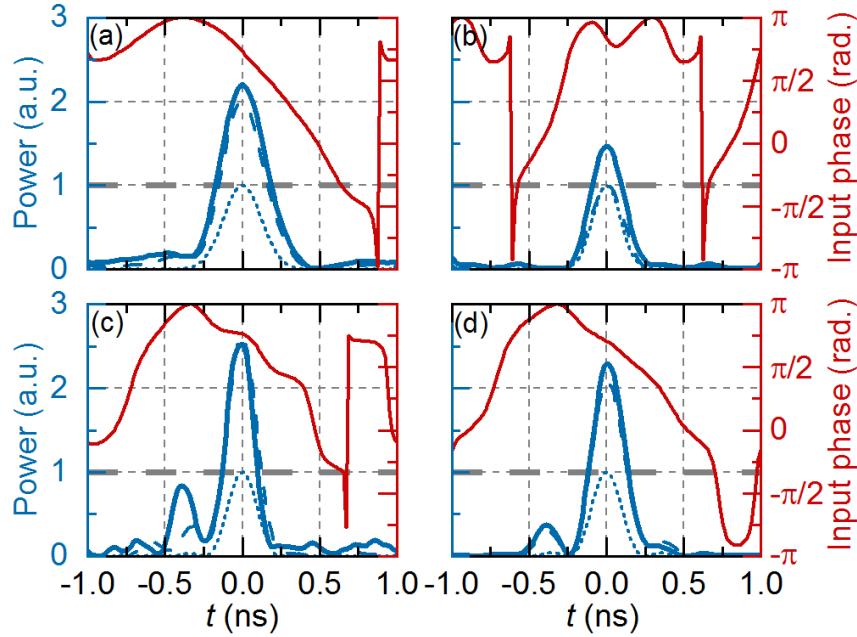
Figure 32 – BTAI gaussian-time waveforms for (a) gain optimization and (b) SNR optimization. RC BTAI time waveforms for (c) gain optimization and (d) gain optimization with constrained side peak amplitude. The target waveforms are shown in dotted blue lines, with simulated and measured results depicted in dashed and solid blue lines, respectively. Note that the target waveform is plotted with peak intensity equal to 1 to highlight the TTE passive amplification. Optimized input phase profiles are shown in red lines while input signal intensity is shown as a thick dashed horizontal line with 1 a.u. power. Note that the RC pulses achieve higher G than Gaussian while maintaining a good SNR in the side peak limited case.

5.5   Conclusion

In this study, we have successfully demonstrated for the first time the implementation of the TTE in the microwave regime using a LCBG designed and fabricated via SLA printing with low permittivity resin. The LCBG was inserted into a 12-inch (304.8 mm) WR-90 waveguide, which provided high dispersive behavior over the entire X-Band. By varying the input pulse period, we indirectly observed the Talbot carpet for fractional Talbot lengths of 1/2 and 1/3 for the first time in the microwave regime. Additionally, we generated passive amplified pulses using PSO-aided BTAI, achieving gains of 3.45 dB and 4.03 dB for Gaussian and raised cosine pulses, respectively, while maintaining high SNR levels of over 12 dB. We observed that the loss tangent of the LCBG's dielectric is the limiting factor of this structure and showed that higher quality dielectrics could increase the gain to over 8 dB while maintaining high SNR levels. We believe that our results could lead to the development of various applications, such as temporal cloaking, sub-noise microwave signal detection, microwave pulse shaping, and microwave noise reduction, among other applications.
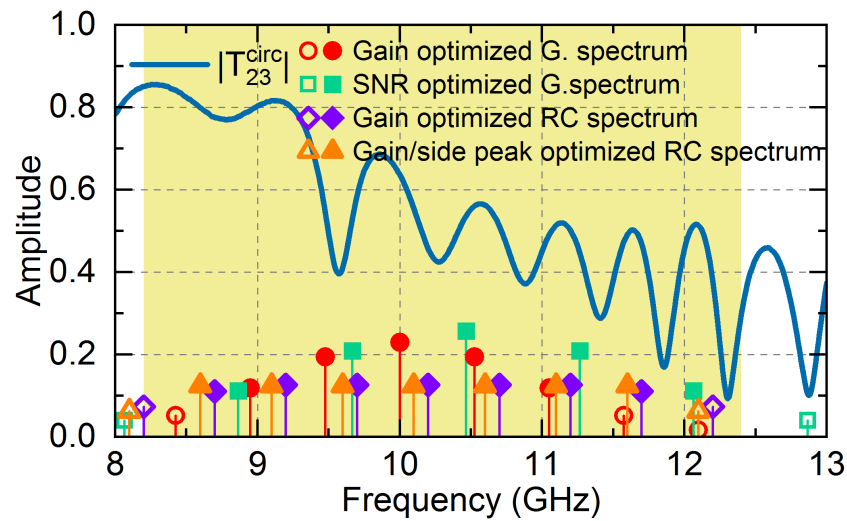
Figure 33 – Frequency components of the optimized Gaussian and RC target pulses. The yellow region limits the X-Band. Filled symbols refer to the frequency harmonics responsible for 90% of the pulse's energy while hollow symbols are the harmonics with less than 10% of the total energy. RC pulses have a more well distributed spectrum which result is a better usage of the available bandwidth, resulting in a narrower pulse width and thus a higher gain. Moreover, the carrier frequency is changed to avoid valleys of T_{23}^{circ} (in solid blue lines).

6 CONCLUSION

This thesis advances the state of the art in the two main subjects, namely meta-surface design and dispersion management. Several innovative designs and results are proposed were presented here. Metamaterials and metasurfaces have been a focus of massive electromagnetic research for the last two decades, however with a lack of dielectric meta-structures in the microwave range, which have limited its efficiency until now. In Chapter 2, we present the first all-dielectric, 3D printed, microwave metasurface. This metasurface has increased the gain of a Ka-band antenna for 5G communications in 7.5 dB, with near diffraction limited (0.85λ) focus. Furthermore, this was realized with a limited phase modulation range of 180°. The antenna HPBW was improved from 36° x 4.5° to 3° x 3°, and its front-back relation presented a 6 dB increase.

Moreover, THz metasurfaces have been extensively studied in the last years, for imaging, communication and sensing applications. However, the lack of high power sources imposes the necessity of high efficiency devices. In Chapter 3, we design and analyze a bi-layer metasurface that generates a tunable non-diffractive beam. The non-diffractive beam fit for free space communication links and long DOF imaging. In this sense, our TBB achieved a tunable DOF from 22 cm to 40 cm and FWHM from 6 mm to 3.7 mm. High resistivity Si is used as the substrate and micro air holes are chosen as the unit cell for complete phase control. Moreover, the beam presents self healing properties that improves its performance in noisy/turbulent communication channels.

Additionally, Chapter 4 proposed a novel passive amplification method in THz, based on the TTE. Three approaches were studied, namely CPA, FTAI and BTAI, where all three manipulate the periodicity of a pulsed signal, being able to stack multiple pulses, and consequently increasing its peak power, and to turn CW signals into pulse trains. The TTE is implemented using a novel metamaterial-based Bragg fiber that presents ultra-high dispersion. The fiber length was considered as an assembly (stacking) of as many silicon wafers as required to obtain the desired fiber length; a planar alternative structure with similar performance was also presented. Moreover, the BTAI method is completely new: it possesses extra degrees of freedom in defining the desired output and compensating for non-idealities of the dispersive medium, using only a phase modulated CW as input, being able to directly turn a sinusoidal input into a pulsed signal with passive gain. Numerical results indicated a 5.8 dB gain for a 9.8 cm long fiber with the CPA method, a 9.9 dB gain with the FTAI (1.37 cm long) method, and a 8.8 dB gain with the BTAI (1.25 cm long) method. We believe that the proposed passive amplification devices based on the TTE may pave the way to a myriad of new applications involving high power THz sources.

Finally, the TTE was also implemented and experimentally observed in microwave

frequencies for the first time in Chapter 5. For this applications, a 3D printed LCBG is designed to obtain an ultra wide-band high dispersion coefficient. The Talbot carpet was observed for 1/2 and 1/3 fractional Talbot lengths, and we generated passive amplified pulses via BTAI, aided by PSO optimization for the target pulse parameters, achieving gains of 3.45 dB and 4.03 dB for Gaussian and raised cosine pulses, respectively, while maintaining high SNR levels of over 12 dB. Additionally, we numerically demonstrated that the gain is limited by the 3D printing resin loss tangent, and that better dielectrics are capable of achieving gains over 8 dB. We believe that our results could lead to the development of various applications, such as temporal cloaking, sub-noise microwave signal detection, microwave pulse shaping, and microwave noise reduction, among other applications.

In this sense, this thesis paved the way for numerous new applications in microwave and THz beam forming and signal processing. We believe that researchers in various areas of electromagnetism can greatly benefit from our findings and results.

REFERENCES

1 ENOCH, J. M. History of Mirrors Dating Back 8000 Years. **Optometry and Vision Science**, v. 83, n. 10, p. 775–781, oct 2006. ISSN 1040-5488. Available at: <https://journals.lww.com/00006324-200610000-00017>.

2 FRIED, M. N.; UNGURU, S. **Apollonius of Perga's Conica: text, context, subtext**. [*S.l.: s.n.*]: Brill, 2001. 162–164 p.

3 The Brithish Museum. **The nimrud lens/The layard lens**. Available at: <https://www.britishmuseum.org/collection/object/W_-90959>.

4 ENOCH, J. M. Remarkable lenses and eye units in statues from the Egyptian Old Kingdom (ca. 4500 years ago): properties, timeline, questions requiring resolution. *In*: GLASS, A. J. *et al.* (ed.). **Proceedings Volume 3749, 18th Congress of the International Commission for Optics**. [*S.l.: s.n.*], 1999. p. 224–225. Available at: <http://proceedings.spiedigitallibrary.org/proceeding.aspx?articleid=993618>.

5 SINES, G.; SAKELLARAKIS, Y. A. Lenses in Antiquity. **American Journal of Archaeology**, v. 91, n. 2, p. 191–196, apr 1987. ISSN 0002-9114. Available at: <https://www.journals.uchicago.edu/doi/10.2307/505216>.

6 NEWTON, I. A letter of Mr. Isaac Newton, Professor of the Mathematicks in the University of Cambridge; containing his new theory about light and colors: sent by the author to the publisher from Cambridge, Febr. 6. 1671/72; in order to be communicated to the R. Socie. **Philosophical Transactions of the Royal Society of London**, Cambridge University Press, v. 6, n. 80, p. 3075–3087, feb 1672. ISSN 0261-0523. Available at: <https://royalsocietypublishing.org/doi/10.1098/rstl.1671.0072>.

7 FARADAY, M. X. The Bakerian Lecture. - Experimental relations of gold (and other metals) to light. **Philosophical Transactions of the Royal Society of London**, v. 147, p. 145–181, dec 1857. ISSN 0261-0523. Available at: <https://royalsocietypublishing.org/doi/10.1098/rstl.1857.0011>.

8 MURRAY, W. A.; BARNES, W. L. Plasmonic Materials. **Advanced Materials**, v. 19, n. 22, p. 3771–3782, nov 2007. ISSN 09359648. Available at: <https://onlinelibrary.wiley.com/doi/10.1002/adma.200700678>.

9 BUTT, M.; KHONINA, S.; KAZANSKIY, N. Plasmonics: A Necessity in the Field of Sensing-A Review (Invited). **Fiber and Integrated Optics**, v. 40, n. 1, p. 14–47, jan 2021. ISSN 0146-8030. Available at: <https://www.tandfonline.com/doi/full/10.1080/01468030.2021.1902590>.

10 ZUEV, V. S.; ZUEVA, G. Y. Very slow surface plasmons: Theory and practice (Review). **Optics and Spectroscopy**, v. 107, n. 4, p. 614–628, oct 2009. ISSN 0030-400X. Available at: <http://link.springer.com/10.1134/S0030400X09100166>.

11 KRASAVIN, A. V.; ZAYATS, A. V. Silicon-based plasmonic waveguides. **Optics Express**, v. 18, n. 11, p. 11791, may 2010. ISSN 1094-4087. Available at: <https://opg.optica.org/oe/abstract.cfm?uri=oe-18-11-11791>.

12 FU, Y. *et al.* Structural colors: from natural to artificial systems. **WIREs Nanomedicine and Nanobiotechnology**, v. 8, n. 5, p. 758–775, sep 2016. ISSN 1939-5116. Available at: <https://onlinelibrary.wiley.com/doi/10.1002/wnan.1396>.

13 SUN, J.; BHUSHAN, B.; TONG, J. Structural coloration in nature. **RSC Advances**, v. 3, n. 35, p. 14862, 2013. ISSN 2046-2069. Available at: <http://xlink.rsc.org/?DOI=c3ra41096j>.

14 SIDDIQUE, R. H. *et al.* Colour formation on the wings of the butterfly Hypolimnas salmacis by scale stacking. **Scientific Reports**, v. 6, n. 1, p. 36204, nov 2016. ISSN 2045-2322. Available at: <https://www.nature.com/articles/srep36204>.

15 ZI, J. *et al.* Coloration strategies in peacock feathers. **Proceedings of the National Academy of Sciences**, v. 100, n. 22, p. 12576–12578, oct 2003. ISSN 0027-8424. Available at: <https://pnas.org/doi/full/10.1073/pnas.2133313100>.

16 KINOSHITA, S.; YOSHIOKA, S. Structural Colors in Nature: The Role of Regularity and Irregularity in the Structure. **ChemPhysChem**, v. 6, n. 8, p. 1442–1459, aug 2005. ISSN 1439-4235. Available at: <https://onlinelibrary.wiley.com/doi/10.1002/cphc.200500007>.

17 RAYLEIGH, L. XVII. On the maintenance of vibrations by forces of double frequency, and on the propagation of waves through a medium endowed with a periodic structure. **The London, Edinburgh, and Dublin Philosophical Magazine and Journal of Science**, v. 24, n. 147, p. 145–159, aug 1887. ISSN 1941-5982. Available at: <https://www.tandfonline.com/doi/full/10.1080/14786448708628074>.

18 YABLONOVITCH, E. Inhibited Spontaneous Emission in Solid-State Physics and Electronics. **Physical Review Letters**, v. 58, n. 20, p. 2059–2062, may 1987. ISSN 0031-9007. Available at: <https://link.aps.org/doi/10.1103/PhysRevLett.58.2059>.

19 RAMSAY, J. Microwave Antenna and Waveguide Techniques before 1900. **Proceedings of the IRE**, v. 46, n. 2, p. 405–415, feb 1958. ISSN 0096-8390. Available at: <http://ieeexplore.ieee.org/document/4065335/>.

20 ENGHETA, N.; ZIOLKOWSKI, R. W. **Metamaterials - Physics and Engineering Explorations**. 1. ed. New Jersey: John Wiley & Sons, 2006.

21 SHIVOLA, A. Metamaterials in electromagnetics. **Metamaterials**, v. 1, n. 1, p. 2–11, Mar 2007.

22 CALOZ, C. Metamaterial Dispersion Engineering Concepts and Applications. **Proceedings of the IEEE**, v. 99, n. 10, p. 1711–1719, oct 2011. ISSN 0018-9219. Available at: <http://ieeexplore.ieee.org/document/5773469/>.

23 BELOV, P. A. *et al.* Strong spatial dispersion in wire media in the very large wavelength limit. **Physical Review B**, v. 67, n. 11, p. 113103.1–113103.4, Mar 2003.

24 PODDUBNY, A. *et al.* Hyperbolic metamaterials. **Nature Photonics**, Springer Nature, v. 7, n. 12, p. 948–957, Nov 2013.

25 YIN, S.; GALIFFI, E.; ALÙ, A. Floquet metamaterials. **eLight**, v. 2, n. 1, p. 8, may 2022. ISSN 2662-8643. Available at: <https://elight.springeropen.com/articles/10.1186/s43593-022-00015-1>.

26 SHADRIVOV, I. V. *et al.* Electromagnetic wave analogue of an electronic diode. **New Journal of Physics**, v. 13, n. 3, p. 033025, mar 2011. ISSN 1367-2630. Available at: <https://iopscience.iop.org/article/10.1088/1367-2630/13/3/033025>.

27 MUN, J. *et al.* Electromagnetic chirality: from fundamentals to nontraditional chiroptical phenomena. **Light: Science & Applications**, v. 9, n. 1, p. 139, sep 2020. ISSN 2047-7538. Available at: <https://www.nature.com/articles/s41377-020-00367-8>.

28 KOCK, W. E. Metallic Delay Lenses. **Bell System Technical Journal**, v. 27, n. 1, p. 58–82, jan 1948. ISSN 00058580. Available at: <https://ieeexplore.ieee.org/document/6767538>.

29 BROWN, J. Artificial dielectrics having refractive indices less than unity. *In*: **Proceedings of the IEE - Part IV: Institution Monographs**. [*S.l.: s.n.*]: Institution of Engineering and Technology (IET), 1953. v. 100, n. 5, p. 51–62.

30 ROTMAN, W. Plasma simulation by artificial dielectrics and parallel-plate media. **IRE Transactions on Antennas and Propagation**, v. 10, n. 1, p. 82–95, jan 1962. ISSN 0096-1973. Available at: <http://ieeexplore.ieee.org/document/1137809/>.

31 THOMPSON, G. H. B. Unusual Waveguide Characteristics associated with the Apparent Negative Permeability obtainable in Ferrites. **Nature**, v. 175, n. 4469, p. 1135–1136, jun 1955. ISSN 0028-0836. Available at: <https://www.nature.com/articles/1751135b0>.

32 PENDRY, J. *et al.* Magnetism from conductors and enhanced nonlinear phenomena. **IEEE Transactions on Microwave Theory and Techniques**, v. 47, n. 11, p. 2075–2084, 1999. ISSN 00189480. Available at: <http://ieeexplore.ieee.org/document/798002/>.

33 VESELAGO, V. G. The electrodynamics of substances with simultaneously negative values of ϵ AND μ. **Soviet Physics Uspekhi**, v. 10, n. 4, p. 509–514, apr 1968. ISSN 0038-5670. Available at: <https://iopscience.iop.org/article/10.1070/PU1968v010n04ABEH003699>.

34 PENDRY, J. B. Negative Refraction Makes a Perfect Lens. **Physical Review Letters**, v. 85, n. 18, p. 3966–3969, oct 2000. ISSN 0031-9007. Available at: <https://link.aps.org/doi/10.1103/PhysRevLett.85.3966>.

35 PENDRY, J. B. *et al.* Extremely Low Frequency Plasmons in Metallic Mesostructures. **Physical Review Letters**, v. 76, n. 25, p. 4773–4776, jun 1996. ISSN 0031-9007. Available at: <https://link.aps.org/doi/10.1103/PhysRevLett.76.4773>.

36 SMITH, D. R. *et al.* Composite Medium with Simultaneously Negative Permeability and Permittivity. **Physical Review Letters**, v. 84, n. 18, p. 4184–4187, may 2000. ISSN 0031-9007. Available at: <https://link.aps.org/doi/10.1103/PhysRevLett.84.4184>.

37 SMITH, D. R.; KROLL, N. Negative Refractive Index in Left-Handed Materials. **Physical Review Letters**, v. 85, n. 14, p. 2933–2936, oct 2000. ISSN 0031-9007. Available at: <https://link.aps.org/doi/10.1103/PhysRevLett.85.2933>.

38 SMITH, D. R. *et al.* Direct calculation of permeability and permittivity for a left-handed metamaterial. **Applied Physics Letters**, v. 77, n. 14, p. 2246–2248, oct 2000. ISSN 0003-6951. Available at: <https://pubs.aip.org/aip/apl/article/77/14/2246-2248/113225>.

39 SHELBY, R. A.; SMITH, D. R.; SCHULTZ, S. Experimental Verification of a Negative Index of Refraction. **Science**, v. 292, n. 5514, p. 77–79, apr 2001. ISSN 0036-8075. Available at: <https://www.science.org/doi/10.1126/science.1058847>.

40 ERGIN, T. *et al.* Three-dimensional invisibility cloak at optical wavelengths. **Science Magazine**, v. 328, n. 5976, p. 337–339, Apr 2010.

41 WOOD, B. Metamaterials and invisibility. **Comptes Rendus Physique**, v. 10, n. 5, p. 379–390, Jun 2009.

42 TEIXEIRA, F. L. FDTD/FETD methods: A review on some recent advances and selected applications. **J. Microwaved Optoelectron. Electromagn. Appl.**, v. 6, n. 1, p. 83–95, 2007.

43 LINDELL, I. V.; SIHVOLA, A. H. Perfect Electromagnetic Conductor. **Journal of Electromagnetic Waves and Applications**, v. 19, n. 7, p. 861–869, jan 2005. ISSN 0920-5071. Available at: <https://www.tandfonline.com/doi/full/10.1163/156939305775468741>.

44 TEIXEIRA, F. L.; ODABASI, H.; WARNICK, K. F. Anisotropic metamaterial blueprints for cladding control of waveguide modes. **Journal of the Optical Society of America B**, v. 27, n. 8, p. 1603, aug 2010. ISSN 0740-3224. Available at: <https://www.osapublishing.org/abstract.cfm?URI=josab-27-8-1603>.

45 ODABASI, H.; TEIXEIRA, F. L. Electric-field-coupled resonators as metamaterial loadings for waveguide miniaturization. **Journal of Applied Physics**, v. 114, n. 21, dec 2013. ISSN 0021-8979. Available at: <https://pubs.aip.org/jap/article/114/21/214901/308871/Electric-field-coupled-resonators-as-metamaterial>.

46 PU, M. *et al.* Design principles for infrared wide-angle perfect absorber based on plasmonic structure. **Optics Express**, v. 19, n. 18, p. 17413, aug 2011. ISSN 1094-4087. Available at: <https://opg.optica.org/oe/abstract.cfm?uri=oe-19-18-17413>.

47 DONDERICI, B.; TEIXEIRA, F. Metamaterial Blueprints for Reflectionless Waveguide Bends. **IEEE Microwave and Wireless Components Letters**, v. 18, n. 4, p. 233–235, apr 2008. ISSN 1531-1309. Available at: <http://ieeexplore.ieee.org/document/4469930/>.

48 MOTA, A. F. *et al.* Dispersion Management With Microwave Chirped Pulses in Metamaterials in the Negative Refraction Regime. **IEEE Antennas and Wireless Propagation Letters**, v. 14, p. 1377–1380, 2015. ISSN 1536-1225. Available at: <http://ieeexplore.ieee.org/document/7047215/>.

49 PODDUBNY, A. N.; BELOV, P. A.; KIVSHAR, Y. S. Purcell effect in wire metamaterials. **Physical Review B**, American Physical Society (APS), v. 87, n. 3, p. 035136.1–035136.8, Jan 2013.

50 MOTA, A. *et al.* 2D semi-analytical model for optimizing the radiation emission of quantum emitters embedded in a bounded nano-patterned hyperbolic metamaterial. *In*: **2018 12th International Congress on Artificial Materials for Novel Wave Phenomena, METAMATERIALS 2018**. [*S.l.: s.n.*], 2018. ISBN 9781538647028.

51 KOSULNIKOV, S. *et al.* Wire-medium hyperlens for enhancing radiation from subwavelength dipole sources. **IEEE Transactions on Antennas and Propagation**, Institute of Electrical and Electronics Engineers (IEEE), v. 63, n. 11, p. 4848–4856, nov 2015.

52 Jing Jing Yang; Ming Huang; Jun Sun. Double Negative Metamaterial Sensor Based on Microring Resonator. **IEEE Sensors Journal**, v. 11, n. 10, p. 2254–2259, oct 2011. ISSN 1530-437X. Available at: <http://ieeexplore.ieee.org/document/5739504/>.

53 ENOCH, S. *et al.* A Metamaterial for Directive Emission. **Physical Review Letters**, v. 89, n. 21, p. 213902, nov 2002. ISSN 0031-9007. Available at: <https://link.aps.org/doi/10.1103/PhysRevLett.89.213902>.

54 CUMMER, S. A.; CHRISTENSEN, J.; ALÙ, A. Controlling sound with acoustic metamaterials. **Nature Reviews Materials**, v. 1, n. 3, p. 16001, mar 2016. ISSN 2058-8437. Available at: <http://www.nature.com/articles/natrevmats20161>.

55 LI, Y. *et al.* Transforming heat transfer with thermal metamaterials and devices. **Nature Reviews Materials**, v. 6, n. 6, p. 488–507, mar 2021. ISSN 2058-8437. Available at: <https://www.nature.com/articles/s41578-021-00283-2>.

56 GLYBOVSKI, S. B. *et al.* Metasurfaces: From microwaves to visible. **Physics Reports**, v. 634, p. 1–72, may 2016. ISSN 03701573. Available at: <http://linkinghub.elsevier.com/retrieve/pii/S0370157316300618>.

57 LUO, X. Engineering Optics 2.0: A Revolution in Optical Materials, Devices, and Systems. **ACS Photonics**, v. 5, n. 12, p. 4724–4738, dec 2018. ISSN 2330-4022. Available at: <https://pubs.acs.org/doi/10.1021/acsphotonics.8b01036>.

58 LIANG, H. *et al.* High performance metalenses: numerical aperture, aberrations, chromaticity, and trade-offs. **Optica**, v. 6, n. 12, p. 1461, dec 2019. ISSN 2334-2536. Available at: <https://www.osapublishing.org/abstract.cfm?URI=optica-6-12-1461>.

59 PADILLA, W. J.; AVERITT, R. D. Imaging with metamaterials. **Nature Reviews Physics**, v. 4, n. 2, p. 85–100, dec 2021. ISSN 2522-5820. Available at: <https://www.nature.com/articles/s42254-021-00394-3>.

60 WEN, D. *et al.* Light field on a chip: Metasurface-based multicolor holograms. **Advanced Photonics**, v. 3, n. 2, p. 1–14, 2021. ISSN 25775421.

61 DEY, S.; DEY, S. Conformal Multifunction FSS with Enhanced Capacitance Loading for High Angle Stable Stopband Filtering and Microwave Absorption. **IEEE Transactions on Electromagnetic Compatibility**, IEEE, v. 64, n. 2, p. 315–326, 2022. ISSN 1558187X.

62 MUNK, B. A. **Frequency selective surfaces: theory and design**. [*S.l.: s.n.*]: John Wiley & Sons, 2005.

63 YIN, X. *et al.* Observation of topologically enabled unidirectional guided resonances. **Nature**, v. 580, n. 7804, p. 467–471, apr 2020. ISSN 0028-0836. Available at: <https://www.nature.com/articles/s41586-020-2181-4>.

64 YANG, Y. *et al.* All-dielectric metasurface analogue of electromagnetically induced transparency. **Nature Communications**, v. 5, n. 1, p. 5753, dec 2014. ISSN 2041-1723. Available at: <https://www.nature.com/articles/ncomms6753>.

65 QIN, J. *et al.* Metasurface Micro/Nano-Optical Sensors: Principles and Applications. **ACS Nano**, v. 16, n. 8, p. 11598–11618, aug 2022. ISSN 1936-0851. Available at: <https://pubs.acs.org/doi/10.1021/acsnano.2c03310>.

66 TRIPATHI, A. *et al.* Lasing Action from Anapole Metasurfaces. **Nano Letters**, v. 21, n. 15, p. 6563–6568, aug 2021. ISSN 1530-6984. Available at: <https://pubs.acs.org/doi/10.1021/acs.nanolett.1c01857>.

67 LI, W. *et al.* A Compact Low-Profile Reconfigurable Metasurface Antenna With Polarization and Pattern Diversities. **IEEE Antennas and Wireless Propagation Letters**, v. 20, n. 7, p. 1170–1174, jul 2021. ISSN 1536-1225. Available at: <https://ieeexplore.ieee.org/document/9410345/>.

68 YOO, I.; SMITH, D. R. Sub-6-GHz Uplink Massive MIMO System Using Holographic Beamforming Metasurfaces: A Conceptual Development. **IEEE Wireless Communications Letters**, v. 12, n. 4, p. 644–648, apr 2023. ISSN 2162-2337. Available at: <https://ieeexplore.ieee.org/document/10018421/>.

69 CHEN, W. T. *et al.* Generation of wavelength-independent subwavelength Bessel beams using metasurfaces. **Light: Science & Applications**, v. 6, n. 5, p. e16259–e16259, may 2017. ISSN 2047-7538. Available at: <http://www.nature.com/articles/lsa2016259>.

70 ZHOU, J. *et al.* Metamaterials and Metasurfaces for Wireless Power Transfer and Energy Harvesting. **Proceedings of the IEEE**, v. 110, n. 1, p. 31–55, jan 2022. ISSN 0018-9219. Available at: <https://ieeexplore.ieee.org/document/9627147/>.

71 GE, J. *et al.* Ultra-Broadband, Tunable, and Transparent Microwave Meta-Absorber Using ITO and Water Substrate. **Advanced Optical Materials**, v. 11, n. 10, may 2023. ISSN 2195-1071. Available at: <https://onlinelibrary.wiley.com/doi/10.1002/adom.202202873>.

72 KIM, J. *et al.* Photonic Encryption Platform via Dual-Band Vectorial Metaholograms in the Ultraviolet and Visible. **ACS Nano**, v. 16, n. 3, p. 3546–3553, mar 2022. ISSN 1936-0851. Available at: <https://pubs.acs.org/doi/10.1021/acsnano.1c10100>.

73 LUO, X. *et al.* Metasurface-enabled on-chip multiplexed diffractive neural networks in the visible. **Light: Science & Applications**, v. 11, n. 1, p. 158, may 2022. ISSN 2047-7538. Available at: <https://www.nature.com/articles/s41377-022-00844-2>.

74 LIU, Q. *et al.* Platform-Tolerant Nested-Slot RFID Tag Antenna Based on Jigsaw-Shaped Metasurface. **IEEE Antennas and Wireless Propagation Letters**, v. 21, n. 5, p. 943–947, may 2022. ISSN 1536-1225. Available at: <https://ieeexplore.ieee.org/document/9716871/>.

75 ZHAO, D. *et al.* Recent advances in ultraviolet nanophotonics: from plasmonics and metamaterials to metasurfaces. **Nanophotonics**, v. 10, n. 9, p. 2283–2308, jul 2021. ISSN 2192-8614. Available at: <https://www.degruyter.com/document/doi/10.1515/nanoph-2021-0083/html>.

76 WOODS, J. S. *et al.* Switchable X-Ray Orbital Angular Momentum from an Artificial Spin Ice. **Physical Review Letters**, v. 126, n. 11, p. 117201, mar 2021. ISSN 0031-9007. Available at: <https://link.aps.org/doi/10.1103/PhysRevLett.126.117201>.

77 YU, N. *et al.* Light Propagation with Phase Discontinuities: Generalized Laws of Reflection and Refraction. **Science**, v. 334, n. 6054, p. 333–337, oct 2011. ISSN 0036-8075. Available at: <https://www.science.org/doi/10.1126/science.1210713>.

78 SHANG, G. *et al.* A non-interleaved bidirectional Janus metasurface with full-space scattering channels. **Nanophotonics**, v. 11, n. 16, p. 3729–3739, 2022. ISSN 21928614.

79 CHEN, C. *et al.* Metasurfaces with Planar Chiral Meta-Atoms for Spin Light Manipulation. **Nano Letters**, v. 21, n. 4, p. 1815–1821, feb 2021. ISSN 1530-6984. Available at: <https://pubs.acs.org/doi/10.1021/acs.nanolett.0c04902>.

80 JIN, L. *et al.* Noninterleaved Metasurface for (2 6 -1) Spin- and Wavelength-Encoded Holograms. **Nano Letters**, v. 18, n. 12, p. 8016–8024, 2018. ISSN 15306992.

81 MARTINS, A. *et al.* Broadband c-Si metasurfaces with polarization control at visible wavelengths: applications to 3D stereoscopic holography. **Optics Express**, v. 26, n. 23, p. 30740, nov 2018. ISSN 1094-4087. Available at: <https://www.osapublishing.org/abstract.cfm?URI=oe-26-23-30740>.

82 WAN, S. *et al.* Angular-Multiplexing Metasurface: Building Up Independent-Encoded Amplitude/Phase Dictionary for Angular Illumination. **Advanced Optical Materials**, v. 9, n. 22, p. 1–7, 2021. ISSN 21951071.

83 ZHOU, H. *et al.* Ultra-dense moving cascaded metasurface holography by using a physics-driven neural network. **Optics Express**, v. 30, n. 14, p. 24285, 2022. ISSN 10944087.

84 KO, B. *et al.* Tunable metasurfaces via the humidity responsive swelling of single-step imprinted polyvinyl alcohol nanostructures. **Nature Communications**, Springer US, v. 13, n. 1, 2022. ISSN 20411723.

85 REN, H. *et al.* Metasurface orbital angular momentum holography. **Nature Communications**, Springer US, v. 10, n. 1, p. 1–8, 2019. ISSN 20411723. Available at: <http://dx.doi.org/10.1038/s41467-019-11030-1>.

86 LI, X. *et al.* Independent Light Field Manipulation in Diffraction Orders of Metasurface Holography. **Laser and Photonics Reviews**, v. 16, n. 8, p. 1–7, 2022. ISSN 18638899.

87 YU, N.; CAPASSO, F. Flat optics with designer metasurfaces. **Nature Materials**, v. 13, n. 2, p. 139–150, feb 2014. ISSN 1476-1122. Available at: <http://www.nature.com/articles/nmat3839>.

88 LI, X. *et al.* Dispersion engineering in metamaterials and metasurfaces. **Journal of Physics D: Applied Physics**, v. 51, n. 5, p. 054002, feb 2018. ISSN 0022-3727. Available at: <http://stacks.iop.org/0022-3727/51/i=5/a=054002?key=crossref.93890548b02e9b5bff999d8466c36325>.

89 SHALTOUT, A. M.; SHALAEV, V. M.; BRONGERSMA, M. L. Spatiotemporal light control with active metasurfaces. **Science**, v. 364, n. 6441, may 2019. ISSN 0036-8075. Available at: <https://www.science.org/doi/10.1126/science.aat3100>.

90 DECKER, M. *et al.* High-Efficiency Dielectric Huygens' Surfaces. **Advanced Optical Materials**, v. 3, n. 6, p. 813–820, jun 2015. ISSN 21951071. Available at: <https://onlinelibrary.wiley.com/doi/10.1002/adom.201400584>.

91 SIEVENPIPER, D. *et al.* Two-dimensional beam steering using an electrically tunable impedance surface. **IEEE Transactions on Antennas and Propagation**, v. 51, n. 10, p. 2713–2722, oct 2003. ISSN 0018-926X. Available at: <http://ieeexplore.ieee.org/document/1236089/>.

92 BROWN, B. R.; LOHMANN, A. W. Complex Spatial Filtering with Binary Masks. **Applied Optics**, v. 5, n. 6, p. 967, jun 1966. ISSN 0003-6935. Available at: <https://opg.optica.org/abstract.cfm?URI=ao-5-6-967>.

93 MARTINS, A. *et al.* Highly efficient holograms based on c-Si metasurfaces in the visible range. **Optics Express**, v. 26, n. 8, p. 9573, apr 2018. ISSN 1094-4087. Available at: <https://www.osapublishing.org/abstract.cfm?URI=oe-26-8-9573>.

94 GOODMAN, J. W. **Introduction to Fourier Optics McGraw-Hill Series in Electrical and Computer Engineering**. [*S.l.: s.n.*], 1996.

95 SO, S. *et al.* Revisiting the Design Strategies for Metasurfaces: Fundamental Physics, Optimization, and Beyond. **Advanced Materials**, apr 2023. ISSN 0935-9648. Available at: <https://onlinelibrary.wiley.com/doi/10.1002/adma.202206399>.

96 SHI, Y. *et al.* Augmented Reality Enabled by OnâChip MetaâHolography Multiplexing. **Laser & Photonics Reviews**, v. 16, n. 6, p. 2100638, jun 2022. ISSN 1863-8880. Available at: <https://onlinelibrary.wiley.com/doi/10.1002/lpor.202100638>.

97 CHRISTIANSEN, R. E.; SIGMUND, O. Inverse design in photonics by topology optimization: tutorial. **Journal of the Optical Society of America B**, v. 38, n. 2, p. 496, feb 2021. ISSN 0740-3224. Available at: <https://opg.optica.org/abstract.cfm?URI=josab-38-2-496>.

98 GUO, X. *et al.* Full-Color Holographic Display and Encryption with Full-Polarization Degree of Freedom. **Advanced Materials**, v. 34, n. 3, 2022. ISSN 15214095.

99 SUN, S. *et al.* Gradient-index meta-surfaces as a bridge linking propagating waves and surface waves. **Nature Materials**, v. 11, n. 5, p. 426–431, may 2012. ISSN 1476-1122. Available at: <https://www.nature.com/articles/nmat3292>.

100 LIU, L. *et al.* Broadband Metasurfaces with Simultaneous Control of Phase and Amplitude. **Advanced Materials**, v. 26, n. 29, p. 5031–5036, aug 2014. ISSN 09359648. Available at: <https://onlinelibrary.wiley.com/doi/10.1002/adma.201401484>.

101 NI, X.; KILDISHEV, A. V.; SHALAEV, V. M. Metasurface holograms for visible light. **Nature Communications**, v. 4, n. 1, p. 2807, nov 2013. ISSN 2041-1723. Available at: <https://www.nature.com/articles/ncomms3807>.

102 PFEIFFER, C.; GRBIC, A. Metamaterial Huygens' Surfaces: Tailoring Wave Fronts with Reflectionless Sheets. **Physical Review Letters**, v. 110, n. 19, p. 197401, may 2013. ISSN 0031-9007. Available at: <https://link.aps.org/doi/10.1103/PhysRevLett.110.197401>.

103 CHEN, M. *et al.* Huygens' metasurfaces from microwaves to optics: a review. **Nanophotonics**, v. 7, n. 6, p. 1207–1231, jun 2018. ISSN 2192-8614. Available at: <https://www.degruyter.com/document/doi/10.1515/nanoph-2017-0117/html>.

104 CHONG, K. E. *et al.* Efficient Polarization-Insensitive Complex Wavefront Control Using Huygens' Metasurfaces Based on Dielectric Resonant Meta-atoms. **ACS Photonics**, v. 3, n. 4, p. 514–519, apr 2016. ISSN 2330-4022. Available at: <https://pubs.acs.org/doi/10.1021/acsphotonics.5b00678>.

105 GIGLI, C. *et al.* Fundamental Limitations of Huygens' Metasurfaces for Optical Beam Shaping. **Laser Photonics Reviews**, v. 15, n. 8, p. 2000448, aug 2021. ISSN 1863-8880. Available at: <https://onlinelibrary.wiley.com/doi/10.1002/lpor.202000448>.

106 GENEVET, P. *et al.* Recent advances in planar optics: from plasmonic to dielectric metasurfaces. **Optica**, v. 4, n. 1, p. 139, jan 2017. ISSN 2334-2536. Available at: <https://www.osapublishing.org/abstract.cfm?URI=optica-4-1-139>.

107 SHI, H. *et al.* Beam manipulating by metallic nano-slits with variant widths. **Optics Express**, v. 13, n. 18, p. 6815, 2005. ISSN 1094-4087. Available at: <https://opg.optica.org/oe/abstract.cfm?uri=oe-13-18-6815>.

108 ZHUO, W. *et al.* A review of high-efficiency Pancharatnam-Berry metasurfaces. **Terahertz Science and Technology**, v. 13, n. 3, p. 73–89, sep 2020. ISSN 1941-7411. Available at: <https://tst.edpsciences.org/10.1051/tst/2020133073>.

109 ZHANG, F. *et al.* Extreme-Angle Silicon Infrared Optics Enabled by Streamlined Surfaces. **Advanced Materials**, v. 33, n. 11, p. 2008157, mar 2021. ISSN 0935-9648. Available at: <https://onlinelibrary.wiley.com/doi/10.1002/adma.202008157>.

110 LUO, X. *et al.* Recent advances of wide-angle metalenses: principle, design, and applications. **Nanophotonics**, v. 11, n. 1, p. 1–20, dec 2021. ISSN 2192-8614. Available at: <https://www.degruyter.com/document/doi/10.1515/nanoph-2021-0583/html>.

111 PU, M. *et al.* Catenary optics for achromatic generation of perfect optical angular momentum. **Science Advances**, v. 1, n. 9, oct 2015. ISSN 2375-2548. Available at: <https://www.science.org/doi/10.1126/sciadv.1500396>.

112 SHI, R. *et al.* Terahertz high-resolution wideband focusing metasurface based on catenary structure. **Optics Communications**, v. 448, p. 124–129, oct 2019. ISSN 00304018. Available at: <https://linkinghub.elsevier.com/retrieve/pii/S0030401819303323>.

113 GRBIC, A.; MACI, S. EM Metasurfaces [Guest Editorial]. **IEEE Antennas and Propagation Magazine**, v. 64, n. 4, p. 16–22, aug 2022. ISSN 1045-9243. Available at: <https://ieeexplore.ieee.org/document/9861303/>.

114   SHEN, Z. *et al.* Liquid crystal integrated metalens with tunable chromatic aberration. **Advanced Photonics**, v. 2, n. 03, p. 1, may 2020. ISSN 2577-5421. Available at: <https://www.spiedigitallibrary.org/journals/advanced-photonics/volume-2/issue-03/036002/Liquid-crystal-integrated-metalens-with-tunable-chromatic-aberration/10.1117/1.AP.2.3.036002.full>.

115   CHEN, X.; FAN, W. Tunable Bound States in the Continuum in All-Dielectric Terahertz Metasurfaces. **Nanomaterials**, v. 10, n. 4, p. 623, mar 2020. ISSN 2079-4991. Available at: <https://www.mdpi.com/2079-4991/10/4/623>.

116   WU, J. *et al.* Liquid crystal programmable metasurface for terahertz beam steering. **Applied Physics Letters**, v. 116, n. 13, p. 131104, mar 2020. ISSN 0003-6951. Available at: <http://aip.scitation.org/doi/10.1063/1.5144858>.

117   SHEN, Z. *et al.* Liquid crystal tunable terahertz lens with spin-selected focusing property. **Optics Express**, v. 27, n. 6, p. 8800, mar 2019. ISSN 1094-4087. Available at: <https://opg.optica.org/abstract.cfm?URI=oe-27-6-8800>.

118   SONG, S. *et al.* Actively Tunable Structural Color Rendering with Tensile Substrate. **Advanced Optical Materials**, v. 5, n. 9, p. 1600829, may 2017. ISSN 21951071. Available at: <https://onlinelibrary.wiley.com/doi/10.1002/adom.201600829>.

119   PARK, J. *et al.* All-solid-state spatial light modulator with independent phase and amplitude control for three-dimensional LiDAR applications. **Nature Nanotechnology**, v. 16, n. 1, p. 69–76, jan 2021. ISSN 1748-3387. Available at: <https://www.nature.com/articles/s41565-020-00787-y>.

120   WANG, H. *et al.* Metasurface with dynamic chiral meta-atoms for spin multiplexing hologram and low observable reflection. **PhotoniX**, v. 3, n. 1, p. 10, dec 2022. ISSN 2662-1991. Available at: <https://photonix.springeropen.com/articles/10.1186/s43074-022-00057-1>.

121   ZHANG, X. G. *et al.* Optoelectronic Metasurface for Free-Space Optical-Microwave Interactions. **ACS Applied Materials & Interfaces**, v. 15, n. 18, p. 22744–22751, may 2023. ISSN 1944-8244. Available at: <https://pubs.acs.org/doi/10.1021/acsami.3c02290>.

122   ZHANG, X. G. *et al.* An optically driven digital metasurface for programming electromagnetic functions. **Nature Electronics**, v. 3, n. 3, p. 165–171, mar 2020. ISSN 2520-1131. Available at: <https://www.nature.com/articles/s41928-020-0380-5>.

123   SHIH, Y.-H. *et al.* Optically Tunable Terahertz Metasurfaces Using Liquid Crystal Cells Coated with Photoalignment Layers. **Crystals**, v. 11, n. 9, p. 1100, sep 2021. ISSN 2073-4352. Available at: <https://www.mdpi.com/2073-4352/11/9/1100>.

124   LI, H. *et al.* Terahertz electrically controlled nematic liquid crystal lens. **Infrared Physics & Technology**, v. 54, n. 5, p. 439–444, sep 2011. ISSN 13504495. Available at: <https://linkinghub.elsevier.com/retrieve/pii/S1350449511000764>.

125   BUCHNEV, O. *et al.* Metasurface-Based Optical Liquid Crystal Cell as an Ultrathin Spatial Phase Modulator for THz Applications. **ACS Photonics**, v. 7, n. 11, p. 3199–3206, nov 2020. ISSN 2330-4022. Available at: <https://pubs.acs.org/doi/10.1021/acsphotonics.0c01263>.

126 LIU, S. *et al.* Terahertz liquid crystal programmable metasurface based on resonance switching. **Optics Letters**, v. 47, n. 7, p. 1891, apr 2022. ISSN 0146-9592. Available at: <https://opg.optica.org/abstract.cfm?URI=ol-47-7-1891>.

127 XU, S.-T. *et al.* Terahertz resonance switch induced by the polarization conversion of liquid crystal in compound metasurface. **Optics Letters**, v. 44, n. 10, p. 2450, may 2019. ISSN 0146-9592. Available at: <https://opg.optica.org/abstract.cfm?URI=ol-44-10-2450>.

128 MIAO, Z. *et al.* Widely Tunable Terahertz Phase Modulation with Gate-Controlled Graphene Metasurfaces. **Physical Review X**, v. 5, n. 4, p. 041027, nov 2015. ISSN 2160-3308. Available at: <https://link.aps.org/doi/10.1103/PhysRevX.5.041027>.

129 KAKENOV, N. *et al.* Graphene based terahertz phase modulators. **2D Materials**, v. 5, n. 3, p. 035018, may 2018. ISSN 2053-1583. Available at: <https://iopscience.iop.org/article/10.1088/2053-1583/aabfaa>.

130 CHENG, Y.; ZHAO, H.; LI, C. Broadband tunable terahertz metasurface absorber based on complementary-wheel-shaped graphene. **Optical Materials**, v. 109, p. 110369, nov 2020. ISSN 09253467. Available at: <https://linkinghub.elsevier.com/retrieve/pii/S0925346720307102>.

131 YAO, W. *et al.* Spectrally and Spatially Tunable Terahertz Metasurface Lens Based on Graphene Surface Plasmons. **IEEE Photonics Journal**, v. 10, n. 4, p. 1–8, aug 2018. ISSN 1943-0655. Available at: <https://ieeexplore.ieee.org/document/8408798/>.

132 ZHENG, S.-q. *et al.* Dynamically Tunable of Terahertz Waves Based on Graphene Metasurface. *In*: **2020 International Conference on Microwave and Millimeter Wave Technology (ICMMT)**. IEEE, 2020. p. 1–3. ISBN 978-1-7281-5733-7. Available at: <https://ieeexplore.ieee.org/document/9386786/>.

133 JUNG, H. *et al.* Reconfigurable Molecularization of Terahertz Meta-Atoms. **ACS Photonics**, v. 9, n. 5, p. 1814–1820, may 2022. ISSN 2330-4022. Available at: <https://pubs.acs.org/doi/10.1021/acsphotonics.2c00397>.

134 ROUHI, K. *et al.* Multi-Channel Near-Field Terahertz Communications Using Reprogrammable Graphene-Based Digital Metasurface. **Journal of Lightwave Technology**, v. 39, n. 21, p. 6893–6907, nov 2021. ISSN 0733-8724. Available at: <https://ieeexplore.ieee.org/document/9516921/>.

135 CHEN, X. *et al.* Reconfigurable and Nonvolatile Terahertz Metadevices Based on a Phase-Change Material. **ACS Photonics**, v. 9, n. 5, p. 1638–1646, may 2022. ISSN 2330-4022. Available at: <https://pubs.acs.org/doi/10.1021/acsphotonics.1c01977>.

136 JEONG, Y.; BAHK, Y.; KIM, D. Dynamic Terahertz Plasmonics Enabled by Phase-Change Materials. **Advanced Optical Materials**, v. 8, n. 3, p. 1900548, feb 2020. ISSN 2195-1071. Available at: <https://onlinelibrary.wiley.com/doi/10.1002/adom.201900548>.

137 CHEN, J. *et al.* A Thermally Switchable Bifunctional Metasurface for Broadband Polarization Conversion and Absorption Based on Phase-Change Material. **Advanced Photonics Research**, v. 3, n. 9, p. 2100369, sep 2022. ISSN 2699-9293. Available at: <https://onlinelibrary.wiley.com/doi/10.1002/adpr.202100369>.

138 ZHAN, A. *et al.* Metasurface Freeform Nanophotonics. **Scientific Reports**, v. 7, n. 1, p. 1673, dec 2017. ISSN 2045-2322. Available at: <http://www.nature.com/articles/s41598-017-01908-9>.

139 HAN, Z. *et al.* MEMS-actuated metasurface Alvarez lens. **Microsystems & Nanoengineering**, v. 6, n. 1, p. 79, dec 2020. ISSN 2055-7434. Available at: <https://www.nature.com/articles/s41378-020-00190-6>.

140 BUSCH, S. F. *et al.* Extending the Alvarez-Lens Concept to Arbitrary Optical Devices: Tunable Gratings, Lenses, and Spiral Phase Plates. **IEEE Transactions on Terahertz Science and Technology**, v. 7, n. 3, p. 320–325, may 2017. ISSN 2156-342X. Available at: <http://ieeexplore.ieee.org/document/7903746/>.

141 CHE, X. *et al.* Generalized phase profile design method for tunable devices using bilayer metasurfaces. **Optics Express**, v. 29, n. 26, p. 44214, dec 2021. ISSN 1094-4087. Available at: <https://opg.optica.org/abstract.cfm?URI=oe-29-26-44214>.

142 KEISER, G. **Optical Fiber Communications**. 4. ed. [*S.l.: s.n.*]: Mc-Graw Hill, 2000.

143 YEH, P.; YARIV, A.; MAROM, E. Theory of Bragg fiber. **Journal of the Optical Society of America**, v. 68, n. 9, p. 1196, sep 1978. ISSN 0030-3941. Available at: <https://www.osapublishing.org/abstract.cfm?URI=josa-68-9-1196>.

144 ENGENESS, T. *et al.* Dispersion tailoring and compensation by modal interactions in OmniGuide fibers. **Optics Express**, v. 11, n. 10, p. 1175, 2003. ISSN 1094-4087.

145 WU, T.-L.; CHAO, C.-H. A novel ultraflattened dispersion photonic Crystal fiber. **IEEE Photonics Technology Letters**, v. 17, n. 1, p. 67–69, jan 2005. ISSN 1041-1135. Available at: <http://ieeexplore.ieee.org/document/1372585/>.

146 SHEN, L. *et al.* Design and optimization of photonic crystal fibers for broad-band dispersion compensation. **IEEE Photonics Technology Letters**, v. 15, n. 4, p. 540–542, apr 2003. ISSN 1041-1135. Available at: <https://ieeexplore.ieee.org/document/1190196/>.

147 RENVERSEZ, G.; KUHLMEY, B.; MCPHEDRAN, R. Dispersion management with microstructured optical fibers: ultraflattened chromatic dispersion with low losses. **Optics Letters**, v. 28, n. 12, p. 989, jun 2003. ISSN 0146-9592. Available at: <https://opg.optica.org/abstract.cfm?URI=ol-28-12-989>.

148 ASPLUND, M. C.; JOHNSON, J. A.; PATTERSON, J. E. The 2018 Nobel Prize in Physics: optical tweezers and chirped pulse amplification. **Analytical and Bioanalytical Chemistry**, v. 411, n. 20, p. 5001–5005, aug 2019. ISSN 1618-2642. Available at: <http://link.springer.com/10.1007/s00216-019-01913-z>.

149 TANAKA, M. *et al.* Control of slow-light effect in a metamaterial-loaded Si waveguide. **Optics Express**, v. 28, n. 16, p. 23198, aug 2020. ISSN 1094-4087. Available at: <https://opg.optica.org/abstract.cfm?URI=oe-28-16-23198>.

150 WANG, Y. *et al.* Outstanding slow-light effect for graphene metasurface in terahertz. **Results in Physics**, v. 23, p. 104002, apr 2021. ISSN 22113797. Available at: <https://linkinghub.elsevier.com/retrieve/pii/S2211379721001716>.

151 GARCIA-VIDAL, F. J. *et al.* Spoof surface plasmon photonics. **Reviews of Modern Physics**, v. 94, n. 2, 2022. ISSN 15390756.

152 HUANG, L. *et al.* Full-Color Metaoptical Imaging in Visible Light. **Advanced Photonics Research**, v. 3, n. 5, p. 2100265, 2022. ISSN 2699-9293.

153 FENG, W. *et al.* RGB Achromatic Metalens Doublet for Digital Imaging. **Nano Letters**, v. 22, n. 10, p. 3969–3975, 2022. ISSN 15306992.

154 LU, X. *et al.* Broadband achromatic metasurfaces for sub-diffraction focusing in the visible. **Optics Express**, v. 29, n. 4, p. 5947, 2021. ISSN 10944087.

155 AZAÑA, J.; MURIEL, M. A. Temporal Talbot effect in fiber gratings and its applications. **Applied Optics**, v. 38, n. 32, p. 6700, nov 1999. ISSN 0003-6935. Available at: <https://opg.optica.org/abstract.cfm?URI=ao-38-32-6700>.

156 MARAM, R. *et al.* Noiseless intensity amplification of repetitive signals by coherent addition using the temporal Talbot effect. **Nature Communications**, v. 5, n. 1, p. 5163, oct 2014. ISSN 2041-1723. Available at: <https://www.nature.com/articles/ncomms6163>.

157 FERNÁNDEZ-POUSA, C. R.; MARAM, R.; AZAÑA, J. CW-to-pulse conversion using temporal Talbot array illuminators. **Optics Letters**, v. 42, n. 13, p. 2427, jul 2017. ISSN 0146-9592. Available at: <https://opg.optica.org/abstract.cfm?URI=ol-42-13-2427>.

158 FETTWEIS, G.; ALAMOUTI, S. 5G: Personal mobile internet beyond what cellular did to telephony. **IEEE Communications Magazine**, v. 52, n. 2, p. 140–145, 2014. ISSN 01636804.

159 ANDREWS, J. G. *et al.* What will 5G be? **IEEE Journal on Selected Areas in Communications**, v. 32, n. 6, p. 1065–1082, jun 2014. ISSN 0733-8716. Available at: <http://ieeexplore.ieee.org/lpdocs/epic03/wrapper.htm?arnumber=6824752>.

160 GE, X. *et al.* 5G ultra-dense cellular networks. **IEEE Wireless Communications**, v. 23, n. 1, p. 72–79, feb 2016. ISSN 1536-1284. Available at: <http://ieeexplore.ieee.org/document/7422408/>.

161 LARSSON, E. *et al.* Massive MIMO for next generation wireless systems. **IEEE Communications Magazine**, v. 52, n. 2, p. 186–195, feb 2014. ISSN 0163-6804. Available at: <http://ieeexplore.ieee.org/document/6736761/>.

162 RAPPAPORT, T. S. *et al.* Millimeter wave mobile communications for 5G cellular: it will work! **IEEE Access**, v. 1, p. 335–349, 2013. ISSN 2169-3536. Available at: <http://ieeexplore.ieee.org/document/6515173/>.

163 SULYMAN, A. I. *et al.* Radio propagation path loss models for 5G cellular networks in the 28 GHZ and 38 GHZ millimeter-wave bands. **IEEE Communications Magazine**, v. 52, n. 9, p. 78–86, sep 2014. ISSN 0163-6804. Available at: <http://ieeexplore.ieee.org/document/6894456/>.

164 INOMATA, M. *et al.* Effects of building shapes on path loss up to 37 GHz band in street microcell environments. *In*: **2017 IEEE International Conference on Computational Electromagnetics (ICCEM)**. IEEE, 2017. p. 249–251. ISBN 978-1-5090-1038-7. Available at: <http://ieeexplore.ieee.org/document/7912782/>.

165 ASHRAF, N. *et al.* 28/38-GHz dual-band millimeter wave SIW array antenna with EBG structures for 5G applications. *In*: **2015 International Conference on Information and Communication Technology Research (ICTRC)**. IEEE, 2015. p. 5–8. ISBN 978-1-4799-8966-9. Available at: <http://ieeexplore.ieee.org/document/7156407/>.

166 HONG, W. *et al.* Multibeam antenna technologies for 5G wireless communications. **IEEE Transactions on Antennas and Propagation**, v. 65, n. 12, p. 6231–6249, dec 2017. ISSN 0018-926X. Available at: <http://ieeexplore.ieee.org/document/7942144/>.

167 ALA-LAURINAHO, J. *et al.* 2-D beam-steerable integrated lens antenna system for 5G E-band access and backhaul. **IEEE Transactions on Microwave Theory and Techniques**, v. 64, n. 7, p. 2244–2255, jul 2016. ISSN 0018-9480. Available at: <http://ieeexplore.ieee.org/document/7494690/>.

168 ZENG, Y.; ZHANG, R.; CHEN, Z. N. Electromagnetic lens-focusing antenna enabled massive MIMO: performance improvement and cost reduction. **IEEE Journal on Selected Areas in Communications**, v. 32, n. 6, p. 1194–1206, jun 2014. ISSN 0733-8716. Available at: <http://ieeexplore.ieee.org/lpdocs/epic03/wrapper.htm?arnumber=6824769>.

169 TORBITT, C. **Antenna gain enhancement and beamshaping using a diffractive optical element (DOE) lens**. 2014. Tese (Doutorado) — Rochester Institute of Technology, 2014. Available at: <http://scholarworks.rit.edu/theses%0D>.

170 ZAINUD-DEEN, S. H. *et al.* Radiation characteristics enhancement of dielectric resonator antenna using solid/discrete dielectric lenses. **Advanced Electromagnetics**, v. 4, n. 1, p. 1–9, 2015. ISSN 2119-0275. Available at: <%3CGo%5Cnto>.

171 LARIBI, M.; HAKEM, N. Gain-bandwidth enhancement of 60 GHz DRA using lens technique. *In*: **2016 IEEE International Symposium on Antennas and Propagation (APSURSI)**. IEEE, 2016. p. 385–386. ISBN 978-1-5090-2886-3. Available at: <http://ieeexplore.ieee.org/document/7695901/>.

172 LEE, E. *et al.* Theoretical investigations on microwave Fano resonances in 3D-printable hollow dielectric resonators. **Scientific Reports**, v. 7, n. 1, p. 16186–1–16186–10, dec 2017. ISSN 2045-2322. Available at: <http://www.nature.com/articles/s41598-017-16501-3>.

173 ARTEMENKO, A. *et al.* Experimental characterization of E-band two-dimensional electronically beam-steerable integrated lens antennas. **IEEE Antennas and Wireless Propagation Letters**, v. 12, p. 1188–1191, 2013. ISSN 1536-1225. Available at: <http://ieeexplore.ieee.org/document/6600766/>.

174 WHITTAKER, D. M.; CULSHAW, I. S. Scattering-matrix treatment of patterned multilayer photonic structures. **Physical Review B**, v. 60, n. 4, p. 2610–2618, jul 1999. ISSN 0163-1829. Available at: <https://link.aps.org/doi/10.1103/PhysRevB.60.2610>.

175 HASAR, U. C. Thickness-invariant complex permittivity retrieval from calibration-independent measurements. **IEEE Microwave and Wireless Components Letters**, v. 27, n. 2, p. 201–203, feb 2017. ISSN 1531-1309. Available at: <http://ieeexplore.ieee.org/document/7827053/>.

176 MOTA, A. F. *et al.* Constitutive parameter retrieval for uniaxial metamaterials with spatial dispersion. **Physical Review B**, v. 115410, p. 1–9, 2016.

177 BALANIS, C. A. **Antenna Theory: Analysis and Design**. 3. ed. [*S.l.: s.n.*]: Wiley, 2005. 1136 p.

178 VISWANATHAN, H.; MOGENSEN, P. E. Communications in the 6G Era. **IEEE Access**, v. 8, p. 57063–57074, 2020. ISSN 2169-3536. Available at: <https://ieeexplore.ieee.org/document/9040431/>.

179 AKYILDIZ, I. F.; KAK, A.; NIE, S. 6G and Beyond: The Future of Wireless Communications Systems. **IEEE Access**, v. 8, p. 133995–134030, 2020. ISSN 2169-3536. Available at: <https://ieeexplore.ieee.org/document/9145564/>.

180 SONG, H.-J. Terahertz Wireless Communications: Recent Developments Including a Prototype System for Short-Range Data Downloading. **IEEE Microwave Magazine**, v. 22, n. 5, p. 88–99, may 2021. ISSN 1527-3342. Available at: <https://ieeexplore.ieee.org/document/9393988/>.

181 SONG, H.-J.; NAGATSUMA, T. Present and Future of Terahertz Communications. **IEEE Transactions on Terahertz Science and Technology**, v. 1, n. 1, p. 256–263, sep 2011. ISSN 2156-342X. Available at: <http://ieeexplore.ieee.org/document/6005345/>.

182 BERUETE, M.; JÁUREGUIâLÓPEZ, I. Terahertz Sensing Based on Metasurfaces. **Advanced Optical Materials**, v. 8, n. 3, feb 2020. ISSN 2195-1071. Available at: <https://onlinelibrary.wiley.com/doi/10.1002/adom.201900721>.

183 MARKELZ, A. G.; MITTLEMAN, D. M. Perspective on Terahertz Applications in Bioscience and Biotechnology. **ACS Photonics**, v. 9, n. 4, p. 1117–1126, apr 2022. ISSN 2330-4022. Available at: <https://pubs.acs.org/doi/10.1021/acsphotonics.2c00228>.

184 BOWMAN, T.; EL-SHENAWEE, M.; BAILEY, K. Terahertz Imaging of Transgenic Murine Breast Cancer Tumors. *In*: **2018 IEEE International Symposium on Antennas and Propagation & USNC/URSI National Radio Science Meeting**. IEEE, 2018. p. 901–902. ISBN 978-1-5386-7102-3. Available at: <https://ieeexplore.ieee.org/document/8609230/>.

185 ZHONG, S. Progress in terahertz nondestructive testing: A review. **Frontiers of Mechanical Engineering**, v. 14, n. 3, p. 273–281, sep 2019. ISSN 2095-0233. Available at: <https://link.springer.com/10.1007/s11465-018-0495-9>.

186 YAN, Z. *et al.* THz medical imaging: from in vitro to in vivo. **Trends in Biotechnology**, v. 40, n. 7, p. 816–830, jul 2022. ISSN 01677799. Available at: <https://linkinghub.elsevier.com/retrieve/pii/S016777992100295X>.

187 VALUŠIS, G. *et al.* Roadmap of Terahertz Imaging 2021. **Sensors**, v. 21, n. 12, p. 4092, jun 2021. ISSN 1424-8220. Available at: <https://www.mdpi.com/1424-8220/21/12/4092>.

188 CARLO, A. D. *et al.* The European project OPTHER for the development of a THz tube amplifier. *In*: **2009 IEEE International Vacuum Electronics Conference**. IEEE, 2009. p. 100–101. ISBN 978-1-4244-3500-5. Available at: <http://ieeexplore.ieee.org/document/5193372/>.

189 DURNIN, J. Exact solutions for nondiffracting beams I The scalar theory. **Journal of the Optical Society of America A**, v. 4, n. 4, p. 651, apr 1987. ISSN 1084-7529. Available at: <https://opg.optica.org/abstract.cfm?URI=josaa-4-4-651>.

190 REN, Y.-X. *et al.* Non-Diffracting Light Wave: Fundamentals and Biomedical Applications. **Frontiers in Physics**, v. 9, sep 2021. ISSN 2296-424X. Available at: <https://www.frontiersin.org/articles/10.3389/fphy.2021.698343/full>.

191 MAZILU, M. *et al.* Light beats the spread: "non-diffracting" beams. **Laser & Photonics Reviews**, v. 4, n. 4, p. 529–547, jun 2010. ISSN 18638880. Available at: <https://onlinelibrary.wiley.com/doi/10.1002/lpor.200910019>.

192 DOSTER, T.; WATNIK, A. T. Laguerre-Gauss and Bessel-Gauss beams propagation through turbulence: analysis of channel efficiency. **Applied Optics**, v. 55, n. 36, p. 10239, dec 2016. ISSN 0003-6935. Available at: <https://opg.optica.org/abstract.cfm?URI=ao-55-36-10239>.

193 AIELLO, A.; AGARWAL, G. S. Wave-optics description of self-healing mechanism in Bessel beams. **Optics Letters**, v. 39, n. 24, p. 6819, dec 2014. ISSN 0146-9592. Available at: <https://opg.optica.org/abstract.cfm?URI=ol-39-24-6819>.

194 AIELLO, A. *et al.* Unraveling beam self-healing. **Optics Express**, v. 25, n. 16, p. 19147, aug 2017. ISSN 1094-4087. Available at: <https://opg.optica.org/abstract.cfm?URI=oe-25-16-19147>.

195 VETTER, C. *et al.* Realization of Free-Space Long-Distance Self-Healing Bessel Beams. **Laser & Photonics Reviews**, v. 13, n. 10, p. 1900103, oct 2019. ISSN 1863-8880. Available at: <https://onlinelibrary.wiley.com/doi/10.1002/lpor.201900103>.

196 WANG, D. *et al.* Extended depth of field in continuous-wave terahertz computed tomography based on Bessel beam. **Optics Communications**, v. 432, p. 20–26, feb 2019. ISSN 00304018. Available at: <https://linkinghub.elsevier.com/retrieve/pii/S0030401818308125>.

197 BITMAN, A.; MOSHE, I.; ZALEVSKY, Z. Improving depth-of field in broadband THz beams using nondiffractive Bessel beams. **Optics Letters**, v. 37, n. 19, p. 4164, oct 2012. ISSN 0146-9592. Available at: <https://opg.optica.org/abstract.cfm?URI=ol-37-19-4164>.

198 BUSCH, S. F. *et al.* Focus free terahertz reflection imaging and tomography with Bessel beams. **Journal of Infrared, Millimeter, and Terahertz Waves**, v. 36, n. 3, p. 318–326, mar 2015. ISSN 1866-6892. Available at: <http://link.springer.com/10.1007/s10762-014-0129-1>.

199 HEEBL, J. D.; ETTORRE, M.; GRBIC, A. Wireless Links in the Radiative Near Field via Bessel Beams. **Physical Review Applied**, v. 6, n. 3, p. 034018, sep 2016. ISSN 2331-7019. Available at: <https://link.aps.org/doi/10.1103/PhysRevApplied.6.034018>.

200 XIE, Y. *et al.* Beam wander relieved optical switch using Bessel beams in turbulent atmosphere. **Chinese Optics Letters**, v. 17, n. 9, p. 090602, 2019. ISSN 1671-7694. Available at: <http://www.clp.ac.cn/EN/Article/OJfa3c64fde3ee0fd8>.

201 NIU, L. *et al.* Diffractive Elements for Zero-Order Bessel Beam Generation With Application in the Terahertz Reflection Imaging. **IEEE Photonics Journal**, v. 11, n. 1, p. 1–12, feb 2019. ISSN 1943-0655. Available at: <https://ieeexplore.ieee.org/document/8579113/>.

202 YAN, B. *et al.* Printing special surface components for THz 2D and 3D imaging. **Scientific Reports**, v. 10, n. 1, p. 20867, dec 2020. ISSN 2045-2322. Available at: <http://www.nature.com/articles/s41598-020-77998-9>.

203 OK, G. *et al.* Foreign Object Detection by Sub-Terahertz Quasi-Bessel Beam Imaging. **Sensors**, v. 13, n. 1, p. 71–85, dec 2012. ISSN 1424-8220. Available at: <http://www.mdpi.com/1424-8220/13/1/71>.

204 FITZGERALD, A. J. *et al.* Catalogue of human tissue optical properties at terahertz frequencies. **Journal of Biological Physics**, v. 29, n. 2-3, p. 123–128, 2003. ISSN 00920606.

205 WANG, D. *et al.* 3D image reconstruction of terahertz computed tomography at sparse angles by total variation minimization. **Applied Optics**, v. 61, n. 5, p. B1, feb 2022. ISSN 1559-128X. Available at: <https://opg.optica.org/abstract.cfm?URI=ao-61-5-B1>.

206 ZHANG, D. *et al.* Enhanced Sub-Terahertz Microscopy based on Broadband Airy Beam. **Advanced Materials Technologies**, v. 7, n. 5, p. 2100985, may 2022. ISSN 2365-709X. Available at: <https://onlinelibrary.wiley.com/doi/10.1002/admt.202100985>.

207 WEI, X. *et al.* Generation of arbitrary order Bessel beams via 3D printed axicons at the terahertz frequency range. **Applied Optics**, v. 54, n. 36, p. 10641, dec 2015. ISSN 0003-6935. Available at: <https://opg.optica.org/abstract.cfm?URI=ao-54-36-10641>.

208 MIYAMOTO, K. *et al.* Tunable terahertz Bessel beams with orbital angular momentum. **Optics Continuum**, v. 1, n. 4, p. 633, apr 2022. ISSN 2770-0208. Available at: <https://opg.optica.org/abstract.cfm?URI=optcon-1-4-633>.

209 MINKEVIČIUS, L. *et al.* Bessel terahertz imaging with enhanced contrast realized by silicon multi-phase diffractive optics. **Optics Express**, v. 27, n. 25, p. 36358, dec 2019. ISSN 1094-4087. Available at: <https://opg.optica.org/abstract.cfm?URI=oe-27-25-36358>.

210 FENG, X. *et al.* Direct emission of broadband terahertz cylindrical vector Bessel beam. **Applied Physics Letters**, v. 119, n. 22, p. 221110, nov 2021. ISSN 0003-6951. Available at: <https://aip.scitation.org/doi/10.1063/5.0068561>.

211 HUANG, Q. *et al.* Structuring a terahertz beam by using a 3D-printed n-faced pyramid lens. **Optics Express**, v. 29, n. 8, p. 12124, apr 2021. ISSN 1094-4087. Available at: <https://opg.optica.org/abstract.cfm?URI=oe-29-8-12124>.

212 LIU, S. *et al.* Anomalous Refraction and Nondiffractive Bessel-Beam Generation of Terahertz Waves through Transmission-Type Coding Metasurfaces. **ACS Photonics**, v. 3, n. 10, p. 1968–1977, oct 2016. ISSN 2330-4022. Available at: <https://pubs.acs.org/doi/10.1021/acsphotonics.6b00515>.

213 MA, Z. *et al.* Terahertz All-Dielectric Magnetic Mirror Metasurfaces. **ACS Photonics**, v. 3, n. 6, p. 1010–1018, jun 2016. ISSN 2330-4022. Available at: <https://pubs.acs.org/doi/10.1021/acsphotonics.6b00096>.

214 LI, X. *et al.* High Efficient Metadevices for Terahertz Beam Shaping. **Frontiers in Physics**, v. 9, mar 2021. ISSN 2296-424X. Available at: <https://www.frontiersin.org/articles/10.3389/fphy.2021.659747/full>.

215 LIU, C. *et al.* Dual non-diffractive terahertz beam generators based on all-dielectric metasurface. **Frontiers of Optoelectronics**, v. 14, n. 2, p. 201–210, jun 2021. ISSN 2095-2759. Available at: <https://link.springer.com/10.1007/s12200-020-1098-8>.

216 JANA, K. *et al.* Reconfigurable terahertz metasurfaces coherently controlled by wavelength-scale-structured light. **Nanophotonics**, v. 11, n. 4, p. 787–795, feb 2022. ISSN 2192-8614. Available at: <https://www.degruyter.com/document/doi/10.1515/nanoph-2021-0501/html>.

217 HAN, J.; LAKHTAKIA, A. Semiconductor split-ring resonators for thermally tunable terahertz metamaterials. **Journal of Modern Optics**, v. 56, n. 4, p. 554–557, feb 2009. ISSN 0950-0340. Available at: <http://www.tandfonline.com/doi/abs/10.1080/09500340802621785>.

218 ALVAREZ, L. W. Development of variable- focus lenses and a new refractor. **Journal of the American Optometric Association**, v. 49, n. 1, p. 24–29, jan 1978. ISSN 0003-0244. Available at: <http://www.ncbi.nlm.nih.gov/pubmed/342589>.

219 LOHMANN, A. W. A New Class of Varifocal Lenses. **Applied Optics**, v. 9, n. 7, p. 1669, jul 1970. ISSN 0003-6935. Available at: <https://opg.optica.org/abstract.cfm?URI=ao-9-7-1669>.

220 SIEBER, I.; STILLER, P.; GENGENBACH, U. Design studies of varifocal rotation optics. **Optical Engineering**, v. 57, n. 12, p. 1, dec 2018. ISSN 0091-3286. Available at: <https://www.spiedigitallibrary.org/journals/optical-engineering/volume-57/issue-12/125102/Design-studies-of-varifocal-rotation-optics/10.1117/1.OE.57.12.125102.full>.

221 BERNET, S. Combined diffractive optical elements with adjustable optical properties controlled by a relative rotation: tutorial. **Journal of the Optical Society of America A**, v. 38, n. 10, p. 1521, oct 2021. ISSN 1084-7529. Available at: <https://opg.optica.org/abstract.cfm?URI=josaa-38-10-1521>.

222 SIEBER, I.; THELEN, R.; GENGENBACH, U. Assessment of high-resolution 3D printed optics for the use case of rotation optics. **Optics Express**, v. 28, n. 9, p. 13423, apr 2020. ISSN 1094-4087. Available at: <https://opg.optica.org/abstract.cfm?URI=oe-28-9-13423>.

223 DIXIT, P.; MIAO, J. High Aspect Ratio Vertical Through-Vias for 3D MEMS Packaging Applications by Optimized Three-Step Deep RIE. **Journal of The Electrochemical Society**, v. 155, n. 2, p. H85, 2008. ISSN 00134651. Available at: <https://iopscience.iop.org/article/10.1149/1.2814081>.

224 BABINGTON, J. Alvarez lens systems: theory and applications. *In*: MAZURAY, L.; WARTMANN, R.; WOOD, A. P. (ed.). [*S.l.: s.n.*], 2015. p. 962615. Available at: <http://proceedings.spiedigitallibrary.org/proceeding.aspx?doi=10.1117/12.2193114>.

225 DAI, J. *et al.* Terahertz time-domain spectroscopy characterization of the far-infrared absorption and index of refraction of high-resistivity, float-zone silicon. **Journal of**

the Optical Society of America B, v. 21, n. 7, p. 1379, jul 2004. ISSN 0740-3224. Available at: <https://www.osapublishing.org/abstract.cfm?URI=josab-21-7-1379>.

226 SLOCUM, D. M. *et al.* Atmospheric absorption of terahertz radiation and water vapor continuum effects. **Journal of Quantitative Spectroscopy and Radiative Transfer**, v. 127, p. 49–63, sep 2013. ISSN 00224073. Available at: <https://linkinghub.elsevier.com/retrieve/pii/S0022407313001702>.

227 MITTLEMAN, D. M. Twenty years of terahertz imaging [Invited]. **Optics Express**, v. 26, n. 8, p. 9417, apr 2018. ISSN 1094-4087. Available at: <https://www.osapublishing.org/abstract.cfm?URI=oe-26-8-9417>.

228 MALHOTRA, I.; JHA, K. R.; SINGH, G. Terahertz antenna technology for imaging applications: a technical review. **International Journal of Microwave and Wireless Technologies**, v. 10, n. 03, p. 271–290, apr 2018. ISSN 1759-0787. Available at: <https://www.cambridge.org/core/product/identifier/S175907871800003X/type/journal_article>.

229 ZHANG, Y. *et al.* Deep learning for subsurface penetrating super-resolution imaging. **2017 10th UK-Europe-China Workshop on Millimetre Waves and Terahertz Technologies, UCMMT 2017**, 2017.

230 YAO, H.; ZHONG, S. High-mode spoof SPP of periodic metal grooves for ultra-sensitive terahertz sensing. **Optics Express**, v. 22, n. 21, p. 25149, oct 2014. ISSN 1094-4087. Available at: <https://www.osapublishing.org/oe/abstract.cfm?uri=oe-22-21-25149>.

231 QIN, F. F. *et al.* Multiple Fano-Like Transmission Mediated by Multimode Interferences in Spoof Surface Plasmon Cavity-Waveguide Coupling System. **IEEE Transactions on Microwave Theory and Techniques**, IEEE, v. 64, n. 4, p. 1186–1194, 2016. ISSN 00189480.

232 CHEON, H. *et al.* Detection and manipulation of methylation in blood cancer DNA using terahertz radiation. **Scientific Reports**, v. 9, n. 1, p. 6413, dec 2019. ISSN 2045-2322. Available at: <http://www.nature.com/articles/s41598-019-42855-x>.

233 SHI, W. *et al.* Detection of living cervical cancer cells by transient terahertz spectroscopy. **Journal of Biophotonics**, v. 14, n. 1, jan 2021. ISSN 1864-063X. Available at: <https://onlinelibrary.wiley.com/doi/10.1002/jbio.202000237>.

234 AFSAH-HEJRI, L. *et al.* A Comprehensive Review on Food Applications of Terahertz Spectroscopy and Imaging. **Comprehensive Reviews in Food Science and Food Safety**, v. 18, n. 5, p. 1563–1621, sep 2019. ISSN 1541-4337. Available at: <https://onlinelibrary.wiley.com/doi/10.1111/1541-4337.12490>.

235 SPIES, J. A. *et al.* Terahertz Spectroscopy of Emerging Materials. **The Journal of Physical Chemistry C**, v. 124, n. 41, p. 22335–22346, oct 2020. ISSN 1932-7447. Available at: <https://pubs.acs.org/doi/10.1021/acs.jpcc.0c06344>.

236 PENG, Y. *et al.* Terahertz spectroscopy in biomedical field: a review on signal-to-noise ratio improvement. **PhotoniX**, v. 1, n. 1, p. 12, dec 2020. ISSN 2662-1991. Available at: <https://photonix.springeropen.com/articles/10.1186/s43074-020-00011-z>.

237 ZHONG, Q. *et al.* CMOS terahertz receivers. *In*: **2018 IEEE Custom Integrated Circuits Conference (CICC)**. IEEE, 2018. p. 1–8. ISBN 978-1-5386-2483-8. Available at: <https://ieeexplore.ieee.org/document/8357054/>.

238 RAZEGHI, M. Terahertz emitters at Center for Quantum Devices: recent advances and future trends. *In*: RAZEGHI, M. *et al.* (ed.). **Terahertz Emitters, Receivers, and Applications VIII**. SPIE, 2017. p. 4. ISBN 9781510612235. Available at: <https://www.spiedigitallibrary.org/conference-proceedings-of-spie/10383/2277609/Terahertz-emitters-at-Center-for-Quantum-Devices--recent-advances/10.1117/12.2277609.full>.

239 VILLEGAS, K. H. A. *et al.* Optical Transistor for Amplification of Radiation in a Broadband Terahertz Domain. **Physical Review Letters**, v. 124, n. 8, p. 087701, feb 2020. ISSN 0031-9007. Available at: <http://arxiv.org/abs/1812.01182https://link.aps.org/doi/10.1103/PhysRevLett.124.087701>.

240 CHEN, J. *et al.* Wavelength beam-combining of terahertz quantum-cascade laser arrays. **Optics Letters**, v. 46, n. 8, p. 1864, apr 2021. ISSN 0146-9592. Available at: <https://www.osapublishing.org/abstract.cfm?URI=ol-46-8-1864>.

241 SIRTORI, C. Terahertz race heats up. **Nature Photonics**, v. 15, n. 1, p. 1–2, jan 2021. ISSN 1749-4885. Available at: <http://www.nature.com/articles/s41566-020-00740-4>.

242 KHALATPOUR, A. *et al.* High-power portable terahertz laser systems. **Nature Photonics**, v. 15, n. 1, p. 16–20, jan 2021. ISSN 1749-4885. Available at: <http://www.nature.com/articles/s41566-020-00707-5>.

243 JONES, R. J.; YE, J. Femtosecond pulse amplification by coherent addition in a passive optical cavity. **Optics Letters**, v. 27, n. 20, p. 1848, oct 2002. ISSN 0146-9592. Available at: <https://www.osapublishing.org/abstract.cfm?URI=ol-27-20-1848>.

244 VIDNE, Y.; ROSENBLUH, M.; HANSCH, T. W. Pulse picking by phase-coherent additive pulse generation in an external cavity. **Optics Letters**, v. 28, n. 23, p. 2396, dec 2003. ISSN 0146-9592. Available at: <https://www.osapublishing.org/abstract.cfm?URI=ol-28-23-2396>.

245 CROCKETT, B. *et al.* Optical signal denoising through temporal passive amplification. **Optica**, v. 9, n. 1, p. 130, jan 2022. ISSN 2334-2536. Available at: <https://opg.optica.org/abstract.cfm?URI=optica-9-1-130>.

246 GHALICHECHIAN, N.; SERTEL, K. Permittivity and Loss Characterization of SU-8 Films for mmW and Terahertz Applications. **IEEE Antennas and Wireless Propagation Letters**, v. 14, p. 723–726, 2015. ISSN 1536-1225. Available at: <http://ieeexplore.ieee.org/document/6982221/>.

247 HEADLAND, D. *et al.* Doped polymer for low-loss dielectric material in the terahertz range. **Optical Materials Express**, v. 5, n. 6, p. 1373, jun 2015. ISSN 2159-3930. Available at: <https://www.osapublishing.org/abstract.cfm?URI=ome-5-6-1373>.

248 PODZOROV, A.; GALLOT, G. Low-loss polymers for terahertz applications. **Applied Optics**, v. 47, n. 18, p. 3254, jun 2008. ISSN 0003-6935. Available at: <https://www.osapublishing.org/abstract.cfm?URI=ao-47-18-3254>.

249 SANJUAN, F.; TOCHO, J. O. Optical properties of silicon, sapphire, silica and glass in the Terahertz range. *In*: **Latin America Optics and Photonics Conference**. Washington, D.C.: OSA, 2012. p. LT4C.1. ISBN 978-1-55752-9589. Available at: <https://www.osapublishing.org/abstract.cfm?URI=LAOP-2012-LT4C.1>.

250 BERDEL, K. *et al.* Temperature dependence of the permittivity and loss tangent of high-permittivity materials at terahertz frequencies. **IEEE Transactions on Microwave Theory and Techniques**, v. 53, n. 4, p. 1266–1271, apr 2005. ISSN 0018-9480. Available at: <http://ieeexplore.ieee.org/document/1420756/>.

251 GOPALAN, P.; SENSALE-RODRIGUEZ, B. 2D Materials for Terahertz Modulation. **Advanced Optical Materials**, v. 8, n. 3, p. 1900550, feb 2020. ISSN 2195-1071. Available at: <https://onlinelibrary.wiley.com/doi/10.1002/adom.201900550>.

252 ROUHI, N. *et al.* Terahertz graphene optics. **Nano Research**, v. 5, n. 10, p. 667–678, oct 2012. ISSN 1998-0124. Available at: <http://link.springer.com/10.1007/s12274-012-0251-0>.

253 WRIGHT, A. R. *et al.* Strong nonlinear optical response of graphene in the terahertz regime. **Applied Physics Letters**, v. 95, n. 7, p. 072101, aug 2009. ISSN 0003-6951. Available at: <http://aip.scitation.org/doi/10.1063/1.3205115>.

254 FAN, Z. *et al.* Characteristics of transition metal dichalcogenides in optical pumped modulator of terahertz wave. **AIP Advances**, v. 10, n. 4, p. 045304, apr 2020. ISSN 2158-3226. Available at: <http://aip.scitation.org/doi/10.1063/1.5141511>.

255 GHALGAOUI, A. *et al.* Resonant Second-Order Nonlinear Terahertz Response of Gallium Arsenide. **Physical Review Letters**, v. 121, n. 26, p. 266602, dec 2018. ISSN 0031-9007. Available at: <https://link.aps.org/doi/10.1103/PhysRevLett.121.266602>.

256 FORONI, M. *et al.* Guiding Properties of Silica/Air Hollow-Core Bragg Fibers. **Journal of Lightwave Technology**, v. 26, n. 13, p. 1877–1884, jul 2008. ISSN 0733-8724. Available at: <http://ieeexplore.ieee.org/document/4608859/>.

257 BERGER, N. *et al.* Compression of Periodic Optical Pulses Using Temporal Fractional Talbot Effect. **IEEE Photonics Technology Letters**, v. 16, n. 8, p. 1855–1857, aug 2004. ISSN 1041-1135. Available at: <http://ieeexplore.ieee.org/document/1316946/>.

258 YEH, P. **Optical Waves in Layered Media**. [*S.l.: s.n.*]: Wiley, 2005. 102–117 p. ISBN 978-0-471-73192-4.

259 SCHLERETH, K.-H.; TACKE, M. The complex propagation constant of multilayer waveguides: an algorithm for a personal computer. **IEEE Journal of Quantum Electronics**, v. 26, n. 4, p. 627–630, apr 1990. ISSN 0018-9197. Available at: <https://ieeexplore.ieee.org/document/53377/>.

260 COMSOL MultiPhysics 5.6, COMSOL Inc., 100 District Avenue, Burlington, MA, USA. Available at: <https://comsol.com/release/5.6>. Access at: November 10th 2021.

261 CORTÉS, L. R.; CHATELLUS, H. Guillet de; AZAÑA, J. On the generality of the Talbot condition for inducing self-imaging effects on periodic objects. **Optics Letters**, v. 41, n. 2, p. 340, jan 2016. ISSN 0146-9592. Available at: <https://www.osapublishing.org/abstract.cfm?URI=ol-41-2-340>.

262 DUCHESNE, D.; MORANDOTTI, R.; AZAÑA, J. Temporal Talbot phenomena in high-order dispersive media. **Journal of the Optical Society of America B**, v. 24, n. 1, p. 113, 2007. ISSN 0740-3224.

263 FATOME, J.; PITOIS, S.; MILLOT, G. Influence of third-order dispersion on the temporal Talbot effect. **Optics Communications**, v. 234, n. 1-6, p. 29–34, 2004. ISSN 00304018.

264 FERNÁNDEZ-POUSA, C. R. On the structure of quadratic Gauss sums in the Talbot effect. **Journal of the Optical Society of America A**, v. 34, n. 5, p. 732, may 2017. ISSN 1084-7529. Available at: <https://www.osapublishing.org/abstract.cfm?URI=josaa-34-5-732>.

265 PEPINO, V. M. *et al.* Terahertz passive amplification via temporal Talbot effect in metamaterial-based Bragg fibers. **Journal of the Optical Society of America B**, v. 39, n. 7, p. 1763, jul 2022. ISSN 0740-3224. Available at: <https://opg.optica.org/abstract.cfm?URI=josab-39-7-1763>.

266 BERRY, M. V.; KLEIN, S. Integer, fractional and fractal Talbot effects. **Journal of Modern Optics**, v. 43, n. 10, p. 2139–2164, 1996. ISSN 13623044.

267 LEGER, J. R.; SWANSON, G. J. Efficient array illuminator using binary-optics phase plates at fractional-Talbot planes. **Optics Letters**, v. 15, n. 5, p. 288, 1990. ISSN 0146-9592.

268 LOHMANN, A. W.; THOMAS, J. A. Making an array illuminator based on the Talbot effect. **Applied Optics**, v. 29, n. 29, p. 4337, oct 1990. ISSN 0003-6935. Available at: <https://opg.optica.org/abstract.cfm?URI=ao-29-29-4337>.

269 TALBOT, H. LXXVI. Facts relating to optical science. No. IV. **The London, Edinburgh, and Dublin Philosophical Magazine and Journal of Science**, v. 9, n. 56, p. 401–407, dec 1836. ISSN 1941-5966. Available at: <https://www.tandfonline.com/doi/full/10.1080/14786443608649032>.

270 WEN, J.; ZHANG, Y.; XIAO, M. The Talbot effect: recent advances in classical optics, nonlinear optics, and quantum optics. **Advances in Optics and Photonics**, v. 5, n. 1, p. 83, mar 2013. ISSN 1943-8206. Available at: <https://opg.optica.org/aop/abstract.cfm?uri=aop-5-1-83>.

271 JANNSON, T.; JANNSON, J. Temporal self-imaging effect in single-mode fibers. **Journal of the Optical Society of America**, v. 71, n. 11, p. 1373, nov 1981. ISSN 0030-3941. Available at: <https://opg.optica.org/abstract.cfm?URI=josa-71-11-1373>.

272 ANDREKSON, P. A. Linear propagation of optical picosecond pulse trains over oceanic distances. **Optics Letters**, v. 18, n. 19, p. 1621, oct 1993. ISSN 0146-9592. Available at: <https://opg.optica.org/abstract.cfm?URI=ol-18-19-1621>.

273 MITSCHKE, F.; MORGNER, U. The Temporal Talbot Effect. **Optics and Photonics News**, v. 9, n. 6, p. 45, jun 1998. ISSN 1047-6938. Available at: <https://opg.optica.org/abstract.cfm?URI=opn-9-6-45>.

274 ARAHIRA, S. *et al.* Repetition-frequency multiplication of mode-locked pulses using fiber dispersion. **Journal of Lightwave Technology**, v. 16, n. 3, p. 405–410, mar 1998. ISSN 07338724. Available at: <http://ieeexplore.ieee.org/document/661368/>.

275 SHAKE, I. *et al.* High-repetition-rate optical pulse generation by using chirped optical pulses. **Electronics Letters**, v. 34, n. 8, p. 792, 1998. ISSN 00135194. Available at: <https://digital-library.theiet.org/content/journals/10.1049/el_19980558>.

276 MARAM, R. *et al.* Energy-Preserving Arbitrary Repetition-Rate Control of Periodic Pulse Trains Using Temporal Talbot Effects. **Journal of Lightwave Technology**, v. 35, n. 4, p. 658–668, feb 2017. ISSN 0733-8724. Available at: <http://ieeexplore.ieee.org/document/7809135/>.

277 MARAM, R.; CORTES, L. R.; AZANA, J. Programmable Fiber-Optics Pulse Repetition-Rate Multiplier. **Journal of Lightwave Technology**, v. 34, n. 2, p. 448–455, jan 2016. ISSN 0733-8724. Available at: <http://ieeexplore.ieee.org/document/7328691/>.

278 XIE, Q.; ZHENG, B.; SHU, C. Adjustable repetition-rate multiplication of optical pulses using fractional temporal Talbot effect with preceded binary intensity modulation. **Optics Communications**, v. 391, p. 16–23, may 2017. ISSN 00304018. Available at: <https://linkinghub.elsevier.com/retrieve/pii/S0030401817300020>.

279 ATKINS, S.; FISCHER, B. All-optical pulse rate multiplication using fractional Talbot effect and field-to- intensity conversion with cross-gain modulation. **IEEE Photonics Technology Letters**, v. 15, n. 1, p. 132–134, jan 2003. ISSN 1041-1135. Available at: <http://ieeexplore.ieee.org/document/1159086/>.

280 KIM, I.; SEO, D. 32 GHz microwave photonic pulse train generation using 1.6 GHz electronics and optical repetition rate multiplication. **Electronics Letters**, v. 46, n. 13, p. 937, 2010. ISSN 00135194. Available at: <https://digital-library.theiet.org/content/journals/10.1049/el.2010.0417>.

281 GUO, R. *et al.* Programmable optical pulse repetition rate multiplication via spectral phase manipulation. **Optics Express**, v. 28, n. 3, p. 4178, feb 2020. ISSN 1094-4087. Available at: <https://opg.optica.org/abstract.cfm?URI=oe-28-3-4178>.

282 AZANA, J. *et al.* Broadband arbitrary waveform generation based on microwave frequency upshifting in optical fibers. **Journal of Lightwave Technology**, v. 24, n. 7, p. 2663–2675, jul 2006. ISSN 0733-8724. Available at: <http://ieeexplore.ieee.org/document/1650542/>.

283 CORTÉS, L. R. *et al.* Subnoise Detection and Passive Amplification of Frequency Combs through Customized Coherent Spectral Energy Redistribution. **Physical Review Applied**, v. 9, n. 6, p. 064017, jun 2018. ISSN 2331-7019. Available at: <https://link.aps.org/doi/10.1103/PhysRevApplied.9.064017>.

284 LI, B. *et al.* Extended temporal cloak based on the inverse temporal Talbot effect. **Optics Letters**, v. 42, n. 4, p. 767, feb 2017. ISSN 0146-9592. Available at: <https://opg.optica.org/abstract.cfm?URI=ol-42-4-767>.

285 CORTÉS, L. R. *et al.* Full-field broadband invisibility through reversible wave frequency-spectrum control. **Optica**, v. 5, n. 7, p. 779, jul 2018. ISSN 2334-2536. Available at: <https://opg.optica.org/abstract.cfm?URI=optica-5-7-779>.

286 OUELLETTE, F. Dispersion cancellation using linearly chirped Bragg grating filters in optical waveguides. **Optics Letters**, v. 12, n. 10, p. 847, oct 1987. ISSN 0146-9592. Available at: <https://opg.optica.org/abstract.cfm?URI=ol-12-10-847>.

287 HILL, K. O. *et al.* Chirped in-fiber Bragg gratings for compensation of optical-fiber dispersion. **Optics Letters**, v. 19, n. 17, p. 1314, sep 1994. ISSN 0146-9592. Available at: <https://opg.optica.org/abstract.cfm?URI=ol-19-17-1314>.

288 DENISOV, G. G.; SHMELYOV, M. Y. Using the Talbot Effect for Summation of Microwave Signals in the Millimeter-Wavelength Band. **Radiophysics and Quantum Electronics**, v. 58, n. 10, p. 789–792, mar 2016. ISSN 0033-8443. Available at: <http://link.springer.com/10.1007/s11141-016-9651-4>.

289 KELLER, M. G. *et al.* Microwave power combining using the Talbot effect. *In*: **2004 10th International Symposium on Antenna Technology and Applied Electromagnetics and URSI Conference**. IEEE, 2004. p. 1–4. ISBN 978-0-9692563-9-7. Available at: <http://ieeexplore.ieee.org/document/7860639/>.

290 LATHI, B. P.; DING, Z. **Modern Analog and Digital Communication Systems**. 4th. ed. [*S.l.: s.n.*]: Oxford University Press, 2010. 343–350 p. ISBN 978-0-19-538493-2.

291 JIN, L. *et al.* Generation of Airy vortex beam arrays using computer-generated holography. **Journal of the Optical Society of America A**, v. 36, n. 7, p. 1215, jul 2019. ISSN 1084-7529. Available at: <https://opg.optica.org/abstract.cfm?URI=josaa-36-7-1215>.

292 TANG, X.; NAN, F.; YAN, Z. Rapidly and accurately shaping the intensity and phase of light for optical nano-manipulation. **Nanoscale Advances**, v. 2, n. 6, p. 2540–2547, 2020. ISSN 2516-0230. Available at: <http://xlink.rsc.org/?DOI=D0NA00167H>.

293 DOELMAN, D. S.; ESCUTI, M. J.; SNIK, F. Multi-color holography with a two-stage patterned liquid-crystal element. **Optical Materials Express**, v. 9, n. 3, p. 1246, mar 2019. ISSN 2159-3930. Available at: <https://opg.optica.org/abstract.cfm?URI=ome-9-3-1246>.

294 KIM, M. K. Principles and techniques of digital holographic microscopy. **Journal of Photonics for Energy**, p. 018005, apr 2010. ISSN 1947-7988. Available at: <http://photonicsforenergy.spiedigitallibrary.org/article.aspx?doi=10.1117/6.0000006>.

295 NETO, L. G.; ROBERGE, D.; SHENG, Y. Programmable optical phase-mostly holograms with coupled-mode modulation liquid-crystal television. **Applied Optics**, v. 34, n. 11, p. 1944–1950, apr 1995. ISSN 0003-6935. Available at: <https://www.osapublishing.org/abstract.cfm?URI=ao-34-11-1944>.

296 Available at: <{https://github.com/vinicius-pepino/thesis-supplementary-file}.>

297 FANO, U. Sullo spettro di assorbimento dei gas nobili presso il limite dello spettro d'arco. **Il Nuovo Cimento**, v. 12, n. 3, p. 154–161, mar 1935. ISSN 0029-6341. Available at: <http://link.springer.com/10.1007/BF02958288>.

298 FANO, U. Effects of configuration interaction on intensities and phase shifts. **Physical Review**, v. 124, n. 6, p. 1866–1878, 1961. ISSN 0031899X.

299 LIMONOV, M. F. *et al.* Fano resonances in photonics. **Nature Photonics**, v. 11, n. 9, p. 543–554, sep 2017. ISSN 1749-4885. Available at: <http://www.nature.com/articles/nphoton.2017.142>.

300 ROTTER, S. *et al.* Tunable Fano resonances in transport through microwave billiards. **Physical Review E - Statistical Physics, Plasmas, Fluids, and Related Interdisciplinary Topics**, v. 69, n. 4, p. 4, 2004. ISSN 1063651X.

301 ROTTER, S. *et al.* Fano resonances and decoherence in transport through quantum dots. **Physica E: Low-Dimensional Systems and Nanostructures**, v. 29, n. 1-2, p. 325–333, 2005. ISSN 13869477.

302 BÄRNTHALER, A. *et al.* Probing decoherence through fano resonances. **Physical Review Letters**, v. 105, n. 5, p. 1–4, 2010. ISSN 00319007.

303 CAPUTO, J. G.; GABITOV, I.; MAIMISTOV, A. I. Electrodynamics of a split-ring Josephson resonator in a microwave line. **Physical Review B - Condensed Matter and Materials Physics**, v. 85, n. 20, p. 1–7, 2012. ISSN 10980121.

304 HAN, S. *et al.* Engineering the fano resonance and electromagnetically induced transparency in near-field coupled bright and dark metamaterial. **Journal of Physics D: Applied Physics**, IOP Publishing, v. 48, n. 3, p. 035104–1–035104–7, 2015. ISSN 13616463.

305 VAISMAN, G.; KAMENETSKII, E. O.; SHAVIT, R. Magnetic-dipolar-mode Fano resonances for microwave spectroscopy of high absorption matter. **Journal of Physics D: Applied Physics**, IOP Publishing, v. 48, n. 11, p. 115003–1 –115003–13, 2015. ISSN 13616463.

306 BEREZIN, M.; KAMENETSKII, E. O.; SHAVIT, R. Novel microwave antennas based on magnetostatic-mode ferrite resonators. **2015 IEEE International Conference on Microwaves, Communications, Antennas and Electronic Systems, (COMCAS), Tel Aviv, 2015**, n. November, p. 1–5, 2015.

307 PAN, X. Y.; WANG, G. Magneto-induced Fano-like cavity interference in three-dimensional metamaterials. **Physica Scripta**, IOP Publishing, v. 91, n. 8, p. 085501–1–085501–7, 2016. ISSN 14024896.

308 FERNANDES, D. E.; SILVEIRINHA, M. G. Bistability in mushroom-type metamaterials. **Journal of Applied Physics**, v. 122, n. 1, p. 014303–1–014303–9, 2017. ISSN 10897550.

309 VOGT, D. W.; LEONHARDT, R. Fano resonances in a high-Q terahertz whispering-gallery mode resonator coupled to a multi-mode waveguide. **Optics Letters**, v. 42, n. 21, p. 4359–4362, 2017. ISSN 0146-9592.

310 YUAN, S. *et al.* Tunable high-quality Fano resonance in coupled terahertz whispering-gallery-mode resonators. **Applied Physics Letters**, AIP Publishing LLC, v. 115, n. 20, p. 201102–1–201102–5, 2019. ISSN 00036951.

311 SINGH, R. *et al.* Sharp Fano resonances in THz metamaterials. **Optics Express**, v. 19, n. 7, p. 1351–1353, 2011.

312 CAO, W. *et al.* Low-loss ultra-high- Q dark mode plasmonic Fano metamaterials. **Optics Express**, v. 37, n. 16, p. 3366–3368, 2012.

313 BANSIWAL, A. *et al.* A Post-Loaded Rectangular Reentrant Cavity for Broadband Multiple-Beam Klystron. **IEEE Electron Device Letters**, v. 41, n. 6, p. 916–919, 2020. ISSN 15580563.

314 FAN, Y. *et al.* Investigation of Higher Order Reentrant Modes of a Cylindrical Reentrant-Ring Cavity Resonator. **IEEE Transactions on Microwave Theory and Techniques**, v. 62, n. 8, p. 1657–1662, aug 2014. ISSN 0018-9480. Available at: <http://ieeexplore.ieee.org/document/6843369/>.

315 HUANG, F.; FOULADI, S.; MANSOUR, R. R. High-Q Tunable Dielectric Resonator Filters Using MEMS Technology. **IEEE Transactions on Microwave Theory and Techniques**, v. 59, n. 12, p. 3401–3409, dec 2011. ISSN 0018-9480. Available at: <http://ieeexplore.ieee.org/document/6082418/>.

316 CARTER, R.; Jinjun Feng; BECKER, U. Calculation of the Properties of Reentrant Cylindrical Cavity Resonators. **IEEE Transactions on Microwave Theory and Techniques**, v. 55, n. 12, p. 2531–2538, dec 2007. ISSN 0018-9480. Available at: <http://ieeexplore.ieee.org/document/4362516/>.

317 FOULADI, S. *et al.* High-Q narrowband tunable combline bandpass filters using MEMS capacitor banks and piezomotors. **IEEE Transactions on Microwave Theory and Techniques**, v. 61, n. 1, p. 393–402, 2013. ISSN 00189480.

318 LIU, X. *et al.* High-Q Tunable Microwave Cavity Resonators and Filters Using SOI-Based RF MEMS Tuners. **Journal of Microelectromechanical Systems**, v. 19, n. 4, p. 774–784, 2010. ISSN 1057-7157. Available at: <http://ieeexplore.ieee.org/lpdocs/epic03/wrapper.htm?arnumber=5512545>.

319 BOURGEOIS, P.-Y.; GIORDANO, V. Simple model for the mode-splitting effect in whispering-gallery-mode resonators. **IEEE Transactions on Microwave Theory and Techniques**, v. 53, n. 10, p. 3185–3190, oct 2005. ISSN 0018-9480. Available at: <http://ieeexplore.ieee.org/document/1516323/>.

320 POZAR, D. M. **Microwave engineering**. 4. ed. [*S.l.: s.n.*]: Wiley, 2012. 309–312 p.

321 HO, C.-H.; FAN, L. F. L.; CHANG, K. C. K. A new type of waveguide ring cavity for resonator and filter applications. **IEEE Transactions on Microwave Theory and Techniques**, v. 42, n. 1, p. 41–51, 1994. ISSN 0018-9480.

322 HFSS: High Frequency Structure Simulator, ANSYS Inc., 774 Canonsburg, PA, USA. Available at: <https://www.ansys.com/products/electronics/ansys-hfss>. Access at: December 6th 2020.

323 MURUGKAR, A.; PANIGRAHI, R.; VINOY, K. J. A novel approach for high Q microwave re-entrant cavity resonator at S-band. **2016 Asia-Pacific Microwave Conference Proceedings, (APMC), New Delhi**, p. 1–4, 2016.

324 GORYACHEV, M. *et al.* High-cooperativity cavity QED with magnons at microwave frequencies. **Physical Review Applied**, v. 2, n. 5, p. 1–11, 2014. ISSN 23317019.

325 PAPAPOLYMEROU, J. *et al.* A Micromachined High- X-Band Resonator. v. 7, n. 6, p. 168–170, 1997.

326   WONG, S. W. *et al.* Individually Frequency Tunable Dual- and Triple-band Filters in a Single Cavity. **IEEE Access**, v. 5, p. 11615–11625, 2017. ISSN 21693536.

327   SAEEDI, S.; ATASH-BAHAR, S.; SIGMARSSON, H. H. Active tunable substrate integrated evanescent-mode cavity resonator using negative resistance. **IEEE Radio and Wireless Symposium, RWS**, v. 2016-March, p. 87–90, 2016. ISSN 21642974.

328   BAHAR, A. A. M. *et al.* High-efficiency microwave planar resonator sensor based on bridge split ring topology. **IEEE Microwave and Wireless Components Letters**, IEEE, v. 27, n. 6, p. 545–547, 2017. ISSN 15311309.

329   PASTERNACK. SMA Female Right Angle Connector Solder Attachment 2 Hole Flange Mount Pin Terminal, .481 inch Hole Spacing, 90 Degree Flange Direction. **Datasheet**, 2016. Available at: <https://www.pasternack.com/images/ProductPDF/PE44237.pdf>.

330   PANDEY, A.; SELVARAJA, S. K. Fano resonance assisted tunable microwave photonic phase shifter in loaded ring resonator. **2018 Conference on Lasers and Electro-Optics, CLEO 2018 - Proceedings**, OSA, v. 1, p. 44–45, 2018.

331   XU, Z. *et al.* UWB Pulses Generation with Fano Resonance Modulation. *In*: **2019 International Topical Meeting on Microwave Photonics (MWP)**. IEEE, 2019. p. 1–3. ISBN 978-1-7281-3625-7. Available at: <https://ieeexplore.ieee.org/document/8892208/>.

332   CHEN, S. *et al.* High-Linearity Fano Resonance Modulator Using a Microring-Assisted Mach-Zehnder Structure. **Journal of Lightwave Technology**, IEEE, v. 38, n. 13, p. 3395–3403, 2020. ISSN 15582213.

333   KOMAROV, V. V. *et al.* Fano-Resonant Frequency-Selective Surface With Cross-Shaped Apertures. **IEEE Microwave and Wireless Components Letters**, v. 29, n. 12, p. 775–778, dec 2019. ISSN 1531-1309. Available at: <https://ieeexplore.ieee.org/document/8896919/>.

334   SINGH, R. *et al.* The fano resonance in symmetry broken terahertz metamaterials. **IEEE Transactions on Terahertz Science and Technology**, IEEE, v. 3, n. 6, p. 820–826, 2013. ISSN 2156342X.

335   ALÙ, A.; ENGHETA, N. Wireless at the nanoscale: Optical interconnects using matched nanoantennas. **Physical Review Letters**, v. 104, n. 21, p. 1–4, 2010. ISSN 00319007.

336   LI, B.-B. *et al.* Experimental observation of Fano resonance in a single whispering-gallery microresonator. **Applied Physics Letters**, v. 98, n. 2, p. 021116–1–021116–3, jan 2011. ISSN 0003-6951. Available at: <http://aip.scitation.org/doi/10.1063/1.3541884>.

337   JOE, Y. S.; SATANIN, A. M.; KIM, C. S. Classical analogy of Fano resonances. **Physica Scripta**, v. 74, n. 2, p. 259–266, 2006. ISSN 00318949.

338   GORI, F.; GUATTARI, G.; PADOVANI, C. Bessel-Gauss beams. **Optics Communications**, v. 64, n. 6, p. 491–495, dec 1987. ISSN 00304018. Available at: <https://linkinghub.elsevier.com/retrieve/pii/0030401887902768>.

339 HWANG, H.; YANG, G.; HAN, P. Study and improvement of near-field diffraction limits of circular aperture imaging systems. **Journal of the Chinese Institute of Engineers**, v. 25, n. 3, p. 335–340, apr 2002. ISSN 0253-3839. Available at: <http://www.tandfonline.com/doi/abs/10.1080/02533839.2002.9670708>.

340 MIELENZ, K. Algorithms for Fresnel diffraction at rectangular and circular apertures. **Journal of Research of the National Institute of Standards and Technology**, v. 103, n. 5, p. 497, nov 1998. ISSN 1044677X. Available at: <https://nvlpubs.nist.gov/nistpubs/jres/103/5/j35mie.pdf>.

341 BADDOUR, N. Operational and convolution properties of two-dimensional Fourier transforms in polar coordinates. **Journal of the Optical Society of America A**, v. 26, n. 8, p. 1767, aug 2009. ISSN 1084-7529. Available at: <https://opg.optica.org/abstract.cfm?URI=josaa-26-8-1767>.

342 CHU, X.; WEN, W. Quantitative description of the self-healing ability of a beam. **Optics Express**, v. 22, n. 6, p. 6899, mar 2014. ISSN 1094-4087. Available at: <https://opg.optica.org/oe/abstract.cfm?uri=oe-22-6-6899>.

343 MIKI, N. *et al.* Multi-stack silicon-direct wafer bonding for 3D MEMS manufacturing. **Sensors and Actuators A: Physical**, v. 103, n. 1-2, p. 194–201, jan 2003. ISSN 09244247. Available at: <https://linkinghub.elsevier.com/retrieve/pii/S0924424702003321>.

344 LIU, S. *et al.* 1 THz Micromachined Waveguide Band-Pass Filter. **Journal of Infrared, Millimeter, and Terahertz Waves**, v. 37, n. 5, p. 435–447, may 2016. ISSN 1866-6892. Available at: <http://link.springer.com/10.1007/s10762-015-0229-6>.

Appendices

Appendix A – EXTRA WORKS

A.1 Static and dynamic stereoscopic computer-generated holography (CGH) with spatial light modulators (SLM)

In this paper we demonstrate for the first time static/dynamic stereoscopic holographic reconstructions in the visible range with two spatial light modulators (SLM). Stereoscopy is achieved by exciting two separate SLMs with two different wavelengths.

The work present in the chapter has been published as: PEPINO, V. M.; MARTINS, A.; MOTA, A. F.; DOMINGUES, C.; BENINI, F. A. V.; NETO, L. G.; MARTINS, E. R.; BORGES, B.-H.V. Static and dynamic stereoscopic computer-generated holography (CGH) with spatial light modulators (SLM). **Imaging and Applied Optics Congress, OSA Technical Digest** (Optica Publishing Group, 2020), paper HF1D.6. Permission for reuse in the author's thesis in allowed by Optica Publishing Group (https://opg.optica.org/submit/review/copyright_permissions.cfm) and is found in Appendix F.

A.1.1 Introduction

Computer-generated holography (CGH) has been gaining increased attention in the last few years not only due to its low cost and high efficiency, but also because it enables a myriad of applications, including generation of Airy vortex beam arrays (291), optical tweezers (292), and multi-color holography (293). Currently, these applications greatly benefit from the versatility of spatial light modulators (SLM) to provide the necessary phase modulation of the incoming wave. However, the literature lacks an investigation of static and dynamic stereoscopic (three-dimensional) holograms with CGH/SLMs, although static stereoscopic holograms based on crystalline silicon metasurfaces have been recently obtained (81). It is noteworthy mentioning that the concept of CGH is fundamentally different from that of digital holography (294), where three-dimensionality is post-processed in a computer rather than been obtained optically. In this chapter, we investigated for the first time (as far as the authors are aware) static and dynamic stereoscopic holography using CGHs and SLMs. This concept can also be used successfully as a testbed for diffractive optics applications, such as optical tweezers, beam shaping, and real-time stereoscopic visualization.

A.1.2 Background and experimental setup

The stereoscopic effect consists of creating three-dimensionality illusion by conveying to the eyes two parallax separated images of the same scene, with each image perceived by one eye and not the other (and vice-versa). The blocking of one of the images to a

given eye can be obtained, for instance, via polarization effects or via color filtering. In the former, both images are orthogonally polarized with respect to each other, and each image is directed to one of our eyes separately with the help of cross-polarized glasses [4]. In the latter, a specific color is associated with each image and then directed to the observer's eye after passing through a color matching filter (color glasses). In this paper, we investigate the stereoscopic effect via color filtering using Fourier CGHs and SLMs. The SLM used here is a repurposed Epson EMP-X5 multimedia projector (1024x768 pixels) with two LCDs exposed to ease the laser illumination. The displays (model L3P06X-82G00, 12.5 μm pixel size) are mounted in a 3D-printed ABS plastic mask to ensure correct positioning and to block unwanted light on the reconstruction plane. Each hologram is modulated with 4 phase levels, obtained from the LCD phase map measured according to (295). The color of each CGH needs to match the display channel (RGB) to which it is connected to minimize color crosstalk. We used the blue (B), instead of red (R), and green (G) channels for the sake of assembly because the phase modulation is not affected by this choice. Different focal lengths are used for each laser beam to ensure a staggered and more compact setup.

Figure 34 shows the optical setup adopted here. The displays are illuminated individually with collimated red ((a) Uniphase 1135P 632.8 nm HeNe laser) and green ((b) Thorlabs CPS523 531.9 nm semiconductor laser) light. The half-wave plates (c,d) guarantee that the polarization of the incident and modulated wavefronts are carefully adjusted to ensure a mostly-phase modulation. (e) and (f) are 45° mirrors to redirect the beams. Next, each laser beam is expanded and collimated with an objective lens and a pinhole spatial filter on a Newport M-900 mount (g,h), followed by a plano-convex lens (i,j) to fully illuminate their respective LCD. Beam collimation is verified individually with a shear interferometer positioned after the plano-convex lens (i,j) at a distance where interference fringes become horizontal (295) (step carried out without the SLMs, not shown in Fig. 34). The repurposed multimedia projector can be seen in (k). Note that the collimated beams (red and green) fully illuminate both displays (l). The Fourier holograms adopted here require Fourier transform (FT) lenses (m,n) after propagation through the LCDs. Each lens is then followed by a polarizer (o,p) and an iris (q,r), with the latter used to avoid unwanted light on the reconstruction plane. The final step is the superposition of both red and green beams. To achieve this, we need to align and scale both images. To this end, we use the original telescopic lenses (s,t) from the Epson EMP-X5 projector and adjust its zoom, incidence angle, and horizontal alignment. This procedure is quicker than rescaling the images during the hologram generation and allows a whole range of distances from the reconstruction plane (u). The image reconstruction plane is placed at 75 cm from the LCDs. Stereoscopic animations can be found in (296).
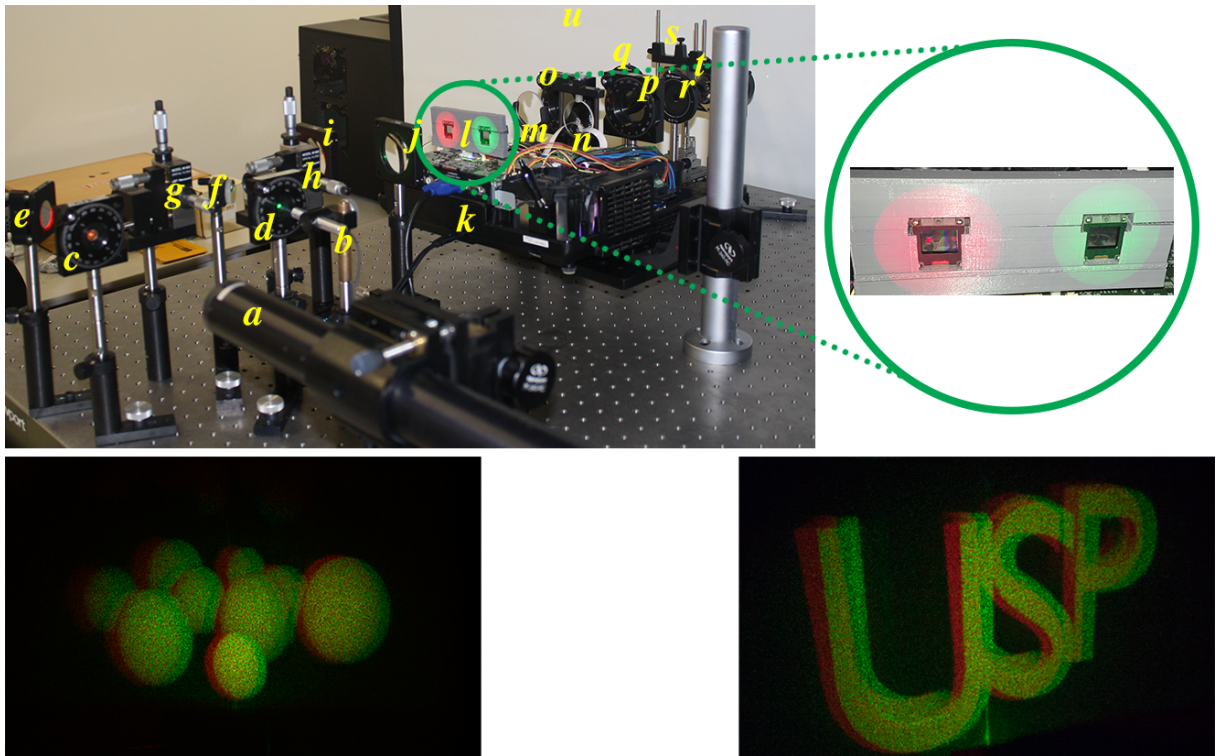
Figure 34 – Experimental setup for stereoscopic holography (top left) with the LCDs illumination shown in detail (top right). (a) 632.8 nm HeNe laser. (b) 531.9 nm semiconductor laser, (c,d) half-wave plates, (e,f) 45° mirrors, (g,h) Newport M-900 three-axis mount with a 60x objective ($NA = 0.85$) for the red beam and 20x ($NA = 0.40$) for the green beam. A 25 μm 900PH pinhole aperture spatial filter is used with both objectives (not shown). (i,j) uncoated BK-7 plano-convex lens for beam collimation, (k) Epson EMP-X5 multimedia projector (repurposed as SLM)) with exposed LCDs, (l) L3P06X-82G00 LCDs in a 3D printed plastic mask, (m,n) uncoated BK-7 plano-convex lens to FT the red and green wave fronts, (o,p) linear polarizer filters, (q,r) iris diaphragms, (s,t) telescopic lenses 145RA/TR27106 from the EMP-X5 projector for image scaling and alignment, (u) hologram reconstruction plane. Stereoscopic reconstructions are shown in the bottom row (animations will be shown during paper presentation). Reproduced with permission from PEPINO, V. M.; MARTINS, A.; MOTA, A. F.; DOMINGUES, C.; BENINI, F. A. V.; NETO, L. G.; MARTINS, E. R.; BORGES, B.-H.V. Static and dynamic stereoscopic computer-generated holography (CGH) with spatial light modulators (SLM). **Imaging and Applied Optics Congress, OSA Technical Digest** (Optica Publishing Group, 2020), paper HF1D.6, 2020© Optica Publishing Group.

A.1.3 Conclusions

This paper has demonstrated for the first time static/dynamic stereoscopic holographic reconstructions in the visible range with two SLMs. Stereoscopy is achieved by exciting two separate SLMs with two different wavelengths. This concept can also be used as a testbed for diffractive optics applications, such as optical tweezers, beam shaping,

and real-time stereoscopic visualization.

A.2   Fano-Assisted Tunable X-Band Microwave Ring Resonator

Control of the resonance frequency of microwave cavities is of great interest in many applications such as sensing and wavelength filtering. However, this task normally relies on active control via functional materials (i.e., polymers and ferrites, or a combination of both) excited by an external electric or magnetic field. In this article, instead, we propose an innovative whispering gallery mode cavity resonator with tunable bandwidth for sensing and wavelength filtering applications. The proposed approach exploits Fano-type resonances (FTRs) to improve the cavity performance in the microwave regime. We have measured a 74% increase in the loaded quality factor compared to regular ring cavities, with only 1.9 dB additional loss. In addition, by carefully choosing the size of the transmitting and receiving monopole antennas placed inside the cavity and their relative angular spacing, we can easily tune the cavity response. The extra degree-of-freedom introduced by such variable angular spacing, responsible for the onset of FTRs, allows the cavity quality factor Q to be continuously tuned from 385 to 670.

The work present in the chapter has been published as: PEPINO, V. M.; MOTA, A. F.; MARTINS, A.; MARTINS, E. R.; BORGES, B.-H.V.; TEIXEIRA, F. L. Fano-Assisted Tunable X-Band Microwave Ring Resonator. **IEEE Transactions on Microwave Theory and Techniques**, vol. 69, no. 4, pp. 2155-2164, April 2021. Permission for reuse is found in Appendix F

A.2.1   Introduction

Fano resonance (FR) was originally introduced by Fano (297, 298) to explain the asymmetric absorption line shape due to inelastic scattering of electrons in the atomic spectra of noble gases. FR involves the interaction of two modes with different damping coefficients or different quality (Q) factors (299). In the photonics community, the low and high Q modes are often referred to as bright and dark modes, respectively. The bright and dark characteristics arise because the first is a radiative mode while the second is a localized mode. This concept also holds in the microwave regime and has been successfully used in resonant scattering structures (300–302), split ring resonators (SRRs) (303, 304), ferrite disks (305, 306), 3D metamaterials (307), wire media (308), dielectric metasurfaces (172), and THz whispering gallery mode (WGMs) (309, 310). FRs have also been successfully used to enhance the Q factor of THz and optical resonators (311, 312) via symmetry breaking of two-gap SRRs. Frequency tuning and quality factor control are important issues in many applications and have been extensively investigated also with microwave re-entrant cavities. In general, these cavities utilize either a central conducting post (313–315) or a gap (316) at the cavity central region that acts as a capacitor that changes the electric field interaction with the adjacent wall (314). In many cases, this control has been achieved with the help of active components (315, 317, 318). Despite the geometrical simplicity of

these cavities, their loaded *Q*-factor cannot be adjusted without shifting the resonant frequency. Therefore, the ability of efficiently controlling the cavity frequency response without resorting to active components is an important asset for any device application.

Although observed in many different geometries, FRs can be more conveniently produced via mode interaction in a waveguide ring resonator (WRR). This geometry allows both forward and backward propagating modes (319) to be excited simultaneously. Thus, each resonance involves two phase degenerate modes, one with sine and other with cosine azimuth dependence. In addition, the relative angular spacing between the excitation (transmitting) and detection (receiving) monopole antennas inside these cavities causes frequency shifts on each of these modes that allow them to interact with each other at the detection antenna, similar to the bright and dark mode interaction of optical FR. Therefore, the FR can be adjusted simply by acting on the mode interaction through a variation of the receiving antenna position. Consequently, if the cavity is correctly tuned, the FR can be used to increase the Q-factor even further.

In this chapter, we propose a WR-90-based WGM ring cavity with an adjustable position of the detection monopole antenna to investigate the generation of Fano-type resonances (FTRs) in the microwave regime. We demonstrate, both theoretically and experimentally, that by changing the relative angular spacing (θ) between the transmitting and receiving antennas, we can adjust both the frequency and intensity of the FTR. Moreover, we extend the cavity perturbation model (320) to investigate how the mode splitting occurs for different monopole antenna lengths and angular spacings while relying only on a single full-wave simulation with a fixed antenna length. We show that a $\sim 74\%$ increase in the cavity *Q*-factor is possible with a proper choice of both the antenna length and relative angular spacing θ.

The remainder of this work is organized as follows. Section 5.2 describes the ring cavity model and design procedure. Section 5.3 shows both the theoretical and experimental results that confirm the onset of FTRs. Section 5.4 carries out a performance evaluation of the WGM ring cavity. Finally, Section 5.5 presents some concluding remarks and Section A.2.6 presents the theory of Fano Resonances, confirming that our resonator is a FTR.

A.2.2 Design procedure and modeling

The design equations of the WR-90-based WGM cavity are the following (321):

$$\frac{1}{\lambda_h^2} = \frac{1}{\lambda_g^2} + \frac{1}{24R_{\text{WRR}}^2} \left[1 - \frac{12 + \pi^2}{24} \left(\frac{2w}{\lambda_o} \right)^2 + \frac{15 - \pi^2}{2\pi^2} \left(\frac{2w}{\lambda_o} \right)^4 \right], \qquad (A.1)$$

$$2\pi R_{\text{WRR}} = i\lambda_h, \qquad (A.2)$$

where λ_h is the guided wavelength for the bent waveguide, λ_g is the guided wavelength for the straight waveguide, λ_o is the free-space wavelength, R_{WRR} is the mean curvature radius, w is the waveguide width, and n is the number of guided wavelengths at resonance. We choose the TE_{10n} mode to resonate at 10 GHz with $i = 5$ because the resulting radius of curvature is large enough to allow for a straight waveguide approximation to be used for λ_g. Applying these parameters into (A.1) and (A.2), we obtain $R_{\mathrm{WRR}} = 31.43$ mm.

The mode designation adopted here follows the standard mode designation of microwave cavities which for TE modes is given by TE_{uvi}, where u and v are the transverse mode labels, and i the number of longitudinal wavelengths at resonance.

The cavity cross section is defined in terms of the WR-90 metallic waveguide standard, because it covers the X-band of the spectrum (8.2–12.4 GHz), with width $w = 22.86$ mm and height $h = 10.16$ mm.

The cavity consists of two separate components, with the top component (lid) rotatable with respect to the bottom component, as depicted in Fig. 35. The transmitting monopole antenna (T) is fixed at the 0° reference angle on the bottom component while the receiving antenna (R) is attached to the top rotating lid. The length of both antennas is denoted as l_{ant}, and the waveguide height h is the standard for the WR-90. This cavity setup allows us to vary the angular spacing between the two antennas by any angle θ between 10 and 360∘. Angles $< 10°$ are possible with smaller antenna sizes, as long as the direct mutual interaction between the antennas is negligible. This angle controls the interaction between the two phase degenerate modes present in the cavity, with azimuthal(ϕ) dependencies of the form $\cos(i\phi)$ for the bright mode (low Q) and $\sin(i\phi)$ for the dark mode (high Q). Note that the $\sin(i\phi)$ mode arises due to the field perturbation produced by the presence of the receiving antenna. When only the transmitting antenna is present inside the cavity, the electric field has a $\cos(i\phi)$ dependence and no FTR occurs.
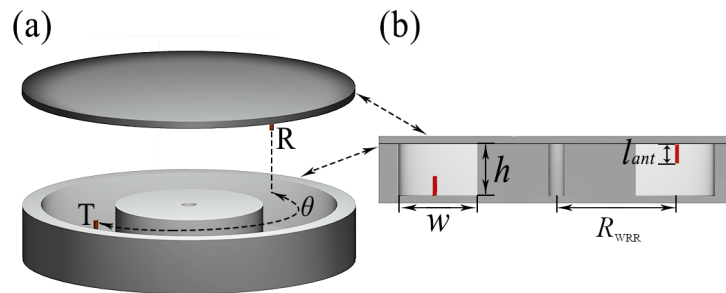
Figure 35 – 3D model of the ring cavity. (a) Internal view (bottom part) and flat lid (top part) with their respective transmitting (T, fixed at the 0° reference position) and receiving (R, with variable θ position) monopole antennas. (b) Transverse section view (with the lid on) with relevant dimensions indicated.

The $\sin(i\phi)$ mode arises due to the field perturbation produced by the presence

of the receiving antenna. When only the transmitting antenna is present (at $\phi = 0^{\text{o}}$), constructive interference (field maximum) between the two counter-propagating modes will occur at this antenna location only for the $\cos(i\phi)$ mode, and no FTR is generated. For the onset of the FTR to occur, the receiving antenna also needs to be present (but at locations different from $(180/2i)°$ relative to the transmitting antenna) to unbalance the electrical length of both modes, resulting in partial interference at these antenna locations.

Next, we adapt the cavity perturbation model proposed in (320) to understand the phenomenology behind the frequency splitting of the bright and dark modes and the generation of the FTR in the proposed cavity. This model helps us to explain the frequency shift $\Delta f = f - f_o$ caused by a perturbation within a given volume in terms of the change in the stored electric and magnetic energies in the cavity, where f is the operating frequency and f_o the unperturbed resonant frequency. This relation is as follows:

$$\frac{\Delta f}{f_o} = \frac{\Delta W_m - \Delta W_e}{W_m + W_e}, \tag{A.3}$$

where W_m and W_e are, respectively, the stored magnetic and electric energies of the unperturbed cavity, with ΔW_m and ΔW_e as their respective energy variations. Assuming the cavity perturbation as a small metallic post (given the monopole antenna geometry), and a uniform field intensity across the post radius (which is a valid assumption for a post diameter much smaller than the waveguide width), we obtain (320):

$$\frac{\Delta f}{f_o} = 2\frac{\Delta Vol}{Vol}\frac{\mu\left|\boldsymbol{H_o}\right|_{\text{post}}^2 - \epsilon\left|\boldsymbol{E_o}\right|_{\text{post}}^2}{\epsilon_o E_o^2}, \tag{A.4}$$

where Vol is the cavity volume and ΔVol the volume of the post or equivalently the cavity
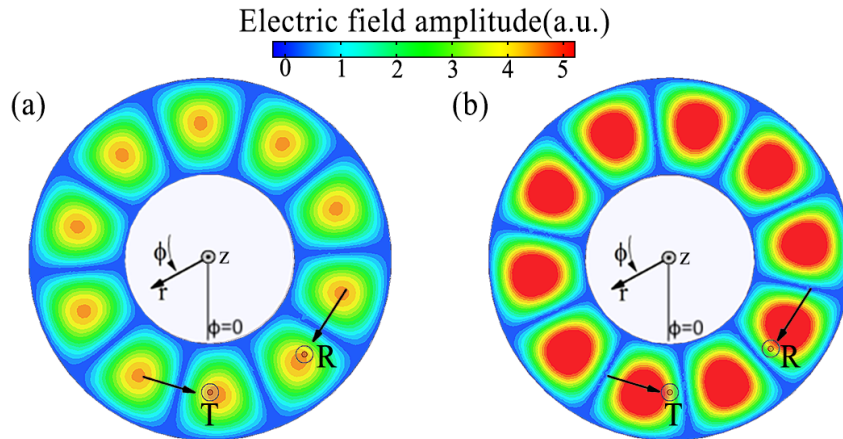
Figure 36 – Electric field magnitude at resonance. (a) Bright mode. (b) Dark mode. Arrows indicate the position of the transmitting and receiving antennas.

volume perturbation due to the presence of the post. $\boldsymbol{E_o}$ and $\boldsymbol{H_o}$ are the unperturbed electric and magnetic fields at the post position, E_o is the electric field amplitude, and ϵ

and μ are the permittivity and permeability of the medium filling the cavity, respectively. Fig. 36 shows the electric field magnitude at resonance with the transmitting and receiving antenna positions as indicated. Note that both modes have a symmetry plane at $\phi = \theta/2$ and that their field magnitudes are the same at both antenna locations. Note also that more energy is stored in the cavity by the dark mode, indicating a higher Q when compared to the bright mode, as expected in an FTR. At resonance, the fields magnitude at the radial position of the antennas are equivalent and expressed as follows:

$$\boldsymbol{E_{ob}}\left(\phi\right) = E_{ob}\cos\left[\beta R_{\mathrm{WRR}}\left(\phi + \alpha_{\mathrm{WRR}}\right)\right]\hat{z}, \tag{A.5}$$

$$\boldsymbol{E_{od}}\left(\phi\right) = E_{od}\sin\left[\beta R_{\mathrm{WRR}}\left(\phi + \alpha_{\mathrm{WRR}}\right)\right]\hat{z}, \tag{A.6}$$

$$\boldsymbol{H_{ob}}\left(\phi\right) = \frac{E_{ob}}{Z_{TE}}\sin\left[\beta R_{\mathrm{WRR}}\left(\phi + \alpha_{\mathrm{WRR}}\right)\right]\hat{r}, \tag{A.7}$$

$$\boldsymbol{H_{od}}\left(\phi\right) = \frac{E_{od}}{Z_{TE}}\cos\left[\beta R_{\mathrm{WRR}}\left(\phi + \alpha_{\mathrm{WRR}}\right)\right]\hat{r}, \tag{A.8}$$

$$\alpha_{\mathrm{WRR}} = \left(\frac{s\pi}{2i} - \frac{\theta}{2}\right), \tag{A.9}$$

where the subindices b and d refer to the bright and dark modes, respectively, ϕ is the azimuthal coordinate, β is the propagation constant, and α_{WRR} a parameter that depends on the angular spacing θ between the antennas, with $s = (\theta + \pi/2i)\mathrm{div}(\pi/i)$ (where div is the integer division operation). After substituting (A.5)–(A.9) into (A.4), and using the relation $Z_o/Z_{TE} = n_{eff}(f)$, where $n_{eff}(f)$ is the frequency-dependent effective index, $Z_o = (\mu_o/\epsilon_o)^{1/2}$ is the free space impedance, and Z_{TE} is the mode impedance, we obtain the bright and dark mode frequency shifts, Δf_b and Δf_d, as follows:

$$\frac{\Delta f_b}{f_o} = \frac{\Delta Vol}{Vol}\left\{n_{eff}^2\sin^2\left[\beta R_{\mathrm{WRR}}\left(\theta + \alpha_{\mathrm{WRR}}\right)\right] - \cos^2\left[\beta R_{\mathrm{WRR}}\left(\theta + \alpha_{\mathrm{WRR}}\right)\right]\right\}, \tag{A.10}$$

$$\frac{\Delta f_d}{f_o} = \frac{\Delta Vol}{Vol}\left\{n_{eff}^2\cos^2\left[\beta R_{\mathrm{WRR}}\left(\theta + \alpha_{\mathrm{WRR}}\right)\right] - \sin^2\left[\beta R_{\mathrm{WRR}}\left(\theta + \alpha_{\mathrm{WRR}}\right)\right]\right\}. \tag{A.11}$$

Equations (A.10) and (A.11) describe the frequency splitting due to variations on the angular spacing between the antennas.

While the original model (320) and its generalization in (A.10) and (A.11) assume *passive* metallic posts perturbing the cavity, here we need to replace these posts by the actual transmitting and receiving antennae. The presence of the antenna (which

absorbs/transmits power) results in a higher effective volume, defined here as $\Delta V' = 2KV_{\text{ant}}$ to be used in place of ΔVol in both (A.10) and (A.11). K is a correction factor which depends on the monopole antenna length and can be determined numerically as discussed later on in more detail. V_{ant} is the antenna volume, and the factor of 2 accounts for the presence of two antennas. Equation (A.4) then becomes

$$\frac{\Delta f}{f_o} = 2\frac{\Delta V'}{Vol}\frac{\mu \left|\boldsymbol{H}\right|^2_{\text{ant}} - \epsilon \left|\boldsymbol{E}\right|^2_{\text{ant}}}{\epsilon_o E_o^2}, \tag{A.12}$$

where $\boldsymbol{E}_{\text{ant}}$ and $\boldsymbol{H}_{\text{ant}}$ are the electric and magnetic fields, respectively, at the antenna position. Equation (A.12) is multiplied by 2 because the $\boldsymbol{E}$ and $\boldsymbol{H}$ fields in (A.5)-(A.8) have each the same magnitude at both $\phi = 0$ and $\phi = \theta$, so it suffices to calculate them for either of the antennae.

Differently from (320) (which uses short metallic posts), the use of antennas inside the cavity perturb the field in their vicinity in such a way as to increase the cavity electrical length, as observed in Fig. 37(a)–(d) for long antennas and different phases ωt. The longer the antennas, the greater the perturbation due to the higher coupling with the cavity mode. This localized effect requires a correction of the propagation constant β. This correction can be carried out by measuring the wavelength between two field minima near both antennas and averaging the results to obtain the correct β'. It is important to note that the constants K and β' can be found with a single simulation only for a given antenna size, as opposed to one simulation for each antenna size and angular spacing required to build the complete numerical solution. The correction factor K is obtained by isolating it from (A.10), with ΔVol replaced by $\Delta V'$, assuming $\theta = 180°$. At this angle, there is no dark mode excitation and the antenna is at an electric field maximum and magnetic field minimum. Therefore,

$$K = \frac{\Delta f_b}{f_o}\frac{Vol}{4V_{\text{ant}}}. \tag{A.13}$$

Figure 37(e) shows the azimuthal electric field distribution at the radial position of the antennas for various antenna lengths. Note that for longer monopole antennas (particularly those longer than 2.5 mm), the spatial distribution of the field near the monopole antennas is no longer sinusoidal as expected [the field magnitude observed around $\phi = 180°$ in Fig. 37(e) becomes narrower as the antenna length increases, rendering our model inaccurate. Fig. 38 shows the propagation constant variation normalized with respect to the unperturbed propagation constant β_h ($\beta_h = 2\pi/\lambda_h = n/a$), given by $\Delta\beta/\beta_h = (\beta' - \beta_h)/\beta_h$ as a function of the antenna length. This figure also shows the dependence of the K-factor with the antenna length. The antenna length is the parameter that most strongly influences these quantities, with the cavity radius producing a variation
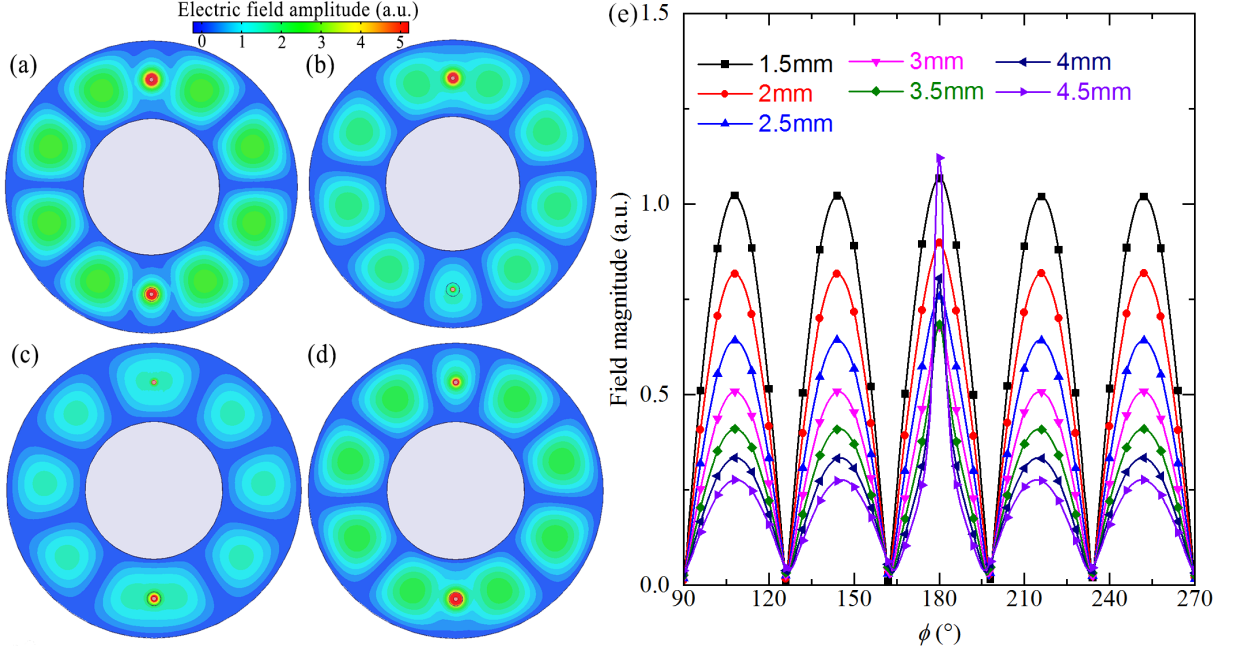
Figure 37 – Electric field modulus at resonance for a 180° relative angle between antennae and antenna length of 7.5 mm for the following ωt phases: (a) 0, (b) $\pi/4$, (c) $\pi/2$, and (d) $3\pi/4$. (e) Azimuthal electrical field distribution at resonance in the radial position of the antennas and a 180° angle between the antennas. The cavity behavior is quite different from a sinusoidal one when the antennae are longer than 2.5 mm.

below 2% (neglected in this analysis) even for a different excited mode. Thus, the final mode splitting equation Δ normalized to f_o is written as:

$$\frac{\Delta}{f_o} = \frac{\Delta f_b - \Delta f_d}{f_o} = 4K\frac{V_{\text{ant}}}{Vol}\left\{n_{eff}^2\left(\sin^2\left[\beta' R_{\text{WRR}}\left(\theta' + \alpha_{\text{WRR}}\right)\right] - \cos^2\left[\beta' R_{\text{WRR}}\left(\theta' + \alpha_{\text{WRR}}\right)\right]\right),\right.$$
$$\left. - \cos^2\left[\beta' R_{\text{WRR}}\left(\theta' + \alpha\right)\right] + \sin^2\left[\beta' R_{\text{WRR}}\left(\theta' + \alpha_{\text{WRR}}\right)\right]\right\}$$
$$(A.14)$$

$$\theta' = \theta - \frac{s\pi}{i}, \tag{A.15}$$

where θ' is the same as θ but with shifted origin (due to the change in the propagation constant) to guarantee it is within $[-\pi/2i, \pi/2i]$.

As will be demonstrated later in Section 5.3, the closer Δ is to zero, the more pronounced is the FR, suggesting the existence of an optimum angle θ (our goal here). Fortunately, the K-factor is not frequency-dependent (it depends only on the antenna size, as verified both numerically and experimentally) because at resonance, the antennas are almost perfectly impedance matched, leaving the field with which they interact as the only unknown. The numerically calculated resonant frequency values with and without the antennas are used to compute f_o and Δf_b.
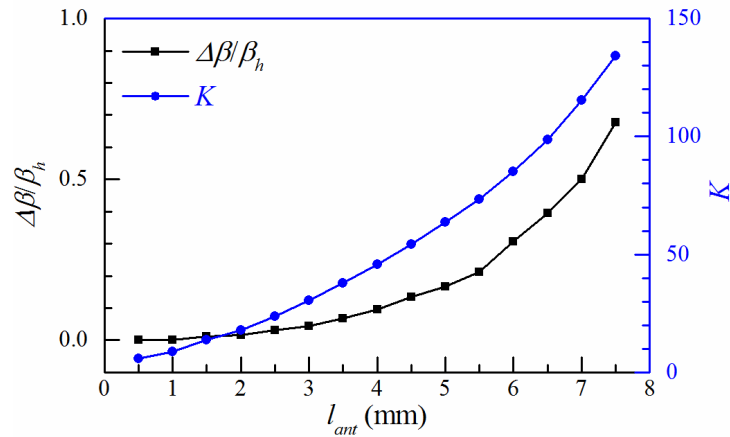
Figure 38 – Propagation constant correction factor $\Delta\beta$ (normalized to the unperturbed propagation constant β_h) and correction factor K as function of the monopole antenna length l_{ant}.

Fig. 39 presents a comparison between our model (blue, solid lines) and ANSYS HFSS (322) full-wave simulations (black, dashed lines), assumed here as benchmark, for antenna lengths ranging from 2 to 5 mm. The analytical model agrees well with the simulated results for antenna lengths smaller than 3 mm (it loses accuracy as the antenna length increases as discussed earlier). Longer antennae cause the mode separation to shift slightly toward lower separation angles. This shift occurs because our model assumes the cavity behavior as periodic with angular period $180°/i$. However, for smaller separation angles, the mutual interaction between both antennae affects the cavity response.
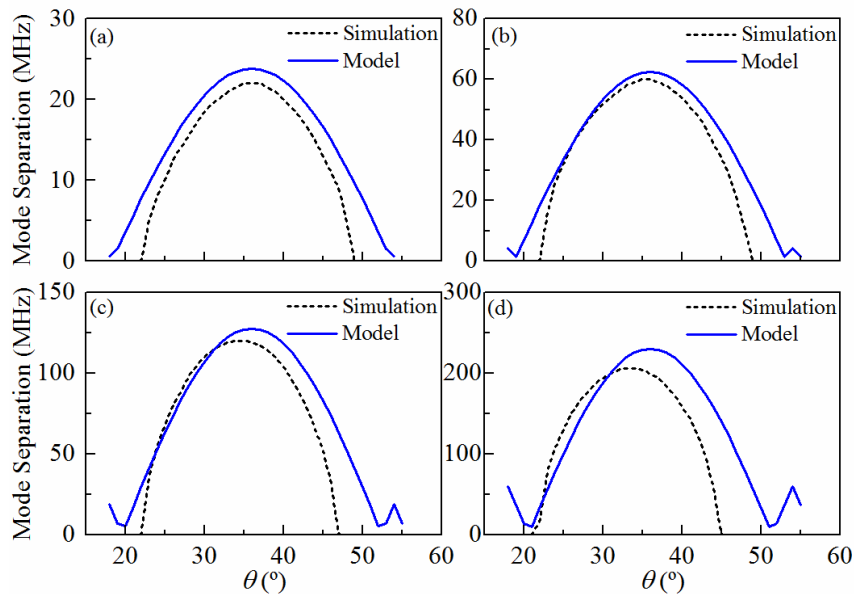
Figure 39 – Mode separation as function of the angular separation between the antennas for antenna lengths of (a) 2, (b) 3, (c) 4, and (d) 5 mm. The blue solid lines refer to our model while the black dashed lines refer to full-wave simulation results.

A.2.3   Results

The FTR dependence on θ is numerically simulated using HFSS assuming a cavity built entirely of aluminum with conductivity $\sigma_{\text{copper}} = 1.3 \times 10^7$ S/m. The WR-90 standard requires a cavity width $w = 22.86$ mm, but the inaccuracy of our fabrication process resulted in $w = 22.92$ mm (also adopted in the simulations for consistency). The cavity experimental characterization setup is shown in Fig. 40, where insets I and II show the cavity birds-eye view and internal view, respectively. The frequency response is obtained by a Rohde&Schwarz ZVA-40 VNA. As explained before, the transmitting and receiving monopole antennas are attached to the bottom (fixed) and top (rotating) surfaces of the cavity, respectively.
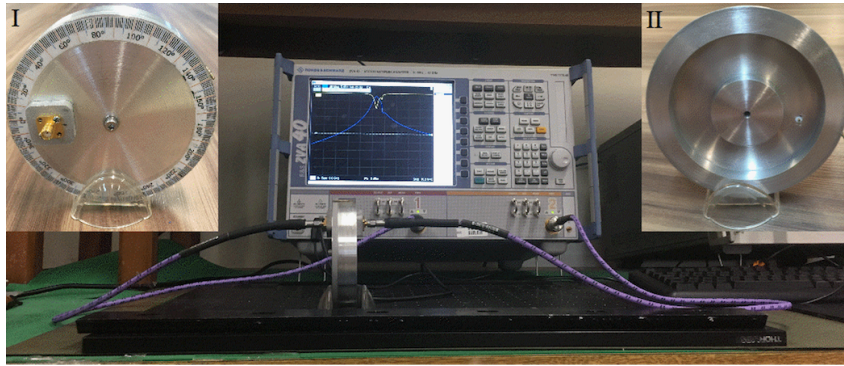
Figure 40 – Experimental setup. Inset I shows the birds-eye view of the fabricated cavity, while inset II shows the cavity internal view.

Before we proceed to the analysis of the ring cavity, it is worth mentioning that the scattering parameters S_{11} and S_{21}, although complementary to each other, are both a great tool to extract some of the figure-of-merits of the present cavity. Thus, it is easier to analyze the resonant frequencies via S_{11} maps due to their pronounced negative peaks (these peaks are less pronounced at lower Q values for the S_{21} maps when long antennas are used). In contrast, the slope of the FR is better observed with the S_{21} maps.

As previously mentioned, the mode coupling at the receiving antenna is highly dependent on θ and is responsible for the onset of FTRs. Fig. 41(a)–(f), where Fig. 41(a)–(c) refers to S_{11} (fraction of the wave reflected to the transmitting antenna) and Fig. 41(d)–(f) to S_{21} (fraction of the wave transmitted to the receiving antenna), shows the simulated reflection (S_{11}) and transmission (S_{21}) scattering parameters as function of the frequency f and angle θ. This analysis is carried out at the X-band (8.2–12.4 GHz) for $10° \leq \theta \leq 180°$. We investigate three different monopole antenna lengths (note that we consider transmitting and receiving antennas of same length) relative to 10 GHz: "small" (2 mm, $\lambda_o/15$) in Fig. 41(a) and (d), "medium" (3.75 mm, $\lambda_o/8$) in Fig. 41(b) and (e), and "long" (7.5 mm, $\lambda_o/4$) in Fig. 41(c) and (f). According to Fig. 41(a) and (d), the S_{11} and S_{21} results indicate four resonances located at 8.9, 10, 11.2, and 12.4 GHz when

excited with the small antenna, corresponding to the modes TE_{104}, TE_{105} (the desired mode), TE_{106}, and TE_{107}, respectively. Table 5 lists the resonant frequency and loaded quality factor (Q_l) for the TE_{105} mode at $\theta = 180°$ for each antenna length. For this angle, there is no mode asymmetry at the receiving antenna, and the cavity response resembles that of a straight cavity, i.e., a pure Lorentzian shape. Note that the long antenna [Fig. 41(f)] has the lowest Q of all three cases, indicating a strong interaction with the cavity modes. In this situation, more energy is collected by the receiving antenna, resulting in a reduced field confinement and a behavior similar to a waveguide. Also, note the absence of a 3-dB bandwidth (typical of straight waveguides) in the S_{21} plot, and how the resonant frequency decreases in inverse proportion to the antenna length as observed in the slice plot for $\theta = 180°$ [Fig. 41(g)] which arises due to the extremely wide band of each TE_{10n} mode.

Table 5 – Resonance parameters relative to Fig. 41 for $\theta = 180°$

Antenna length (mm)	Resonant frequency (GHz)	3-dB bandwidth (MHz)	Loaded Q
2.00	10.03	20.80	482
3.75	9.953	114.2	87.2
7.50	9.374	-	-

Regarding the angular spacing, each resonant mode TE_{10n} presents an angle periodicity of $180°/n$, associated with the number n of wavelengths along the cavity. Since both S_{11} and S_{21} present a behavior close to periodic as the function of θ and f, we analyze only one period of the TE_{105} mode in the ranges $18° \leq \theta \leq 54°$ and $9.8\,\text{GHz} \leq f \leq 10.2\,\text{GHz}$ (small antenna), $9.5\,\text{GHz} \leq f \leq 10.5\,\text{GHz}$ (medium antenna), and $8.5\,\text{GHz} \leq f \leq 10.5\,\text{GHz}$ (long antenna). These ranges correspond to the marked areas in Fig. 41, which are zoomed-in in Fig. 42(a), (c), (e), (g), (i), and (k) with their respective experimental results in Fig. 42(b), (d), (f), (h), (j), and (l) for comparison. Despite the small frequency shift, both simulated and experimental results agree very well. At $\theta = 36°$, there is no FTR. But as θ moves to $18°$ or $55°$, the FTR appears and undergoes a frequency splitting as shown in the S_{11} maps [Fig. 42(a), (b), (e), and (f)] and predicted by our model. In this region, sharp dips follow the S_{21} peaks, which are a clear indication of FTRs, see Fig. 42(c), (d), (g), and (h). Note that as θ moves closer to $18°$ or $55°$, the FTR dip approaches the cavity resonant frequency, thus reducing the resonance bandwidth and increasing the quality factor. In contrast, the longer the monopole antennas, the broader the bandwidth (consequently, the lower the Q-factor), as shown in Fig. 42(i)–(l). Interestingly, the long antenna cavity also exhibits narrowband and low transmission behavior at $\theta = 18°$ or $55°$ close to FTR dips, as seen in Fig. 42(k) and (l), which is suitable for bandstop filter applications. In contrast, the small and medium antenna cavities are suitable for bandpass applications, as discussed next.
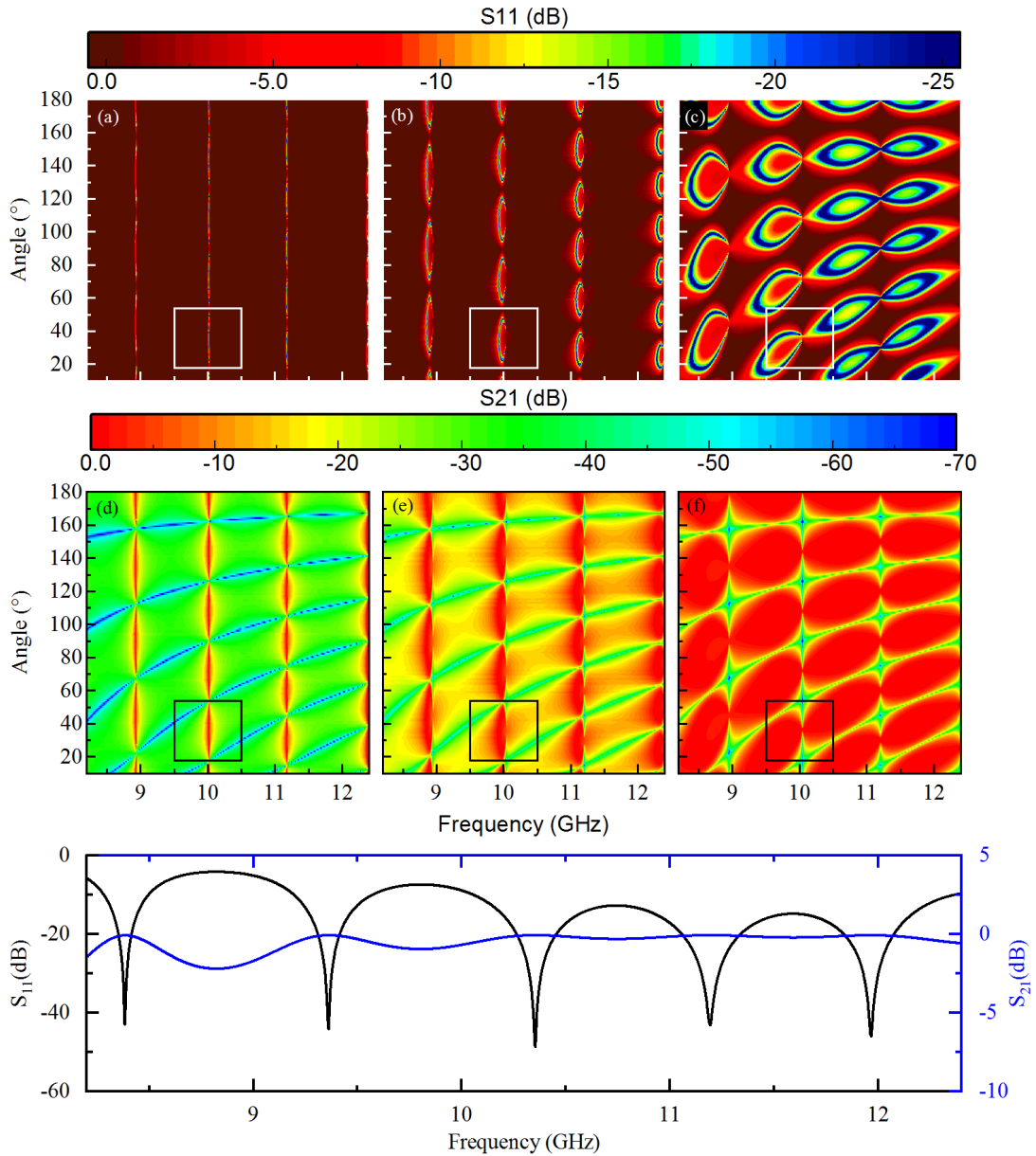
Figure 41 – Simulated 2D maps of the cavity S parameters. (a)–(c) S_{11} maps for small, medium, and long antennas, respectively. (d)–(f) S_{21} maps for small, medium, and long antennas, respectively. Smaller antennas improve the quality factor while longer antennas widen the bandwidth. (g) Slice of (c) and (f) at $\theta = 180°$. Selected areas are zoomed-in and compared numerically and experimentally in Fig. 42.

In order to confirm the role of the interaction between bright and dark modes, we show in Appendix C that the main resonance features can be well described by a coupled oscillator model.

A video of the cavity frequency response as a function of the angular separation θ between transmitting and receiving antennas is available in (296), for 2- and 7.5-mm-long antennas.
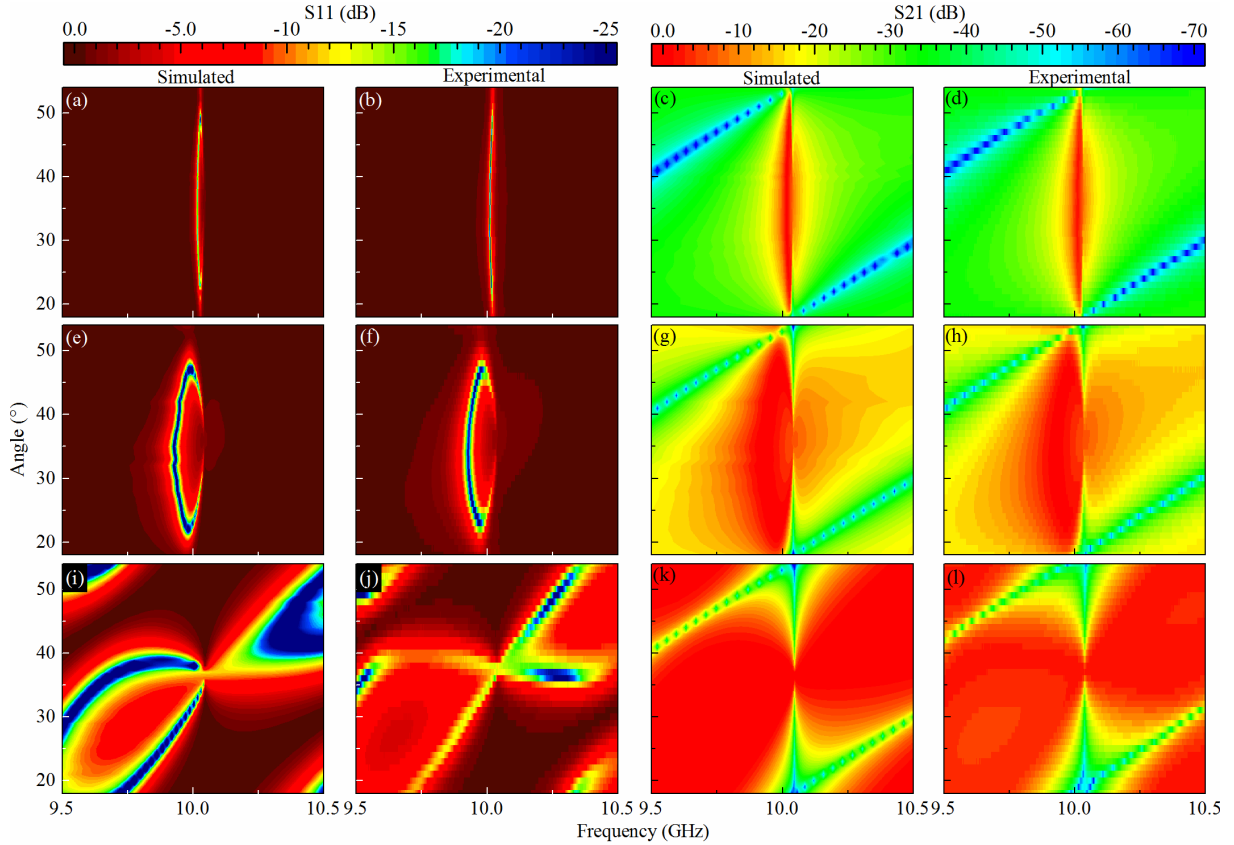
Figure 42 – (a), (c), (e), (g), (i), and (k) Numerical and (b), (d), (f), (h), (j), and (l) experimental S_{11} (left) and S_{21} (right) parameters of the ring cavity using the small (top row), medium (middle row) and long (bottom row) antennas.

A.2.4   Cavity performance

The cavity bandpass characteristics are now investigated for both small and medium antennas to further evaluate the influence of θ on the cavity Q-factor and transmission properties. Fig. 43 shows the simulated (hollow squares) and measured (full squares) Q_l (black lines) values calculated from the 3-dB bandwidth along with the maximum transmission (S_{21}) (blue lines). The highlighted areas in this figure indicate the regions (I) where both Q_l and insertion loss are low (with little to no influence of the angle-dependent FTR), and (II) with variable (low to high) Q_l and insertion loss (where the angle-dependent FTR plays an important role). The angles at which the frequency splitting Δ approaches zero [according to our model, see Fig. 39(a)] are $\theta = 18°$ and $53°$ for the 2-mm antenna, and $\theta = 19°$ and $52°$ for the 3.75-mm antenna. The experimental and measured results agree very well, and the difference between them can be attributed to the aluminum conductivity adopted in the simulations (connectors and cable losses not included). The insertion loss observed in Region II of both antennae occurs when the receiving antenna is at a region of low-intensity electric field. Note that Q_l reaches 670 at $\theta = 49°$, with an additional insertion loss of 1.9 dB when compared to $\theta = 36°$ for the 2-mm antenna. Similar behavior is observed for the medium size antenna at the same angle, with Q_l as
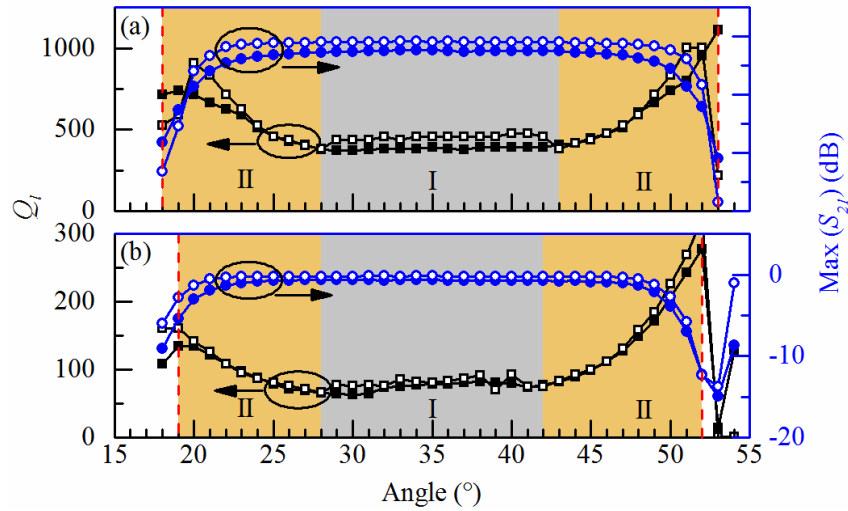
Figure 43 – Cavity $Q_l \times \theta$ (black lines) and maximum $S_{21} \times \theta$ (blue lines) in the passband regime with (a) 2- and (b) 3.75-mm antennas. Filled symbols refer to measured results while hollow symbols refer to simulations. In region I (light gray), there is no influence of both the angle and FTR on the cavity Q_l. In contrast, in region II (light brown) we observe a significant increase in Q_l due to the FTR excited via θ. The red dashed lines indicate the angles where the frequency splitting $\Delta = 0$, as predicted with the proposed model.

high as 172 for an additional insertion loss of 1.4 dB. Therefore, the optimum angle for a given application is within region II, and there is a compromise between the highest possible Q for an acceptable insertion loss.

Table 6 provides a comparison between our cavity, when excited with a 2-mm antenna (our best case) and several other microwave cavity types (315, 321, 323–328), along with their performance and dimensions. Observe that the performance of the proposed WRR with FTR (WRR-FTR) cavity is unmatched by any of the structures listed.

Table 6 – Performance comparison between the proposed cavity and published works. The cavity types are WRRs, WRR-FTR, waveguide resonators (WRs), microstrip resonators (MRs), substrate integrated waveguide (SIW), evanescent mode cavities (EMCs), and MEMS adjusted resonators. Ø stands for diameter

Reference	Type	S_{21} (dB)	Q_l	Size (mm)
This work	WRR-FTR	$-2.0 \sim -20$	$385 \sim 1110$	Ø90.0 x 16.0
(321)	WRR	-5.0	776	Ø24.0 x 10.0 (internal)
(323)	EMC	-	250	14.0 x 14.0 x 5.00
(324)	WR (low temp.)	-	714	Ø10.0 x 1.40 (internal)
(325)	SIW	-0.4	20.6	16.0 x 32.0 x 1.00
(326)	WR	$-0.6 \sim -2.6$	22.2	31.5 x 24.0 x 20.0
(327)	EMC	Active circuit	253	-
(328)	MR	-8.1	487 (unloaded)	112 x 49.0 x 3.20
(315)	MEMS	-1.0	229	17.0 x 17.0 x 6.00

Next, we assess the cavity frequency response at a specific angle within the optimum range (Region II), namely $\theta = 23°$ and $49°$, for the three antenna cases. Fig. 44 shows the measured (solid lines) and simulated (dashed lines) results relative $\theta = 23°$ (blue lines) and $\theta = 49°$ (black lines) for the small (a), medium (b), and (c) long antenna cases. At these angles, the resonance frequency is followed by a steep dip, clearly indicating the presence of an FTR. The FTR steep slope decreases the overall bandwidth, resulting in a higher Q_l. Furthermore, in addition to yielding a broader passband, the medium antenna case also yields a larger splitting between the main resonance and the FTR, resulting in a lower Q_l as compared to the small antenna case, as shown in Fig. 44(a)–(c). Thus, small antennas are appropriate for applications that require high-quality factors, and medium or long antennas for those requiring broader bandwidths. We have observed that the SMA connectors, rated at 500 V_{rms} (329), or equivalently to 67 dBm with a 50-Ω load, are the cavity power limiting factor. The wide dynamic range for tuning both the Q-factor and the resonance frequency suggests that this cavity can be useful for both sensing and wavelength filtering applications. Note further that in the optimum regions of both antennas, even the smallest change in the operating frequency dramatically changes the measured output power (due to the FTR steep slope), significantly improving the sensitivity in this region. This property may prove useful not only for wavelength filtering and sensing but also for modulator and oscillator applications.
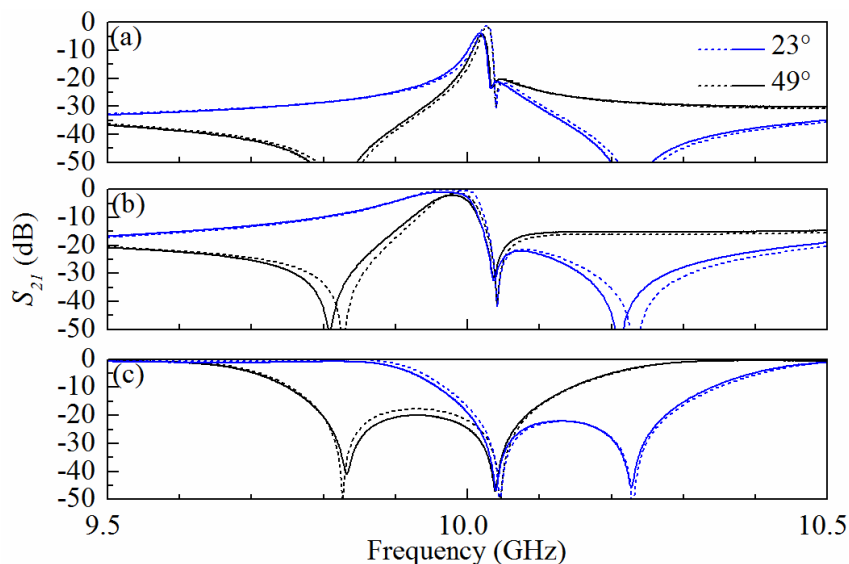
Figure 44 – Cavity response for $\theta = 23°$ (blue lines) and $49°$ (black lines) with (a) 2-, (b) 3.75-, and (c) 7.5-mm-long antennas. Solid and dashed lines refer to measured and simulation data, respectively.

In summary, the choice of applications that may benefit from this cavity design is only limited by the antenna length and the relative angle separation between transmitting and receiving antennas. The degrees-of-freedom provided by this cavity design allows both the Q-factor and free-spectral range of the cavity to be broadly tuned. Moreover,

based on recently published Fano resonant-based structures (231, 330–336), we believe that our approach, which is, to the best of our knowledge, the only so far capable of controlling the onset of FRs without resorting to active components, has a great potential to be used in sensing and wavelength filtering applications (because of the easy control of both the sensitivity and/or selectivity of these devices). More importantly, this approach also bridges the gap for improving more sophisticated applications, such as microwave modulators, microwave phase shifters, and switches.

A.2.5 Conclusion

In this chapter, we have proposed a novel bandpass/bandstop ring-type microwave WGM cavity resonator with tunable bandwidth for sensing and wavelength filtering applications. The approach adopted here uses for the first time FTRs excited via continuous angular variation between transmitting and receiving monopole antennas. We have described the onset of the FTR, and how mode splitting and mode interaction occur inside the cavity. We have measured an $\sim 74\%$ increase in the loaded quality factor compared to regular ring cavities with only 1.9 dB (1.4 dB) additional loss when using a 2-mm (3.75-mm) length antennas. We were able to increase the quality factor up to 190% with a 2-mm-long antenna and up to 249% with a 3.75-mm-long antenna with acceptable insertion loss. We have also shown that, by carefully choosing the size of the transmitting and receiving antennas and the angular spacing between them, we can easily tune the cavity. The extra degree-of-freedom provided by the angular spacing variation is responsible for the onset of the FTRs and allowed us to tune the quality factor Q continuously from 385 to 670.

A.2.6 Fano resonances

A commonly used model to help understand the onset of FR is the coupled oscillator model (299, 337), consisting of two weakly coupled oscillators with slightly different resonant frequencies. The excitation is assumed to be present in the first oscillator (bright mode), while the second (dark mode) is indirectly excited via coupling with the first. Mathematically, this coupling is governed by the following matrix equation (299):

$$\begin{pmatrix} f_1 - f - i\alpha_1 & g \\ g & f_2 - f - i\alpha_2 \end{pmatrix} \begin{pmatrix} x_1 \\ x_2 \end{pmatrix} = i \begin{pmatrix} F_1 \\ F_2 \end{pmatrix}, \tag{A.16}$$

where $x_{1,2}$ are the oscillator amplitudes, $f_{1,2}$ the resonant frequencies, $\alpha_{1,2}$ the damping coefficients, $F_{1,2}$ the external forces with driving frequency ω, and g the coupling factor. Assuming the excitation in oscillator 1 ($F_2 = 0$), (A.16) simplifies to

$$x_1 = iF_1 \left(\frac{f_2 - f - i\alpha_2}{(f_1 - f - i\alpha_1)(f_2 - f - i\alpha_2) - g^2} \right). \tag{A.17}$$

According to (299), for the FR to occur, the two oscillators require strongly different damping coefficients ($|\alpha_1| \neq |\alpha_2|$) and weak coupling ($|g| < |\alpha_1|$ or $|g| < |\alpha_2|$). We can confirm that the resonance type observed in our results is indeed an FR by using the perturbation model described in the previous section to find the frequency splitting ($f_1 - f_2$) and by fitting the remaining parameters into (B.1). To verify the cavity behavior, we carry out a parameter fitting at an arbitrary angle (say $134\,\circ$) using (A.17), with $f_1 = 10.034$ GHz, $f_2 = 10.057$ GHz, $\alpha_1 = 5.6 \times 10^7$ 1/s, $\alpha_2 = -2.92 \times 10^6$ 1/s, and $g = 3.87 \times 10^6$ 1/s^2 . Note that these values fully satisfy the conditions to obtain a classical FR. Fig. 45 shows the fitted (blue, dashed lines) and simulated (black, solid lines) curves.
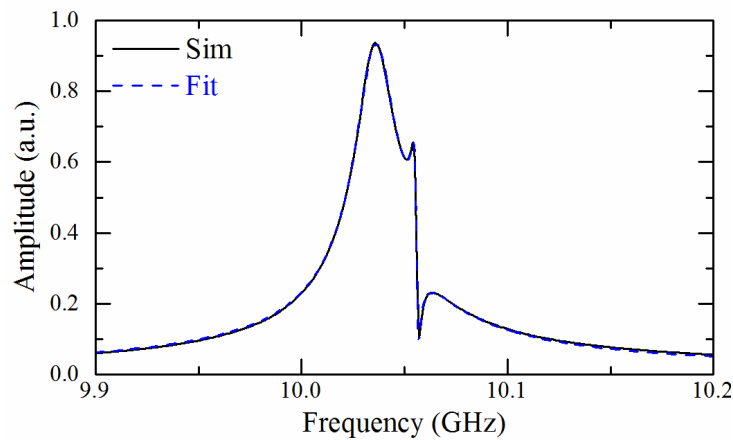
Figure 45 – Fitted (blue, dashed lines) and simulated (black, solid lines) FR transmission data for a 2-mm-long antenna at $\theta = 134°$.

Appendix B – TUNABLE TERAHERTZ BESSEL BEAM GENERATION USING DUAL COMPLEMENTARY MICROHOLED METASURFACES: APPENDICES

B.1 Scalar diffraction theory of an aperture-limited Bessel beam

A non-diffracting beam is a solution of the Helmholtz equation in which the field intensity at a given point (x, y) does not change along the propagation direction z (189). We write the Helmholtz equation below:

$$\left(\nabla^2 - k^2\right) \boldsymbol{E}\left(x, y, z\right) = 0, \tag{B.1}$$

where $\boldsymbol{E}$ is the electric field and $k = \sqrt{k_x^2 + k_y^2 + k_z^2}$ is its wavenumber. Since we are using scalar optics for the analysis, we only use E as the scalar version of the electrical vectorial field $\boldsymbol{E}$ from now on. The simplest non trivial solution of (B.1) is a plane wave with amplitude E_o, which can be written as:

$$E\left(x, y, z\right) = E_o \mathrm{e}^{j(k_x x + k_y y + k_z z)}. \tag{B.2}$$

Since (B.1) is a linear differential equation, any sum of different plane waves is also a solution. Thus, we can define a beam as a coherent superposition of infinite plane waves with different propagation directions. Since we want this beam to be non-diffracting in the z direction, we define its dependence in the propagation direction as $\mathrm{e}^{jk_z z}$ and apply the same momentum k_r in the transverse direction $r = \sqrt{x^2 + y^2}$.

$$E\left(x, y, z\right) = E_o \mathrm{e}^{jk_z z} \int_0^{2\pi} f\left(\phi\right) \mathrm{e}^{jk_r(x \cos \phi + y \sin \phi)} \, \mathrm{d}\phi. \tag{B.3}$$

In the equation above, $f\left(\phi\right)$ is a complex function of the angle $\phi = \tan^{-1}\left(y/x\right)$. The simplest solution of (B.3) is when $f\left(\phi\right) = 1$. Note that it describes a superposition of infinite plane waves circularly distributed bur with the same radial wavenumber k_r. The solution of the integral and the required phase discontinuity $\varphi\left(r\right)$ to generate this non-diffracting beam are:

$$E\left(x, y, z\right) = E_o \mathrm{e}^{jk_z z} \mathrm{J}_o\left(k_r r\right), \tag{B.4}$$

$$\varphi\left(r\right) = -k_o r NA, \tag{B.5}$$

$$NA = \frac{k_r}{k_o}, \tag{B.6}$$

where J_b is the Bessel function of the first type and b-th order, NA is defined as the numerical aperture of the axicon used to generate the Bessel beam. Unfortunately, the presented solution, although very elegant, is not physically realizable due to it possessing infinite energy. Thus, only truncated versions of the Bessel beam are realizable, either limited by a circular aperture of the size of the axicon, or soft-limited beams, like the Bessel-Gauss beam (338), which is more common in optical systems exited by Gaussian profile lasers. From a geometric optics standpoint, the incident rays are bent with an angle equal to $\sin^{-1} NA$. Inside the interference region, the resulting waveform is a Bessel beam and outside this region, the wavefront starts to diffract. The non-diffracting distance DOF for an axicon with radius R is defined as:

$$DOF = \frac{R_{ax}}{\tan\left(\sin^{-1} NA\right)} \simeq \frac{R_{ax}}{NA}, \tag{B.7}$$

Note that the approximation in (B.7) is valid only in the paraxial regime satisfying $\sin\theta_t \simeq \tan\theta_t$, $\theta_t \in (0, 2\pi)$. However, the geometric optics approximation ($k \to \infty$) neglects the diffraction caused by the beam aperture. A complete analysis in present for Bessel-Gauss beams form a wave optics standpoint (338), but unfortunately a similar analysis is not existent for hard circular apertures due to its more complex solution via Lommel functions (339, 340). Nonetheless, we investigate the conditions of validity of the ray optics approximation using scalar diffraction theory. According to the angular spectrum formalism (94), the diffraction of a given field distribution $E(x, y, 0)$ at a distance z is given by:

$$E(x, y, z) = \mathcal{F}^{-1}\left\{e^{jk_z z}\mathcal{F}\left[E(x, y, 0)\right]\right\}, \tag{B.8}$$

$$k_z = \sqrt{k^2 - k_x^2 - k_y^2}, \tag{B.9}$$

where $\mathcal{F}$ and $\mathcal{F}^{-1}$ denote the direct and inverse Fourier transforms, respectively.

$$\mathcal{F}\left[o(x, y)\right] = O(k_x, k_y) = \iint_{\mathbb{R}_2} o(x, y)\, e^{-j(k_x x + k_y y)}\, \mathrm{d}x\mathrm{d}y, \tag{B.10}$$

$$\mathcal{F}^{-1}\left[O(k_x, k_y)\right] = o(x, y) = \frac{1}{4\pi^2}\iint_{\mathbb{R}_2} O(k_x, k_y)\, e^{j(k_x x + k_y y)}\, \mathrm{d}k_x\mathrm{d}k_y. \tag{B.11}$$

Since we are dealing with circularly symmetric functions, we choose to use the Fourier-Bessel transform instead, noted as $\mathcal{B}$ and $\mathcal{B}^{-1}$.

$$\mathcal{B}\left[o(r)\right] = O(\kappa) = 2\pi \int_0^\infty o(r)\, J_o(\kappa r)\, r\, \mathrm{d}r, \tag{B.12}$$

$$\mathcal{B}^{-1}\left[O\left(\kappa\right)\right] = o\left(r\right) = \frac{1}{2\pi}\int_0^\infty O\left(\kappa\right)\mathrm{J}_o\left(\kappa r\right)\kappa\,\mathrm{d}\kappa, \tag{B.13}$$

where $\kappa = \sqrt{k_x^2 + k_y^2}$ is the spatial frequency in radial coordinates. Rewriting (B.8) using Fourier-Bessel transforms, we get

$$E\left(r,z\right) = \mathcal{B}^{-1}\left\{\mathrm{e}^{jz\sqrt{k^2-\kappa^2}}\mathcal{B}\left[E\left(r,0\right)\right]\right\}, \tag{B.14}$$

Now, we define the incident field $E\left(r,0\right)$ as the axicon response multiplied by a circular aperture:

$$E\left(r,0\right) = \mathrm{e}^{-jk_r r}\Theta\left(\frac{r}{R_{ax}}\right), \tag{B.15}$$

$$\Theta\left(\frac{r}{R}\right) = \begin{cases} 1 & ,\text{for } r \leq R_{ax} \\ 0 & ,\text{for } r > R_{ax} \end{cases}. \tag{B.16}$$

Due to the convolution property, we can separate the two terms of (B.15) as below:

$$\mathcal{B}\left[E\left(r,0\right)\right] = \mathcal{B}\left[\Theta\left(\frac{r}{R_{ax}}\right)\right]**\mathcal{B}\left[\mathrm{e}^{-jk_r r}\right]. \tag{B.17}$$

Note that the operator $**$ denotes the two dimensional convolution, as defined in (341) for circularly symmetric functions. It should be especially noted that this operation breaks the circular symmetry of the system. The angular spectrum of the circular aperture (94) and of the axicon (342) are given by:

$$\mathcal{B}\left[\Theta\left(\frac{r}{R_{ax}}\right)\right] = 2\pi R_{ax}\frac{\mathrm{J}_1\left(\kappa R_{ax}\right)}{\kappa}, \tag{B.18}$$

$$\mathcal{B}\left[\mathrm{e}^{-jk_r r}\right] = \frac{\delta\left(\kappa - k_r\right)}{\kappa}, \tag{B.19}$$

where $\delta\left(\kappa - k_r\right)$ is a ring impulse at $\sqrt{k_x^2 + k_y^2} = k_r$ and equal to 0 otherwise. Due to it being a ring impulse function, the two dimensional convolution operation $O\left(\kappa\right)**\delta\left(\kappa - k_r\right)/\kappa$ is not conducted by simply shifting the origin of $O\left(\kappa\right)$ by k_r, but rather by shifting and integrating $O\left(k_x, k_y\right)$ in the ring $\sqrt{k_x^2 + k_y^2} = k_r$ for $\tan^{-1}\left(k_y/k_x\right) = (0, 2\pi)$. While this is not a trivial operation, we make a qualitative analysis here. It's easy to see that the circular aperture spreads the angular spectrum of the axicon. The geometric optics approximation for calculating DOF is valid when the diffraction induced by the circular aperture is

negligible. That is, when the bandwidth of its angular spectrum is much smaller than the angular spectrum of the axicon.

$$FWHM \left[2\pi R_{ax} \frac{\mathrm{J}_1\left(\kappa R_{ax}\right)}{\kappa} \right] \ll k_o NA. \tag{B.20}$$
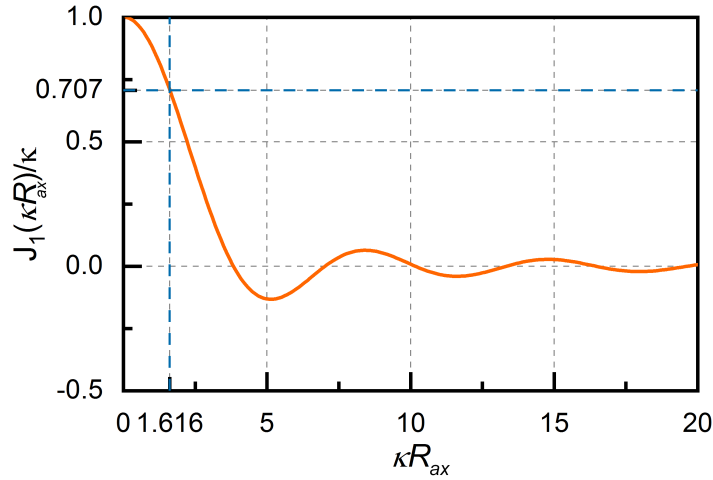
Figure 46 – Fourier-Bessel transform of a circular aperture of radius R_{ax}. Vertical axis shows its normalized amplitude and horizontal axis shows the product of the aperture radius R_{ax} and the spatial frequency κ.

Figure 46 shows the normalized angular spectrum of a circular aperture of radius R_{ax}, for normalized values of R_{ax}. Its FWHM happens for $\kappa = \pm 1.616/R$. Therefore,

$$NA \gg \frac{3.232\lambda}{2\pi R_{ax}}. \tag{B.21}$$

Equation (B.21) must be satisfied when the ray optics approximation is used.

Figure 47 shows the *DOF* and *FWHM* values for varying values of R_{ax}, when using $NA = 0.02$ and $\lambda = 350$ μm. Orange curves refer to values obtained via geometric optics (where *DOF* is obtained from (B.7) and *FWHM* is obtained from (3.4) in the main manuscript, which is the *FWHM* of an ideal J$_o$ diffraction free Bessel beam). Blue curves are obtained via angular spectrum simulations. The dashed blue curve refers to the distance between $z = 0$ until the beam intensity at $(x, y) = (0, 0)$ is equal to half of its maximum value, while the solid curve refers to the depth of focus where the beam intensity is higher than half of its maximum. To better visualize its meaning, see Figures S3 and S4, which show the diffraction patterns for $R_{ax} = 1$ cm and 50 cm, respectively. Orange lines in panels (a) show the ray optics approximation, showing the non-diffracting region. However, it doesn't predict oscillations along the propagating distance before the non-diffracting distance is reached, while in practice these oscillations exist (see panels (c)). This explains why the dashed blue line in Figure 47(a) asymptotically approach the

orange line while the solid blue curve initially approaches it but as the oscillations in the z direction become more intense the difference between them increases. Moreover, panels (b) and (d) in Figures 48 and 49 explain the behavior observed in Figure 47. As the aperture increases, the beam cross section in more similar to a Bessel function, while for smaller apertures, the resulting beam is a composition of a Bessel J_o function and Lommel functions, resulting in a smaller beam waist and less intense side lobes. A similar phenomenon happens in Bessel-Gauss beams, where when the angle applied by the axicon is smaller than the angles of the waves that compose the Gaussian beam, the resulting beam resembles a pure Gaussian profile (338).

B.2   Self healing properties of the Bessel beam

A Bessel beam is known to regenerate its original profile after being partly obstructed $(193, 195, 342)$, recovering its original intensity profile after propagating for a distance z_{sh}. From a ray optics stand point, its regeneration property is analyzing by noting that the superposition of plane waves is only blocked by a given obstruction for a limited distance. After this distance, the beam profile is recovered. This effect is shown in Figure 50. If the obstruction is coaxial with the Bessel beam and has radius r_{ob}, the self-healing distance is given by:

$$z_{sh} \simeq \frac{r_{ob}}{NA}. \tag{B.22}$$

Wave optics analyses of this phenomenon are present in the literature for Bessel-
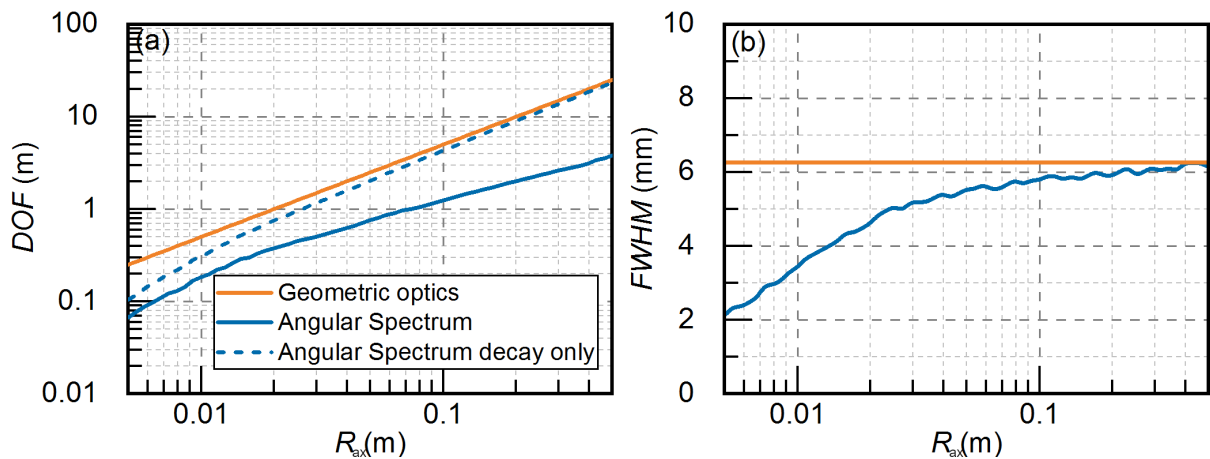
Figure 47 – Comparison of (a) DOF and (b) $FWHM$ values in the geometric optics approximation (orange lines) and simulates with the angular spectrum formalism (blue lines) for varying aperture values of the incident wave, with $NA = 0.02$ and $\lambda = 350 \ \mu$m. Solid blue lines in panel (a) refer to the distance between half power points while dashed lines refer to the distance from $z = 0$ to the highest value of z where the intensity is equal to half of the maximum value.
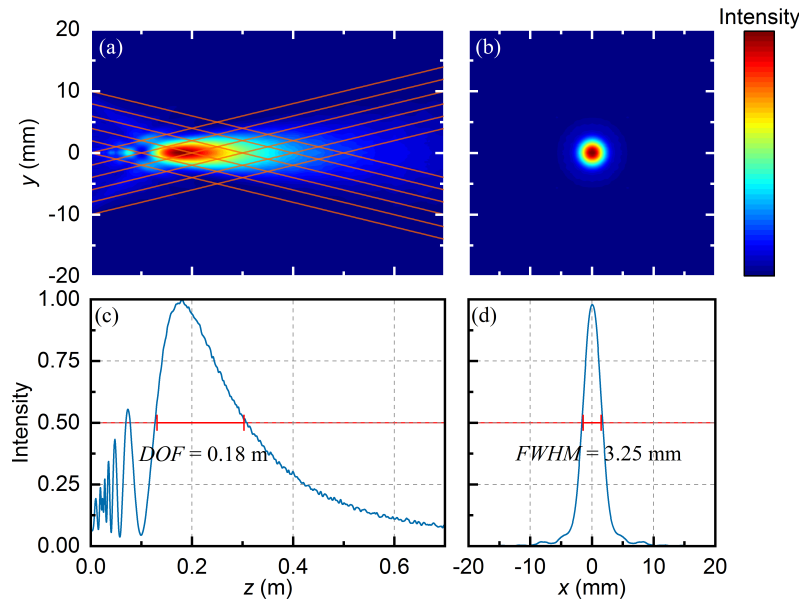
Figure 48 – (a) Longitudinal section and (b) cross section for the propagation of a Bessel beam with $NA = 0.02$, $\lambda = 350$ μm and $R_{ax} = 1$ cm. Orange lines show the ray optics approximation. (c) and (d) show the a slice of (a) and (b) at $y = 0$. Red lines limit the half power region that defines DOF and $FWHM$. Note in panel (c) that there are intensity oscillations in the z direction that are not predicted when using ray optics. These increase the difference between the approximated and actual DOF values.
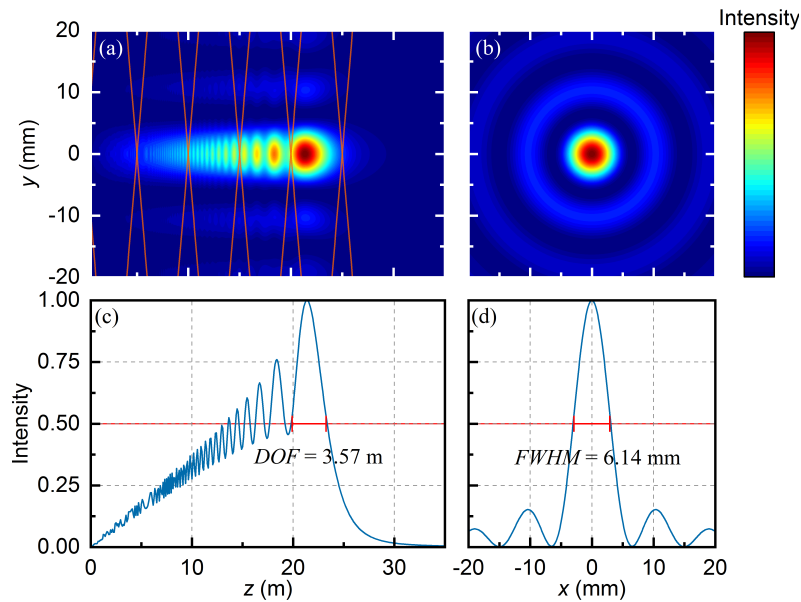
Figure 49 – (a) Longitudinal section and (b) cross section for the propagation of a Bessel beam with $NA = 0.02$, $\lambda = 350$ μm and $R_{ax} = 50$ cm. Orange lines show the ray optics approximation. (c) and (d) show the a slice of (a) and (b) at $y = 0$. Red lines limit the half power region that defines DOF and $FWHM$. Note in panel (c) that there are intensity oscillations in the z direction that are not predicted when using ray optics. These increase the difference between the approximated and actual DOF values.
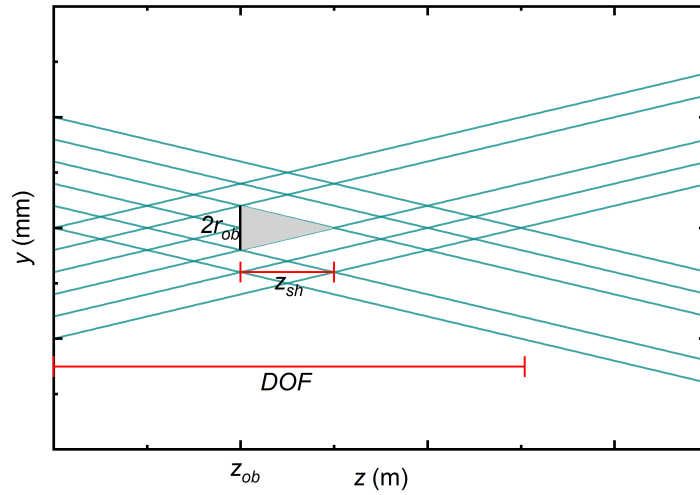
Figure 50 – Geometric optics representation of the self-healing property of Bessel beams. The output of an axicon is a coherent superposition of plane waves with the same radial momentum. At a distance z_{ob} the beam is obstructed by an opaque object with radius r_{ob}, partially blocking the rays. This shadow exists for a distance z_{sh}, after which the rays interference (and thus the Bessel beam profile) is recovered. If $z_o + z_{sh} < DOF$, the beam regenerates. If $z_o + z_{sh} > DOF$, the beam isn't regenerated. For the sake of cleanness of the diagram, reflected rays are not shown.

Gauss beams with soft Gaussian obstructions (342) and for arbitrary obstructions with ideal Bessel beams (infinite energy) (193). When the condition in (B.21) isn't satisfied, a complete wave optics analysis results in complex equations based on Lommel functions, as discussed in the previous section. Nevertheless, we provide a qualitative background to understand the mechanisms behind the beam regeneration, while the quantitative analysis is obtained via angular spectrum simulations. Consider a circular opaque object centered at $(x, y) = (0, 0)$ in the plane $z = z_{ob}$. The transmission function of such object is:

$$T(r) = 1 - \Theta\left(\frac{r}{r_{ob}}\right), \tag{B.23}$$

where the second term is equivalent to the transmission function of a circular aperture, which diffraction pattern is described in the previous section. Thus, we can write an expression for the obstructed field $E^{ob}(r, z_{ob})$ in the position z_{ob}:

$$E^{ob}(r, z_{ob}) = E(r, z_{ob}) - E(r, z_{ob})\,\Theta\left(\frac{r}{r_{ob}}\right). \tag{B.24}$$

By using the angular spectrum formalism from (B.8), the obstructed field $E^{ob}(r, z)$ for $z > z_{ob}$ is equal to:

$$E^{ob}(r, z > z_{ob}) = E(r, z) - \mathcal{B}^{-1}\left\{ e^{jk_z(z - z_{ob})} \mathcal{B}\left[E(r, z_{ob})\,\Theta\left(\frac{r}{r_{ob}}\right) \right] \right\}. \tag{B.25}$$

Knowing that the angular spectrum of $\Theta\left(r/r_{ob}\right)$ can be obtained from (B.18), it's intuitive that the second term in (B.25) is diffractive. Finally, when the amplitude of this term is negligible when compared to the term $E\left(r,z\right)$, $E^{ob}\left(r,z\right) \to E\left(r,z\right)$ and the Bessel beam profile is recovered. In our numerical simulations, we define z_{sh} as the distance $\left(z - z_{ob}\right)$ when the correlation coefficient between $\left|E(r < R, z_{ob})\right|$ and $\left|E^{ob}(r < R, z > z_{ob})\right|$ is above 0.9, similarly to previous work in self-healing beams (195). The correlation coefficient is defined as:

$$
\text{corr}\left[E\left(r, z_{ob}\right), E^{ob}\left(r, z\right)\right] = \frac{\text{cov}\left[\left|E\left(r < R_{ax}, z_{ob}\right)\right|, \left|E^{ob}\left(r < R_{ax}, z\right)\right|\right]}{\varsigma\left[\left|E\left(r < R_{ax}, z_{ob}\right)\right|\right]\varsigma\left[\left|E^{ob}\left(r < R_{ax}, z\right)\right|\right]}, \tag{B.26}
$$

where $\varsigma\left(\left|E\right|\right)$ is the standard deviation function of the amplitude of a given field E and $\text{cov}\left(\left|E\right|, \left|E_{ob}\right|\right)$ is the covariance between the amplitudes of two field distributions.

B.3   Choice of phase levels for the unit cell and inter-layer axial separation

Figure 51(a) shows the phase error between our bi-layer meta-axicon (3.10) and an ideal axicon (3.2), averaged for values of d ranging from 100 μm to 7 mm, as a function of the inter-layer separation t_{ax} and using 16 level phase discretization and Figure 51(b) shows the phase error for a fixed value of $t_{ax} = 700$ μm as a function of d. It is clear from Fig. 51(a) that the phase error is minimum for $t_{ax} = 700$ μm, but almost constant until $t_{ax} = 2.5$ mm. The minimum error doesn't occur at $t_{ax} = 0$ because the diffraction in the inter-layer gap removes some of the error induced by the metasurface phase discretization. In the Fig. 51(b), the error starts to increase rapidly for $d > 7$ mm. This is due to the approximation $d \ll (x, y)$ used in (3.6) losing its validity.

Finally, Table 7 summarizes the diameters of the micro holes and its transmittance and phase shift values. A constant phase value $\varphi_o = 45°$ is added, resulting in the normalized phase column, so the holes with the least transmittance are the least used in the necessary phase distribution of the metasurfaces, maximizing the transmission.
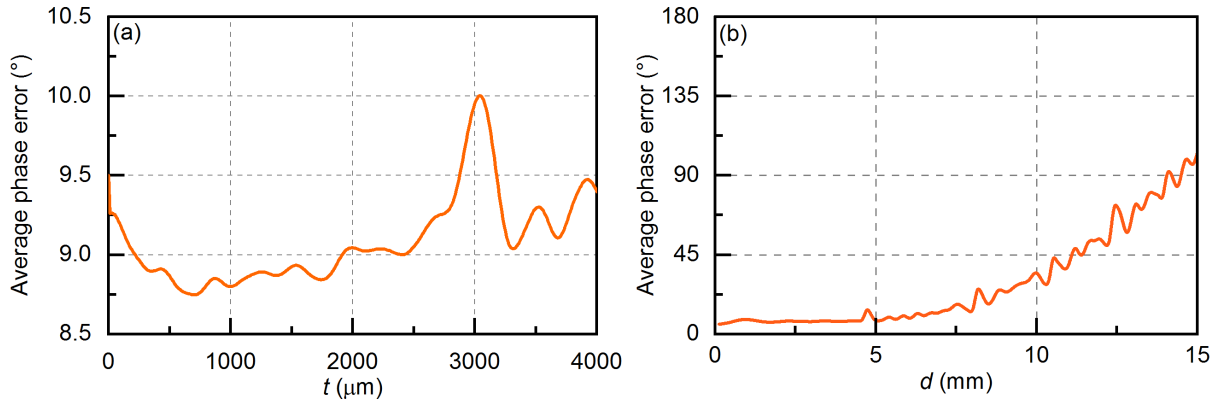
Figure 51 – (a) Phase error induced by the bilayer metasurface approach averaged for 100 μm $< d, 7$ mm. Its minimum occurs for $t_{ax} = 700$ μm. Note that negligible extra phase error is induced by the diffraction in the inter-layer gap for $t_{ax} \leq 2.5$ mm. (b) Phase error induced by the bilayer metasurface approach with $t_{ax} = 700$ μm. When the approximation used for the Alvarez's approach loses validity, the phase error starts to increase, as observed for $d > 7$ mm.

Table 7 – Characteristics of chosen meta-cells

Diameter (μm)	Transmittance (%)	Simulated phase (°)	Target phase (°)	Normalized phase (°)
67	35.6	-22.6	22.5	22.4
72	44.9	-45.5	0.0	0.4
75	66.7	-67.2	-22.5	-22.2
77	90.5	-91.0	-45.0	-46.0
79	99.8	-112.7	-67.5	-67.7
80	93.4	-133.6	-90.0	-88.6
82	71.5	-157.7	-112.5	-112.7
85	50.6	179.4	-135.0	-135.6
88	42.9	156.9	-157.5	-158.1
90	51.2	135.8	-180.0	-179.2
92	72.1	112.1	157.5	157.1
93	90.5	91.4	135.0	136.4
94	99.9	66.1	112.5	111.1
95	92.8	45.1	90.0	90.1
96	74.5	22.1	67.5	67.1
98	57.3	0.0	45.0	45.0

Appendix C − TERAHERTZ PASSIVE AMPLIFICATION VIA THE TEMPORAL TALBOT EFFECT IN METAMATERIAL-BASED BRAGG FIBERS: APPENDICES

C.1   Silicon metamaterial homogenization

As mentioned earlier, the choice of low-loss materials plays a crucial role in our design because it affects the overall achievable gain. Table 8 summarizes the electromagnetic properties of various dielectric materials in the THz range. Note that silicon has a loss tangent two orders of magnitude lower than any other material listed. To take advantage of such a low loss tangent and yet allow a monolithic structure, we analyze the metamaterial shown in the inset of Fig. 52, which consists of silicon with air holes with dimensions much smaller than the wavelength, via the homogenization process from (176). The hole periodicity varies from 20 to 40 μm, with a fill factor ranging from 5% to 75%. Figs. 52(a-b) show the effective relative permittivity and loss tangent, respectively, for an operating wavelength of 376 μm. Since the spatial period of the structure is much smaller than the operating wavelength, its influence on the effective permittivity and loss tangent is negligible. We achieve permittivity values between 3 and 11 and loss tangent between 1.4×10^{-5} and 2.0×10^{-5}.

Table 8 − Electromagnetic Properties of materials in THz

Materials	Frequency (THZ)	Real relative permittivity	Loss tangent
High resistivity Si (225)	1	11.68	2.095×10^{-5}
Al2O3 (Sapphire) (249)	1	10.96	0.003
SiO2 (249)	1	3.92	0.02
SU8 (246)	1	3.02	0.0521
Al2O3 (Alumina) (250)	1	9.00	0.005
PSX (248)	1	2.12	1×10^{-3}
TPX (248)	1	2.52	1×10^{-3}
Zeonor (248)	1	2.28	1×10^{-3}
Alumina-doped PDMS (40% alumina) (247)	1	2.80	0.05

We use this procedure to obtain the effective permittivity of each metamaterial layer, both in the primary and secondary Bragg reflectors (see Section 4.3).

C.2   FEM simulation data processing

Full-wave simulations of our Bragg fiber are carried out by finite element method (FEM) simulations based on the Comsol Multiphysics$^{\text{TM}}$ software to validate the TMT-S and TMT-W results. However, numerical (grid) dispersion and other discretization errors
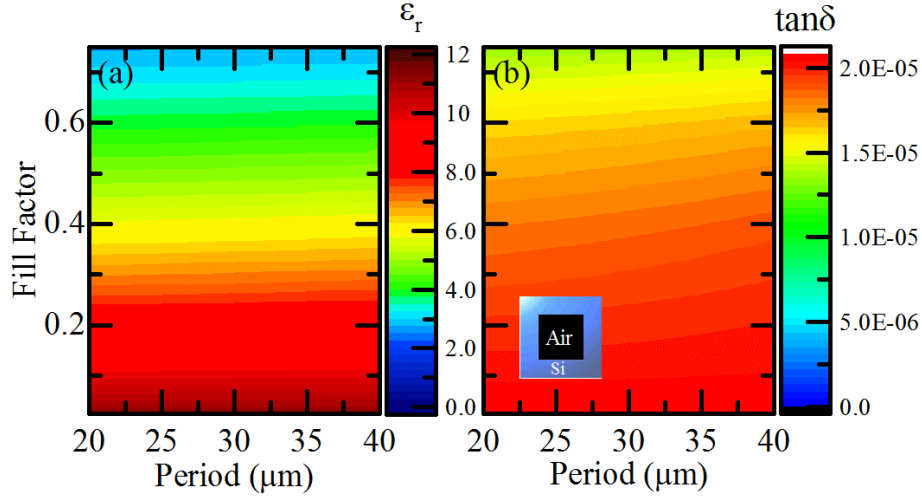
Figure 52 – (a) Effective permittivity and (b) loss tangent of the homogenized silicon structure patterned with air holes. The pattern period is much smaller than the operating wavelength. As a result, the extracted parameters are affected almost exclusively by the fill factor. Adapted with permission from (265)© Optica Publishing Group.

inherent to FEM (42) cause small fluctuations in the real and imaginary parts of the effective index. Therefore, a fitting procedure is used to better represent these values. The FEM simulations comprise 151 frequency points each, in the 810 to 840 GHz range. The dispersion coefficient from the TMT-W resembles the sum of two Gaussian curves with opposite signs. By integrating this sum twice, we obtain a fitting equation for the real part of the refractive index from the FEM results:

$$n_{\text{real\_fit}} = -A_{fit}\left[\frac{a_{fit}}{\sqrt{\pi}}e^{\frac{-(f-df_1)^2}{a_{fit}^2}} + (f-df_1)\operatorname{erf}\left(\frac{f-df_1}{a_{fit}}\right)\right] + B_{fit}\left[\frac{b_{fit}}{\sqrt{\pi}}e^{\frac{-(f-df_2)^2}{b_{fit}^2}} + , \right.$$

$$\left. (f-df_2)\operatorname{erf}\left(\frac{f-df_2}{b_{fit}}\right)\right] + K_1\left(f-8.26\cdot10^{11}\right) + K_2 \tag{C.1}$$

where A_{fit}, a_{fit}, B_{fit}, b_{fit}, df_1, df_2, K_1, K_2 are the fitting parameters, and erf is the error function. Table 9 (upper part) lists the fitting parameters for the three heights. In addition, we use the following skewed Gaussian function to fit the imaginary part of the effective index:

$$n_{\text{imag\_fit}} = K_3 e^{-\frac{(\lambda-\lambda_{sk})^2}{\sigma^2}}\operatorname{normcdf}\left(S_{fit}\lambda, S_{fit}\lambda_{sk}, \sigma_{fit}\right), \tag{C.2}$$

$$n_{\text{fit}}\left(f\right) = n_{\text{real\_fit}} + jn_{\text{imag\_fit}}, \tag{C.3}$$

where normcdf is the standard normal cumulative distribution function, S_{fit} is the fitting skew factor, K_3 is the amplitude fitting constant, λ is the operating wavelength, and λ_{sk}

and σ_{fit} are fitting constants. Table 9 (bottom part) lists the employed fitting parameters for the imaginary part of the refractive index of the three structures.

Table 9 – Fitting parameters for the effective index of the proposed fiber

Parameter	$H = 3000\ \mu$m	$H = 5000\ \mu$m	$H = 7000\ \mu$m
A_{fit} [s]	5.007×10^{-12}	5.044×10^{-12}	4.857×10^{-12}
a_{fit} [Hz]	2.135×10^{-9}	2.157×10^{-9}	2.064×10^{-9}
B_{fit} [s]	4.342×10^{-12}	4.376×10^{-12}	4.161×10^{-12}
b_{fit} [Hz]	5.254×10^{9}	5.297×10^{9}	4.875×10^{9}
K_1 [s]	1.198×10^{-12}	1.234×10^{-12}	1.261×10^{-12}
K_2	0.940	0.941	0.942
df_1 [Hz]	8.323×10^{11}	8.323×10^{11}	8.323×10^{11}
df_2 [Hz]	8.237×10^{11}	8.239×10^{11}	8.237×10^{11}
λ_{sk} [μm]	359.5	359.0	360.0
S_{fit}	2.5	1.5	5.0
σ_{fit} [μm]	3.5	6.0	5.0
K_3	0.50	0.25	0.18

C.3 Time domain waveforms

To understand the phenomena behind our results, we examine further the time waveforms of both the CPA and FTAI approaches. We also address the case in which the phase profile is that of a 40 GHz bandwidth phase modulator instead of an ideal one. Some of these scenarios correspond to a gain above the theoretical limit $\sqrt{q}$. Figure 53 presents time domain waveforms for the CPA ($q = 3$, $m = 2$(a,e) and $m = 4$(b,f), $T' = 280$ ps) and FTAI cases ($T = 500$ ps, $q = 3$(c,g) and $q = 5$(d,h)). Thick blue lines represent amplitude and thin red lines represent phase, while dashed and solid lines represent input and output waveforms, respectively. In panels (a)-(d) we assume the input signal modulated by an ideal phase profile, while in panels (e)-(h) the input signal is modulated by a bandwidth-limited phase profile. Note that the signals in (a)-(d) vary only slightly when compared to those in (e)-(h). Therefore, the abrupt change in the phase profile is not a critical issue for the proposed passive gain approaches. Note that although the FTAI gain is higher than the CPA gain, it spreads the energy outside the pulse slot, which contributes to the SNR degradation observed in Fig. 26 on page 98. In Figure 24, we observe that gains higher than $\sqrt{q}$ are obtained for high values of T'. This suggests than the pulse must have been compressed for its peak to reach a higher value. This pulse compression effect is akin to the compression observed in chirped pulses (48). New frequency components are not generated during propagation, but rather through the phase modulation. Figures 53 (b) and (f) show time-domain waveforms for the highest gain case ($T' = 280$ ps, $m = 4$, $q = 3$).

Next, we analyze how the parameter Ov in (4.26) changes the performance of the BTAI passive amplification. The BTAI method steps are shown in Fig. 54. The first
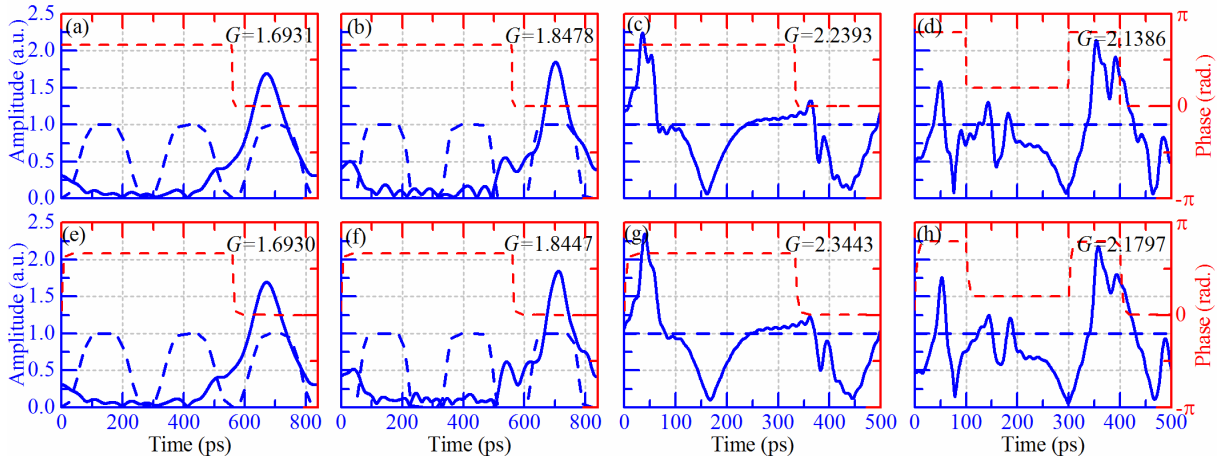
Figure 53 – CPA and FTAI time domain results. (a) and (e) CPA with $T' = 280$ ps , $q = 3$ and $m = 2$, (b) and (f) CPA with $T' = 280$ ps , $q = 3$ and $m = 4$, (c) and (g) FTAI with $T = 500$ ps, $q = 3$, (d) and (h) FTAI with $T = 500$ ps and $q = 5$. Top panels use ideal phase profiles while bottom panels use 40 GHz bandwidth limited phase profiles. Note that the output pulse changed its shape due to compression and presents a gain higher than $\sqrt{3}$ in (b), (c), (f) and (g). Dashed lines refer to input waveforms while solid lines refer to output waveforms. Thick blue lines refer to amplitude and thin red lines refer to phase. Adapted with permission from (265)© Optica Publishing Group.

line shows the target signal. The target signal is then backpropagated from $z = 0$ until $z = -z_{TT}/2$ and we search for the length where the ripple $V_r = \Delta V/V_{\text{avg}}$, where ΔV is the amplitude variation and V_{avg} is the average amplitude, is minimized. The next column shows the input CW (and respective phase modulation obtained via backpropagation of the target signal). Lastly, the output signal (normalized to amplitude $= 1$) is shown. Amplitudes are shown in blue lines and phases are shown in red lines. The second line shows the same curves for $Ov = 5\%$, where the SNR peaks (output overmodulation and noises are reduced). The last line shows the curves for $Ov = -13\%$, maximizing the gain at the cost of a lower SNR. Thus, Ov can be used as a parameter to maximize the gain or to reduce unwanted noise or overmodulation. Note that when Ov has negative values, V_r increases, and the output overmodulation also increases. When Ov has positive values, V_r decreases, and the backpropagated signal is closer to a CW wave. The output is then closer to the desired pulse shape.

C.4   Wafer stacking and fabrication

As discussed in Section C.1, we assume silicon with air holes as our dielectric. However, our necessary propagation lengths are much longer than the thickness of typical silicon wafers, which are on the order of $500 - 600$ μm. Thus, to fabricate our dispersive medium, wafer stacking is required after etching each layer.

A direct wafer bonding process is described in (343). The etched wafers are cleaned
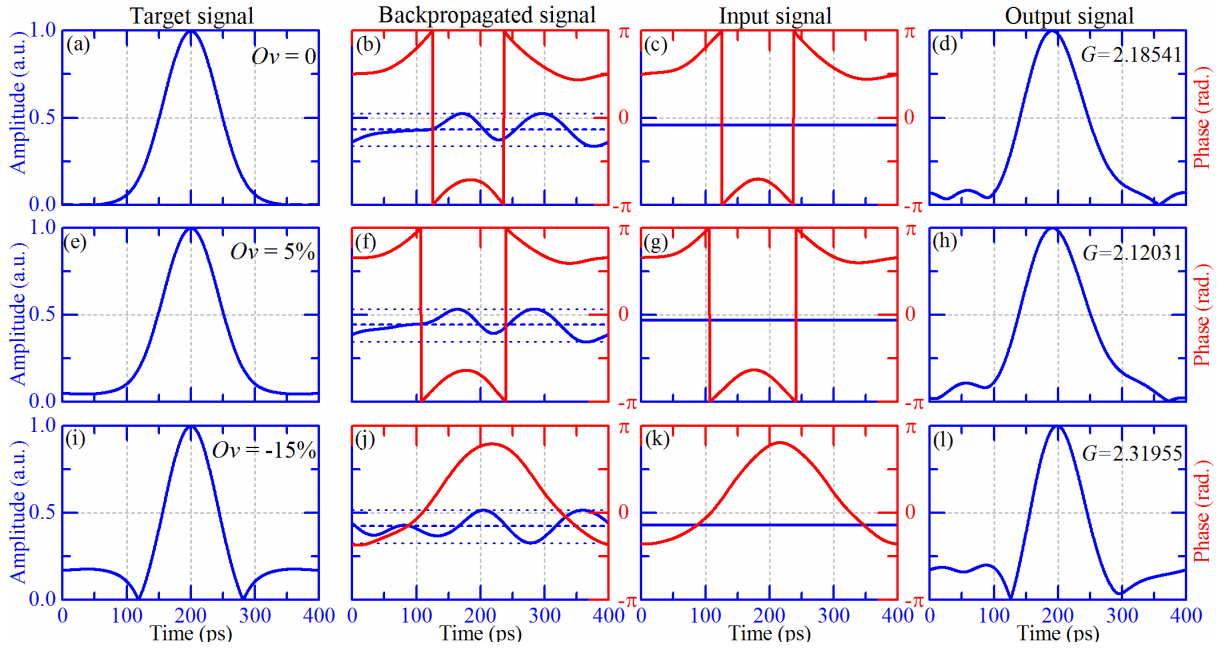
Figure 54 – Time waveforms for BTAI with $T_{FHWM} = 70$ ps and $T = 400$ ps. (a) Target signal with $Ov = 0$. (b) Backward propagation of (a) for minimum ripple. The amplitude is normalized for a target signal of unit amplitude. (c) Input signal with phase profile obtained from (b). (d) Obtained output when propagating (c). Amplitude is normalized to 1. (e) and (i) Target signals with $Ov = 5\%$ and -15% respectively. Plots (f)-(h) show each step relative to the target signal in (e) and plots (j)-(l) show relative to (i). In (b),(f),(j), the ripple maximum and minimum is shown with dotted lines and the signal average is shown with a dashed line. Adapted with permission from (265)© Optica Publishing Group.

with a buffered oxide etchant solution or hydrofluoric acid. Then, they are prepared with a standard RCA clean. Alignment and contact is then performed using the necessary microscopy equipment. A CCD is used to examine the contacting with the aid of an infrared source. Finally the stacked wafers are annealed for 1h at 1050 °C and the bonding process is finished. Figure 55 shows how the final structure looks like, with air core of size $H \times t_{\text{core}}$, total length L, and composed of $n_{wafers} = L/t_{wafer}$ layers of silicon, where t_{wafer} is the thickness of a single silicon wafer.

C.5   Alternative planar structure

To avoid the use of multiple Si wafers and the stacking process, we propose an alternative planar structure, composed of a single microholed high-resistivity 600 μm Si wafer, metalized with gold ($\sigma = 4 \times 10^7$ S/m at 1 THz (344)) in its top and bottom faces, as shown in Fig. 56. This method reduces the number of fabrication steps and provides a reduced size monolithic structure, eliminating layer alignment issues.

Figure 57(a)-(c) shows the simulated dispersion characteristics of the planar structure in comparison with the previously analyzed rectangular structure ($H = 7000~\mu$m).
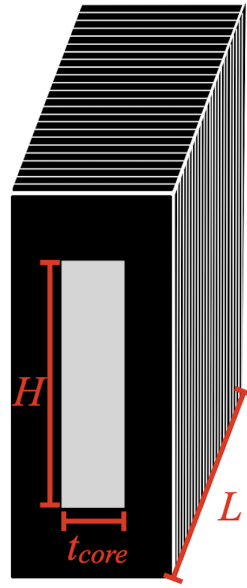
Figure 55 – Illustration of the bonded Si wafers to form our dispersive THz fiber. A number of wafers is stacked to achieve the necessary propagation length L. Adapted with permission from (265)© Optica Publishing Group.
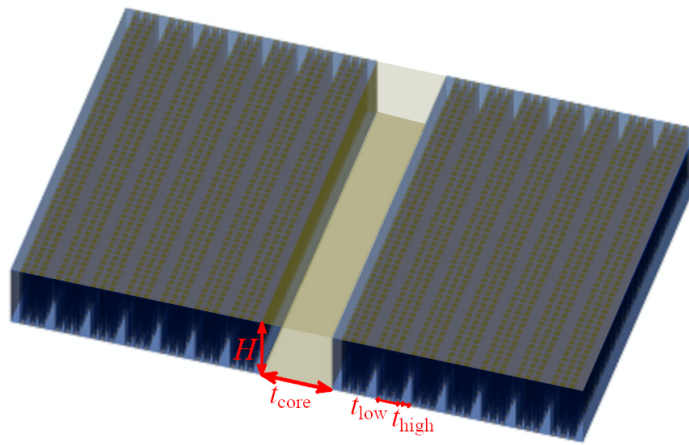

Figure 56 – 3D model of the proposed planar alternative structure. The air core has dimensions of $t_{\mathrm{core}} \times H$ and each period of the Bragg reflector is equal to $(t_{\mathrm{low}} + t_{\mathrm{high}})$. Gold layers are present in the top and bottom faces of the Bragg waveguide. Not in scale.

Note in 57(b) that there the dispersion peak redshifts in 2.05 μm and the maximum value of $2\pi |\beta_2|$ increases from 7.2 ns^2/m to 8.1 ns^2/m, while the dispersive bandwidth is slightly reduced. Moreover, 57(c) shows that the ohmic losses in the top and bottom layers add an extra 0.064 dB/cm propagation loss (at their respective maximum dispersive wavelengths) in the planar structure, which won't substantially reduce G in FTAI and BTAI approaches, since L is on the order of 1 cm.
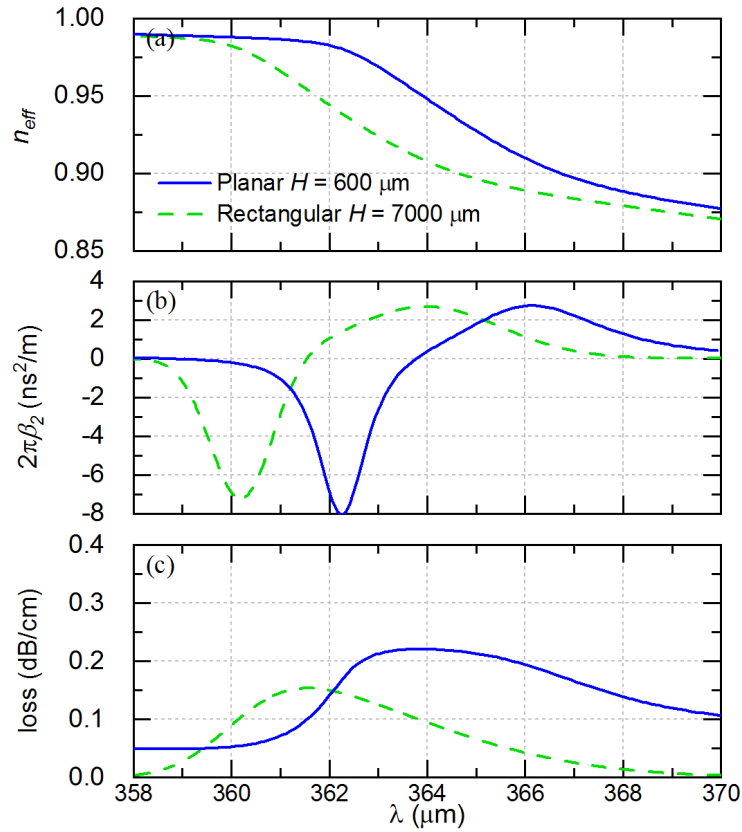
Figure 57 – Simulation results of the proposed planar fiber ($H = 600$ μm,solid blue lines) compared to the wafer-stacked rectangular one ($H = 7000$ μm, dashed green lines). (a) Effective index, (b) dispersion coefficient, and (c) propagation losses. The planar structure redshifts the dispersion peak in 2.05 μm and increases $2\pi |\beta_2|$ from 7.2 ns^2/mto 8.1 ns^2/m. An extra loss of 0.064 dB/cm is observed in the planar structure due to ohmic losses on the gold layers. However, this doesn't significantly affect the gain for short propagation length cases, such as FTAI and BTAI.

Appendix D – ROLE OF DIELECTRIC LOSS IN REALIZED PASSIVE GAIN

In section 4, we obtained a maximum gain of 4.03 dB. However, looking at $|T_{23}^{\text{circ}}|$ in Fig. 33, it is easy to see that it its far below the unity value limits the realized gain. Since the LCBG is a reflective structure, we know that its reflectivity can only be reduced by two factors: ohmic losses in the waveguide walls and dielectric losses of the SLA resin (please, see Fig. 58 for frequency dependent relative permittivity (blue curve) and loss tangent (red curve) of the resin). Since the waveguide walls are made of copper, which possesses an extremely high electric conductivity $\sigma = 5.8 \times 10^7$ S/m, we proceed to analyze the role of dielectric losses by simulating the designed LCBG with $\tan \delta = 0.005, 0.010,$ 0.015, 0.020, and 0.025. The simulated values of $|S_{22}^{\text{wg}}|$ are shown in Fig. 59, along with their measured values (in black lines). Thick blue and red lines, thin green lines, dashed purple lines, and dotted orange lines are used for $\tan \delta$ ranging from 0.005 to 0.025. Note how higher losses reduce the average value of the reflectivity and increase the peak-valley contrast.
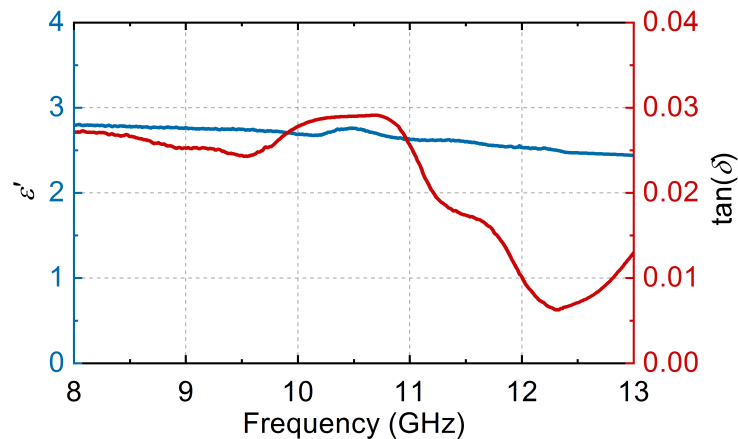

Figure 58 – Measured frequency dependency of the SLA resin used for fabricating the LCBG. Left axis shows the real part of the relative permittivity in blue lines and right side shows the dielectric loss tangent. Note that there is some dispersive behavior to the resin, with its real part reducing from approximately 2.8 to 2.5 as the frequency increases, while the loss tangent experiences a fast decrease in frequencies above 11 GHz.

To evaluate how much a reduced reflectivity affects G, we simulate all four cases analyzed in Section 5.4 with varying losses. Table 10 summarizes the simulated G and SNR values for the different values of $\tan \delta$. Cases 1 to 4 refer to Gaussian G optimization, Gaussian SNR optimization, RC G optimization, and RC G optimization with side peak limitation. The results show that an extra 4.13 dB of gain can be obtained by using a low-loss dielectric for the LCBG. Furthermore, a flatter response in the reflectivity translates into a higher SNR for cases 1 and 3. In the cases optimized for SNR or side
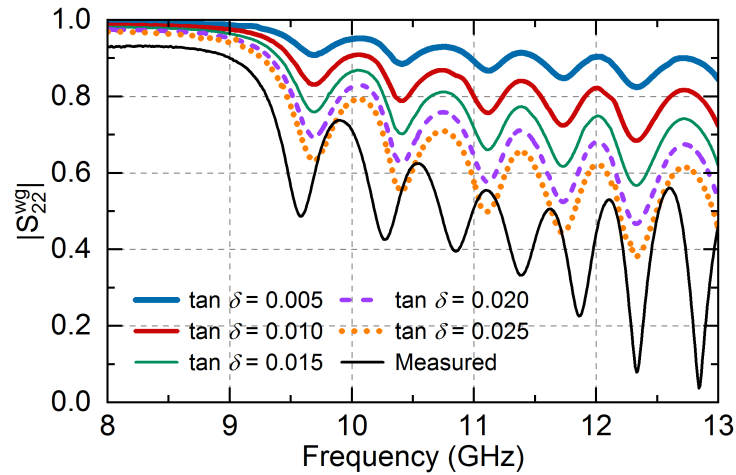
Figure 59 – Simulated values of the reflection coefficient of a WR-90 waveguide loaded with our designed LCBG for different values of dielectric loss tangent. From lowest to higher, they are shown as thick blue and red solid lines, and thin green, dashed purple, and dotted orange lines. Measured values are shown with solid black lines for reference. The influence of the losses in the reflectivity is clear. Both its average value and the depth of the valleys are severely affected as $\tan\delta$ increases, suggesting it is indeed the main limiting factor for G.

peak intensity, the achieved SNR is lower than the measured values. This happens because the phase profile optimization was carried out considering the measured frequency response pattern and thus any change in it will decrease the SNR.

Table 10 – BTAI G and SNR for different $\tan\delta$ values

$\tan\delta$	Parameter	Case 1	Case 2	Case 3	Case 4
0.005	G (dB)	6.53	5.04	8.16	7.07
	SNR (dB)	12.37	5.04	12.35	9.87
0.010	G (dB)	6.08	4.41	7.65	6.44
	SNR (dB)	11.78	4.42	11.87	9.47
0.015	G (dB)	5.68	3.82	7.11	5.86
	SNR (dB)	11.24	3.82	11.25	9.06
0.020	G (dB)	5.13	3.22	6.57	5.12
	SNR (dB)	10.60	3.22	10.75	8.72
0.025	G (dB)	4.51	2.62	5.96	4.31
	SNR (dB)	10.01	2.62	10.22	8.27
Measured	G (dB)	3.45	1.68	4.03	3.60
	SNR (dB)	8.89	12.34	7.10	12.12

Appendix E – METASURFACE DESIGN AND FABRICATION PROCEDURE

E.1   Metasurface design

Figure 60 shows the design and fabrication flow chart of a metasurface. It starts with two independent steps: Defining the desired phase profile and simulating it via ASF; and defining and optimizing the metasurface unit cell via RCWA. The ASF simulation is then repeated with discrete phase levels (that will be used for fabrication), while the RCWA simulation returns a map of the amplitude and phase responses for a given unit cell geometry, in our case as a function of its period and radius. This map is used to obtain a look up table (Tables 1 and 7) for the desired phase levels, with its exact geometry and complex transmission values. The RCWA data is then used to perform a rigorous simulation of the whole metasurface.

After the simulations are complete, a Matlab script transforms the phase distribution and look up table in a CAD file containing the complete metasurface geometry. The CAD file is then processed for the desired application (3D prinitng/laser machining), to generate the required output file.

Finally, the structures are fabricated and experimentally characterized, as described in their respective Chapters. The fabrication processes are described in the next section.

E.2   Fabrication procedures

E.2.1   Fused deposition modeling (FDM) printing

For FDM printing, the CAD file must be sliced in a 3D printing software. We use Simplify 3D for the slicing. In this file, important information such as printing bed and extruder temperatures, layer thickness, infill percentage and printing velocity are defined. For ABS plastic, used in the metalens from Chapter 2, the bed temperature is set as 110 °C, the extruder temperature is set to 233 °C (240 °C in the first 4 layers), the layer thickness is equal to 0.2 mm, the infill percentage is 100% and the maximum printing velocity is 4800 mm/min [80 mm/s] (the first 4 layers, the infill, and the external layers are limited to 40%, 70% and 90% of the maximum velocity, respectively). The FDM printer is a GTMax 3D Core A1, with a 0.4 mm extruder nozzle, a maximum printing volume of 300 (width) x 200 (depth) x 250 (height) mm, a maximum priting (moving) speed of 120 (200) mm/s, and layer thickness ranging from 0.05 to 0.32 mm.

Note that imperfections might occur due to the 0.4 mm nozzle and air gaps inside the printed structure. In the microwave metalens, these imperfections shifted the focal length from 10 to 13.2 cm. However, this wasn't an issue for this application since the lens' DOF is 5 cm, greater than the shift.
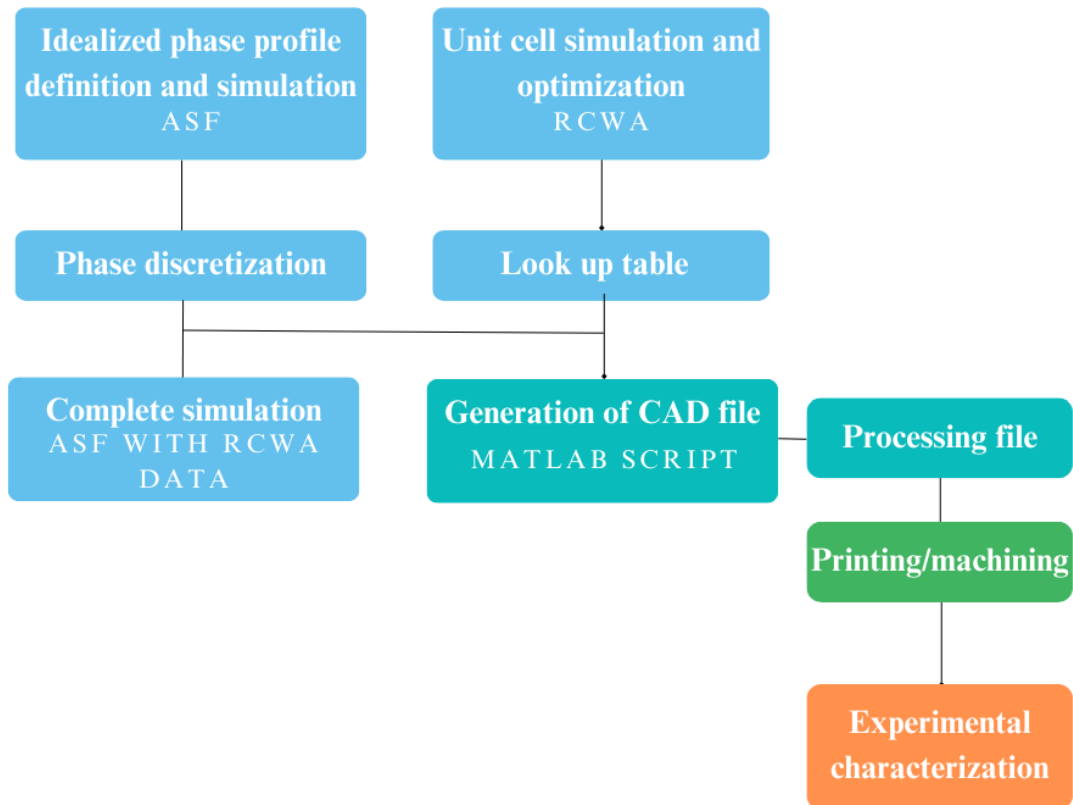
Figure 60 – Metasurface design and fabrication flow chart. The idealized metasurface and unit cell simulations are conduced independently with their respective methods (ASF and RCWA). A final simulation is done using the RCWA data in ASF for a more exact result. The final metasurface is then converted into a CAD file that is processed to generated the necessary files for the 3D printers and laser machining centers. The structures are finally fabricated and experimentally characterized.

E.2.2 SLA printing

The slicing software for resin printing is CHITUBOX. The printer model is Anycubic Photon Mono X 6K. It has a 6K resolution (0.034mm pixels) LCD that is illuminated by 405 nm light. It has a maximum printing volume of 197 (width) x 122 (depth) x 245 (height) mm, with layer thickness ranging from 0.01 to 0.10 mm. The photo-curable Anycubic Craftsman resin was used. The exposure time is set to 1.7 s (40 s for the first 4 layers), with a layer thickness of 0.05 mm and 10 transition layers are used.

The fabricated LCBG is then removed from the printer and washed with 99.8% isopropyl alcohol in an Anycubic Wash&Cure 2. After washing, it is dried and exposed to 405 nm light for 5 minutes in the same Wash&Cure 2 module. This provides a final cure of the piece for extra resistance and toughness, finishing the fabrication process.

E.2.3   Silicon micro-machining

For laser micro-machining, a LPKF ProtoLaser U3 is used. The CAD file is opened in its native software. Extra concentric holes are inserted in the CAD file to guarantee precise machining while reducing the laser exposure time in each hole. This is necessary to reduce substrate overheating that could result in craking. To further reduce overheating, the machining process is divided in two parts. First, half of the substrate thickness (150 μm) is machined. The, the substrate is turned upside down, and the final half is done. The alignment is realized via fiducial holes inserted in the project. The LPKF ProtoLaser U3 has an active area of 229 (width) x 305 (depth) mm, and can machined substrates up to 7 mm thick. It uses a 355 nm wavelength laser with 5W power and 20 μm beam waist. It has an accuracy of 1.22 μm, a repeatability of 2 μm and a focus accuracy of 50 μm, therefore the minimum hole diameter is set to be greater than 50 μm. After machining, the Si substrates are mounted stacked and held together to obtain the necessary (600 μm) thickness and mounted into an FR-4 frame that allows them to be held by micro-positioners for experimental characterization.

Appendix F – PERMISSION FOR REUSE OF PUBLISHED MATERIAL
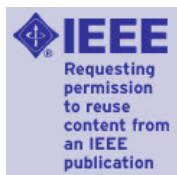
3-D-Printed Dielectric Metasurfaces for Antenna Gain Improvement in the Ka-Band

Author: Vinicius M. Pepino

Publication: IEEE Antennas and Wireless Propagation Letters

Publisher: IEEE

Date: November 2018

Copyright © 2018, IEEE

Thesis / Dissertation Reuse

The IEEE does not require individuals working on a thesis to obtain a formal reuse license, however, you may print out this statement to be used as a permission grant:

Requirements to be followed when using any portion (e.g., figure, graph, table, or textual material) of an IEEE copyrighted paper in a thesis:

1) In the case of textual material (e.g., using short quotes or referring to the work within these papers) users must give full credit to the original source (author, paper, publication) followed by the IEEE copyright line © 2011 IEEE.
2) In the case of illustrations or tabular material, we require that the copyright line © [Year of original publication] IEEE appear prominently with each reprinted figure and/or table.
3) If a substantial portion of the original paper is to be used, and if you are not the senior author, also obtain the senior author's approval.

Requirements to be followed when using an entire IEEE copyrighted paper in a thesis:

1) The following IEEE copyright/ credit notice should be placed prominently in the references: © [year of original publication] IEEE. Reprinted, with permission, from [author names, paper title, IEEE publication title, and month/year of publication]
2) Only the accepted version of an IEEE copyrighted paper can be used when posting the paper or your thesis on-line.
3) In placing the thesis on the author's university website, please display the following message in a prominent place on the website: In reference to IEEE copyrighted material which is used with permission in this thesis, the IEEE does not endorse any of [university/educational entity's name goes here]'s products or services. Internal or personal use of this material is permitted. If interested in reprinting/republishing IEEE copyrighted material for advertising or promotional purposes or for creating new collective works for resale or redistribution, please go to http://www.ieee.org/publications_standards/publications/rights/rights_link.html to learn how to obtain a License from RightsLink.

If applicable, University Microfilms and/or ProQuest Library, or the Archives of Canada may supply single copies of the dissertation.

BACK   CLOSE WINDOW

RE: Reuse permission for thesis {260}

1 message

Optica Publishing Group Copyright <copyright@optica.org>   Mon, Jul 31, 2023 at 4:51 PM
Reply-To: copyright@optica.org
To: vinicius.pepino@usp.br

--reply above this line--

Dear Vinicius Marrara Pepino,

Thank you for contacting Optica Publishing Group.

For the use of material from Vinicius M. Pepino, Achiles F. da Mota, Ben-Hur V. Borges, and Fernando L. Teixeira, "Terahertz passive amplification via temporal Talbot effect in metamaterial-based Bragg fibers," J. Opt. Soc. Am. B 39, 1763-1774 (2022):

> Because you are the author of the source paper from which you wish to reproduce material, Optica Publishing Group considers your requested use of its copyrighted materials to be permissible within the author rights granted in the Copyright Transfer Agreement submitted by the requester on acceptance for publication of his/her manuscript. If the entire article is being included, it is requested that the **Author Accepted Manuscript** (or preprint) version be the version included within the thesis and that a complete citation of the original material be included in any publication. This permission assumes that the material was not reproduced from another source when published in the original publication.
>
> The **Author Accepted Manuscript** version is the preprint version of the article that was accepted for publication but not yet prepared and/or formatted by Optica Publishing Group or its vendors.

While your publisher should be able to provide additional guidance, we prefer the below citation formats:

> For citations in figure captions:
>
> [Reprinted/Adapted] with permission from [ref #] © Optica Publishing Group. (Please include the full citation in your reference list)
>
> For images without captions:
>
> Journal Vol. #, first page (year published) An example: Opt. Express 19, 2720 (2011)

Please let me know if you have any questions.

Kind Regards,

Hannah Greenwood

Hannah Greenwood
July 31, 2023
Authorized Agent, Optica Publishing Group

Dear sir/madam,

I am writing to ask for a permission of reuse of the material submitted in JOSAB as "Terahertz passive amplification via the temporal Talbot effect in metamaterial-based Bragg fibers", in July 2022, Vol. 39, No. 7, 1763-1774 for my Ph.D. Thesis called "Metamaterials and metasurfaces for wavefront shaping and dispersion management".

Thanks in advance,
--

Experimental demonstration of passive microwave pulse amplification via temporal Talbot effect

SPRINGER NATURE

Author: Vinicius M. Pepino et al

Publication: Scientific Reports

Publisher: Springer Nature

Date: Sep 15, 2023

Copyright © 2023, Springer Nature Limited

Creative Commons

Fano-Assisted Tunable X-Band Microwave Ring Resonator

Author: Vinicius M. Pepino

Publication: IEEE Transactions on Microwave Theory and Techniques

Publisher: IEEE

Date: Apr 1, 2021

Copyright © 2021, IEEE

Thesis / Dissertation Reuse

The IEEE does not require individuals working on a thesis to obtain a formal reuse license, however, you may print out this statement to be used as a permission grant:

Requirements to be followed when using any portion (e.g., figure, graph, table, or textual material) of an IEEE copyrighted paper in a thesis:

1) In the case of textual material (e.g., using short quotes or referring to the work within these papers) users must give full credit to the original source (author, paper, publication) followed by the IEEE copyright line © 2011 IEEE.
2) In the case of illustrations or tabular material, we require that the copyright line © [Year of original publication] IEEE appear prominently with each reprinted figure and/or table.
3) If a substantial portion of the original paper is to be used, and if you are not the senior author, also obtain the senior author's approval.

Requirements to be followed when using an entire IEEE copyrighted paper in a thesis:

1) The following IEEE copyright/ credit notice should be placed prominently in the references: © [year of original publication] IEEE. Reprinted, with permission, from [author names, paper title, IEEE publication title, and month/year of publication]
2) Only the accepted version of an IEEE copyrighted paper can be used when posting the paper or your thesis on-line.
3) In placing the thesis on the author's university website, please display the following message in a prominent place on the website: In reference to IEEE copyrighted material which is used with permission in this thesis, the IEEE does not endorse any of [university/educational entity's name goes here]'s products or services. Internal or personal use of this material is permitted. If interested in reprinting/republishing IEEE copyrighted material for advertising or promotional purposes or for creating new collective works for resale or redistribution, please go to http://www.ieee.org/publications_standards/publications/rights/rights_link.html to learn how to obtain a License from RightsLink.

If applicable, University Microfilms and/or ProQuest Library, or the Archives of Canada may supply single copies of the dissertation.

BACK   CLOSE WINDOW